PNL-5777 Vol. II
UC-85

2F

BWR Spent Fuel Storage Cask Performance Test

Volume II

Pre- and Post-Test Decay Heat, Heat Transfer, and Shielding Analyses

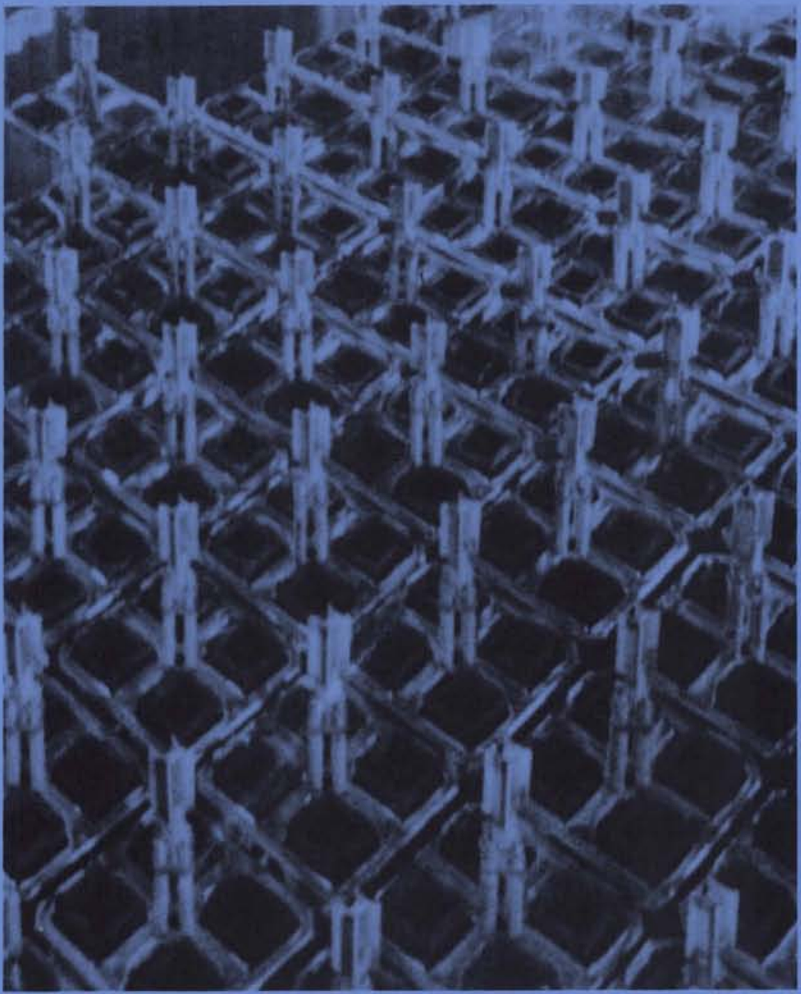

June 1986

Prepared for the U.S. Department of Energy
under Contract DE-AC06-76RLO 1830

Pacific Northwest Laboratory
Operated for the U.S. Department of Energy
by Battelle Memorial Institute

PNL-5777 Vol. II

PACIFIC NORTHWEST LABORATORY
operated by
BATTELLE
for the
UNITED STATES DEPARTMENT OF ENERGY
under Contract DE-AC06-76RLO 1830

Printed in the United States of America
Available from
National Technical Information Service
United States Department of Commerce
5285 Port Royal Road
Springfield, Virginia 22161

NTIS Price Codes
Microfiche A01

Printed Copy

Pages	Price Codes
001-025	A02
026-050	A03
051-075	A04
076-100	A05
101-125	A06
126-150	A07
151-175	A08
176-200	A09
201-225	A010
226-250	A011
251-275	A012
276-300	A013

PNL-5777 Vol. II
UC-85

BWR SPENT FUEL STORAGE CASK PERFORMANCE TEST

VOLUME II

PRE- AND POST-TEST DECAY HEAT, HEAT TRANSFER, AND SHIELDING ANALYSES

L. E. Wiles
N. J. Lombardo
C. M. Heeb
U. P. Jenquin
T. E. Michener
C. L. Wheeler
J. M. Creer
R. A. McCann

June 1986

Prepared for
the U.S. Department of Energy
under Contract DE-AC06-76RLO 1830

Pacific Northwest Laboratory
Richland, Washington 99352

ACKNOWLEDGMENTS

Appreciation is extended to J. L. Daily, P. A. Craig, and G. J. Bracken of the U.S. Department of Energy, Richland Operations Office, for sponsoring this work. D. R. Oden, Jr., D. F. Newman, and G. H. Beeman of the Commercial Spent Fuel Management Program Office managed by the Pacific Northwest Laboratory are acknowledged for their support and guidance during the study.

Thanks are extended to Ridihalgh, Eggers & Associates for providing details of the REA 2023 BWR spent fuel storage cask required for input to the analyses. Appreciation is extended to M. A. McKinnon and J. E. Tanner of the Pacific Northwest Laboratory and to J. W. Doman and C. E. King of the General Electric Company for supplying spent fuel assembly information and cask test data for comparisons with, and evaluation of, the computer codes. In addition, the cooperation of the Nebraska Public Power District in supplying Cooper Nuclear Station operating information is appreciated.

EXECUTIVE SUMMARY

This report describes the decay heat, heat transfer, and shielding analyses conducted in support of performance testing of a Ridihalgh, Eggers & Associates REA 2023 boiling water reactor (BWR) spent fuel storage cask. The cask testing program was conducted for the U.S. Department of Energy (DOE) Commercial Spent Fuel Management Program by the Pacific Northwest Laboratory (PNL) and by General Electric at the latters' Morris Operation (GE-MO) as reported in Volume I.

The analyses effort consisted of performing pretest calculations to 1) select spent fuel for the test; 2) symmetrically load the spent fuel assemblies in the cask to ensure lateral symmetry of decay heat generation rates; 3) optimally locate temperature and dose rate instrumentation in the cask and spent fuel assemblies; and 4) evaluate the ORIGEN2 (decay heat), HYDRA and COBRA-SFS (heat transfer), and QAD and DOT (shielding) computer codes. The emphasis of this second volume is on the comparison of code predictions to experimental test data in support of the code evaluation process. Code evaluations were accomplished by comparing pretest (actually pre-look, since some predictions were not completed until testing was in progress) predictions with experimental cask testing data reported in Volume I. No attempt was made in this study to compare the two heat transfer codes because results of other evaluations have not been completed, and a comparison based on one data set may lead to erroneous conclusions.

After the cask test was completed, the test data were provided to the analysts. Post-test predictions were then performed, if needed, to 1) improve pretest predictions; 2) investigate effects of fuel assembly and cask basket emissivity values; and 3) predict the maximum heat load the cask can dissipate in a vertical orientation with both helium and nitrogen backfill environments. It is important to note that the analysts did not have access to the test data until after their pretest (pre-look) analyses had been completed. This approach ensured an unbiased evaluation of each computer code.

The REA 2023 spent fuel storage cask consists of a double containment design with silicone rubber O-rings for sealing the primary lid of the inner

cavity and a welded final closure on the secondary cover. The cask has a smooth, painted, stainless steel outer skin; a lead/stainless steel gamma shield; and an ethylene glycol/water neutron shield. The fuel basket is constructed of stainless steel clad Boral for criticality control, copper plates for heat conduction to the cask wall, and stainless steel for structural strength. The loaded cask is approximately 5 m (16 ft) long and 2.25 m (8 ft) in diameter, and weighs approximately 100 tons when loaded with 52 unconsolidated BWR spent fuel assemblies. The assemblies were of the General Electric 7x7 rod design from Nebraska Public Power District's Cooper Nuclear Station. The REA 2023 BWR spent fuel storage cask design and manufacturing rights have been acquired by Mitsubishi of Japan, and the cask model designation has been changed to MSF IV.

The ORIGEN2 computer code is a general purpose burnup and decay code featuring extensive data libraries containing information on over 1,200 nuclides. The code is used widely in the nuclear industry to predict decay heat generation rates of BWR and pressurized water reactor (PWR) spent fuel assemblies. The code can be used to perform transmutation calculations in steps of constant power or constant neutron flux level. The resulting nuclide concentrations can be decayed with user-specified time intervals.

This decay heat analysis effort is an extension of similar analyses performed on pressurized water reactor (PWR) assemblies and other BWR assemblies. Results of the ORIGEN2 pretest decay heat analysis are shown in Figures S.1 and S.2. In Figure S.1, predictions of 77 calorimetry measurements of decay heat from 52 spent fuel assemblies are compared to calorimetry data. On the average, predicted values were 2.3 W (1.2%) greater than measured values. The standard deviation about the average difference between predicted and measured values was ±18.0 W (±6.2%). The standard deviation of 14 repeat calorimeter measurements on one of the 52 assemblies used in the cask performance test was ±14 W, which indicates that the agreement between predictions and measured data (±18 W) is almost as good as the repeatability of the measured data. A statistical analysis showed no significant trend in differences between predictions and measured data with either burnup or decay time.

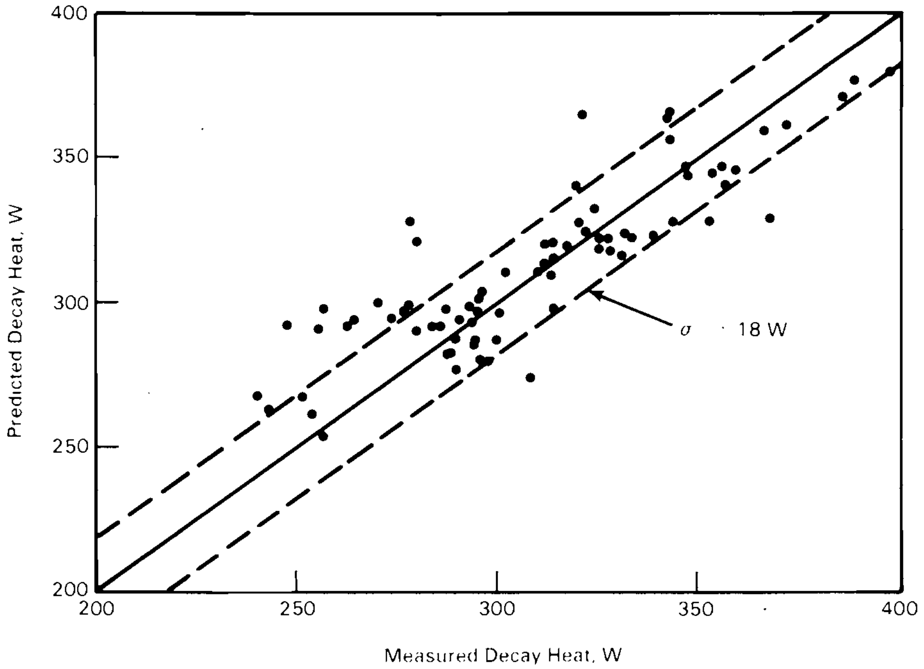

FIGURE S.1. Comparisons of Predicted to Measured Decay Heat Generation Rates

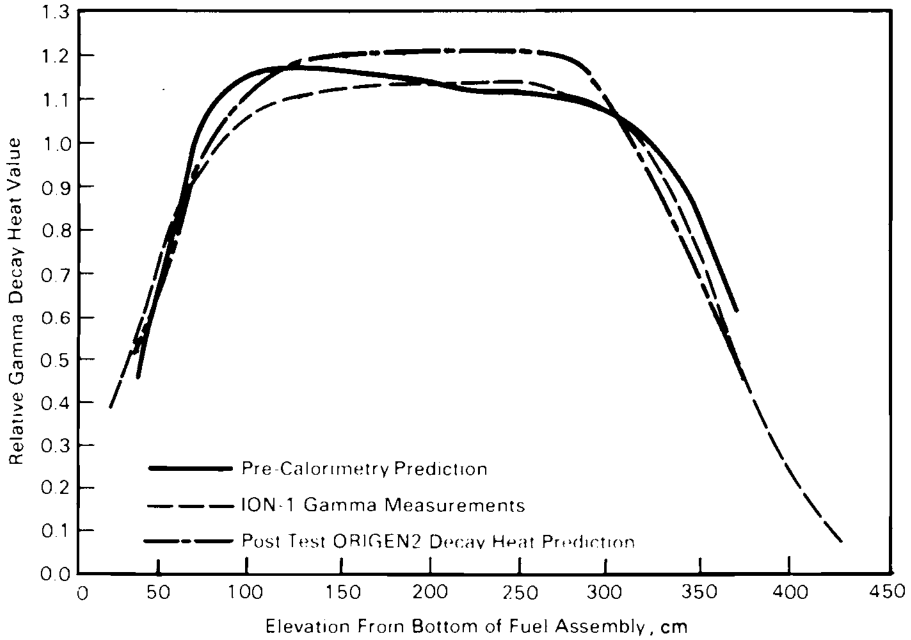

FIGURE S.2. Comparisons of Pre-Calorimetry Predicted Axial Decay Heat Profile with Measured Gamma Radiation Activity and ORIGEN2 Decay Heat Prediction Derived from Measured Gamma Activity

Comparisons of predicted fuel assembly axial decay heat generation profiles with a measured average gamma activity profile are shown in Figure S.2. The pre-calorimetry prediction was made using core-averaged axial burnup distributions contained in Cooper reactor operating histories. Measured gamma data were obtained with an ION-1 detector discussed in Volume I. Post-test ORIGEN2 predictions were obtained using the ION-1 measurements of gamma activity as input.

The pre-calorimetry prediction of the relative axial decay heat profile departs from the measured gamma activity profile near the bottom and top of the active zone of the fuel assemblies. Differences indicate that the assemblies have experienced local irradiation conditions that depart from core average conditions. Differences could be due to any one or a combination of 1) high gadolinium content in the fuel in the lower region of the rods to suppress burnup in the initial operating cycles; 2) partial insertion of control rods during reactor operation; or 3) a reactor power coastdown during the last operating cycle, which decreased the steam void fraction in the upper region of the reactor core and resulted in higher burnup in the fuel near the top of the assemblies. Because a long power coastdown was not evident in the Cooper operating history, the difference between pre-calorimetry predictions and ION-1 gamma data was probably due to either 1) or 2) or both.

The ION-1 gamma activity measurements for each assembly were averaged to produce the composite measured gamma activity curve shown in Figure S.2. This curve was used to calculate an axial node burnup distribution. Several ORIGEN2 cases were then run with the same Cooper operating history, but at various specific powers that, when integrated over the irradiation time, covered the range of axial node burnup values. The axial decay heat rate profile in Figure S.2 was then developed. Differences between the post-calorimetry predicted axial decay heat rate profile and the ION-1 gamma profile are small. Decay heat calculations tend to exaggerate high values and minimize low values because the relationship between burnup and decay heat is slightly nonlinear.

The undocumented HYDRA steady-state thermal hydraulics computer code used to perform heat transfer analyses is fully three-dimensional with user-oriented input. The HYDRA code has been evaluated since 1982 using two single assembly sets of experimental data and two sets of multiassembly data of which this REA cask test data is one multiassembly data set. Once HYDRA is evaluated and if the code performs satisfactorily, documentation is planned during 1987.

The governing equations in HYDRA that define the conservation of mass, momentum, and energy are solved using finite-difference formulations. The equations apply to single-phase, compressible flow. The momentum equation includes convection of momentum, Darcy drag, and orifice drag, and gravitational, pressure, and viscous force terms. Coupled heat transfer modes of conduction, convection, and radiation are accounted for in conjunction with volumetric heat generation. Rod-to-rod and enclosure radiation models can be constructed by input. There is a significant degree of flexibility in specifying temperature boundary conditions. Output consists of steady-state temperatures, pressures, and velocities.

Results of the HYDRA heat transfer analysis are indicated in Figures S.3, S.4, and S.5. In Figure S.3, HYDRA pretest temperature predictions are compared to measured peak temperatures in the form of bar graphs. The test run descriptors on the abscissa are consistent with those specified in Volume I. The top of each bar represents the peak fuel temperature for each run; the bottom of each bar is the ambient temperature. The peak temperature was taken from the center rod of one of the four centermost assemblies. In addition, predicted and measured temperature differences between peak temperatures and the ambient are shown by the length of each bar.

Nonsymmetry between measured peak fuel-to-ambient temperature differences averaged ±3% in the cask and fuel assemblies. This suggests that, if predictions of peak-to-ambient temperature differences throughout the cask are within ±3% of measured values, the predictions are the best that they can possibly be. Predictions for 3 of the 12 vertical runs of Figure S.3 fall within this range, and 9 of the 12 vertical runs fall within ±6% of the measured temperature differences. Overall, this agreement is viewed as exceptional because the predictions are pre-look and the analyst did not have access to the data (with the exception of ambient temperatures) until after the pretest predictions were completed. However, as shown in Figure S.4, comparisons of local temperature differences reveal greater disagreements between predictions and data.

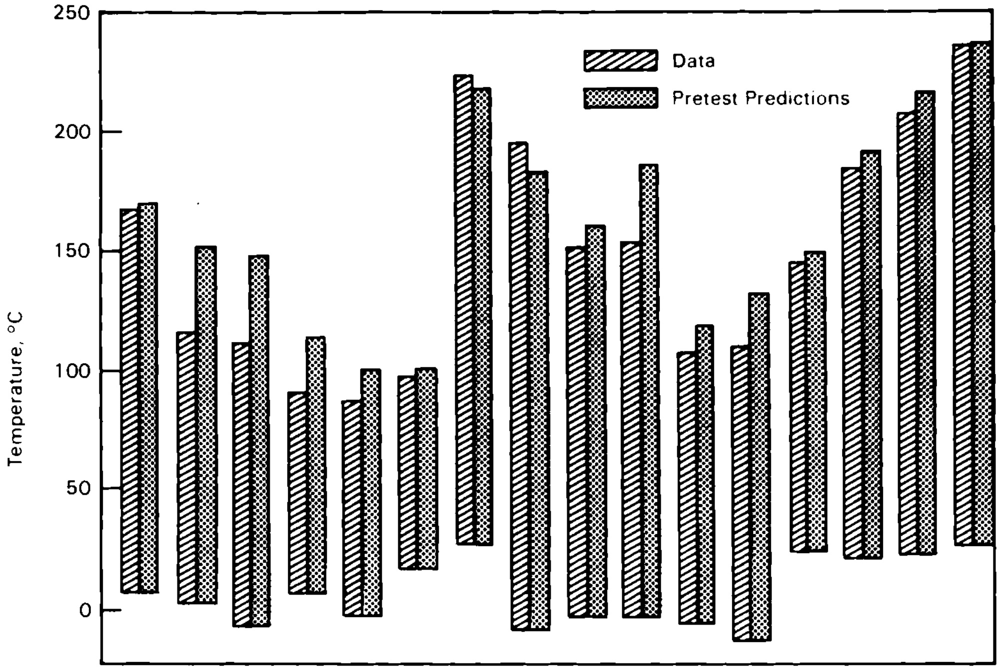

Run No.	1	2	3	4	5a	5b	6a	6b	7	9	10	11a	11b	12	13	14
Orientation	V	V	H	H	V	V	V	V	V	H	H	V	V	V	V	V
Load	P	P	P	P	P	P	F	F	F	F	F	F	F	F	F	F
Backfill	V	N	N	H	H	H	V	V	N	N	H	H	H	H	N	V

Notes: Orientation V = Vertical; H = Horizontal; Load P = Partial (28 assemblies); F = Full (52 assemblies);
Backfill V = Vacuum; N = Nitrogen; H = Helium

FIGURE S.3. HYDRA Pretest Predictions of Peak Fuel Temperatures and Overall Cask Temperature Differences Compared to Data

HYDRA predictions of axial temperature profiles (Figure S.4) for full load, vertical, vacuum, nitrogen, and helium cases are all relatively close to test data. The predicted profiles for the vacuum and helium runs, where convection was not dominating, are in exceptionally good agreement with test data (<30°C). The predicted profile for nitrogen shows the effects of convection and agrees well with data in the upper one-third of the fuel assembly, but deviates from test data by approximately 30°C in the lower part of the assembly. However, peak clad temperatures were predicted exceptionally well (<10°C).

HYDRA predictions of radial temperature profiles are compared to data in Figure S.5. The indicated elevation was that of the peak cladding temperature in nitrogen. Predictions agree exceptionally well (<20°C) with test data.

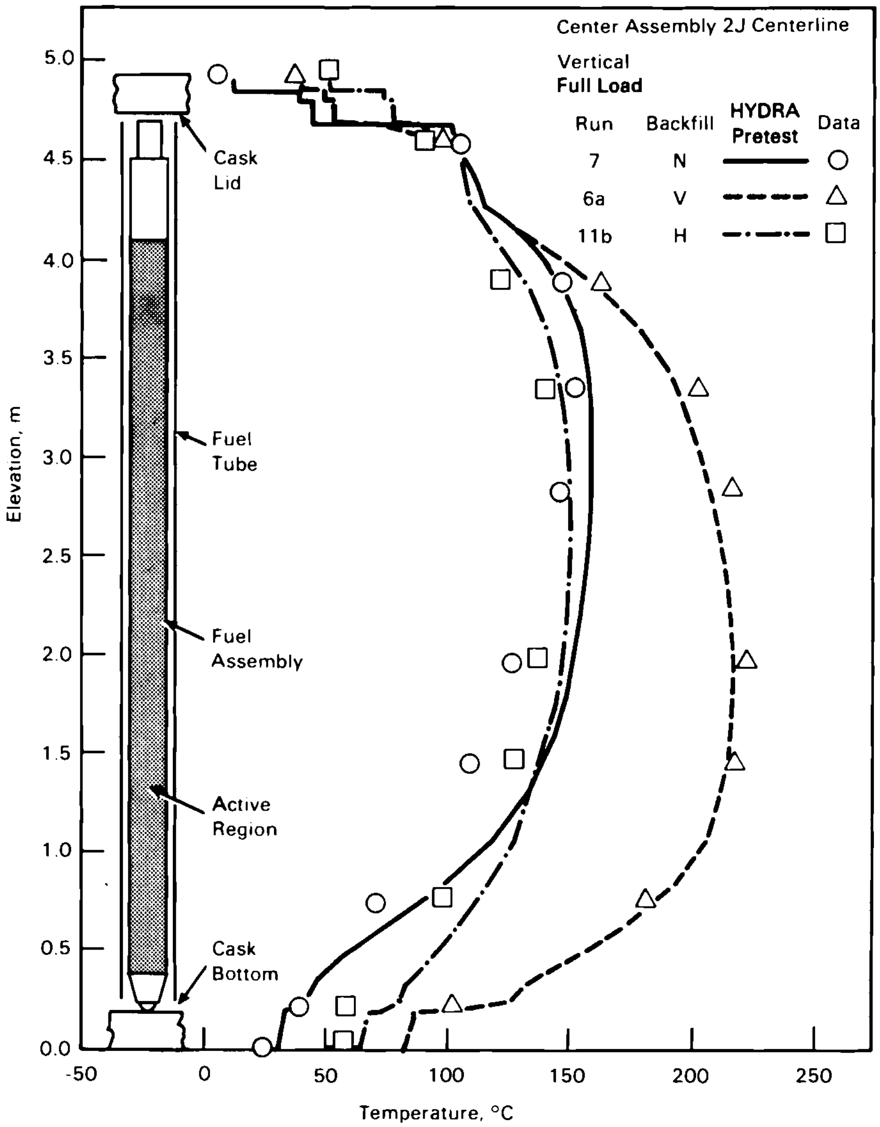

FIGURE S.4. HYDRA Pretest Predictions of Center Assembly Axial Temperature Profiles Compared to Full Load, Vertical, Vacuum, Nitrogen, and Helium Data

The undocumented COBRA-SFS (spent fuel storage) thermal hydraulics computer code was also used to perform REA cask heat transfer analyses. Like HYDRA, COBRA-SFS has been evaluated since 1982 with the same four data sets, two single assembly and two multiassembly. Once COBRA-SFS has been evaluated and if it performs satisfactorily, documentation is planned to be completed in 1986.

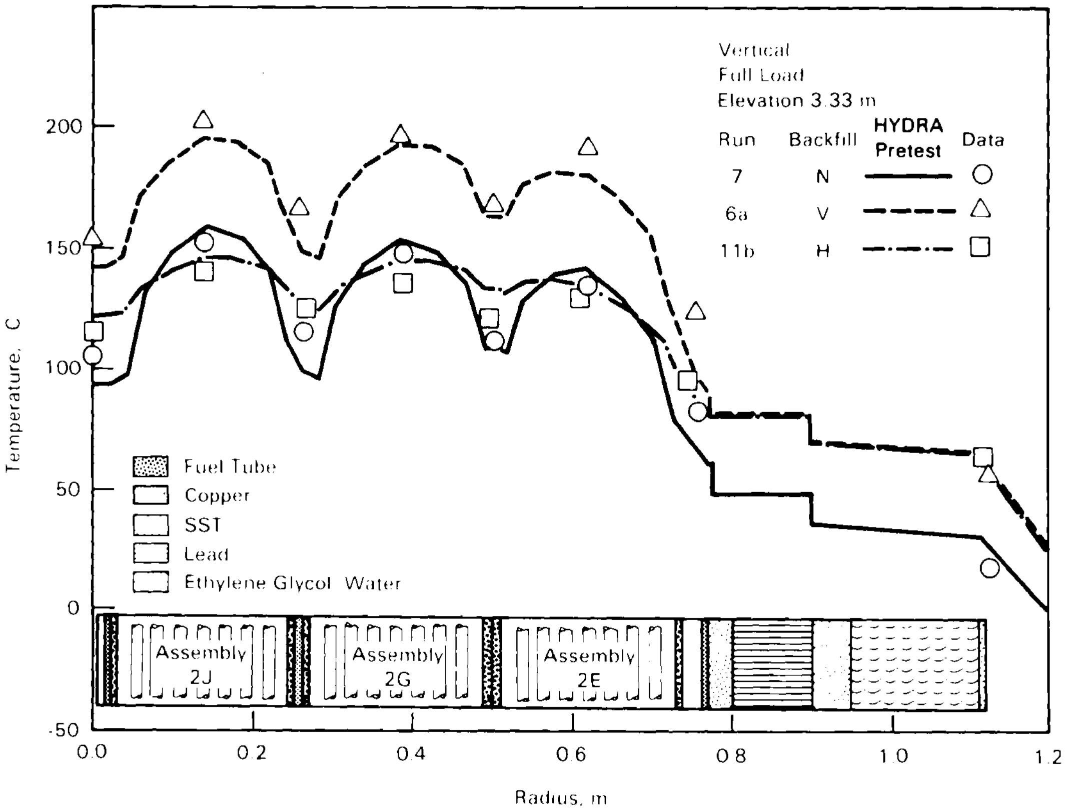

FIGURE S.5. HYDRA Pretest Predictions of Radial (Diagonal) Temperature Profiles Compared to Full Load, Vertical, Vacuum, Nitrogen, and Helium Data

COBRA-SFS predicts steady-state three-dimensional velocity, pressure, and temperature distributions within spent fuel storage systems. The code uses an iterative procedure to solve finite-difference equations for mass, momentum, and energy conservation for an interconnected array of channels and structural members. It uses subchannel representations with arbitrary flow and thermal connections; therefore, the user has a great deal of flexibility in modeling complex geometries. Although COBRA-SFS assumes that the fill medium is incompressible, it uses a thermally expandable model to produce buoyancy-driven circulating flows within the system. Heat is transported throughout the system by conduction (fluid-to-fluid and solid-to-solid), natural convection, and planer radiation (rod-to-rod, rod-to-surface, and surface-to-surface).

COBRA-SFS pretest predictions of cask test data are presented in Figures S.6, S.7, and S.8. Figure S.6 indicates that predictions for 4 of the 12 vertical runs agree within ±3% of measured peak fuel-to-ambient temperature differences. Furthermore, the overall temperature differences of 7 of the 12 vertical runs were predicted within ±6% of measured values. This agreement is considered to be exceptional when considering the pre-look nature of the predictions and the complexities of the REA cask and heat transfer mechanisms.

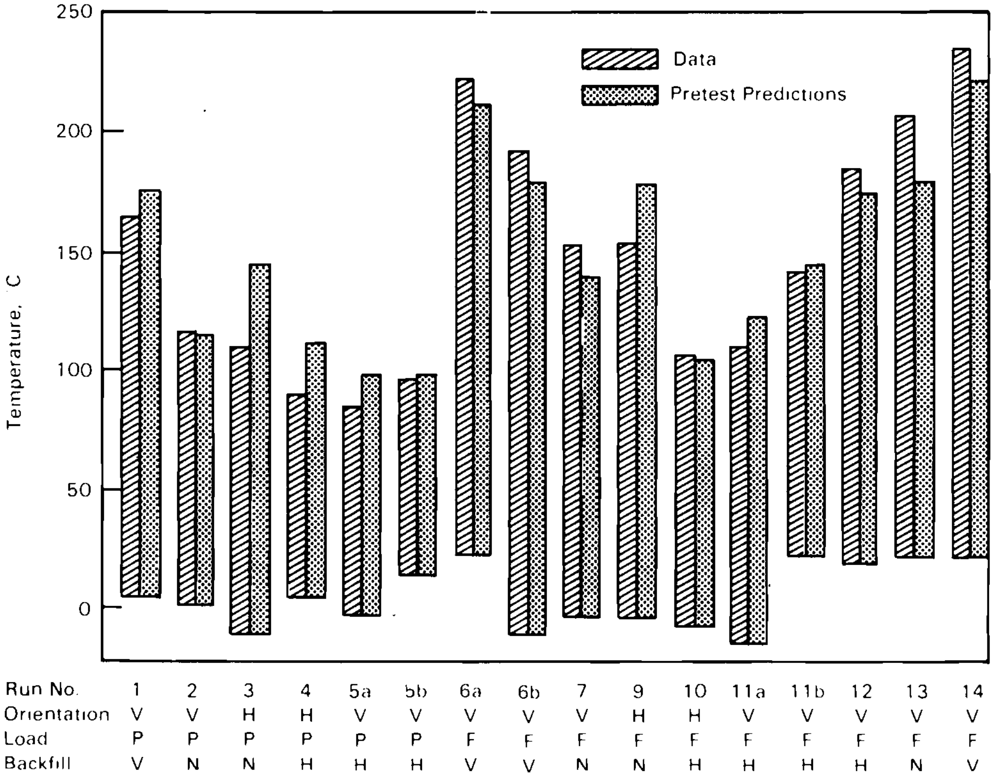

FIGURE S.6. COBRA-SFS Pretest Predictions of Peak Fuel Temperatures and Overall Cask Temperature Differences Compared to Data

COBRA-SFS predictions of axial temperature profiles for full load, vertical, vacuum, nitrogen, and helium cases are shown in Figure S.7. COBRA-SFS predictions compare to data in a manner similar to that of HYDRA. Peak fuel cladding temperatures were predicted within 15°C. The predicted axial profiles for the vacuum and helium runs and horizontal nitrogen runs, which are radiation and/or conduction dominated, agree exceptionally well (<15°C) with experimental profiles. The predicted profile in the vertical nitrogen run shows the effect of convection and agrees reasonably well in the center region of the assembly. However, it differs from data by as much as 30°C near the ends of the assemblies.

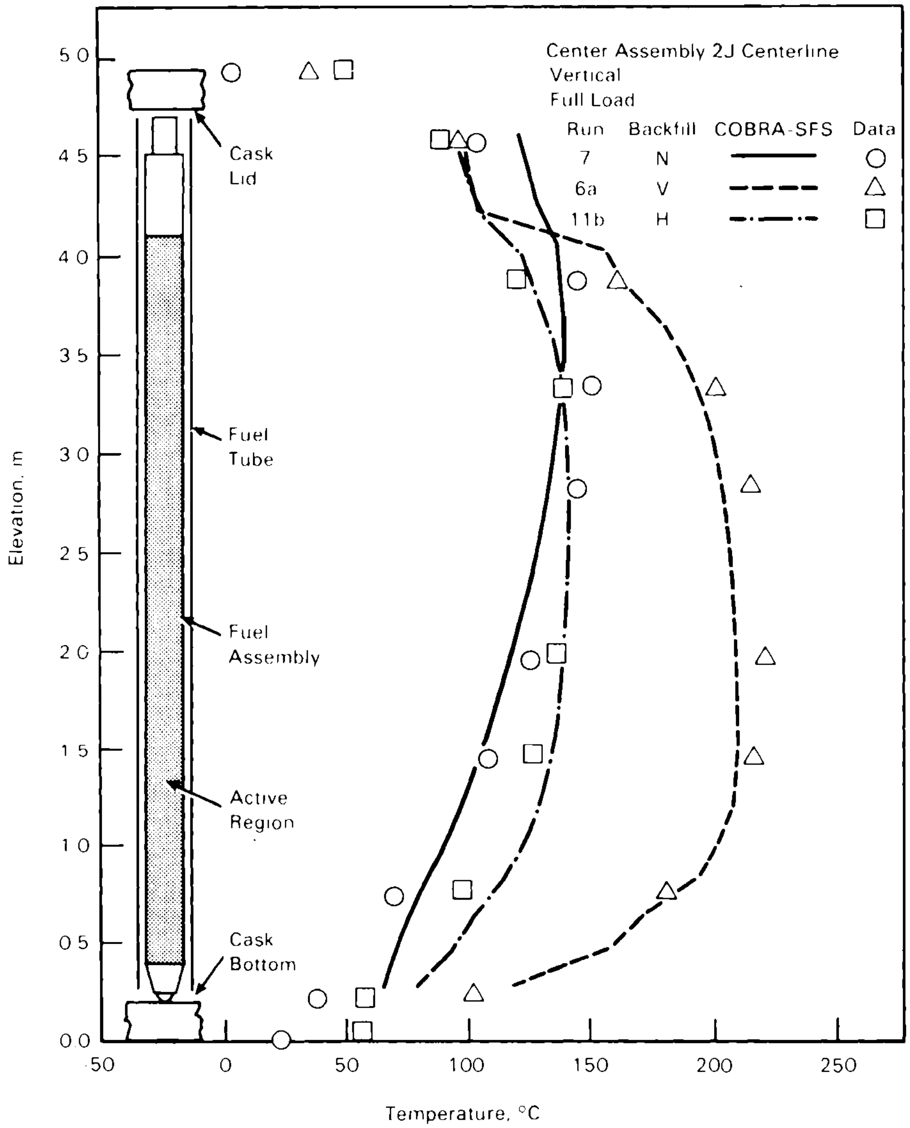

FIGURE S.7. COBRA-SFS Pretest Predictions of Center Assembly Axial Temperature Profiles Compared to Vertical, Full Load, Vacuum, Nitrogen, and Helium Data

COBRA-SFS predictions of radial temperature profiles are compared to test data in Figure S.8. The indicated elevation was that of the peak fuel cladding temperature in nitrogen. All predictions agree exceptionally well (<30°C) with experimental data.

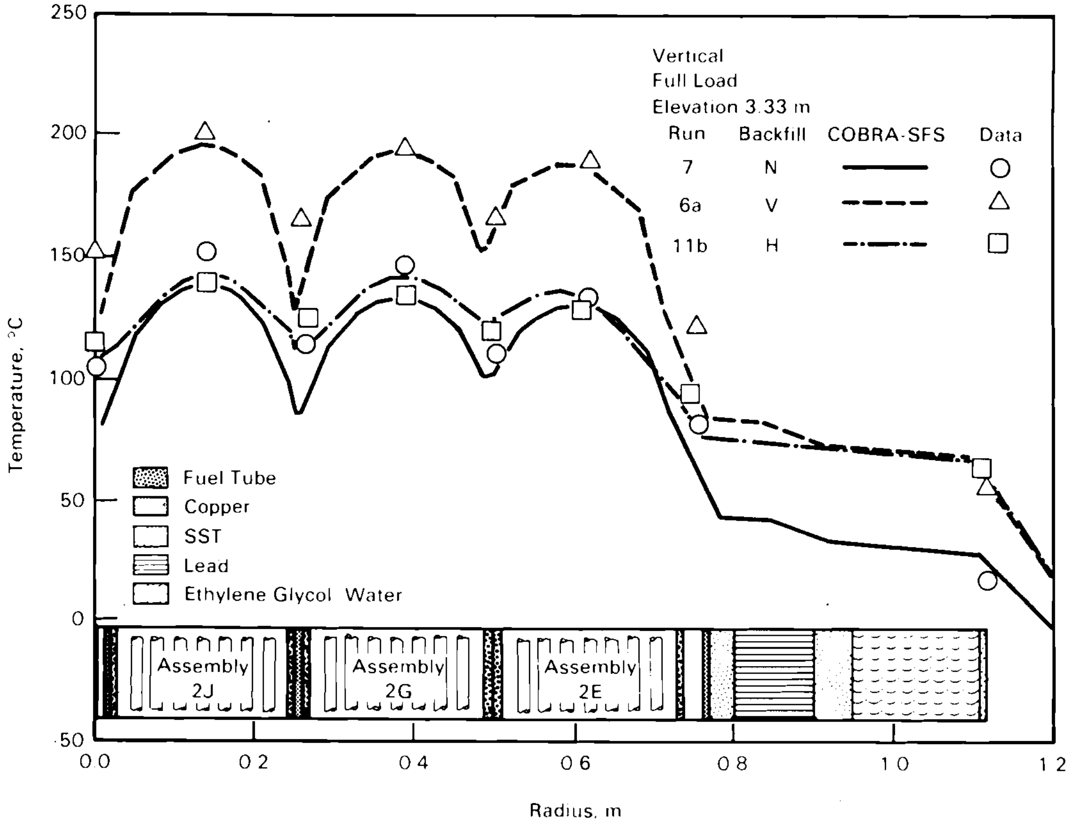

FIGURE S.8. COBRA-SFS Pretest Predictions of Radial (Diagonal) Temperature Profiles Compared to Vertical, Full Load, Vacuum, Nitrogen, and Helium Data

Results of the QAD (primary gamma) and DOT (secondary gamma and neutron) shielding analyses are shown in Figures S.9 and S.10. Shielding predictions are compared to experimental gamma and neutron data obtained on the side of the REA cask.

The QAD computer code used to predict gamma radiation dose rates on the surface of the cask calculates fast-neutron and gamma-ray penetrations through shielding systems using the point-kernel method. The point-kernel method involves representing the source volume by a number of point isotropic sources and computing line-of-sight distances from each source point to points of interest. Geometric and material attenuations are determined from distances through the shielding regions and attenuating characteristics of the shielding materials.

Predicted and measured gamma-ray dose rates are presented in Figure S.9. Over the length of the neutron shield, predictions agree well with measured data. Above and below the ends of the neutron shield, dose rate peaks are underpredicted by a factor of two. This difference is probably due to an

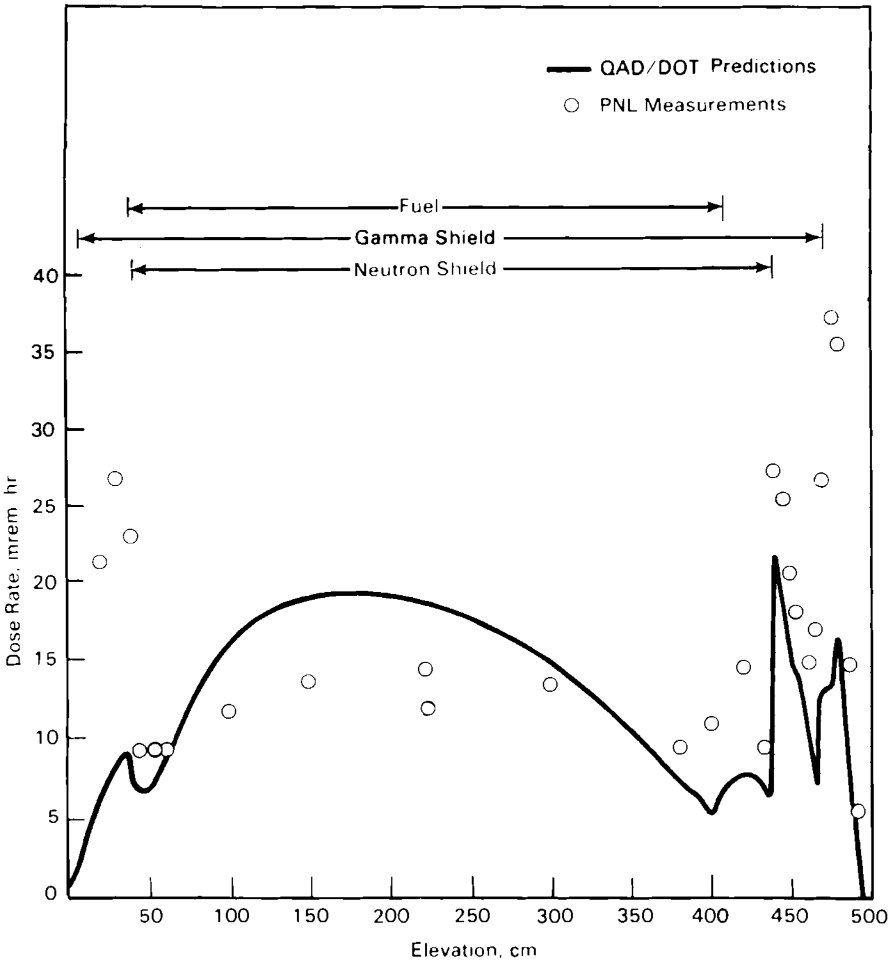

FIGURE S.9. Predicted and Measured Gamma-Ray Dose Rates on Side of Fully Loaded Cask incorrectly assumed cobalt content (source strength) in the stainless steel assembly end fittings because the exact amount of cobalt was unknown.

The DOT computer code used to predict neutron dose rates on the cask surface calculates neutron and photon particle fluxes in two dimensions using the method of discrete ordinates to solve the Boltzmann transport equation. Balance equations are solved for the flow of particles moving in a set of discrete directions in each cell of a space mesh and in each group of a multigroup energy structure. Mesh spacing and discrete directions are selected by the user, and anisotropic cross sections can be expressed in a Legendre expansion of arbitrary order.

The DOT neutron predictions (Figure S.10) agree well with data along the neutron shield of the cask. Agreement is not as good directly above and below the neutron shield. Predictions are as much as three times as high as the actual measurements in these areas. This difference may be the result of inaccurate neutron source rates. Adjacent to the bottom end of the fuel,

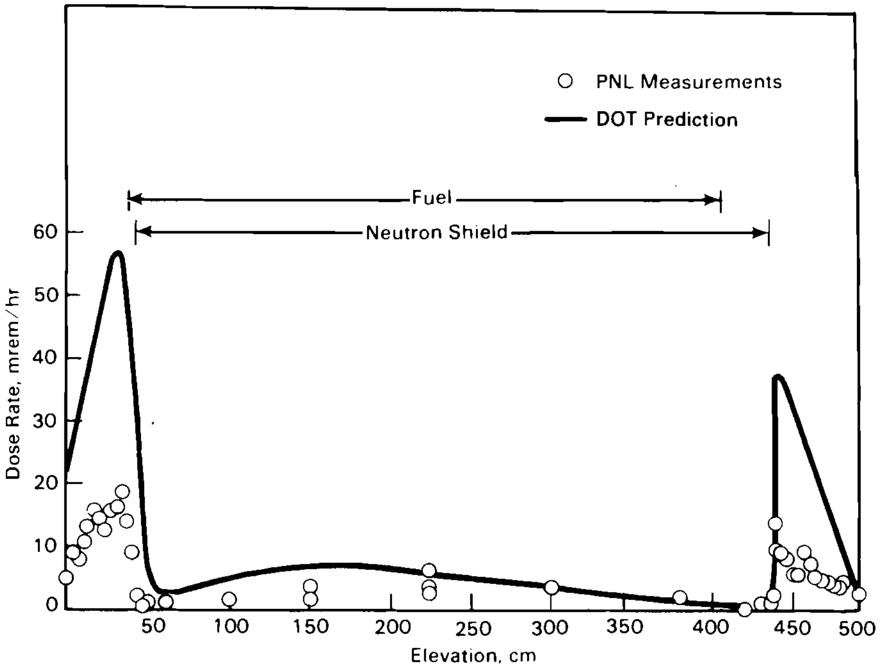

FIGURE S.10. Predicted and Measured Neutron Dose Rates on Side of Fully Loaded Cask predicted dose rates are a factor of two or three higher than measured dose rates. However, adjacent to the top of the fuel, predicted rates are in good agreement with measured rates. This effect is probably due to an inaccurate axial neutron source distribution.

Overall, the predictions of both the gamma and neutron dose rates are considered to be satisfactory. When consideration is given to the fact that the cask must attenuate a radiation source several orders of magnitude, and reduce the level to a relatively low value, agreement between predictions and data within a factor of two or three times is relatively good.

The results of this study led to the conclusion that all the computer codes performed satisfactorily. Pretest predictions compared satisfactorily with experimental data. The only post-test predictions that were warranted were in the heat transfer area, and they resulted in slightly enhanced predictions. No major changes to the codes themselves were required to improve comparisons between predictions and data; only changes to input information, especially geometry, were necessary to improve heat transfer predictions. It is recommended that use of these codes to support spent fuel storage system testing be continued, that their evaluation be continued, and that the undocumented heat transfer codes be documented if they perform satisfactorily, to allow their use for future design and licensing safety analyses.

CONTENTS

FIGURES

TABLES

NOMENCLATURE

ACRONYMS AND INITIALISMS

BWR	boiling water reactor
DOE	U.S. Department of Energy
EOC	end-of-cycle
EPRI	Electric Power Research Institute
GE-MO	General Electric-Morris Operation
H/U	hydrogen-to-uranium (ratio)
NWPA	Nuclear Waste Policy Act
ORNL	Oak Ridge National Laboratory
PNL	Pacific National Laboratory
PWR	pressurized water reactor
R&D	research and development
REA	Ridihalgh, Eggers & Associates
TC	thermocouple
TLD	thermoluminescent dosimeter
TED	track etch dosimeter

SYMBOLS AND NOTATIONS

α_m	set of wall numbers with a thermal conduction connection to wall node m
β_n	set of wall numbers with a thermal radiation connection to rod n
γ_i	set of subchannel numbers with a thermal connection to rod i
Δt	time step
Δx	axial step
ε	surface emittance or a member of a set
ζ_n	set of rod numbers with a thermal radiation connection to rod n
θ	problem orientation, angle from vertical

SYMBOLS AND NOTATIONS (contd)

κ_n	set of rod numbers with a thermal radiation connection to wall n
λ	thermal conductivity
λ_i	set of rod numbers with a thermal connection to subchannel i
μ	viscosity
ξ_m	set of subchannel numbers with a thermal connection to wall m
ρ	density
σ	Stephan-Boltzmann constant
σ_m	set of wall numbers with a thermal radiation connection to wall m
τ_i	set of wall numbers for walls that connect to subchannel i
ϕ	area fraction
ϕ_i	rod to subchannel i heat fraction
ψ_i	set of transverse gap connections to subchannel i
ℓ	length of transverse momentum control volume
A	area
B	empirical coefficent
C	drag, axial loss coefficient, empirical coefficient, or specific heat
D	Darcy and orifice drag
D_h	hydraulic diameter
e_k	multiplier (±1) that gives the correct sign to the transverse connection terms
f	friction factor
F_{ij}	radiation exchange factor, surface i to j
g	acceleration due to gravity
$\vec{g}$	gravitational vector

SYMBOLS AND NOTATIONS (contd)

Gr	Grashoff number
h,H	fluid enthalpy, average film coefficient, or heat transfer coefficient
H_g	fuel-cladding gap conductance
H_{ij}	radiation exchange factor based on geometry and emittances
k,K,λ	thermal conductivity
L	length
$\vec{m}$	mass flux
Nu	Nusselt number
P, p	pressure
Pr	Prandtl number
$\dot{q}$	heat generation rate
$\dot{q}_{rad}$	thermal radiation transport
q'''	volumetric heat generation in wall
R	radial thermal resistance or radius
r	radius
Ra	Rayleigh number
R_c	outer radius of the cladding
Re	Reynolds number
R_f	outer radius of the fuel material
S	transverse gap width
T	temperature
T_a	ambient temperature
T_c	cladding temperature
T_{fs}	temperature of the fuel surface

SYMBOLS AND NOTATIONS (contd)

T_s	local surface temperature
T_W	wall temperature
t	time
t_w	effective wall thickness for heat storage
U	effective wall conductance
u	transverse velocity
V_∞	free stream velocity
v	axial velocity
$\vec{v}$	superficial velocity
w_T	crossflow due to turbulent exchange
y_c	cladding thickness
z	factor for effective fluid radial conduction length

SUPERSCRIPTS

n	time step level or Nusselt number exponent
N	empirical coefficient
$*$	donor cell quantity
$\overline{\quad}$	average value

SUBSCRIPTS

a	ambient
c	cladding or convection
D	diameter
f	friction or fuel
i	subchannel number or generalized subscript for matrix notation
HTR	heat transfer from a rod

SUBSCRIPTS (contd)

HTW	heat transfer from a wall
j	axial level or generalized subscript for matrix notation
II JJ	refer to channel numbers on either side of a transverse gap
k	transverse gap number
L	length
m	mixed convection or wall number
n	rod number
o	outside
p	pressure
r	radiation
R	rod
s	surface
T	transverse
w	wall
X	local parameter

BWR SPENT FUEL STORAGE CASK PERFORMANCE TEST
VOLUME II
PRE- AND POST-TEST DECAY HEAT, HEAT TRANSFER, AND SHIELDING ANALYSES

1.0 INTRODUCTION

Implementation of spent fuel dry storage systems may be required in the late 1980s because several at-reactor storage pools will attain maximum capacity by that time (DOE 1985). The Nuclear Waste Policy Act (NWPA) of 1982 assigns the U.S. Department of Energy (DOE) the responsibility for assisting utilities with their spent fuel storage problems. An additional provision of the NWPA is that DOE shall provide generic research and development (R&D) of alternative spent fuel storage systems to enhance utility-provided at-reactor storage capability. As a result of these NWPA provisions and because some utilities had expressed interest in using large metal spent fuel storage casks, a cask performance testing program using a Ridihalgh, Eggers & Associates REA 2023 boiling water reactor (BWR) spent fuel storage cask was performed from 1983 through 1985 by Pacific Northwest Laboratory (PNL) and General Electric (GE) at the latter's Morris Operation (GE-MO) facility (McKinnon et al. 1986a).

An important first activity of the REA BWR cask performance testing effort was to identify analytical tools (computer codes) to assist in planning the test and to evaluate and better understand the results. Analysis tools are needed to effectively select test conditions, identify spent fuel assemblies, select spent fuel loading patterns, and determine instrumentation placements. Once test data are obtained, they can be used to establish qualified computer codes. These codes can then be used to support design and licensing efforts and to reduce the need for expensive, time-consuming tests and demonstrations.

Five computer codes were selected to support the REA BWR cask performance test. The codes were ORIGEN2 (decay heat), HYDRA and COBRA-SFS (heat transfer), and QAD and DOT (shielding).

ORIGEN2 (Croff 1980a,b) was selected to predict spent fuel assembly decay heat generation rates and radiation source rates. Because calorimetry of each

BWR spent fuel assembly placed in the REA cask was performed, evaluation of ORIGEN2 was possible by comparing pre-calorimetry predictions to calorimeter data. Comparisons of ORIGEN2 predictions with BWR data reported in this study are extensions of comparisons with pressurized water reactor (PWR) data reported by Schmittroth (1984) and BWR data reported by McKinnon et al. (1986b).

The undocumented heat transfer codes HYDRA and COBRA-SFS were chosen based on their use of the first principles of mass, momentum, and energy. The codes have been evaluated since 1982 using two sets of single assembly data and two sets of multiassembly data of which these REA cask test data are one multiassembly data set (Creer 1984). If the codes satisfactorily predict the four sets of data, documentation is planned for 1986 and 1987. HYDRA and COBRA-SFS were used to select spent fuel assemblies with the desired decay heat generation rates and to select thermocouple (TC) placements. Measured cask and spent fuel temperatures provided a database for evaluation of HYDRA and COBRA-SFS. No attempt was made in this study to compare the two heat transfer codes, because results of the other evaluations have not been completed and a comparison based on one data set may lead to erroneous conclusions.

The QAD (Malenfant 1967) and DOT (Rhoads and Childs 1982) computer codes were selected to predict gamma-ray and neutron dose rates, respectively, on the cask outer surface. Pretest dose rate predictions were used to plan the test relative to personnel and site dose accumulations and to select sensor locations on the cask outer surface. Measurements of gamma and neutron dose rates with portable instruments, thermoluminescent dosimeters (TLDs), and track etch dosimeters (TEDs) were used to evaluate QAD and DOT.

The REA BWR cask performance test itself is documented in Volume I of this report (McKinnon et al. 1986a). This second volume documents analyses required to support that cask performance test. The objectives of the analyses were to 1) perform pretest decay heat, heat transfer, and shielding analyses to select test operating conditions and identify instrumentation placements; 2) compare pretest predictions (actually pre-look, since some predictions were performed when testing was in progress) with test data to evaluate the codes; and 3) perform post-test analyses to improve predictions, if appropriate. Emphasis of this volume is on comparisons of pre- and post-test computer code predictions with experimental REA cask performance test data from Volume I. Comparisons of code predictions with experimental data reported in Volume I will be used, along with additional future comparisons, to qualify the codes for later use in design and licensing safety analyses of candidate dry storage systems.

Section 2.0 of this report presents the major conclusions drawn from this work, as well as the important recommendations permitted by the results and conclusions. The REA BWR spent fuel storage cask performance test is summarized briefly in Section 3.0. The decay heat, heat transfer, and shielding analyses are discussed in detail and results compared to data in Sections 4.0, 5.0, and 6.0, respectively.

2.0 CONCLUSIONS AND RECOMMENDATIONS

The major conclusions and important recommendations resulting from this study are presented in this section. In general, all the codes performed well and pre-test predictions compared satisfactorily with experimental data. Selected post-test heat transfer analyses were performed with improved input and resulted in slightly better predictions. In all cases, no major changes to the codes themselves were required to improve comparisons between predictions and data. Changes to only input information were necessary to improve heat transfer predictions. The documented decay heat and shielding codes should be used for design and licensing safety analyses of dry storage systems. Once the heat transfer codes have been successfully evaluated and documented, they should also be used for these analyses.

2.1 CONCLUSIONS

The following specific conclusions resulted from these analyses:

ORIGEN2 Decay Heat Analysis

- Decay heat generation rates of Cooper BWR spent fuel assemblies can be predicted, using ORIGEN2, within a standard deviation of ±18 W (±6.2%), which is relatively good because the standard deviation of calorimeter repeatability measurements was ±14 W (±5%).
- On the average, ORIGEN2 predictions were 2.3 W (1.2%) higher than measured decay heat values.
- Cycle-by-cycle burnup values must be used to accurately predict BWR spent fuel assembly decay heat values.
- Differences between ORIGEN2 predictions and calorimeter decay heat measurements do not appear to be dependent on the magnitudes of decay heat outputs (240 W to 397 W) of spent fuel assemblies considered.
- Predicted axial decay heat profiles are in good agreement with measured axial gamma radiation profiles. Gadolinium contents,

control rod insertions, and reactor power coastdown histories must be known to accurately predict decay heat profiles near the ends of BWR spent fuel assemblies.

- Results and conclusions of this study may not pertain to spent fuel assemblies with long cooling times where actinide decay heat rates are significant fractions of totals.

HYDRA Heat Transfer Predictions

- For a complex heat transfer system such as the REA cask, exceptionally good predictions of overall thermal performance can be obtained in spite of the effects of uncertainties in the description of the system on some of the computational models. HYDRA pretest (pre-look) peak cladding temperature predictions for 9 of the 12 vertical runs were predicted within ±6%, based on total peak rod-to-ambient temperature differences.
- HYDRA pretest predictions of axial and radial temperature profiles for helium and vacuum backfills, and for nitrogen backfills in a horizontal orientation, show good local, as well as overall, agreement (generally within 35°C) with test data.
- HYDRA pretest predictions of vertical axial temperature profiles for nitrogen backfills show some disagreement (up to 60°C) with data. The coarseness of the HYDRA computational grid made it necessary to apply a fine mesh fuel tube model (computer code) to predict local assembly temperatures using HYDRA mass fluxes and temperatures as input data. Momentum equations were not solved in the fuel tube model, and assumptions were made regarding the distribution of flow within assemblies/fuel tubes. This approach is responsible for most of the noted disagreement between predicted and measured profiles, but had little influence on the ability to predict peak cladding temperatures where agreement was generally within 20°C.
- HYDRA post-test predictions showed improved agreement (up to 15°C) with the data. In particular, local temperature differences were improved.

- Most of the differences between pre- and post-test HYDRA predictions and test data resulted because the actual geometry, especially gap widths and characteristics of contacting surfaces, were unknown and, therefore, could not be modeled exactly. In the basket, a significant part of the differences between predictions and data was caused by uncertainties in basket thermocouple locations. Considerable scatter also existed in the assembly center rod-to-outer rod data, which resulted in variable agreement between predictions and data.

- Accurate temperature predictions in a horizontal orientation require implementation of nonsymmetry between fuel assemblies and basket fuel tubes. Predictions of temperatures in a horizontal orientation are conservatively high (up to 30°C), partly because the assembly-to-fuel tube contact was not modeled in HYDRA.

- Pretest predictions were based on a predicted axial decay heat profile that was not prototypic. When a measured axial gamma profile was used in post-test predictions, improved agreement with data was obtained, as indicated by improved predictions for nonconvecting vacuum runs.

- With a nitrogen backfill gas, HYDRA peak rod temperature predictions are not significantly affected (<10°C) by fuel rod or fuel tube emittances, within the range of expected values.

- Existing standard correlations for cask surface-to-ambient natural and forced convection heat transfer consistently underpredicted the actual heat transfer. The resulting calculated cask surface temperatures were high by 3°C to 25°C. Use of standard correlations will result in conservatively high predictions of cask surface temperatures (and, hence, internal temperatures) under stagnant or forced convection atmospheric conditions.

COBRA-SFS Heat Transfer Analysis

- The agreement of COBRA-SFS pretest (pre-look) predictions with data from 16 test runs is exceptionally good for different fill media, orientations, and fuel loadings. The most accurate predictions of peak cladding temperatures were in the vertical orientation where 7 of 12 runs were predicted within ±6% of measured peak-to-ambient temperature differences.

- COBRA-SFS pretest predictions of axial and radial temperature profiles for helium and vacuum backfills, and for nitrogen backfills in a horizontal orientation, show good local, as well as overall, agreement (generally within 35°C) with test data.
- COBRA pretest predictions of vertical axial temperature profiles for nitrogen backfills show some disagreement (up to 50°C) with data. This disagreement is mainly attributed to the one-dimensional models of momentum and heat transfer used in the regions immediately above and below the fuel basket.
- COBRA-SFS post-test predictions showed improved agreement (up to 25°C) with the data. Both local temperature differences and peak temperatures were generally improved.
- Most of the differences between pre- and post-test COBRA-SFS predictions and test data resulted because the actual geometry, especially gap widths and characteristics of contacting surfaces, were unknown and, therefore, could not be modeled exactly. In the basket, a significant part of the differences between predictions and data was caused by uncertainties in basket thermocouple locations. Considerable scatter also existed in the assembly center rod-to-outer rod data, which resulted in variable agreement between predictions and data.
- The benefit of fuel assembly/fuel tube contact in a horizontal orientation is on the order of that from natural convection in a vertical orientation. Thus, fuel assembly/fuel tube contact is effective in reducing peak cladding temperatures in a horizontal orientation. COBRA-SFS predictions of temperatures in horizontal orientations are conservatively high (up to 35°C) partly because assembly-to-fuel tube contact was not modeled.

- With a helium backfill gas, COBRA-SFS predicted peak rod temperatures are not significantly affected (<15°C) by fuel rod or fuel tube emittance values.
- Modeling the heat transfer in the open regions above and below the fuel basket (upper and lower plenums) is important in determining the axial and radial varying thermal characteristics of the REA cask. The COBRA-SFS simplified upper and lower plenum heat transfer models were not able to predict the radial variations in the fuel tube inlet temperatures shown by the data. This had some effect on the ability to predict axial temperature profiles, but had little effect on the ability to predict peak cladding temperatures where agreement was generally within 20°C.
- Existing standard correlations for cask surface-to-ambient natural and forced convection heat transfer consistently underpredicted the actual heat transfer. The resulting calculated cask surface temperatures were high by 3°C to 25°C. Use of standard correlations will result in conservatively high predictions of cask surface temperatures (and, hence, internal temperatures) under stagnant or forced convection atmospheric conditions.

Cask Heat Transfer Performance

- The copper conduction plates in the REA cask basket are very effective heat transfer paths.
- The gaps between basket components and the basket and inner cask wall are very important to the heat transfer performance of the REA cask.
- Analysis of the test data showed little effect of precipitation or solar insolation on the cask thermal performance. The exclusion of these natural phenomena in the heat transfer code models did not introduce detectable differences between predictions and test data.
- The cask surface heat transfer distribution was affected by the backfill medium in a vertical orientation. For vacuum, the primary mode of heat transfer was by radiation in the radial direction. With helium, the primary mode of heat transfer was radial conduction

resulting from the relatively high helium thermal conductivity. In contrast, the significant axial convection in nitrogen caused a greater fraction of heat to be transferred through the cask lid. Therefore, when dissipating the same total amount of heat, cask side wall temperatures were a minimum with a nitrogen backfill gas because side wall heat fluxes were less than those with vacuum or helium backfills.

- For both nitrogen and helium backfill gases, the best-estimate predictions of the maximum allowable uniform heat loads that the REA cask can dissipate in a vertical orientation under assumed licensing conditions (stagnant, 52°C ambient) are 750 W/assembly (39 kW total). The peak cladding temperature (380°C) will be the limiting parameter with nitrogen because the lower effective conductance of the basket region with nitrogen produces higher fuel rod temperatures. In contrast, the higher heat transfer through the side walls of the cask with helium will cause higher liquid neutron shield temperatures to be the limiting parameter.
- Providing more flow area near the top and bottom of the fuel basket will reduce flow resistances and increase convection heat transfer in the REA cask. However, the associated added length will result in the significant disadvantage that the cask weight will be increased.

QAD AND DOT Shielding Analyses

- The QAD code gives satisfactory overall predictions of measured gamma-ray radiation dose rates. The code underpredicts, by as much as a factor of 2, gamma-ray radiation dose peaks; this underprediction is thought to be a limitation of the point-kernel method.
- Sixty percent of the predicted gamma-ray dose rate on the side of the REA cask (i.e., mid-plane) is due to secondary gamma rays.
- Cobalt-60 is a major contributor to predicted gamma-ray dose rates on the top, bottom, and side (near the top and bottom) of the cask. Thus, the ^{59}Co content in the handles, plenum, tie plates, and end fittings needs to be accurately known.

- The DOT code is conservative in predicting neutron radiation dose rates, with calculated dose rates being a factor of 2 to 4 higher. The neutron source strengths used in the analyses are possibly high, and source codes such as ORIGEN2 and XSDRN (ORNL 1969) may be predicting high source strengths and source strenth profiles.

2.2 RECOMMENDATIONS

Based on the results and conclusions of these analyses, the following recommendations are offered:

ORIGEN2 Decay Heat Predictions

- ORIGEN2 should be used to predict decay heat generation rates of spent fuel assemblies for interim storage system design and licensing safety analyses. This recommendation is based on the results of this study and McKinnon et al.'s study (1986b) for BWR assemblies and Schmittroth's study (1984) for PWR assemblies.
- When ORIGEN2 is used to predict decay heat generation rates of BWR spent fuel assemblies, cycle-by-cycle burnup values must be used to ensure good accuracies (±10%).
- ORIGEN2 should be evaluated for predicting decay heat rates of long cooled spent fuel because actinide decay heat rates are significant fractions of totals, whereas in 10 to 12 years or less cooled fuel, fission products account for the major part of total decay heat generation rates.
- Other decay heat codes should be used to predict calorimeter data presented in this volume and in Volume I of this report, to evaluate their effectiveness in predicting BWR spent fuel assembly decay heat rates.

HYDRA Heat Transfer Analysis

- HYDRA should continue to be used to predict temperatures in spent fuel dry storage systems and, once successfully evaluated and documented, should be used for design and licensing safety analyses.

- HYDRA predictions of dry storage system temperatures within 30°C can be obtained. Further, if it is desirable to improve this agreement, the following, in order of importance, should be pursued:
    - System geometries, especially gap widths and characteristics of contacting surfaces, must be better known.
    - The HYDRA computational mesh should be made finer, and the fuel tube model eliminated, or the HYDRA/fuel tube analysis technique should be improved to include corresponding fuel tube/assembly mass fluxes.
    - For a horizontal orientation, fuel assembly-to-fuel tube contact should be modeled.
    - The effects of free-stream turbulence and mixed convection (free and forced) adjacent to the exterior surface of the cask should be modeled.
    - Velocity fields should be measured in simulated casks, and HYDRA predictions should be evaluated with the measured distributions.
- The heat transfer data contained in this volume and in Volume I should be used to evaluate other heat transfer codes.

COBRA-SFS Heat Transfer Analysis

- COBRA-SFS should continue to be used to predict temperatures in spent fuel dry storage systems and, once successfully evaluated and documented, should be used for design and licensing safety analyses.
- COBRA-SFS predictions of dry storage system temperatures within 30°C can be obtained. Further, if it is desirable to improve this agreement, the following, in order of importance, should be pursued:
    - Geometries, especially gap widths and characteristics of contacting surfaces, must be better known.
    - In a horizontal orientation, fuel assembly-to-fuel tube contact should be modeled.

- The effects of free-stream turbulence and mixed convection (free and forced) adjacent to the exterior surface of the cask should be modeled.
- Two-dimensional momentum and heat transfer in the regions above and below the basket should be modeled. Suggestions for refinements include radially varying inlet conditions, multidimensional heat transfer between solid structures, and a computed velocity field.
- Velocity fields should be measured in simulated casks, and COBRA-SFS predictions should be evaluated with the measured distributions.

QAD and DOT Shielding Analyses

- QAD and DOT should continue to be used to predict dose rates in spent fuel dry storage systems.
- If better prediction accuracy is desired, magnitudes of source terms will need to be determined more accurately. Space- and energy-dependent neutron and gamma-ray source measurements are desirable.
- One or two casks should be analyzed with a Monte Carlo code to determine if more accurate predictions are practical.

3.0 BWR SPENT FUEL STORAGE CASK PERFORMANCE TEST

This section contains a brief summary of the REA BWR cask performance test presented in detail in Volume I of this report (McKinnon et al. 1986a). The REA cask and Cooper reactor BWR spent fuel are briefly described and the test matrix is presented.

3.1 CASK DESCRIPTION

The REA 2023 BWR spent fuel storage cask is shown in Figure 3.1 and is discussed in detail in REA's topical report submittal to the U.S. Nuclear Regulatory Commission (NRC) (REA 1983) and in Volume I of this report. The cask is of the double containment design with silicone elastomer O-rings to seal the inner cavity and a seal-welded final closure as a secondary cover. The cask has a smooth, painted, outer shell, an ethylene glycol/water neutron shield, and a lead gamma shield. The spent fuel basket is constructed of stainless steel clad Boral for criticality control, copper plates to conduct heat to the cask inner wall, and stainless steel for structural strength. The cask is ~2.25 m (8 ft) in diameter and 5 m (16 ft) long, and weighs ~100 tons when loaded with 52 unconsolidated BWR spent fuel assemblies.

The inner cask containment shell is 1.91-cm- (0.75-in.-) thick stainless steel. The cask inner bottom plate, outer bottom plate, and outer shell are 5-cm- (2-in.-) thick stainless steel. Lead gamma shielding, 10.8 cm (4.25 in.) thick in the sidewall, 8.26 cm (3.25 in.) thick in the bottom, and 7.62 cm (3.0 in.) thick in the primary lid, is provided.

Each of two 1.27-cm- (0.5-in.-) diameter drain lines, which penetrate the cavity bottom plate and the lead, terminates at the outer wall of the cask, where they are sealed by a 1.27-cm (0.5-in.) pipe plug and a 1.91-cm (0.75-in.) pipe plug in series. Both plugs are recessed into the 5.08-cm- (2.0-in.-) thick outer shell.

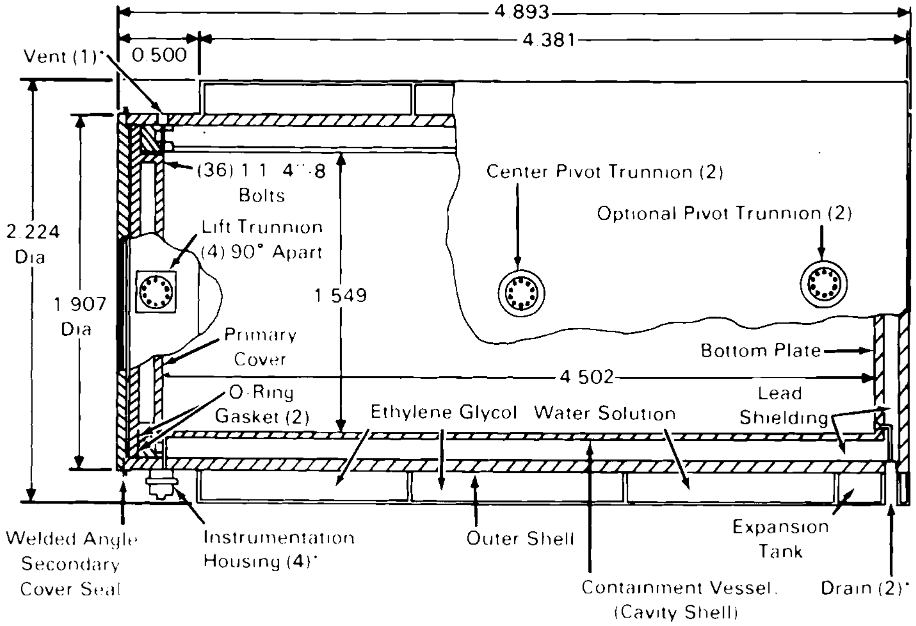

Dimensions are in Meters

*Rotated From True Position

FIGURE 3.1. REA 2023 BWR Spent Fuel Storage Cask

Near the top of the cask, slightly below the primary cover, a 1.27-cm (0.5-in.) vent/sampling line penetrates the cask wall and lead, and terminates with a dual plug arrangement at the outer wall of the cask similar to that for the drain lines.

The cask body has eight attachment points or trunnion supports for bolt-on trunnions. Four of these are located near the top, spaced 90 degrees apart, and may be used for lifting the cask while it is in a vertical position. Two trunnion supports, 180 degrees apart, are located at an elevation slightly above the center of gravity of the cask when the cask is vertical. These trunnions are used when lifting the cask in a horizontal position and for rotating the cask from a vertical to a horizontal position, or vice versa. The two trunnion supports near the bottom may be used when rotating the cask, and can be used together with those at the top for supporting the cask in a horizontal position during transport or storage on a skid.

The neutron shield outer shell is a 0.64-cm- (0.25-in.-) thick stainless steel plate approximately 399 cm (157 in.) long. The shield contains 15.24 cm (6 in.) of 50/50 ethylene glycol/water solution. Within the neutron shield are trunnion supports, to which the trunnions may be externally bolted. The neutron shield is divided into two sections. When the cask is positioned vertically, the bottom section (expansion tank) begins 0.64 cm (0.25 in.) from the cask bottom and extends up 4.44 cm (15.75 in.). The adjoining top section (neutron shield cavity) is 398 cm (156.75 in.) long. The only connection between the two sections is a 1.91-cm (0.75-in.) schedule 40 stainless steel siphon pipe. This pipe runs from the top of the neutron shield cavity to the bottom of the expansion tank when the cask is in either the vertical or horizontal orientation. The neutron shield cavity has top and bottom fill and drain plugs. The expansion tank has a bottom drain plug and a liquid level-indicating plug.

The inner or primary lid, which is recessed into the cask cavity, has a bottom plate 2.54 cm (1.0 in.) thick, a top plate 5.08 cm (2.0 in.) thick, and 7.62 cm (3.0 in.) of lead between the plates. The lid is secured to the cask body with 36 high-strength bolts 3.18 cm (1.25 in.) in diameter. Sealing is accomplished by two silicone elastomer O-rings. A hole through the top plate and between the O-rings is tapped for a 0.32-cm (1/8-in.) pipe plug, which permits checking for leak-tightness.

The outer or secondary lid, of 5.08-cm- (2.0-in.-) thick stainless steel, has a stainless steel angle welded around its circumference, to mate with a similar angle at the top of the outer wall of the cask body. These angles are sealwelded, after loading, to provide high integrity, long-term leak tightness. The angles are of such size that they may be ground and rewelded twice before requiring replacement.

The basket is fabricated in four sections, which are located in the cask inner cavity as shown in Figures 3.2 and 3.3. Contact is made with the inner wall of the cask, thus minimizing thermal resistance. Each basket section has

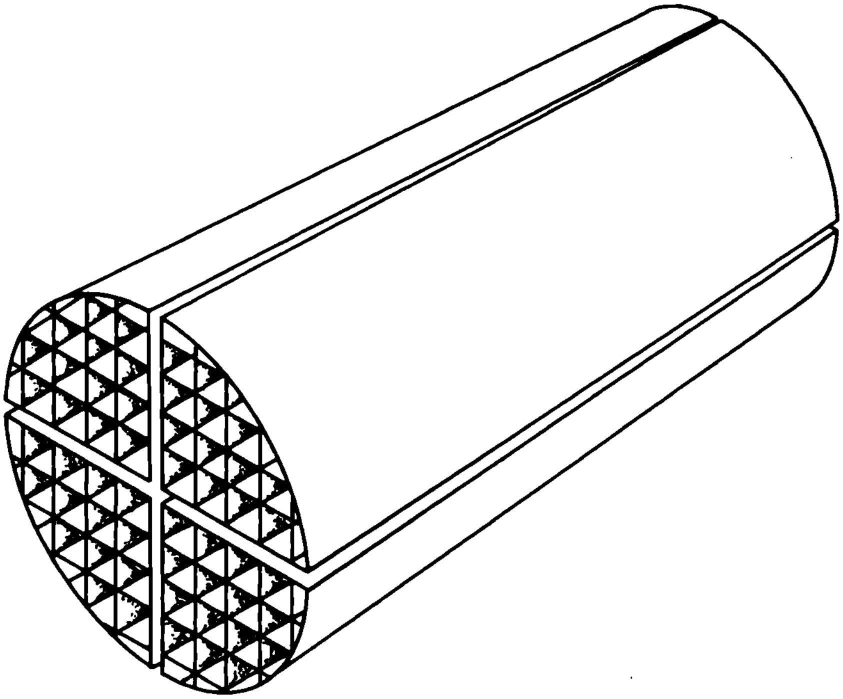

FIGURE 3.2. REA 2023 Cask Basket for 52 BWR Fuel Assemblies

thirteen 15.2-cm (6-in.) square Brooks and Perkins fuel tubes, each of which contains one BWR spent fuel assembly. These fuel tubes are essentially identical to the fuel tubes currently licensed for use in spent fuel storage pools. Each tube consists of concentric inner and outer square "shrouds", which integrally encapsulate Boral neutron absorber plates. Boral is a neutron poison material consisting of boron carbide uniformly dispersed within a matrix of aluminum alloy. The Boral neutron absorber plates extend above and below the active length of the fuel, are 0.185 cm (0.073 in.) thick, and contain a ^{10}Bo content of 0.02 g/cm^2 to provide adequate neutron attenuation.

The outer shell of each basket section and two internal ribs are constructed of 0.64-cm- (0.25-in.-) thick copper plates for conduction of heat out to the inner wall of the cask (Figure 3.3). Other structural members of the basket are fabricated from stainless steel. The basket rests on the bottom of the cask, and has cutouts to permit drainage of water and circulation of gas.

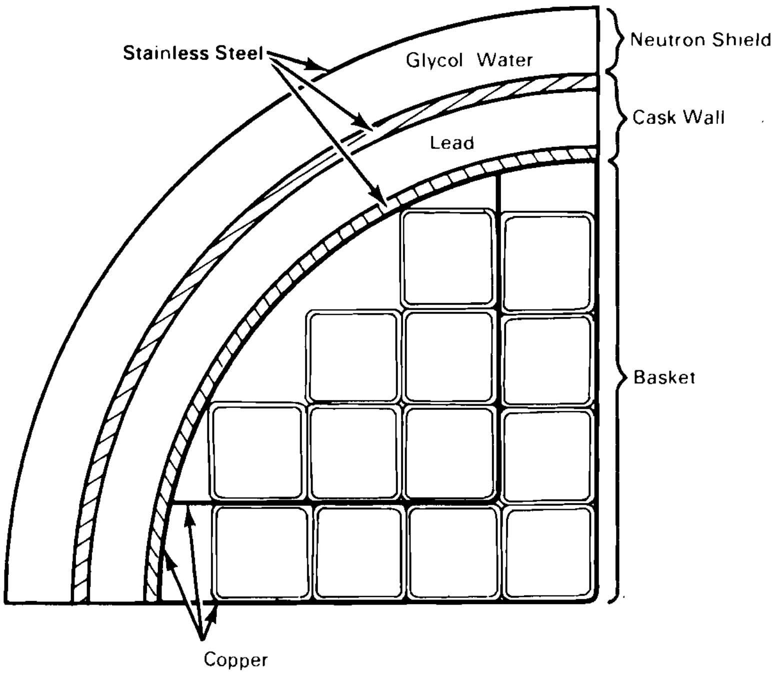

FIGURE 3.3. Plan View of Quarter Section of REA 2023 BWR Cask

3.2 COOPER BWR SPENT FUEL ASSEMBLIES

All 52 BWR spent fuel assemblies used in the cask performance test were from Nebraska Public Power District's Cooper Nuclear Station. The fuel assemblies were of the General Electric 7x7 design as shown in Figure 3.4, with design characteristics given in Table 3.1. The upper and lower tie plates are 304 stainless steel castings. The lower tie plates have nose-pieces that support the fuel assemblies in the reactor. The upper tie plates have lifting bails for handling the fuel assemblies.

Besides standard fuel rods, each assembly has eight fuel rods that are used as tie rods that thread into the lower tie plate casting. The upper end of the fuel/tie rods extend through and are fastened to the upper tie plate with stainless steel nuts and locking tabs. These fuel/tie rods support the

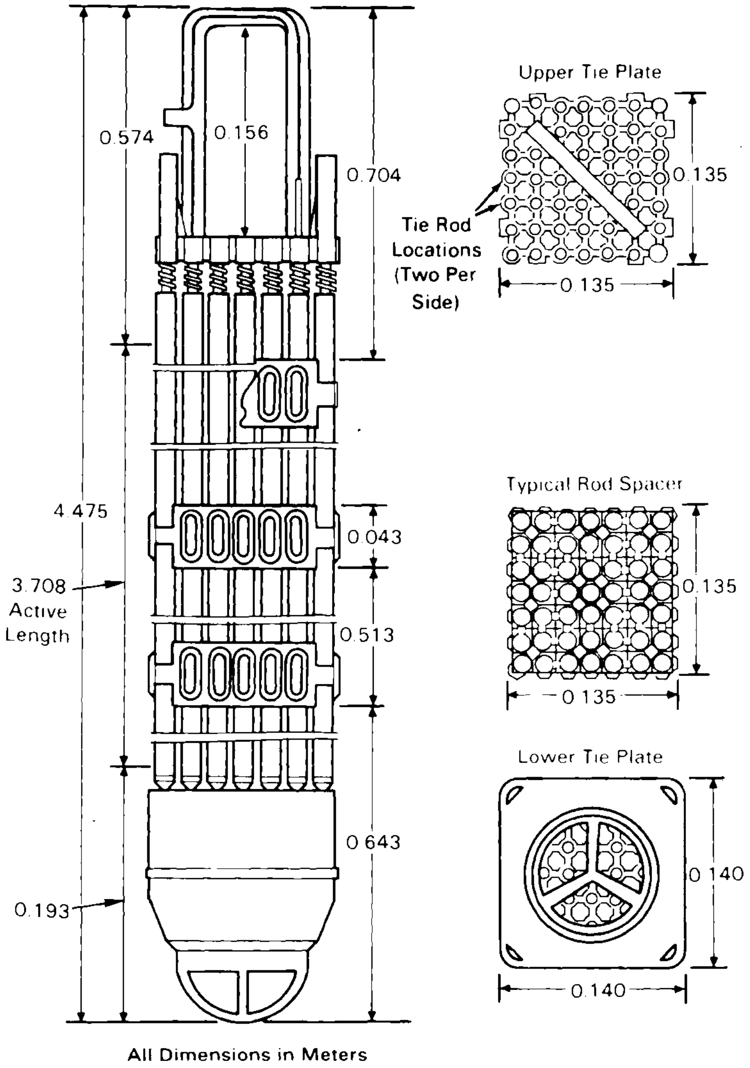

FIGURE 3.4. Cooper BWR Spent Fuel Assembly

weight of an assembly only during fuel handling operations when the assembly hangs by the bail. The center rod of each fuel assembly has been designed to maintain the position of the fuel rod spacers. It is inserted into the fuel assembly and rotated to lock the spacers into their respective locations. The spacers have Inconel springs to maintain rod-to-rod spacing. The fuel rods were pressurized with helium and sealed by welding end plugs on each end.

TABLE 3.1. Cooper BWR Spent Fuel Assembly Design Parameters

Fuel rod array	7x7	
Overall length	4.47 m	175.83 in.
Nominal active fuel length	3.66 m	144 in.
Fuel rod pitch	1.87 cm	0.738 in.
Space between fuel rods	0.445 cm	0.175 in
Outside rod diameter	1.43 cm	0.563 in.
Cladding thickness	0.081 cm	0.032 in.
Cladding material	Zircaloy-2	
Pellet outside diameter	1.24 cm	0.487 in.
Fuel pellet material	UO_2	
Pellet immersion density	10.42 g/cc	0.38 lb/in.^{3}
Fission gas plenum length	40.6 cm	16 in.
Helium fill gas pressure	1.0 atm	14.7 psia
Zircaloy-2 weight/assembly	48 kg	106 lb
304 stainless steel weight/assembly	8.6 kg	19 lb

Spent fuel assembly characterization consisted of sipping tests, calorimetry, axial radiation scans, photography, and video scans. Calorimetry and sipping tests were performed on all 52 spent fuel assemblies prior to their use in the cask during the performance test. Calorimetry water samples were taken at the conclusion of each calorimetry run to assess fuel integrity. Gas sampling during cask performance testing also contributed to the fuel integrity information base. Gamma/neutron scans at nine preselected axial elevations were performed on each fuel assembly. The scans were performed with an ION-1/fork measurement system provided to GE-MO by Los Alamos National Laboratory (LANL) (Halbig and Caine 1985). Representative photographs and video scans were obtained for five fuel assemblies both prior to and at the conclusion of cask performance testing.

3.3 TEST MATRIX

Cask performance testing consisted of 14 primary runs conducted in the sequence shown in Table 3.2. The test runs were performed after the cask was vacuum-dried, backfilled with helium, leak-checked, evacuated, backfilled with the desired backfill gas, evacuated again, and refilled with the desired backfill gas. At any time the fill gas was changed, the cask was evacuated, filled with the new gas, evacuated again, and then refilled with the new gas to ensure purity, i.e., double backfilled each time the backfill gas was changed. Gas samples were taken before and after the cask backfill gas was changed. The cask was always purged with nitrogen prior to a vacuum run to ensure that a vacuum/nitrogen atmosphere existed and that no residual helium was present.

TABLE 3.2. Test Matrix

Run Number	Number of Assemblies	Backfill	Cask Orientation
1	28	Vacuum	Vertical
2	28	Nitrogen	Vertical
3	28	Nitrogen	Horizontal
4	28	Helium	Horizontal
5(a)	28	Helium	Vertical
6(a)	52	Vacuum	Vertical
7	52	Nitrogen	Vertical
8(b)	52	Nitrogen	Vertical
9	52	Nitrogen	Horizontal
10	52	Helium	Horizontal
11(a)	52	Helium	Vertical
12	52	Helium	Vertical-Insulated
13	52	Helium	Vertical-Insulated
14	52	Vacuum	Vertical-Insulated

(a) Two runs at different environmental conditions were obtained.

(b) Repeat of Run 7 after cask had been rotated to shift fuel assemblies.

Cask temperatures were recorded hourly until steady state was attained during each test run. Gamma-ray and neutron dose rates were obtained with the cask in a horizontal orientation during both partial load and full load testing.

The load patterns for partial and full load testing are shown in Figure 3.5. The load and assembly decay heat generation patterns were selected to maintain quarter symmetry for the convenience of computer code simulations.

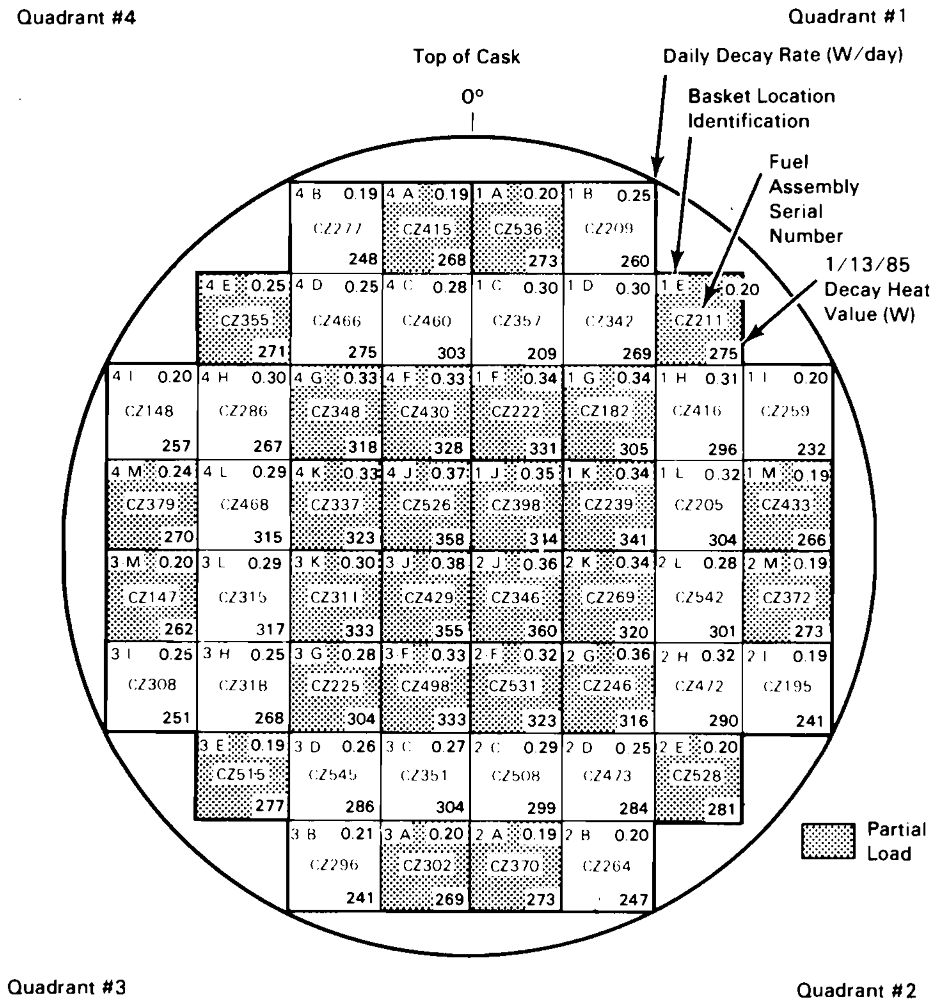

FIGURE 3.5. Partial and Full Load Patterns

4.0 DECAY HEAT ANALYSIS

The ORIGEN2 code (Croff 1980a,b) was used to predict decay heat generation rates of the Cooper BWR spent fuel assemblies used in the REA cask performance test. Results of the pre-calorimetry decay heat analysis are presented in this section. A brief description of ORIGEN2, a summary of the input, and comparisons of predictions to calorimeter data are provided. Agreement between pre-calorimetry predictions and data was satisfactory, and no post-calorimetry predictions were warranted.

4.1 ORIGEN2 COMPUTER CODE

The ORIGEN2 code is widely used in the nuclear industry to predict decay heat rates of spent fuel assemblies. A general purpose burnup and decay code, ORIGEN2 features extensive data libraries containing information on over 1200 nuclides. The code can be used to perform transmutation calculations in steps of constant power or constant neutron flux level. The resulting nuclide concentrations can be decayed with user-specified time intervals. Output options are available for decay heat rate as well as spent fuel compositions and radioactivity.

A standard version of the ORIGEN2 code was used to predict the decay heat rates of the 52 Cooper BWR spent fuel assemblies used during REA cask performance testing. Eight of the 52 assemblies placed in the REA cask had calorimeter measurements and ORIGEN2 decay heat predictions performed under the sponsorship of the Electric Power Research Institute (EPRI). Results using these eight assemblies were reported earlier (McKinnon et al. 1986b), but are included here for completeness. The code was benchmarked to ensure that the predictions are what would be expected from the code as it would be received from the Oak Ridge National Laboratory (ORNL) Radiation Shielding Information Center.

ORIGEN2 results are based on a large library of one energy group cross sections of the nuclides. These cross sections are the result of extensive calculations starting with a numerical description of the cross section of each isotope as a function of neutron energy. The basic cross sections are averaged over the energy range of 17 MeV to 0 eV using a computed neutron energy spectrum. Neutron spectrum calculations are done with a composition appropriate to a specific reactor core design and operating condition. The user is provided with various data libraries, each representing a reactor type, core loading, and operating condition. There is one BWR cross section library for a ^{235}U-enriched core; this actinide library has the numerical designation 252. Associated with it are activation product library 251 and fission product library 253, which were generated using the same neutron spectrum used to generate library 252.

A special concern in making decay heat rate predictions with ORIGEN2 for BWR fuel, as opposed to PWR fuel, is the effect of appreciable steam voids on the neutron spectrum. The ratio of plutonium to uranium fissions and the actinide composition at a given burnup are influenced by differences in the neutron spectrum. Assembly decay heat rates are determined by the different fission product yields of uranium and plutonium and by the mix of actinide isotopes in the spent fuel. A series of calculations was performed to evaluate the sensitivity of decay heat rates to variations of core steam void fractions. A version of the LEOPARD code (Barry 1963) was used to calculate the effect of unit cell steam voiding on the one group spectrum-averaged cross sections of the isotopes responsible for most of the decay heat. The change in the spectrum-averaged cross section at a given void fraction relative to the ORIGEN2 library default void fraction of 31.6% was determined for a range of void fractions. These relative change factors were used to alter the cross section of ORIGEN2 library 252 via code input for a series of ORIGEN2 cases, each representing a particular core steam void fraction in the range of 0% to 90%. As a result of these sensitivity calculations, it was found that core void variations of 0 to 90% can cause the decay heat rate to vary by 11% to 30%, depending on the time out of reactor.

The spectrum used in computing libraries 251, 252, and 253 was calculated assuming a General Electric BWR-6 assembly (8x8 rod array) at 31.6% core average steam void fraction (Croff et al. 1978). The Cooper fuel assemblies used in this study were of an earlier 7x7 rod design. The void fraction that has the same hydrogen-to-uranium (H/U) ratio as the 31.6% used in calculating the

ORIGEN2 library is 36% for the 7x7 rod design. The H/U ratio is a reasonable basis to use to determine the equivalent void fraction because it is a measure of the relative moderation and absorption rates that determine the form of the neutron spectrum. The Cooper BWR assemblies had operating void fractions of 39% to 40% void, which is close to the 36% equivalent void fraction of the library. Therefore, no corrections for void fraction were made.

4.2 ORIGEN2 INPUT SPECIFICATIONS

Features of Cooper fuel assemblies were shown in Table 3.1. Fuel assembly burnup data are listed in Table 4.1. Because the fraction of decay heat from neutron activation of the assembly structural materials is less than 5% of the total decay heat, generic values given by Croff et al. (1978) were used. The two elements that contribute the major share of activation heating are cobalt and gadolinium. A value of 1573 ppm was assumed for the gadolinium concentration in the uranium fuel. The cobalt content of the stainless steel was assumed to be 800 ppm. The Zircaloy-2 cladding was assumed to contain 10 ppm cobalt, and the uranium oxide was assumed to contain 1 ppm cobalt.

Assembly burnup values listed in Table 4.1 were determined from two different accounting methods. One method, referred to as Form 30 Reporting, is used to meet fuel storage requirements and lists only the final total burnup. The other method, referred to as Cycle Summary Reporting, contains end-of-cycle (EOC) burnup values. Form 30 total burnup values were considered to be the best final burnup values prior to making any calorimetry measurements. However, prior to calorimetry it was anticipated that individual cycle burnup values would be required for accurate ORIGEN2 decay heat predictions, and Form 30 reports do not contain EOC burnup values. Consequently, the Form 30 total burnup values were used to adjust the Cycle Summary EOC burnup values by multiplying each Cycle Summary EOC burnup value by the ratio of Form 30 discharge burnup to Cycle Summary discharge burnup. Burnup values in Table 4.1 reflect this adjustment.

All assemblies were initially enriched to 2.5 wt% ^{235}U averaged over all rods in each assembly. Sensitivity studies were conducted using ORIGEN2 with

TABLE 4.1. Cooper Fuel Assembly Burnup Data

Assembly No.	^{235}U, Kg	Adjusted Burnup, GWd/MTU						
		EOC 1	EOC 2	EOC 3	EOC 4	EOC 5	EOC 6	EOC 7
CZ147	190.2	6.773	10.381	13.490	21.231	23.421	26.709	
CZ148	190.2	5.887	10.126	13.220	20.883	23.049	26.310	
CZ182	190.2	10.710	18.421	20.412	(a)		24.464	26.824
CZ195	190.2	5.999	10.319	12.622	21.395	23.523	26.392	
CZ205(b)	190.2	10.298	17.712	20.699			22.563	25.344
CZ209(b)	190.2	10.651	18.320	21.430			23.726	25.383
CZ211	190.2	6.770	10.339	13.462	21.197	23.387	26.668	
CZ222	190.2	10.728	18.452	21.519			23.759	26.692
CZ225	190.2	10.672	18.355	21.455			23.489	25.796
CZ239	190.2	10.500	18.059	21.175			24.742	27.246
CZ246	190.2	10.964	18.858	22.052			24.065	27.363
CZ259(b)	190.2	6.026	10.365	12.920	21.431	23.596	26.466	
CZ264	190.2	5.938	10.213	12.782	21.404	23.601	26.496	
CZ277	190.2	6.012	10.341	12.885	21.427	23.599	26.478	
CZ286	190.2	11.071	19.042	22.218			24.916	27.141
CZ296	190.2	5.964	10.258	13.323	20.971	22.547	26.388	
CZ302	190.5	11.637	20.016			22.174	26.594	
CZ308	190.5	11.826	20.340	21.780			23.983	25.815
CZ311	190.5	11.236	19.325	22.322			25.314	27.392
CZ315	190.5	11.415	19.634	22.565			24.526	26.881
CZ318	190.5	11.387	19.585	22.537			24.902	26.568
CZ337	190.5	10.861	18.681	21.594			23.806	26.720
CZ342	190.5	11.396	19.600	22.788			24.680	27.066
CZ346	190.5	11.651	20.039	21.920			25.203	28.048
CZ348	190.5	11.063	19.028	22.169			24.773	27.481
CZ351	190.5	10.741	18.475	21.287			23.859	25.753
CZ355	190.5	11.654	20.046	21.468			23.620	25.419

(a) If the end-of-cycle burnup did not increase from one cycle to the next, the assembly was out-of-reactor for the cycle; this condition is denoted by a blank entry.

(b) Burnup calculations for these assemblies were performed previously under Electric Power Research Institute sponsorship (McKinnon et al. 1986b).

TABLE 4.1. (contd)

Assembly No.	^{235}U, Kg	Adjusted Burnup, GWd/MTU						
		EOC 1	EOC 2	EOC 3	EOC 4	EOC 5	EOC 6	EOC 7
CZ357	190.5	11.136	19.153	22.060	(a)		25.023	27.140
CZ369(b)	190.5	11.162	19.197	21.678			23.660	26.576
CZ370	190.5	11.511	19.799			21.946	26.342	
CZ372	190.5	11.051	19.008				21.708	25.848
CZ379	190.5	11.142	19.165	21.907			24.286	25.925
CZ398	190.5	11.221	19.300	22.212			24.499	27.478
CZ415	190.5	11.058	19.020			21.726	25.863	
CZ416	190.5	11.572	19.904	22.906			25.051	27.461
CZ429(b)	190.5	10.878	18.711	21.610			24.842	27.641
CZ430	190.5	10.774	18.531	21.626			24.176	26.825
CZ433	190.5	11.350	19.522	19.522			21.639	25.977
CZ460	190.5	10.932	18.804	21.938			24.570	26.512
CZ466	190.5	11.012	18.940	22.148			24.290	26.077
CZ468	190.5	11.130	19.143	21.603			24.823	26.757
CZ472	190.5	10.806	18.587	21.272			23.173	25.957
CZ473	190.5	11.305	19.444	22.448			24.840	26.519
CZ498	190.5	10.853	18.666	21.362			23.584	26.482
CZ508	190.5	12.368	21.273	21.921			24.014	26.357
CZ515(b)	190.5	11.003	18.924			21.637	25.737	
CZ526(b)	190.5	10.938	18.814	21.548			24.788	27.596
CZ528(b)	190.5	10.996	18.913			21.604	25.715	
CZ531	190.5	10.906	18.758	21.471			24.036	26.699
CZ536	190.5	10.996	18.913				21.604	25.715
CZ542	190.5	11.109	19.108	22.062			24.717	26.691
CZ545	190.5	11.311	19.454	22.675			24.856	26.668

(a) If the end-of-cycle burnup did not increase from one cycle to the next, the assembly was out-of-reactor for the cycle; this condition is denoted by a blank entry.

(b) Burnup calculations for these assemblies were performed previously under Electric Power Research Institute sponsorship (McKinnon et al. 1986b).

different enrichments to ensure that calculated decay heat rates based on single average assembly enrichments closely approximated average decay heat rates from ORIGEN2 based on individual rod enrichments in the assemblies.

The Cooper reactor power history for the first seven operating cycles is shown in Figure 4.1. The specific powers are presented in Appendix A and are based on a design core power of 22.1 MW/MTU when the reactor is operated at its full thermal power of 2381 MWTh.

Power histories for the assemblies were determined from burnup histories shown in Table 4.1, and from the reactor power history shown in Figure 4.1 and Appendix A. Assembly power histories within a reactor operating cycle were calculated by multiplying ratios of incremental burnup for the cycle to the core average incremental burnup for that cycle by the core average power history. The resulting specific power history used as input to ORIGEN2 is shown in Figure 4.2 for assembly CZ205. The input file for the ORIGEN2 prediction of the decay heat from CZ205 is presented in Appendix B.

In the implementation of the ORIGEN2 code used to perform the calculations, the data arrays were dimensioned to permit only 52 irradiation and decay steps. To meet the 52-step limitation, the Cycle 1 operating history consisting of 14 irradiation steps was collapsed to 7 irradiation steps. A sensitivity calculation was done to determine the effect of this approximation. The last operating cycle was eliminated, and the operating history was run both with and without the collapsed first cycle. It was found that the effect was less than 0.2% on the decay heat rate prediction.

4.3 ORIGEN2 PREDICTIONS COMPARED TO DATA

This section presents comparisons of ORIGEN2 predictions to calorimeter decay heat generation rate measurements. Also included are comparisons of calculated to measured fuel assembly axial decay heat generation profiles. Both decay heat magnitudes and axial profiles are needed as input to heat transfer computer codes, as discussed in Section 5.0.

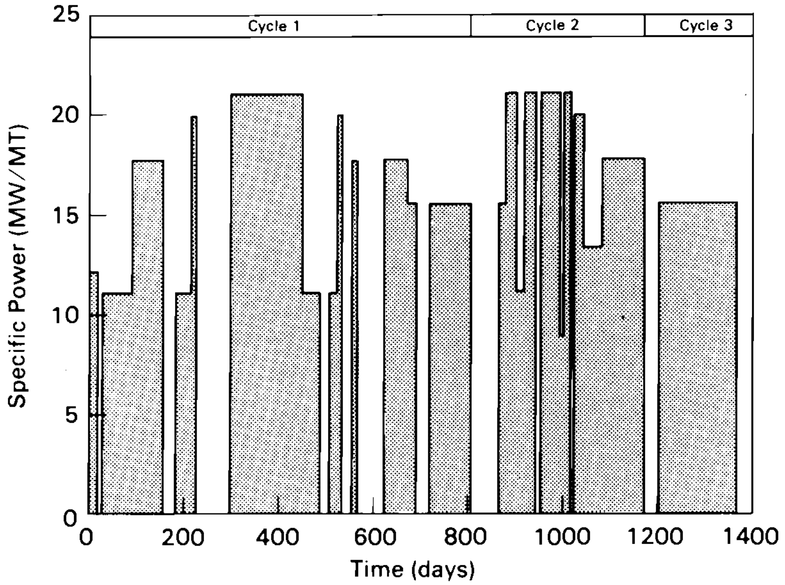

Cooper Station Operating History (Cycles 1 to 3)

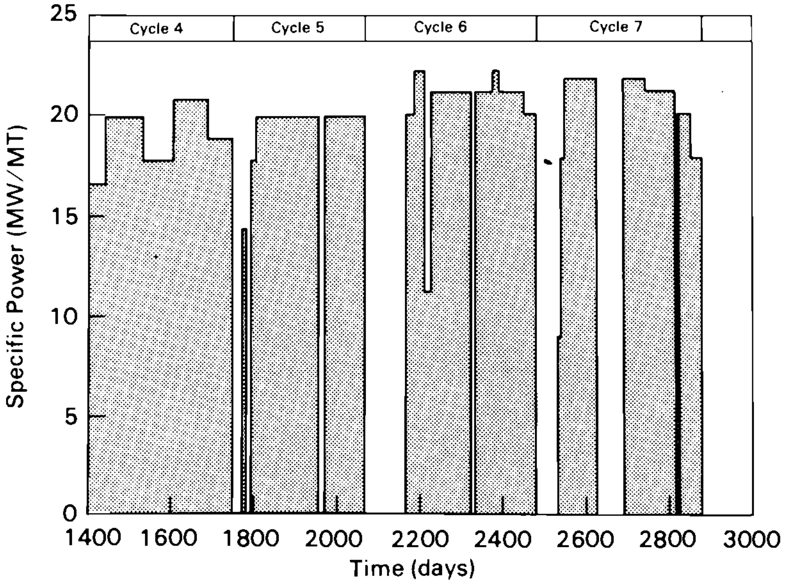

Cooper Station Operating History (Cycles 4 to 7)

FIGURE 4.1. Cooper Nuclear Station Operating History

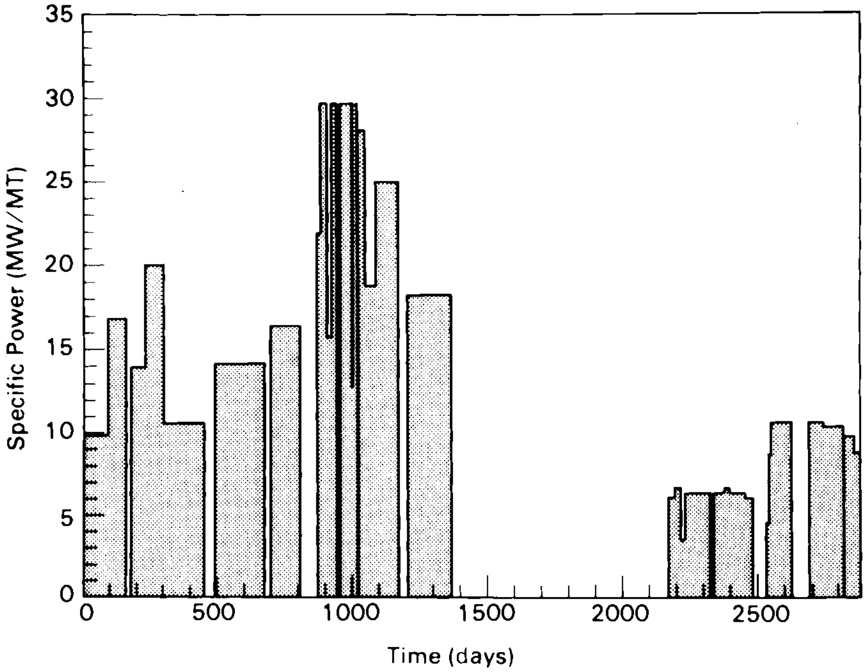

FIGURE 4.2. Assembly CZ205 Operating History

4.3.1 Decay Heat Generation Rates

Comparisons of predicted with measured decay heat generation rates are presented in Figure 4.3 and Appendix C for 77 measurements of decay heat rates of 52 Cooper spent fuel assemblies. ORIGEN2 predictions were performed before calorimetry was conducted, to facilitate unbiased comparisons of predictions with data. Predicted decay heat rates were obtained for the first day of each month for the period March 1, 1984, through December 1, 1985. These decay heat rates were corrected to the days on which calorimetry measurements were performed. Interpolations of predicted values to the exact measurement data (day of the measurement) were done for measurement dates between two ORIGEN2 prediction dates. Extrapolation of predicted values to measurement dates beyond December 1, 1985, was also necessary. For measurement dates in December 1984, predicted decay rates for November 1984 were applied to December 1, 1984, prediction values. For May 1985 measurements dates, predicted decay heat rates were determined by fitting a second-order polynominal to the predicted decay heat rates for September 1, October 1, November 1, and December 1, 1984, and

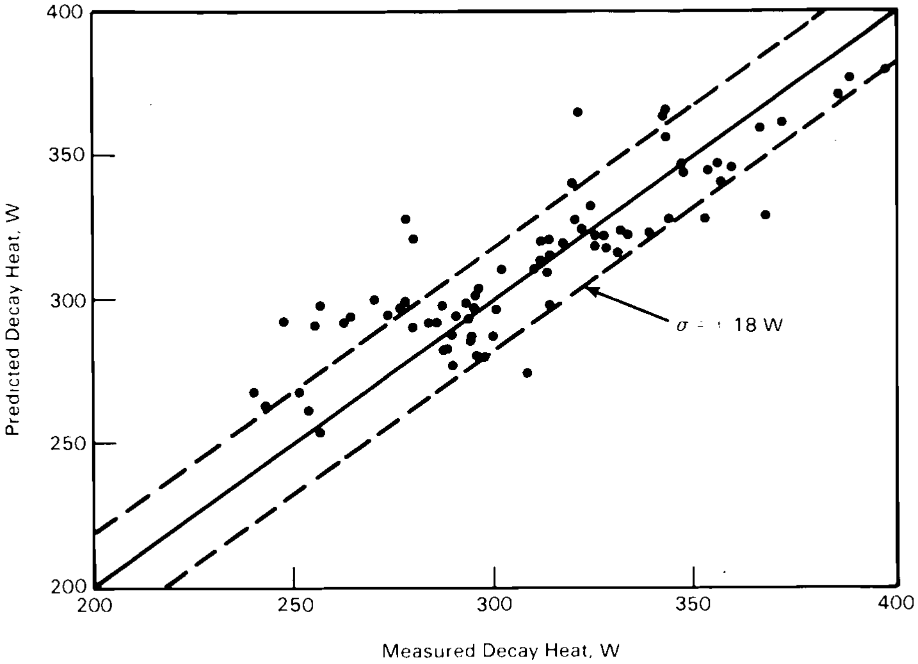

FIGURE 4.3. Comparisons of Predicted to Measured Decay Heat Generation Rates

extending the curve through May 1985. All curve fits were excellent and should not add to uncertainties of ORIGEN2 predictions.

On the average, predictions were 2.3 W greater than measured values (Appendix C). The standard deviation about the average difference between predicted and measured values was ±18 W. The average percentage difference between predictions and measurements was 1.2%, with predictions being higher than measured values. The standard deviation about the average percentage difference was ±6.2%. A statistical analysis showed no significant correlation between the percentage difference and either burnup or decay time.

The standard deviation of 14 repeat calorimeter measurements performed under EPRI sponsorshop on assembly CZ205 used in the cask performance test was ±14 W, which indicates that the agreement between predictions and data (±18 W) is almost as good as the repeatability of the test data itself. The source of assembly-to-assembly variation is eliminated when the 14 repeated measurements of CZ205 are analyzed separately. The average percentage difference between predictions and measurements of the decay heat of assembly CZ205 is 3.3% with a standard deviation of ±4.3% about this average.

4.3.2 Axial Decay Heat Generation Profiles

Comparisons of predicted axial decay heat generation profiles with a measured average gamma activity profile of the fuel assemblies are shown in Figure 4.4. The pre-calorimetry prediction was made using core-averaged axial burnup distributions from Cycles 6 and 7 contained in Cooper reactor operating histories. Measured gamma data were obtained with the ION-1 detector discussed in Section 3.2 and Volume I (McKinnon et al. 1986a). Post-test ORIGEN2 predictions were obtained using the ION-1 measurements of gamma activity as input.

The pre-calorimetry prediction of the relative axial decay heat profile departs from the measured gamma activity profile near the bottom of the active zone of the fuel assemblies. The difference is an indication that the assemblies have experienced local irradiation conditions that depart from core average conditions. The difference could be due to any one or a combination of three factors: 1) high gadolinium content in the fuel in the lower region of the rods to suppress burnup in the initial operating cycles; 2) partial insertion of control rods during reactor operation; or 3) a reactor power coastdown during the last operating cycle, which decreased the steam void fraction in the upper region of the reactor core and resulted in higher burnup in the fuel near the top of the assemblies. Because a long power coastdown was not evident in the Cooper operating histories, the difference between pre-calorimetry predictions and ION-1 gamma data was probably due to factor 1) or 2) or both.

The ION-1 gamma activity measurements for each assembly were averaged to produce the composite gamma activity curve shown in Figure 4.4. This curve was used to calculate an axial node burnup distribution. Several ORIGEN2 cases were then run with the same Cooper operating history, but at various specific powers that, when integrated over the irradiation time, covered the range of axial node burnups. The axial decay heat rate profile in Figure 4.4 was then developed. Differences between the post-calorimetry predicted decay heat rate profile and the ION-1 gamma profile are small. Decay heat calculations tend to exaggerate high values and minimize low values because the relationship between burnup and decay heat is slightly nonlinear.

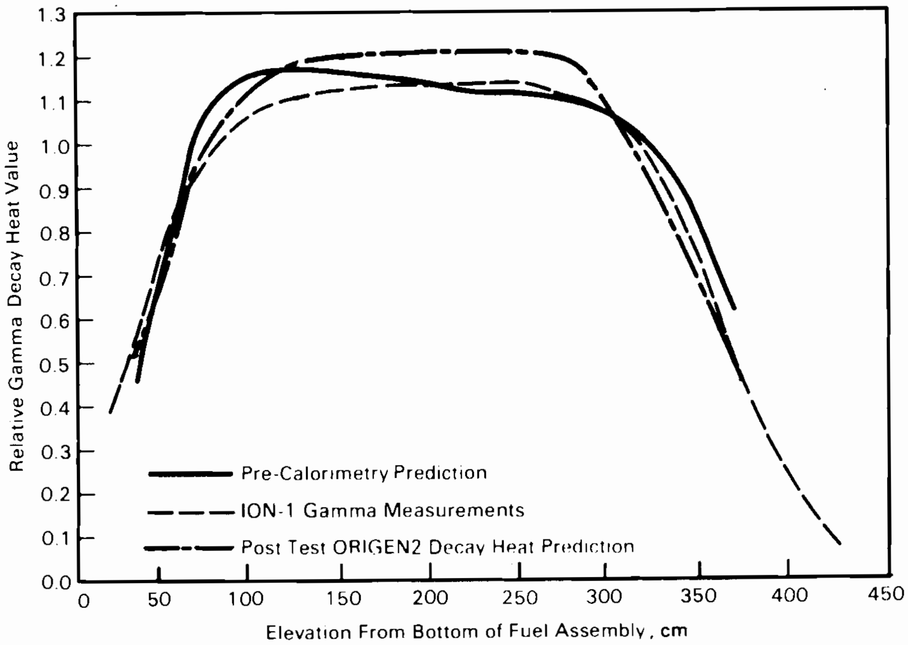

FIGURE 4.4. Comparisons of the Pre-Calorimetry Predicted Axial Decay Heat Profile with the Measured Gamma Radiation Output and the ORIGEN2 Decay Heat Prediction Derived from the Measured Gamma Activity

5.0 HEAT TRANSFER ANALYSES

The undocumented HYDRA and COBRA-SFS codes were used to predict temperatures in the spent fuel assemblies and cask during the performance test. Results of the pre- and post-test analyses are presented in this section and compared to experimental cask performance testing data obtained by McKinnon et al. (1986a). Brief descriptions of each code and summaries of the input are also included.

Effects of fuel rod emissivities are examined, and best-estimate predictions of the maximum heat that can be dissipated by the REA cask in a vertical orientation with nitrogen and helium backfill gases are provided.

5.1 HYDRA ANALYSIS

The HYDRA computer code was used to simulate the REA cask under performance testing conditions. A description of HYDRA is presented, followed by a description of its application in simulating the REA cask. Included in this section are a discussion of the computational model of the cask, a comparison of pretest (actually pre-look, since some predictions were performed while the cask test was in progress) HYDRA predictions to data, and a post-test re-evaluation of selected components of the model.

5.1.1 HYDRA Computer Code

HYDRA is a fully three-dimensional thermal hydraulic computer code with user-oriented input. The governing equations that define the conservation of mass, momentum, and energy are solved using finite-difference formulations. The equations apply to single-phase, compressible flow. The momentum equation includes convection of momentum, Darcy drag, and orifice drag, and gravitational, pressure, and viscous force terms. The gravitational vector is input in three single valued components to allow a computational model to be reoriented in space by merely changing the components. Coupled heat transfer modes of conduction, convection, and radiation are accounted for in conjunction with volumetric heat generation. Rod-to-rod radiation and enclosure radiation models can be constructed by input. There is a significant degree of flexibility in specifying temperature boundary conditions. HYDRA obtains a steady-state solution by a technique using a pseudo transient until converged.

Two coordinate systems are available in HYDRA. In Cartesian coordinates, there is complete freedom in specifying the shape of the boundary. In a second, more specialized arrangement, a Cartesian coordinate system is bounded by a cylindrical coordinate system. This arrangement is often found in dry storage casks where the interior of the cask lends itself to modeling with a Cartesian grid, while the cask body is more readily modeled with a cylindrical grid. The momentum/continuity equations are solved only in the Cartesian portion of the grid. The thermal solution is obtained in both the Cartesian and cylindrical domains.

Both fluid and thermal properties can be spatially and temperature dependent. The thermal conductivity and permeability may also be anisotropic. Furthermore, the thermal conductivity within a computational grid can be constructed to represent a composite of various materials. The composite thermal conductivity is based on either a series or parallel thermal resistive path using the analogy between the heat transfer path and the equivalent electrical circuit. Complex composites can be addressed by combining series and parallel networks either through input or preprocessing. Radiation between parallel surfaces separated by a thin, transparent material is included in the specification of film resistances.

5.1.1.1 Governing Equations in HYDRA

HYDRA solves the equations that describe the conservation of mass, momentum, and energy within the domain of interest. The equations are as follows:

Mass

$$\frac{\partial}{\partial t}(\rho) = -\nabla\cdot(\vec{m}) \tag{5.1}$$

Momentum

$$\frac{\partial}{\partial t}(\vec{m}) = \Phi S\,(\rho\vec{g} - \vec{\nabla}P - D\vec{m} + \nabla\cdot\mu\nabla\vec{\sim}) - \nabla\cdot(\vec{\sim}\vec{m}) \qquad (5.2)$$

Energy

$$\frac{\partial}{\partial t}(\rho C_p T) = \nabla\cdot(\lambda\nabla T) - \nabla\cdot(C_p\vec{m}\,T) + \dot{q} \qquad (5.3)$$

In the momentum equation, $D\vec{m}$ is a drag term that includes Darcy drag and orifice drag. An equation of state, e.g., the perfect gas law, is required for closure.

In the energy equation, $\dot{q}$ is used to represent heat sources due to heat generation and thermal radiation. Heat transfer by radiation, either rod-to-rod or between the surfaces of an enclosure, is computed by the following expression:

$$\dot{q}_{\text{rad } i\rightarrow j} = H_{ij}(T_i^{\,4} - T_j^{\,4}) \qquad (5.4)$$

where H_{ij} is a thermal connector that is based on geometry and emittances.

5.1.1.2 HYDRA Input Specifications

All applications for which HYDRA is intended can be specified through input. The input fits into one of the following eight categories:

- controls (program execution, user interface)
- convergence enhancement
- geometry (computational grid)
- material properties and correlations
- heat generation rates
- radiation
- boundary conditions
- initial conditions.

The last six categories define the problem and the first two categories permit the user to control executions. Through user interface control features, a variety of diagnostic information can be provided. This allows the user to readily confirm the accuracy of the problem definition and to monitor the progress of a simulation.

5.1.1.3 HYDRA Solution Technique

A HYDRA simulation begins by reading an input file that describes the application. The initial conditions establish the starting point. In general, the closer the initial conditions approximate the steady-state solution, the easier it is to obtain a converged solution. It may be beneficial to begin a steady-state simulation by using a solution tape from a related problem.

The solution of the coupled set of conservation equations proceeds sequentially through a number of pseudo time steps defined by input. At the outset of a psuedo time step, radiation heat transfer is computed using temperatures from the previous time step, or the initial temperatures at the outset of a simulation. The radiation heat transfer is added to the source term in the energy equation. Temperatures are computed within the Cartesian portion of the grid using the heat sources and mass fluxes from the previous time step, or the initial mass fluxes at the outset of a simulation. If an outer cylindrical grid is coupled to an inner Cartesian grid, the heat transfer at the grid boundary is computed using new temperatures from the Cartesian grid and the grid boundary temperatures from the previous pseudo time step. Heat transfer from the Cartesian grid is treated as a source term on the inside cylindrical boundary for the computation of temperatures in the outer cylindrical portion of the grid. New time temperatures on both sides of the grid interface boundary are then used to update the grid boundary temperatures.

The momentum equations are solved for the approximate or "tilde" phase mass fluxes in the three coordinate directions. The tilde phase mass fluxes are used in the continuity equation to compute the pressure field. The new time pressures are then used to update the tilde phase mass fluxes to the new time level.

The energy equation and the three momentum equations are each solved implicitly and are thus free of the common explicit time-step limitations and instabilities. However, the explicit coupling of radiation to the energy equation, the explicit coupling of the heat transfer across the Cartesian/ cylindrical interface, and the explicit coupling of temperatures and mass fluxes between the energy and mass transfer equations introduce limitations on the pseudo time-step size. These limitations are dealt with automatically by HYDRA through appropriate input control.

HYDRA writes the current solution to a tape when the number of pseudo time steps prescribed by input have been completed. This tape may be used to continue the simulation. A number of criteria are evaluated to judge whether or not convergence has been achieved.

5.1.2 HYDRA Computational Model

The analysis of the REA cask requires specification of the geometry and material properties for the cask interior and cask body, and specification of the thermal connection of the outer cask surface to the ambient. Specific details of the cask were provided in as-built drawings provided by REA. A brief description of the cask was presented in Section 3.0. A detailed physical description of the cask is included in Volume I of this report (McKinnon et al. 1986a).

5.1.2.1 HYDRA Geometry Model

The REA cask simulation was performed using two related computational models. With the cask in the vertical orientation, quarter symmetry was invoked. The computational grid arrangement in the plane perpendicular to the axis of the cask is shown in Figure 5.1 for quarter symmetry. The corresponding grid dimensions are given in Table 5.1. In the rectangular portion of the quarter symmetry grid, the grid dimensions in the x- and y-directions are symmetric. In the cask body, the radial grid dimensions are specified, and the angular grid dimensions are generated internally by HYDRA.

With the cask in the horizontal orientation, half symmetry was invoked. To obtain the half-symmetry grid, the quarter-symmetry grid was folded over the quadrant axis. The computational grid arrangement in the plane perpendicular

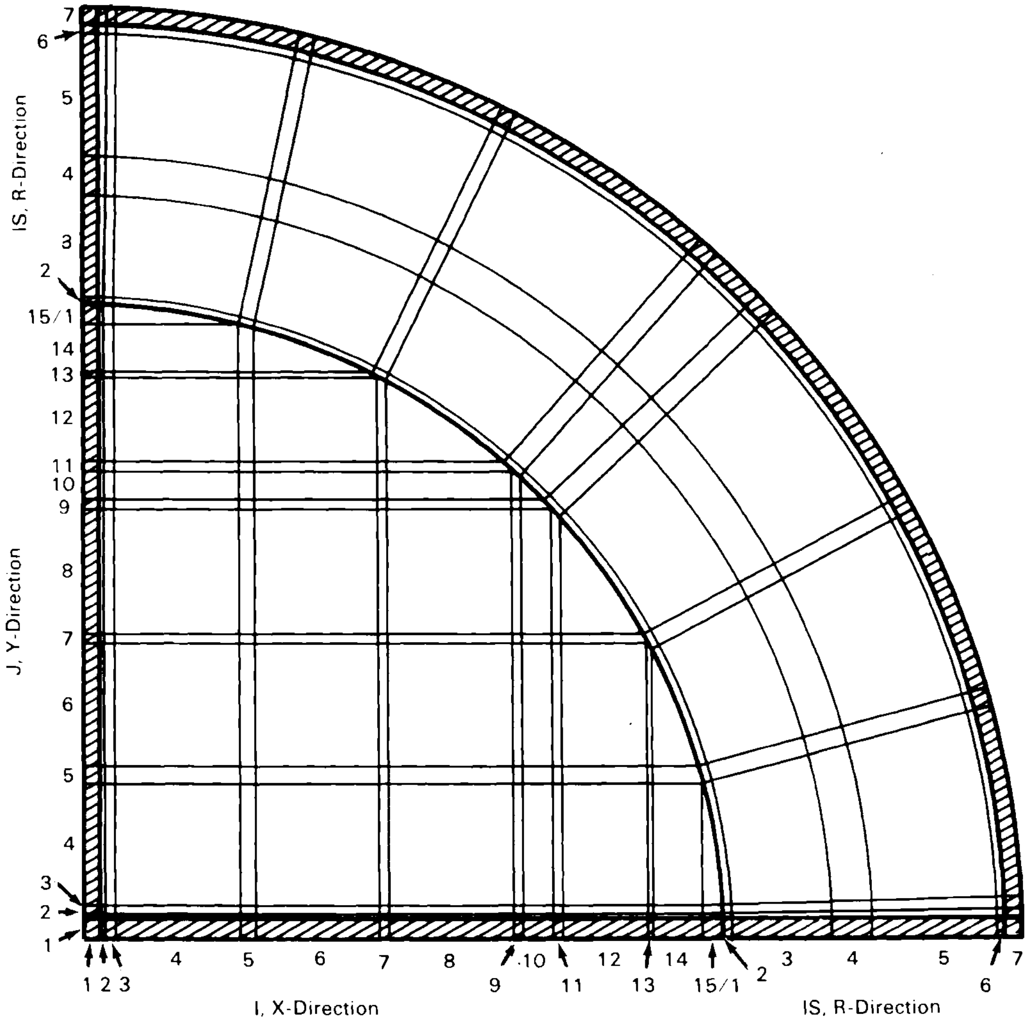

FIGURE 5.1. HYDRA Quarter-Symmetry Computational Grid Arrangement in the Plane Perpendicular to the Axis of the Cask

to the longitudinal axis of the cask is shown in Figure 5.2 for half symmetry. The I-direction grid arrangement is identical to those given in Table 5.1 for quarter symmetry. The grid dimensions in the J-direction are identical to the I-direction when viewed from the line of symmetry between the grids at J = 14 and J = 15. The radial grid dimensions for the cylindrical portion of the grid are, of course, identical for quarter and half symmetry. All of the REA cask simulations could have been performed with the half-symmetry grid. The quarter symmetry was used when possible to reduce computational expense.

TABLE 5.1. HYDRA Computational Grid Dimensions in the X-Direction

I or J	DX(I) or DY(J), m	Description
1	--	Boundary grid insulated by symmetry
2	0.00574	Open channel
3	0.01242	Wall: basket, fuel tube
4	0.15387	Fuel assembly
5	0.01849	Wall: fuel tube, copper, fuel tube
6	0.15387	Fuel assembly
7	0.01087	Wall: adjacent fuel tubes
8	0.15387	Fuel assembly
9	0.01087	Wall: adjacent fuel tubes
10	0.03670	Fuel assembly
11	0.00996	Fuel assembly
12	0.10722	Fuel assembly
13	0.00562	Wall: fuel tube, basket
14	0.05808	Open channel
15	--	Boundary grid for cask interior

IS	DR(IS), m	Description
1	--	Boundary grid for inside of cask body
2	0.00635	Copper shell of basket
3	0.12700	Inner cask wall and lead
4	0.05080	Outer cask body wall
5	0.15240	Neutron shield
6	0.00635	Outer neutron shield containment
7	--	Boundary grid for side of cask-to-ambient

The computational grid arrangement in the plane parallel to the longitudinal axis of the cask is shown in Figure 5.3. The grid dimensions for the axial direction are given in Table 5.2. Axial grid dimensions are continuous between the interior and the cask body. The same axial grid arrangement was applied to both quarter and half symmetry.

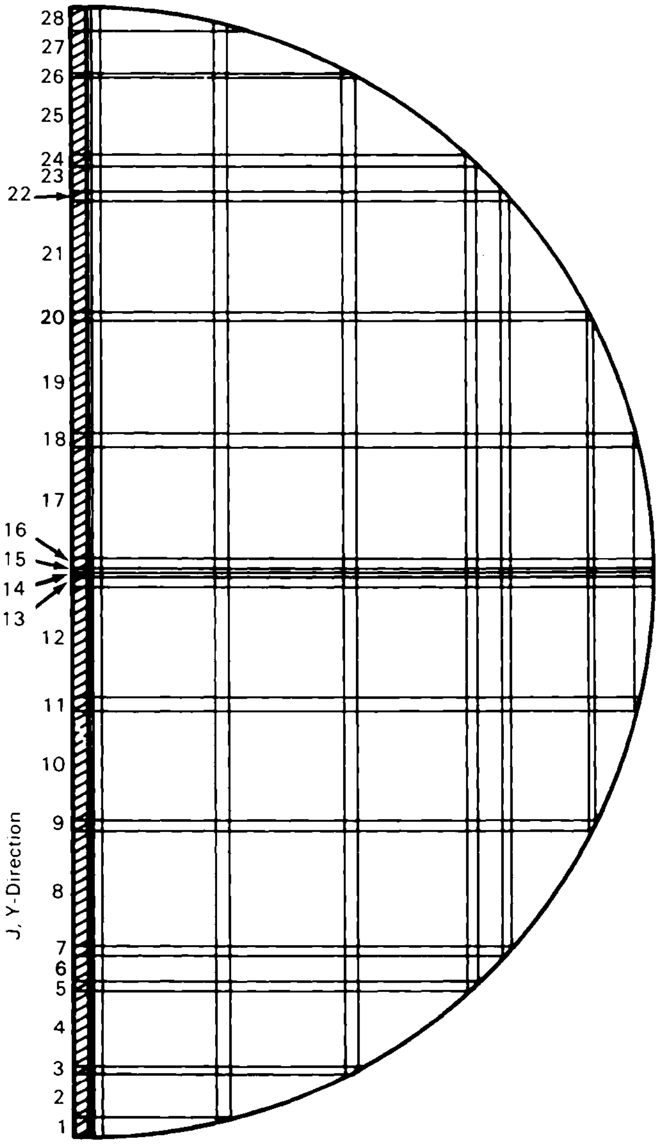

FIGURE 5.2. HYDRA Half-Symmetry Computational Grid Arrangement in the Plane Perpendicular to the Axis of the Cask

It should be noted that in the X-Y plane of the HYDRA grid (Figures 5.1 and 5.2), the fuel assemblies are represented by either one or three computational cells (four grid lines define a cell). This coarseness of the computational grid in the X-Y plane presents a problem with respect to predictions of local temperatures within the fuel tubes/fuel assemblies. To resolve this problem, a fine mesh fuel tube model was applied. The application of the fuel tube model was necessary only because of the coarse grid. If sufficient grid

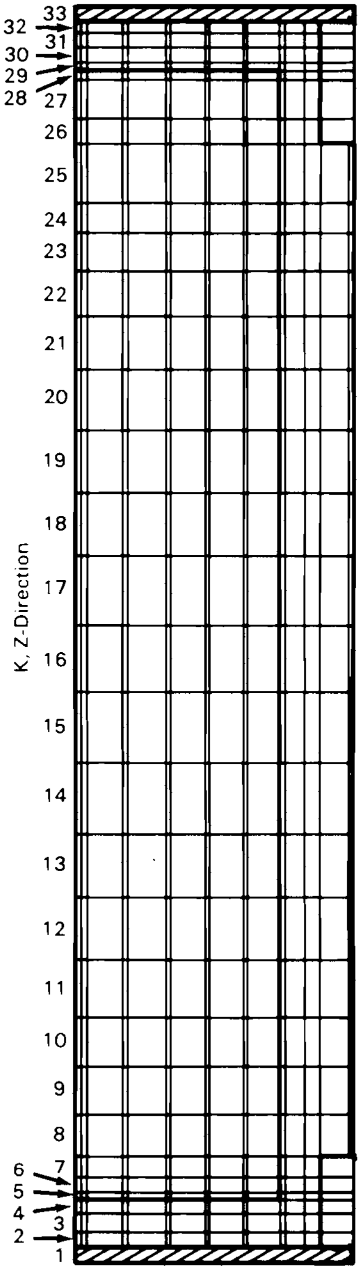

FIGURE 5.3. HYDRA Axial Computational Grid Arrangement

TABLE 5.2. HYDRA Computational Grid Dimensions in the Axial Direction

K	DZ(K), m	Description
1	--	Boundary grid for bottom of cask to ambient
2	0.0508	Cask bottom (outer)
3	0.0826	Lead
4	0.0508	Cask bottom (inner)
5	0.0187	Partially open grid below basket
6	0.0756	Bottom nozzle
7	0.1000	Bottom nozzle
8	0.1600	Heat generation region (Boral and neutron shielding begin at bottom of grid)
9	0.1900	
10	0.2124	↓
11	0.2330	
12	0.2500	
13	0.2600	
14	0.2700	
15	0.2788	
16	0.2788	
17	0.2700	
18	0.2600	
19	0.2500	
20	0.2330	
21	0.2124	
22	0.1900	
23	0.1600	Heat generation region
24	0.0784	Boral ends at top of grid
25	0.2286	Neutron shield ends at top of grid
26	0.1019	Top of fuel assembly including tie plate
27	0.1648	Fuel tubes end at top of grid
28	0.0257	Open grid above fuel tubes
29	0.0254	Lid bottom
30	0.0762	Lead in lid
31	0.0538	Lid top
32	0.0508	Lid top
33	--	Boundary grid for top of cask to ambient

resolution existed to satisfactorily define local temperatures, then the solution of temperatures from HYDRA would be adequate. However, such resolution in the REA cask, with its large number of fuel assemblies, would require a mesh containing substantially more cells than are in the current model. Comparison of predicted and measured temperatures is an evaluation of the effectiveness of this method.

The fuel tube model relies on a derivative computer program of HYDRA to solve the energy equation for the local temperatures within a fuel tube/fuel assembly. The fuel tube program uses appropriate coarse mesh temperatures and mass fluxes from HYDRA as boundary conditions for the solution of local temperatures within the specified fuel tube. The fuel tube program does not solve the momentum equation. However, the total mass fluxes can be redistributed locally by specifying relative flow resistances.

Thermal and fluid properties are input to the fuel tube program in much the same way as in HYDRA. The computational grid in the fuel tube program for the current analysis includes a 5x5 mesh in each assembly, as shown in Figure 5.4. Adjacent to the four faces of each assembly, gaps between the faces and the fuel tube walls are represented by one cell. The axial grid used in the fuel tube model includes the grids from K = 4 to K = 29 shown in Figure 5.3 and defined in Table 5.2. Further grid resolution is possible; however, numerical investigations with grids having more cells in either the transverse or axial directions show little or no effect on predicted temperatures.

5.1.2.2 HYDRA Material Properties and Correlations

Thermal conductivities of the constituent materials of the cask were obtained from Touloukian and Ho (1970). The thermal properties of the ethylene glycol were obtained from Curme and Johnston (1952). Well-established material properties and material property correlations used by HYDRA for pretest predictions of the REA cask are given in Table 5.3. Emittances of fuel tubes and the painted cask outer surface were measured by Taylor (1983, 1984). The remaining emittances are estimated values. Some computational cells include a composite

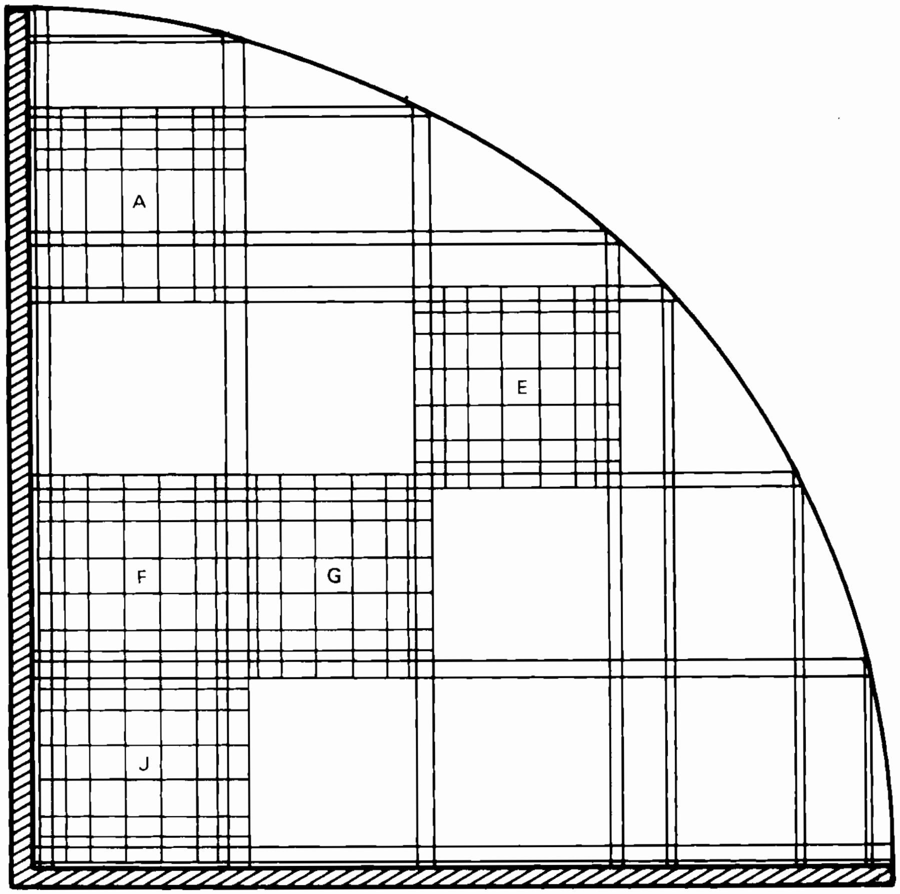

FIGURE 5.4. Fuel Tube Model Computational Grid for Assemblies A, E, F, G, and J

of several materials. For these cells appropriate effective thermal conductivities are defined. Anisotropic effective thermal conductivities are computed if necessary.

The Nusselt number correlation for the neutron shield was obtained from Catton (1978). The correlation is

$$Nu = 0.22\ A^{-1/4}\ [(Pr\ Ra)/(0.2+Pr)]^{0.28} \qquad (5.5)$$

where A is the area, Pr is the Prandtl number, and Ra is the Rayleigh number.

TABLE 5.3. HYDRA Material Properties

Thermal conductivity, W/cm^2°C	
Boral	0.6770 - (0.6670•10-3)*T
Copper	4.0500 - (0.8000•10-3)*T
Lead	0.3920 - (0.1333•10-3)*T
Stainless steel	0.09215 + (0.1465•10-3)*T
Air	0.688•10-4 + (0.634•10-6)*T
Nitrogen	0.768•10-4 + (0.609•10-6)*T
Helium	0.600•10-3 + (0.300•10-5)*T
Specific heat, W•sec/gm°C	
Nitrogen	1.040
Helium	5.234
Viscosity, gm/cm•9sec	
Nitrogen	0.802•10-4 + (0.352z10-6)*T
Helium	0.800•10-4 + (0.379z10-6)*T
Emittance	
Fuel rods	0.8
Fuel tubes (stainless steel)	0.2 (Measured)
Other stainless steel surfaces	0.2
Copper	0.5
Lead	0.6
Outside stainless steel surfaces	0.3
Outside painted surface	0.78 (Measured)

The correlations for the natural convection heat transfer coefficients on the outer cask surface were obtained from Sissom and Pitts (1972). For flat horizontal surfaces the correlation is

$$Nu = 0.14\ (Gr\ Pr)^{1/3} \tag{5.6}$$

where Gr is the Grashoff number.

For flat vertical surfaces the correlation is

$$\mathrm{Nu} = 0.13\ (\mathrm{Gr\ Pr})^{1/3} \qquad (5.7)$$

When the cask is in a horizontal orientation, natural convection off the horizontal cylinder is computed with Equation (5.7).

Many of the REA cask test runs were conducted outdoors where the cask was subjected to variable wind speed. Under these conditions the outside heat transfer coefficient was computed from forced convection correlations defined in Welty, Wicks, and Wilson (1969). For cask surface orientations that were similar to a cylinder in cross flow, the following correlation was used:

$$\mathrm{Nu}_D = 0.0266\ \mathrm{Pr}^{1/3}\ \mathrm{Re}_D{}^{0.805} \qquad (5.8)$$

where Re is the Reynolds number. For surfaces that looked like flat plates, the equation

$$\mathrm{Nu}_L = 0.0360\ \mathrm{Pr\ ReL}^{0.800} \qquad (5.9)$$

was used. Equation (5.9) follows from the Reynolds analogy integrated to obtain an average Nusselt number. The skin friction correlation used in the Reynolds analogy was that for turbulent flow over a flat plate:

$$C_f = 0.0576/\mathrm{Re}_{\mathring{A}}{}^{0.2} \qquad (5.10)$$

For the cask in a vertical orientation, Equation (5.8) was applied to the barrel of the cask using a significant length of D = 220 cm (86.6 in.), and Equation (5.9) was applied to the ends of the cask with a significant length of L = 195 cm (76.8 in.). For the cask in a horizontal orientation, Equation (5.9) was applied to the entire outside surface using a significant length of L = 330 cm (129.9 in.).

Heat transfer from the outside surface of the cask involves both convection and radiation. Thermal radiation heat transfer from the outside surface was computed using a heat transfer coefficient defined as

$$h_r = \sigma \, \varepsilon_s \, (T_s^2 + T_a^2)(T_s + T_a) \tag{5.11}$$

where σ is the Stefan-Boltzmann constant, ε is the surface emittance, T_s is the local surface temperature, and T_a is the ambient temperature. The total outside heat transfer coefficient is

$$h_o = h_c + h_r \tag{5.12}$$

where hc is the convective heat transfer coefficient and hr is the radiation heat transfer coefficient.

For runs 12, 13, and 14, thin blanket insulation was wrapped around the outside of the cask. With the cask in the vertical orientation, the insulation covered the neutron shield and expansion chamber. The thermal resistance of the material is known but, in applying more than one layer, the total thermal resistance was not defined. For these cases, the outside heat transfer coefficient on the barrel was not used. Instead, measured cask surface temperatures were applied directly, being specified through input.

In a vertical orientation, the cask rested on a wooden spacer in the shape of a large ring that created an unvented air space below the cask. The cask and spacer were mounted on a depressed-center rail car. Thus, the thermal connection between the bottom surface of the cask and the ambient was cluttered by the intervening structure. An effective heat transfer coefficient was developed that approximately accounted for this structure.

5.1.2.3 Spent Fuel Heat Generation Rates

The measured and predicted decay heat generation rates of the Cooper BWR spent fuel assemblies were discussed in Section 4.0. For the partial load runs, the decay heat rates were provided based on measured values for November 19, 1984. For the full load runs, the decay heat rates were based on values for January 13, 1985. Decay heat values applicable to each run were determined by adjusting measured values by the product of the daily decay rate predicted by ORIGEN2 and the number of days between the reference date and the date that steady state was achieved for the run.

The fuel assembly load patterns were previously indicated in Figure 3.6 (Section 3.3) for both partial and full load runs. Assemblies are identified along with fuel tubes, quadrants, heat generation rates on reference dates, and the daily decay rate predicted by ORIGEN2 (Section 4.3). For the analysis of the runs with the cask in the vertical orientation, the assembly heat generation rates were averaged based on quarter symmetry. For example, the heat generation rates of assemblies 1-J, 2-J, 3-J, and 4-J were averaged. For the analysis of the runs with the cask in the horizontal orientation, the assembly heat generation rates were averaged based on half symmetry across the vertical midplane. For example, the heat generation rates of assemblies 1-J and 4-J were averaged.

The axial distribution of heat was established based on the pre-calorimetry ORIGEN2 prediction shown in Figure 4.4 (Section 4.3). This curve is a prediction based on core-average axial burnup, and a single curve was applied for all of the assemblies.

5.1.2.4 Modeling Uncertainties

A number of modeling uncertainties exist because of the construction of the cask and basket, and other aspects of the performance test. The heat transfer from the outside surface to the ambient is difficult to predict accurately. Available heat transfer correlations do not account for the nonideal environment under which the cask test was performed. Within the cask, the following design features introduce further uncertainty into the analysis:

- The lead in the cask body, lid, and bottom, was subject to shrinkage as it cooled from the molten pour. This left gaps that could not be measured. For the pretest analysis, these gaps were assigned a value of 0.051 cm (0.020 in.).
- The assembly of the basket quadrants into the cask left a gap of unknown, variable thickness between the copper shell of the basket

and the inner wall of the cask body. For the pretest analysis, this gap was assigned a uniform value of 0.056 cm (0.022 in.).

- The thermal resistance between the copper conduction strips in the basket and the copper shell of the basket is influenced by unknown gaps and contact resistances. A similar problem exists at the contact of the basket support structure with the copper shell of the basket. REA used a laboratory model to measure the contact resistance of a prototypic section of the copper-to-copper contact. However, the total thermal resistance includes the effects of intermittent gaps along the contact surface. The gaps may not be as severe in the laboratory model. The gaps are alluded to in the design drawings supplied by REA.
- The basket quadrants consist of 13 fuel tubes. A tolerance is specified for straightness of the individual tubes. As-built design drawings and measurements suggest that the fuel tubes are not in good thermal contact with adjacent tubes or conduction strips.
- Fuel assemblies fit into fuel tubes with nominal gaps of 2 cm (0.79 in.). It is assumed in this analysis that the gap is uniformly distributed; that is, there is a gap of about 1 cm (0.39 in.) between the outer row of rods and the adjacent fuel tube wall on each face of the assembly. In reality, because the fuel assembly is not fixed in place, it can tilt to one side or another and can shift as the result of cask-handling activities. The fuel assembly location affects the heat distribution throughout the basket. The precise location is unknown and variable.
- The bottom of the cask is not flat. Measurements indicate that the gap between the bottom of the basket and the bottom surface of the cask cavity increases from the center. The actual flow area below the basket is not well defined. This flow area is very important in determining the total resistance to natural circulation. The flow area determined from measurements is greater than what would be available if the bottom of the cask were flat.

Material properties are generally well known, excluding the effective thermal conductivity in the neutron shield. However, one property that is not so well known is emittances. Of the values given in Table 5.3, only the fuel tubes and painted surface emittances were measured. Emittances are particularly important in the vacuum and nitrogen cases where radiation heat transfer is of the same order of magnitude as conduction heat transfer in the gas.

Solar insolation data were not used in the analysis. The data indicated insolation during the day, but not radiation loss at night.

5.1.3 HYDRA Predictions Compared to Data

In this section, HYDRA pretest and post-test predictions of REA cask temperatures are compared to measured test data. The pretest predictions were developed without any previous review of the data, except that actual test boundary conditions were applied. The measured boundary conditions are cavity pressure, ambient temperature, and wind speed. The date of the run established the heat generation rate. Comparisons of pretest predictions with data provided information that justified changes to the cask description and to various code input models. The subsequent post-test predictions display improved agreement with data. Some disagreement between predictions and data remains unresolved. Some particular issues are the subject of special studies that quantify possible causes of the disagreement.

To achieve meaningful agreement between predictions and data, the following three ingredients must be reliable:

- cask description
- computer model
- data.

In the comparison of pretest predictions with data, deficiencies were found in each of these groups. The REA cask/basket/fuel assembly is a complex system. Considerable uncertainty exists regarding the description of a number of features of this system. Changes to the cask description that could be justified on the basis of comparisons of predictions with data were implemented in the computer model in the post-test analysis. However, there was no artificial attempt to computationally resolve differences between predicted and measured temperatures.

5.1.3.1 HYDRA Pretest Predictions

In this section HYDRA pretest predictions and the experimental data are presented and compared. Pretest analyses were conducted for the 16 experimental runs identified in Table 5.4. The results are presented in this section and in Appendix D in the form of axial and radial temperature profiles. It is emphasized that the pretest predictions were developed without previous review of the experimental data.

An important part of the analysis of cask performance is the accurate prediction of peak rod temperatures. In Figure 5.5, HYDRA pretest predicted peak temperatures and measured peak temperatures are compared in the form of bar graphs. The run descriptors on the abscissa are consistent with those specified in Table 5.4. The tops of each bar represent peak temperatures, and the bottoms represent ambient temperatures. Peak temperatures were taken from the center rod of one of the center four assemblies (assembly 2J). In addition, predicted and measured temperature differences between peak temperatures and the ambient are shown by the length of each bar.

Figure 5.6 shows asymmetry between center rod temperatures of outer assemblies 1A and 2A, at an elevation of 3.33 m. The assemblies are identified in Figure 3.6 of Section 3.0, and the elevation is from the bottom of the cask. As fractions of measured peak-to-ambient temperature differences, the asymmetrical temperature differences average ±3% for the 12 vertical runs. This suggests that, if predictions of the peak-to-ambient temperature difference are within ±3% of measured values, predictions are relatively good. Predictions for 3 of the 12 vertical runs fall within this range. Nine of the 12 vertical runs fall within ±6% of measured temperature differences.

On an overall basis, this agreement is considered to be exceptionally good. As will be seen, however, comparisons of local temperature differences reveal greater disagreement between predictions and data. Comparisons of predicted temperatures with measured temperatures on the surface and throughout the internals of the cask serve to confirm the validity of various components of the input model and to improve the understanding of the cask performance. This process will contribute to the reliability of future cask performance predictions.

TABLE 5.4. REA Cask Run Matrix

Run No.	Run Descriptor[(a)]	Date of Steady State	Cavity Pressure, atm	Ambient Temperature, °C	Wind Speed, m/sec	Insolation, W/m^2
1	VPV	11/24/84	1.5(e)	5.0	2.0	90.0
2	VPN	12/01/84	1.39	1.0	1.3	84.4
3	HPN	12/06/84	1.36	-10.0	3.6	94.1
4	HPH	12/10/84	1.50	4.5	1.3	86.7
5a	VPH	12/19/84	1.46	-3.0	0.0	21.3
5b	VPH	12/28/84	1.48	16.0	6.3	25.0
6a(b)	VFV	01/13/85	1.0(e)	24.0	0.0	0.0
6b	VFV	01/19/85	4.4(e)	-10.0	3.6	60.0
7	VFN	01/25/85	1.40	-4.0	3.1	43.0
8(c)	VFN	02/03/85	1.37	-16.5	1.3	143.0
9	HFN	01/30/85	1.42	-3.9	2.0	47.5
10	HFH	02/14/85	1.37	-8.0	4.2	127.0
11a	VFH	02/08/85	1.39	-14.0	0.9	141.0
11b	VFH	02/25/85	1.52	22.3	0.0	0.0
12(d)	VFH	03/11/85	1.74	20.2	0.0	0.0
13(d)	VFN	03/13/85	1.47	21.9	0.0	0.0
14(d)	VFV	03/19/85	3.5(e)	23.5	0.0	0.0

(a) Descriptor identification: orientation/load/backfill

V = vertical P = part load V = vacuum
H = horizontal F = full load N = nitrogen
H = helium

(b) Run conducted indoors.
(c) This run was not simulated.
(d) Run conducted indoors with cask insulated.
(e) For the vacuum runs, the pressure is reported in mm Hg.

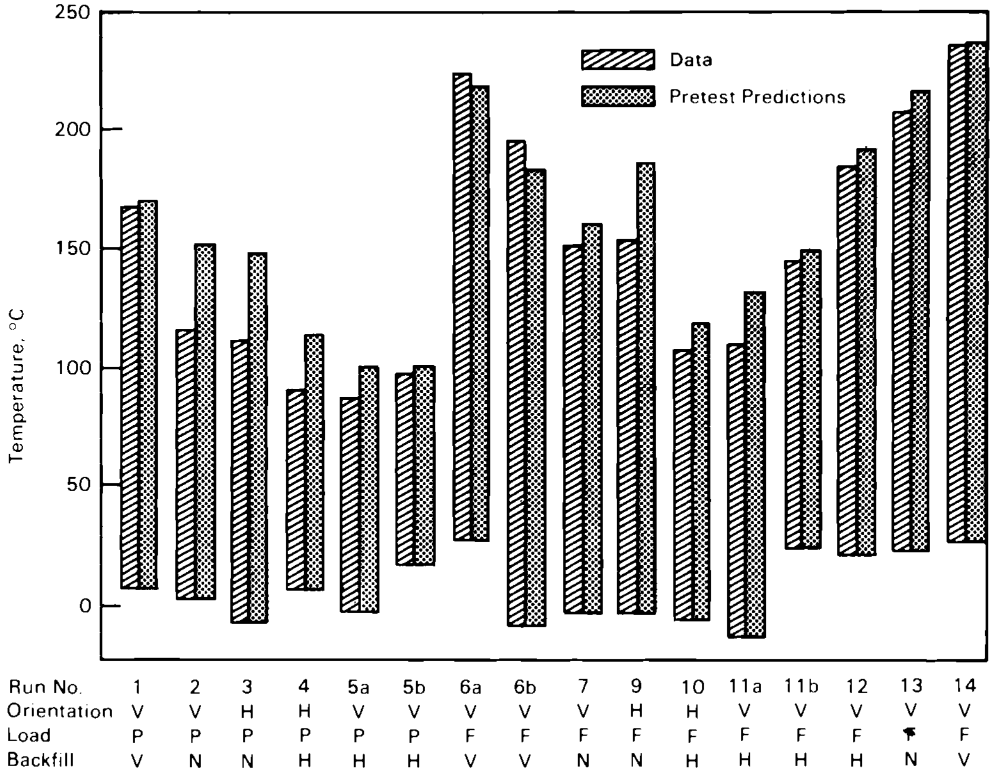

Notes: Orientation V = Vertical; H = Horizontal; Load P = Partial (28 assemblies); F = Full (52 assemblies); Backfill V = Vacuum; N = Nitrogen; H = Helium

FIGURE 5.5. HYDRA Pretest Predictions of Peak Temperatures and Overall Temperature Differences Compared to Data

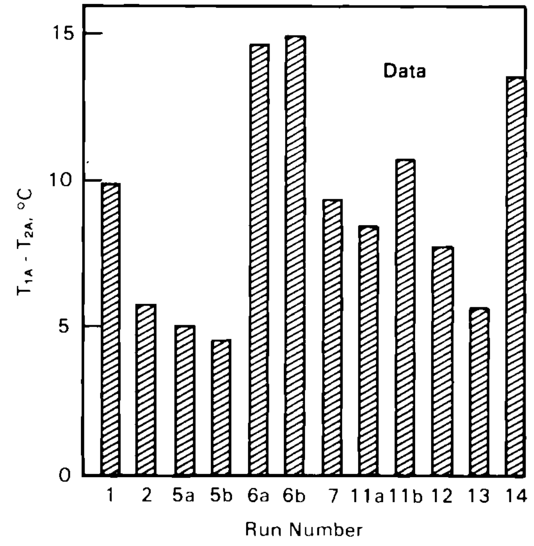

FIGURE 5.6. Asymmetry of Measured Peak Temperatures in Outer Assemblies 1A and 2A

The validity of the computational models and an understanding of cask performance can be assessed by segmenting the heat transfer path into its various components and closely examining each component. Beginning at the thermal boundary, i.e., the ambient, and moving toward the cask center, the components are:

- surface-to-ambient
- cask body
- fuel basket
- fuel assembly.

Each of these components is reviewed in the following sections. However, before examining comparisons of predictions to data in these components, general observations about the predictions and data are appropriate. These general observations identify some of the issues that are addressed in the following sections. From conclusions drawn from comparisons of predictions with data, changes are recommended for the post-test analysis.

5.1.3.1.1 General Observations. Predictions for selected runs are compared to data in Figures 5.7 to 5.14. These illustrations bring together results representing cask orientation, heat load, and backfill gas. The axial temperature profiles represent the centerline in center assembly 2J. The radial temperature profiles represent the diagonal of quadrant 2 from the cask centerline to the ambient, taken at an elevation of 3.33 m above the outside bottom of the cask. Figures 5.7 and 5.8 apply to the vertical part load runs. Figures 5.9 and 5.10 apply to the vertical full load runs. Figures 5.11 and 5.12 apply to the horizontal full load runs. Each set of figures contains predictions and data for each backfill gas. In addition, Figures 5.13 and 5.14 compare predictions and data for the vertical and horizontal full load nitrogen runs.

In every case, surface temperatures are overpredicted. This is seen in the illustrations showing the radial temperature profiles. The effect of the outside surface heat transfer coefficient will be eliminated in the following sections by comparing in terms of temperature differences.

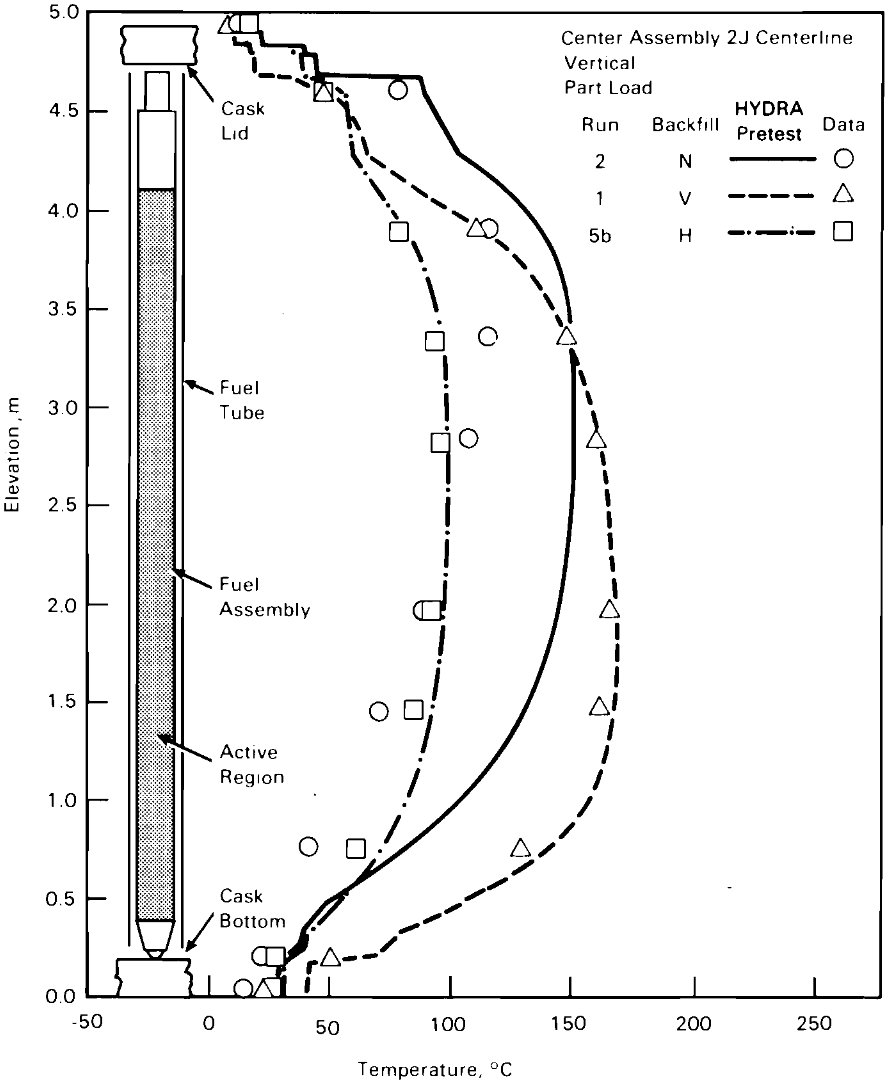

FIGURE 5.7. HYDRA Pretest Predictions of Center Assembly 2J Centerline Axial Temperature Profiles Compared to Part Load, Vertical, Vacuum, Nitrogen, and Helium Data

Temperature predictions for vertical vacuum and helium runs (Figures 5.7 and 5.9) are in excellent agreement (10°C) with experimental data. Predicted temperature magnitudes and axial profiles both agree well with test data. Comparisons of predicted radial vacuum and helium temperatures (Figures 5.8 and 5.10) are also in excellent agreement with data.

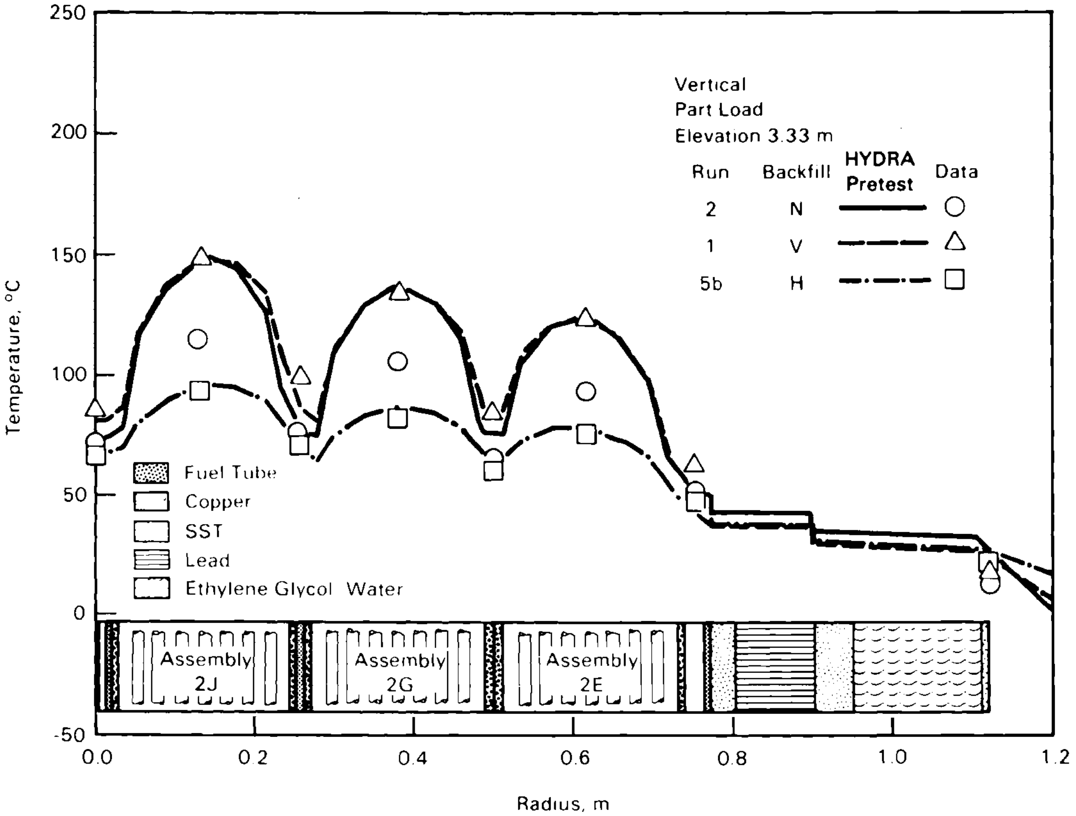

FIGURE 5.8. HYDRA Pretest Predictions of Radial (Diagonal) Temperature Profiles Compared to Part Load, Vertical, Vacuum, Nitrogen, and Helium Data at 3.33 m Elevation

Both vacuum and helium lack significant convection because of their relatively low density. The vacuum runs were actually ultra-low pressure nitrogen (~1 mm Hg). The thermal conductivity of nitrogen at this low pressure is approximately equal to the value near atmospheric pressure except in the narrowest gaps. The thermal conductivity is not significantly affected by low pressures, provided that controlling gap widths exceed the molecular mean free path of nitrogen molecules.

Temperature predictions for the vertical nitrogen runs (Figures 5.7 and 5.9) are in some disagreement (up to 60°C) with data. This is most apparent for run 2, the partial load case (Figure 5.7). Axial temperature data for this run are skewed by convection, causing a distinct peak in measured temperature near the top of the active region of assembly 2J. Comparison of the shape of

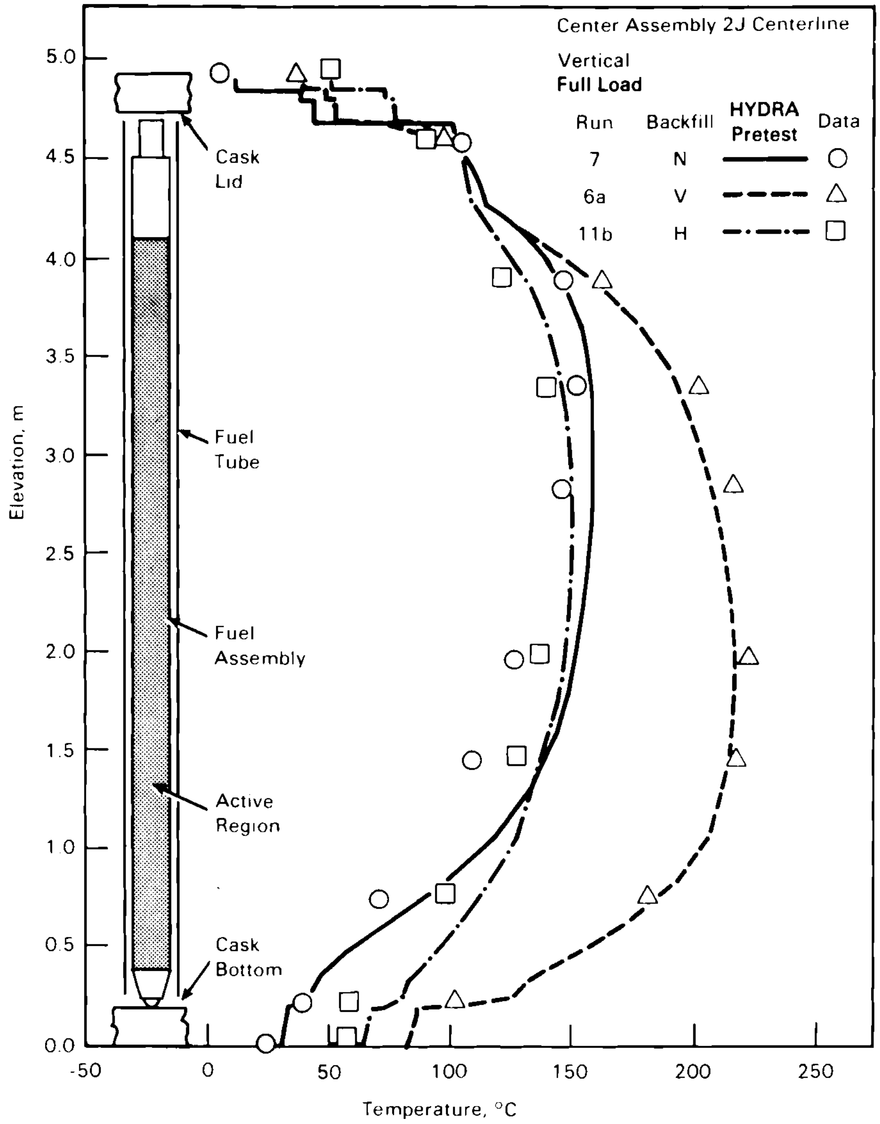

FIGURE 5.9. HYDRA Pretest Predictions of Center Assembly 2J Centerline Axial Temperature Profiles Compared to Full Load, Vertical, Vacuum, Nitrogen, and Helium Data

the predicted assembly centerline axial temperature profile with data indicates that a problem exists in the computational treatment of convection. Comparisons of predicted radial temperature profiles with data for run 2 (Figure 5.8) indicate that most of the disagreement between predicted and measured temperatures is confined to the temperature difference between the fuel tube wall and the assembly centerline. Typical velocity profiles predicted to exist in the REA cask for several test runs are presented in Table 5.5.

TABLE 5.5. Typical Predicted Velocity Magnitudes

		Peak Velocity, cm/sec		
Run No.	Run Descriptor[(a)]	Assembly	Fuel Tube	Support Channel
2	VPN	11.69	0.13	21.62
5	VPH	6.56	4.14	9.71
7	VFN	8.77	--	31.02
11a	VFH	5.20	--	9.65
9	HFN	0.53	--	2.93
10	HFH	0.07	--	4.11

(a) Descriptor identification: orientation/load/backfill
V = vertical P = part load N = nitrogen
H = horizontal F = full load H = helium

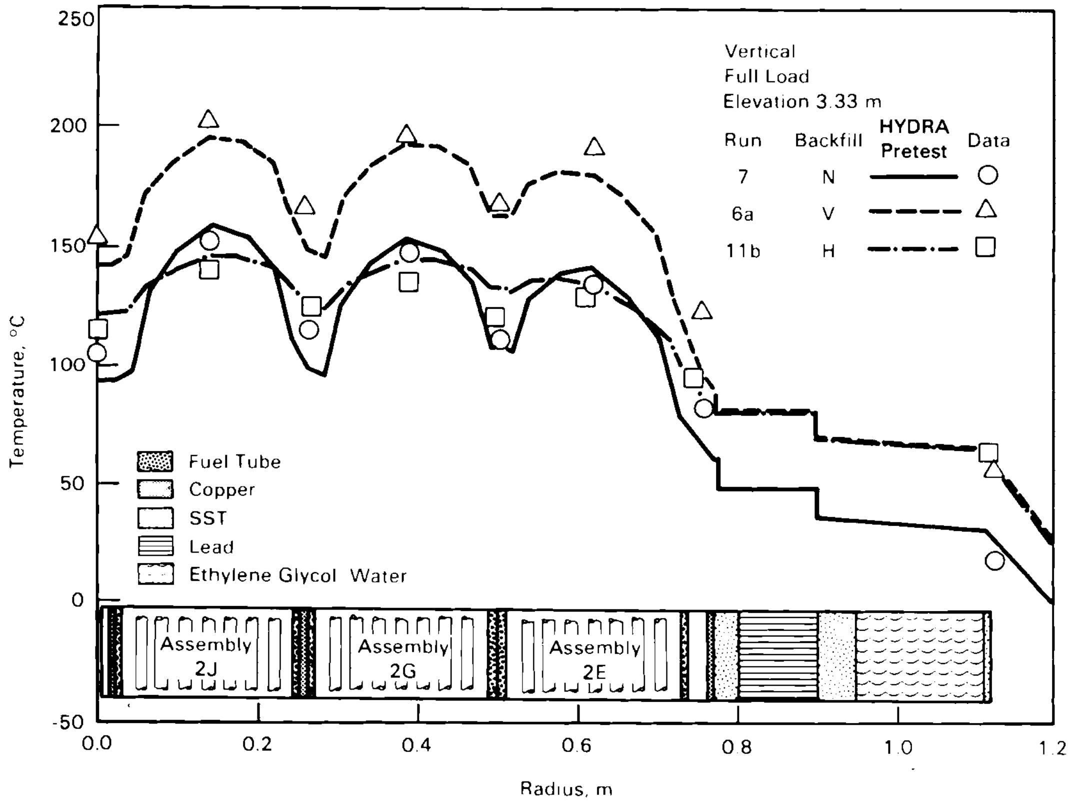

FIGURE 5.10. HYDRA Pretest Predictions of Radial (Diagonal) Temperature Profiles Compared to Full Load, Vertical, Vacuum, Nitrogen, and Helium Data at 3.33 m Elevation

Although not so pronounced, similar results are observed for run 7, the vertical, full load, nitrogen run (Figures 5.9 and 5.10). These results support the conclusion that the disagreement is related to convection. For run 2, the open fuel tubes permitted gas circulation in fuel assemblies that is predicted to be about one and one-half times that for run 7. Because the predicted assembly mass flux is greater for run 2, the problem with the convection

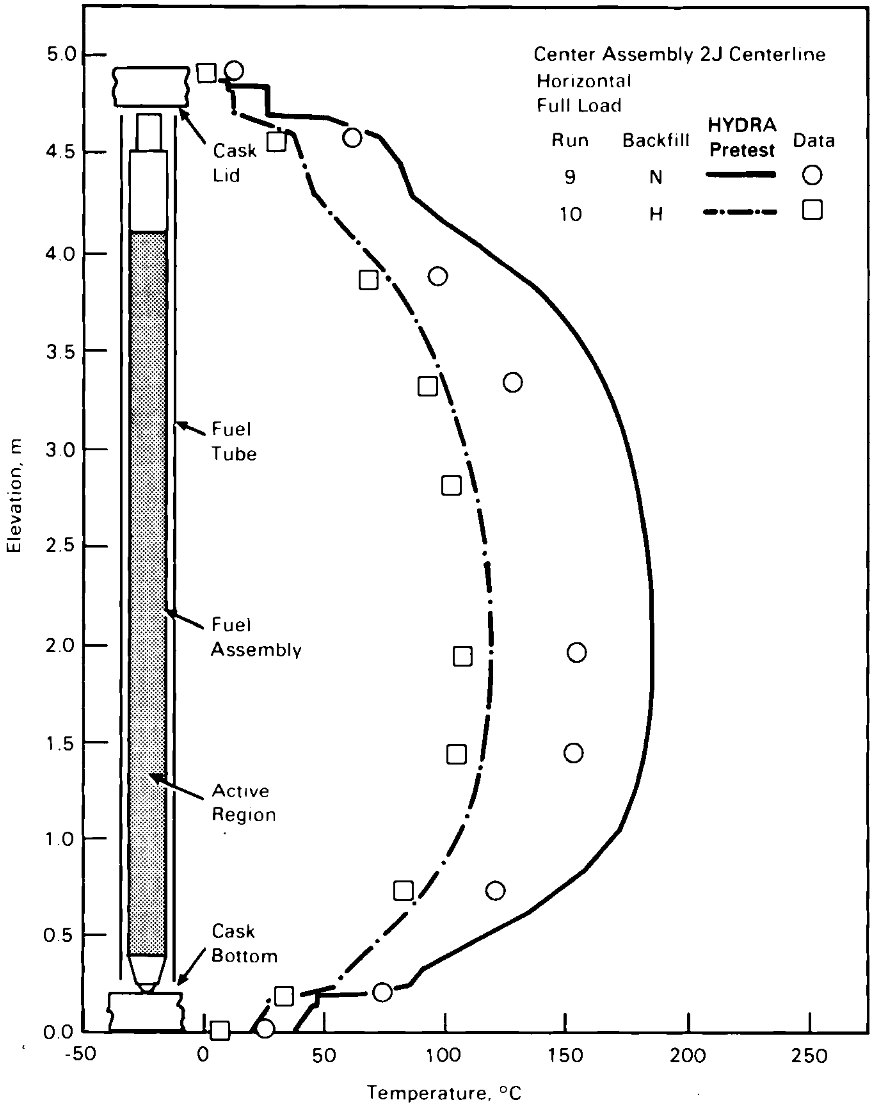

FIGURE 5.11. HYDRA Pretest Predictions of Center Assembly 2J Centerline Axial Temperature Profiles Compared to Full Load, Horizontal, Nitrogen, and Helium Data

model is more pronounced. Also, results for the other backfill gases suggest that the conduction and radiation models are performing adequately. For both the helium and vacuum cases, convection is a less significant heat transfer mode. For these cases, the agreement between predictions and data is relatively good.

Temperatures for the horizontal runs in nitrogen and helium are shown in Figures 5.11 and 5.12. Predictions of both temperature profiles agree well with data. However, the predicted temperature magnitudes are greater than test data. Predictions in helium are only slightly higher than data (15°C), but predictions with nitrogen are significantly higher than data (40°C).

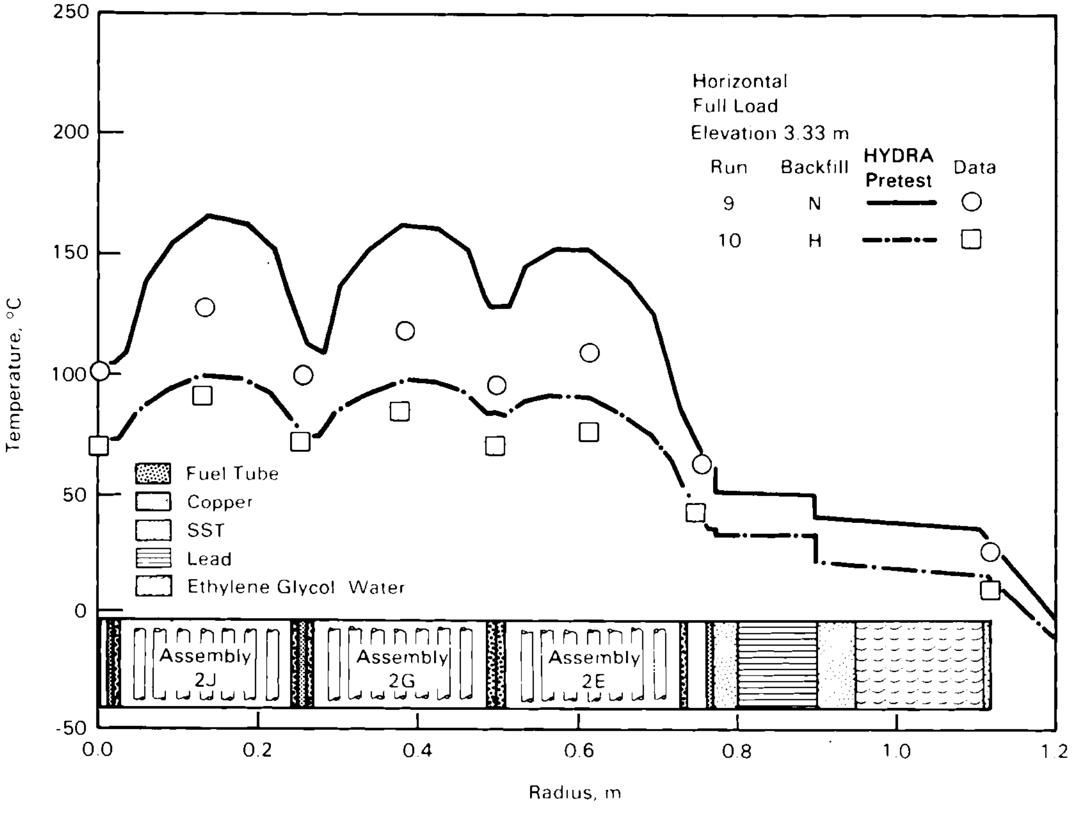

FIGURE 5.12. HYDRA Pretest Predictions of Radial (Diagonal) Temperature Profiles Compared to Full Load, Horizontal, Nitrogen, and Helium Data at 3.33 m Elevation

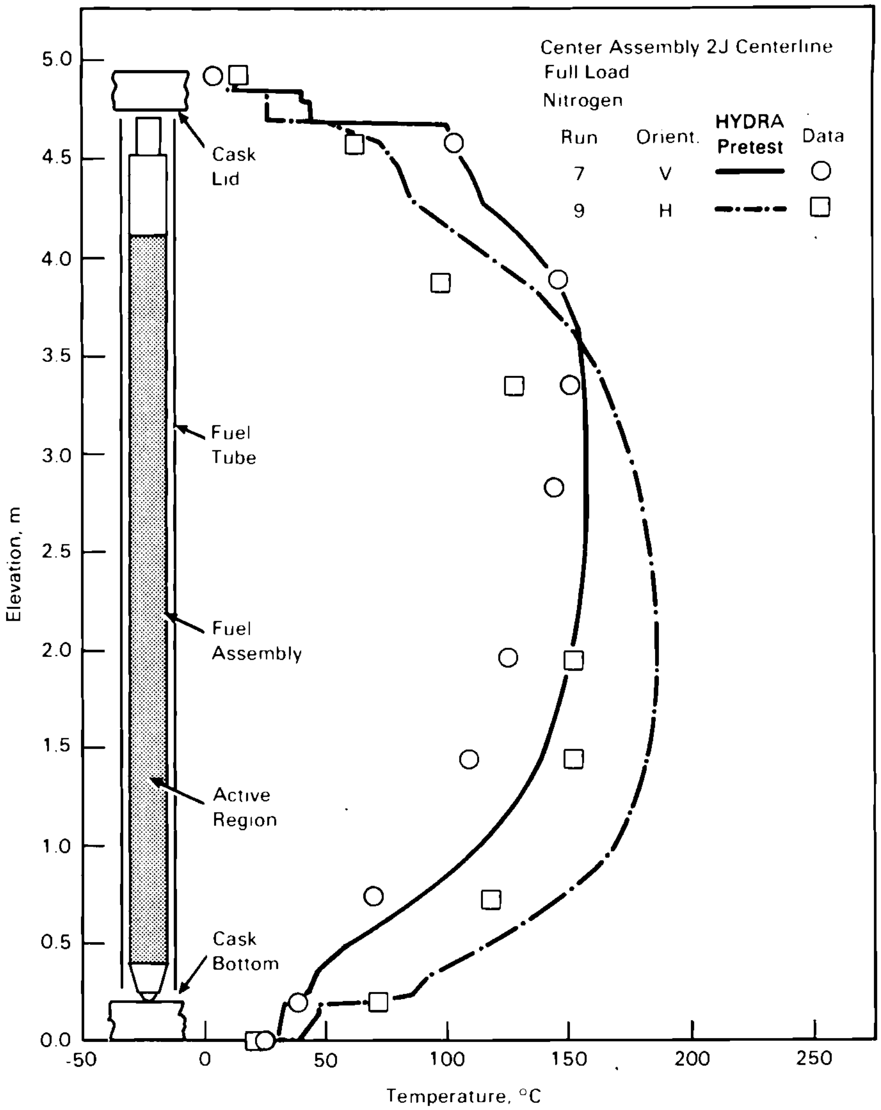

FIGURE 5.13. HYDRA Pretest Predictions of Center Assembly 2J Centerline Axial Temperature Profiles Compared to Full Load, Vertical and Horizontal, Nitrogen Data

The fuel assemblies were modeled with a single cell in the X-Y plane and, therefore, local axial or transverse circulation is neglected. Neglecting local circulation may be at least partially responsible for the observation that predictions for the horizontal nitrogen run are in greater disagreement with data than predictions for the horizontal helium run. With helium, this local circulation is less significant.

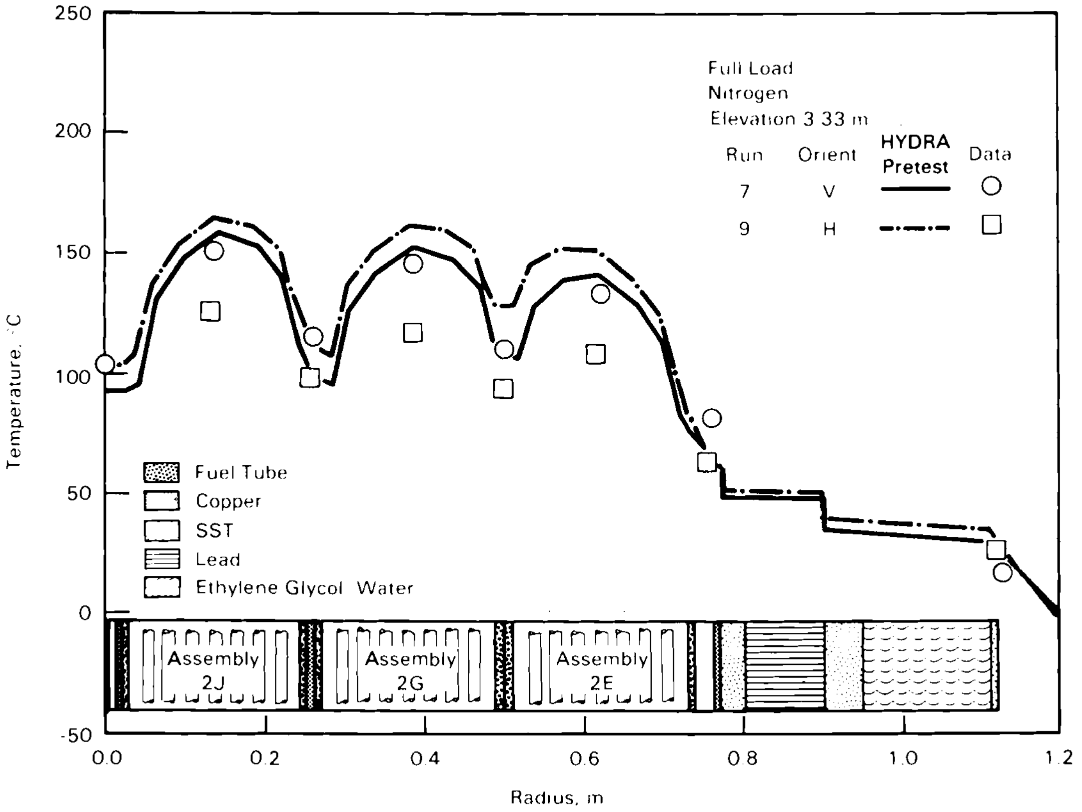

FIGURE 5.14. HYDRA Pretest Predictions of Radial (Diagonal) Temperature Profiles Compared to Full Load, Vertical and Horizontal, Nitrogen Data at 3.33 m Elevation

Fuel assembly orientation may also contribute to the disagreement between predictions and data for the horizontal runs. When the cask is in a horizontal orientation, each assembly rests against a fuel tube wall. Contact of an assembly with the wall reduces temperatures in the assembly. Because the fuel assembly is modeled in the center of the fuel tube, the thermal resistance of the gas between the assembly and adjacent fuel tube walls elevates predicted temperatures and distorts the predicted heat transfer distribution in the basket. The relatively high thermal conductivity of helium results in the gap thickness being less sensitive than the low conductivity of nitrogen or vacuum. Also, the high conductivity of helium overshadows radiation heat transfer and natural convection.

The effect of orientation on temperatures in nitrogen is presented in Figures 5.13 and 5.14. Predictions of temperature magnitudes are closer to data in a vertical orientation than in a horizontal orientation, but horizontal profiles are predicted much better than vertical profiles. This again indicates that convection was not modeled as accurately as conduction and radiation. Also, fuel assembly orientation may be important in predicting temperatures in a horizontal orientation where fuel assemblies contact basket fuel tubes. Notice that measured peak temperatures are approximately the same in both vertical and horizontal orientations, but their locations are not (1.45 m versus 3.33 m). This would indicate that, in nitrogen, the contact in a horizontal orientation is almost enough to make up for higher convection in a vertical orientation (McKinnon et al. 1986a).

5.1.3.1.2 Surface-to-Ambient. The cask outer surface-to-ambient heat transfer was evaluated by comparing data and predictions for four of the 30 thermocouples attached to the outer cask surface. The four thermocouples used in the comparison were located at circumferential orientations of -45° and 135° and at elevations of 1.45 and 3.33 m. These locations were considered less likely to be influenced by end effects.

The predicted surface temperatures for the four locations were averaged, as were the measured surface temperatures at these locations. Differences between averaged surface temperatures and the ambient temperature are shown in Figures 5.15 and 5.16. Figure 5.15 shows the temperature differences on the same scale as Figure 5.5, thereby demonstrating the relative magnitude of the surface-to-ambient temperature difference to the total temperature difference from peak-to-ambient. Figure 5.16 compares measured and predicted surface-to-ambient temperature differences with all values referenced to zero. The results from insulated cask runs 12, 13, and 14 are not included. In those pretest simulations, the measured surface temperatures were used as boundary conditions to avoid uncertainties associated with the insulation material.

Ratios of predicted temperature differences to measured temperature differences are an indication of how well the surface-to-ambient heat transfer is modeled by conventional correlations defined in the computational model description. In all cases, the ratio is above unity, with the range being

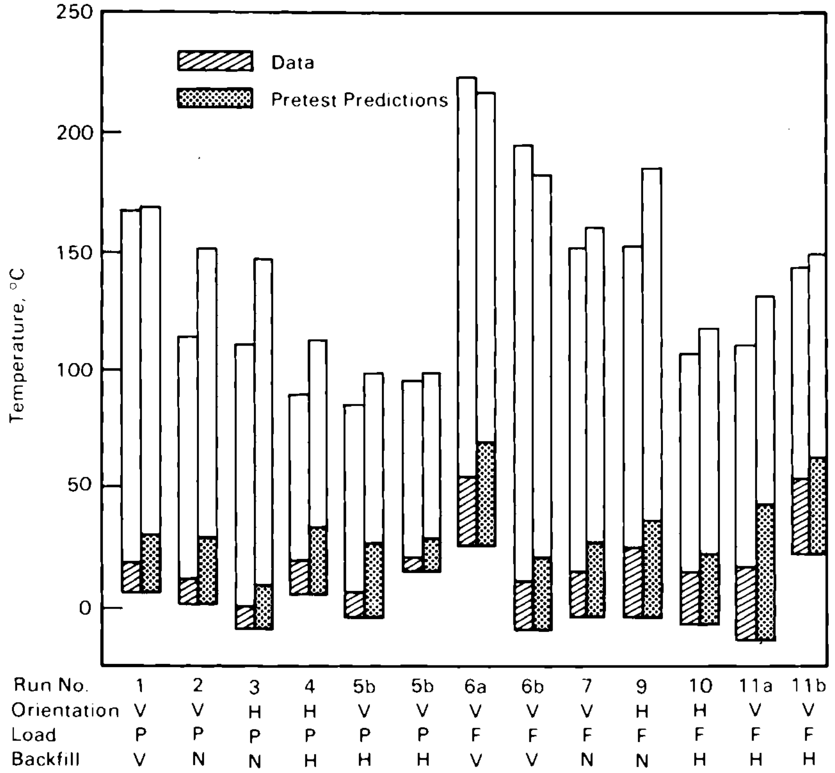

FIGURE 5.15. HYDRA Pretest Predictions of Cask Outer Surface-to-Ambient Temperature Differences Compared to Data and Peak-to-Ambient Temperature Differences

1.25 (run 11b) to 3.06 (run 5a), which indicates conventional correlations result in conservatively high predicted cask surface temperatures. It should be noted that the gross disagreement in test 5a is due to application of a reported zero wind speed when the actual value may have been 3.4 m/sec (7.5 mph). The anemometer may have been stuck because of an accumulation of frozen rain (McKinnon et al. 1986a). The revised wind speed is based on data from a weather station near the test site. Possible reasons for the relatively large and variable disagreements are discussed in the paragraphs that follow. The reasons focus on actual correlations used for the test, flow field characteristics, and mixed convection.

The correlations for the heat transfer coefficients used in the pretest analyses (Section 5.1.2.2) are based on idealized conditions. It is apparent that test conditions departed significantly from idealized conditions. The laboratory-derived correlations apply strictly to long cylinders and flat

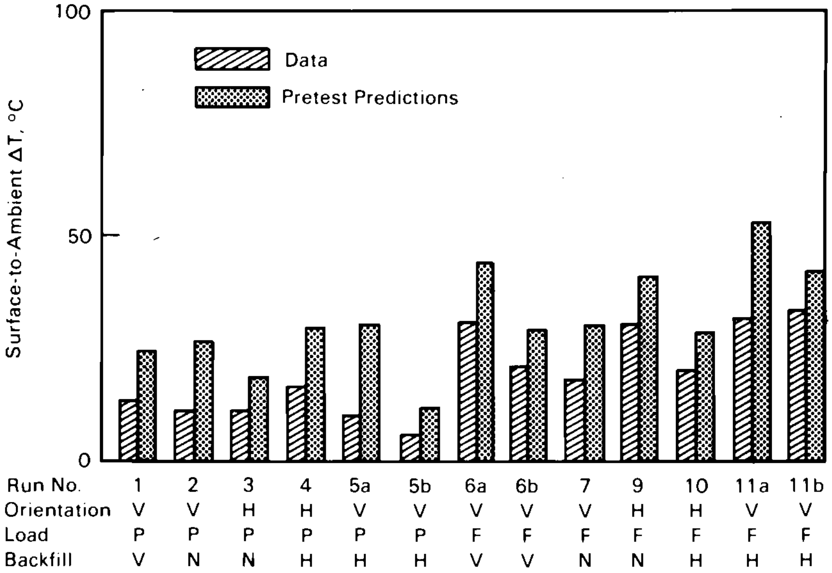

FIGURE 5.16. HYDRA Pretest Predictions of Cask Outer Surface-to-Ambient Temperature Differences Compared to Data

plates with sharp leading edges. The height-to-diameter aspect ratio of the cask is 2 to 1, and the leading edge seen by the wind was blunt. The wind direction and speed were variable so that the free stream about the cask was unsteady, nonuniform, and turbulent.

The presence of the rail car and other test site structures (chain link fences and buildings) may have contributed to the variable conditions of the free stream. Not only does the rail car perturb the flow field, but wind directed over the end of the rail car produces an entirely different flow field than that resulting from a wind directed at the side. The wind speeds used were averages of 24 hourly wind speeds. A time-averaged wind speed may not be appropriate. To accurately predict cask surface temperatures, time-averaged effective mixed heat transfer coefficients are needed. The effect of the rail car also influenced zero wind speed runs that required application of natural convection correlations. As air rises about the rail car, it pours over the edges, cables, and other appurtenances, and rolls along the cask surface.

An indication that mixed convection is involved in the heat transfer is shown in Figure 5.17. The ratio of the predicted surface-to-ambient temperature difference to the measured value is plotted against wind speed. There is

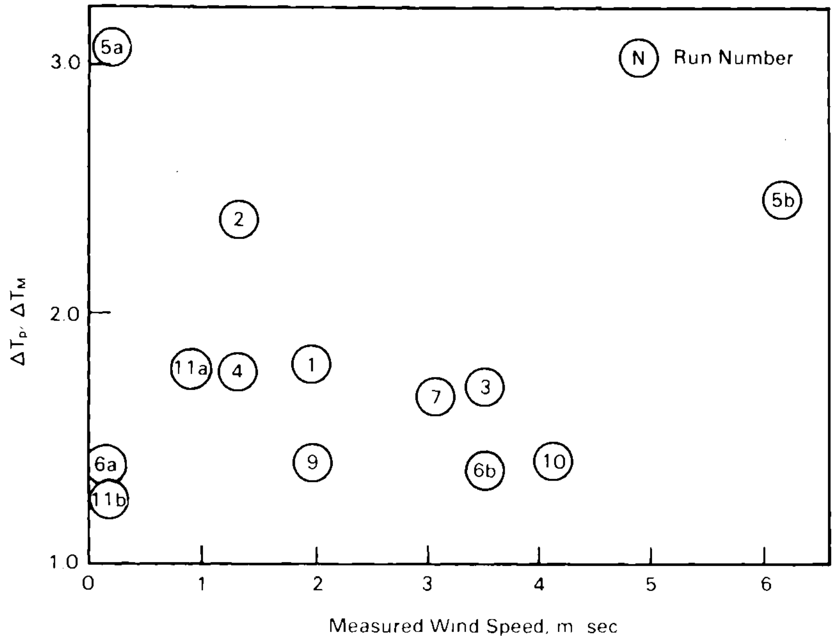

FIGURE 5.17. Ratio of HYDRA Pretest Predicted to Measured Cask Outer Surface-to-Ambient Temperature Difference Versus Measured Wind Speed

a vague trend toward greater disagreement at lower wind speeds. Inclusion of a natural convection component could improve the predictions. A review of the pertinent literature (Leung 1975; Oosthuizen and Leung 1978) suggests that a mean Nusselt number for mixed convection be computed according to

$$Nu_m = (Nu^n_{forced} + Nu^n_{natural})^{1/n} \tag{5.13}$$

The exponent n is unique to each application.

One additional issue regarding predicted surface temperatures is that insolation, or solar gain, was neglected. Figure 5.18 shows the ratio of predicted to measured surface-to-ambient temperature differences plotted against insolation. If insolation were important, the ratio would increase for increasing values of insolation. Because no increase is evident, it was concluded that the exclusion of insolation in the model was appropriate. Evidently, the solar gain during the day was approximately equal to the radiation loss at night.

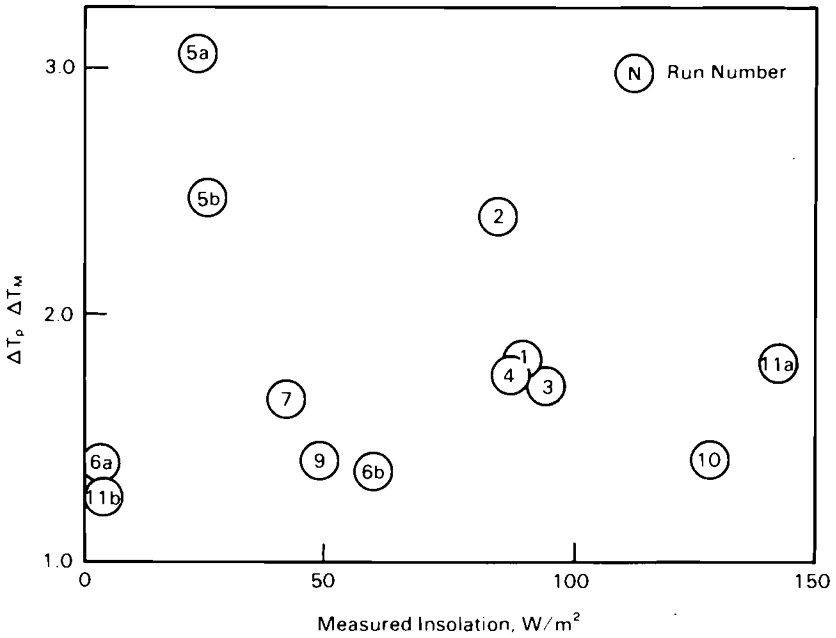

FIGURE 5.18. Ratio of HYDRA Pretest Predicted to Measured Cask Outer Surface-to-Ambient Temperature Difference Versus Measured Solar Insolation

Reviews of predictions and data support the conclusion that the surface-to-ambient heat transfer cannot be modeled accurately by conventional correlations. Conventional correlations result in conservatively high cask surface temperature predictions. Lacking a meaningful improved correlation, measured surface temperatures were used in the post-test analysis to conveniently evaluate predictions of the other cask component temperature differences discussed in the following sections.

5.1.3.1.3 Cask Body. The cask body heat transfer is evaluated from surface temperatures and temperatures at six internal locations on the basket diagonal (Figure 5.19) at two axial elevations. In the basket, interstices exist between the corners of adjacent fuel tubes and at the corners between fuel tubes and adjacent basket support structures. Temperatures were measured in the interstices on the diagonal of quadrant 2 at numerous elevations (McKinnon et al. 1986a). The six temperatures used to evaluate the cask body heat transfer were taken from the interstice at the outside corner of assembly 2E and from the two interstices at the diagonal corners of assembly 2J (center basket node and basket node 2J) at elevations of 1.45 m and 3.33 m. The

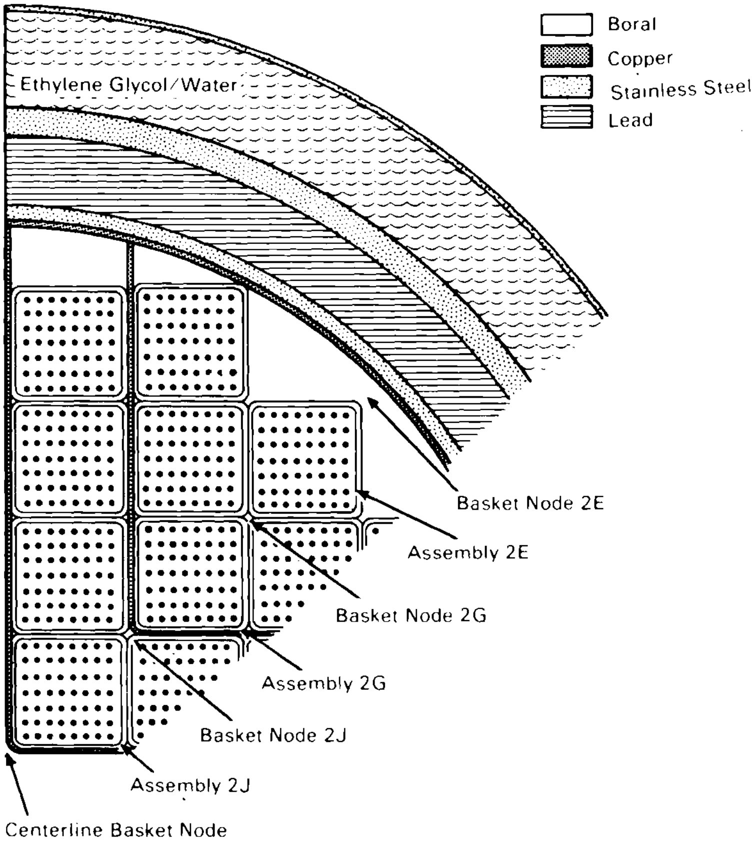

FIGURE 5.19. Identification of Assemblies and Basket Nodes on the Quadrant Diagonal

temperatures measured in the interstitial locations on the diagonal corners of assembly 2J are used to evaluate the cask body heat transfer because the copper conduction strips that connect these locations to the cask body are well known and represent a small thermal resistance. The interstitial locations are referred to throughout the remainder of this section as basket nodes. Basket node 2E is not as open as it appears. Details of the support structure are proprietary and have not been included in Figure 5.19.

Temperature differences between basket node 2E and the cask surface at the lower elevation of 1.45 m are shown in Figures 5.20 and 5.21. Figure 5.20 shows temperature differences on the same scale as Figure 5.5, thereby demonstrating relative magnitudes of cask body temperature drops to total temperature drops. Figure 5.21 compares measured and predicted cask body temperature drops with all values referenced to zero. Predicted temperature drops are

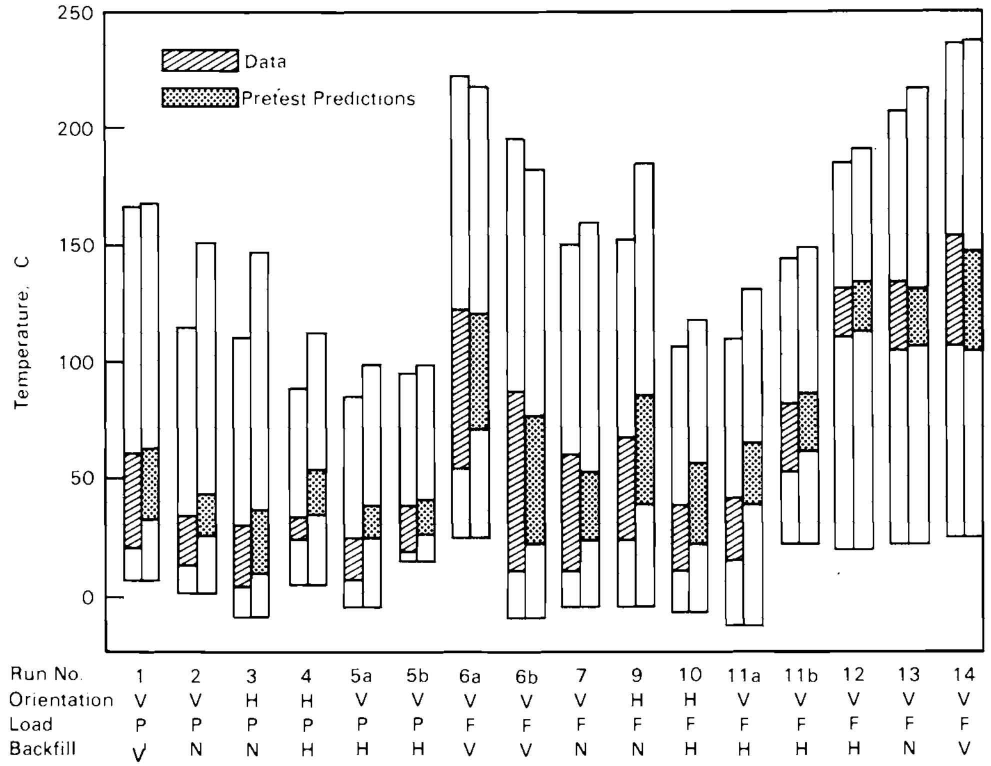

FIGURE 5.20. HYDRA Pretest Predictions of Temperature Differences from Basket Node 2E to Cask Outer Surface at 1.45 m Elevation Compared to Data and Peak-to-Ambient Temperature Differences

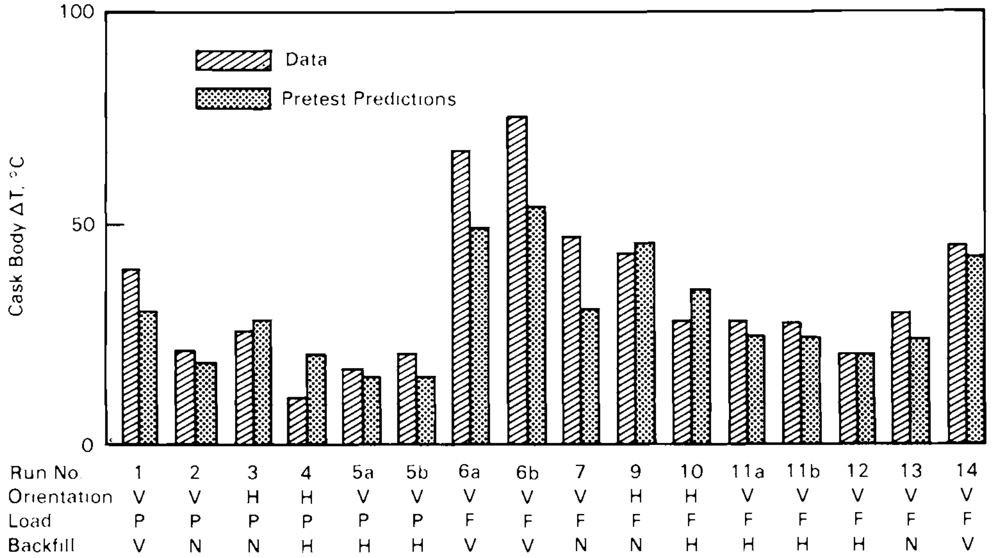

FIGURE 5.21. HYDRA Pretest Predictions of Temperature Differences from Basket Node 2E to Cask Outer Surface at 1.45 m Elevation Compared to Data

equal to or less than (by up to 20°C) measured temperature drops for the vertical runs. This trend is typical at all six of the aforementioned locations.

Accurate predictions of heat transfer through the cask body are difficult because of a number of uncertainties that exist in the description of the cask between the relevant internal basket nodes and the cask outer surface. These uncertainties include:

- contact of the copper conduction strips and basket support structure with the copper shell of the basket
- contact of the copper shell of the basket with the stainless steel inner wall of the cask body
- gaps between the lead and stainless steel making up the cask body
- convection in the ethylene glycol/water neutron shield
- basket node thermocouple locations.

Contact of the copper conduction strips and basket support structure with the copper shell of the basket is included in the discussion of the cask body heat transfer because the thermal resistance of these contacts lies between available internal and cask outer surface thermocouple locations. The available measured temperature drop through the cask body depends on the thermal resistance of these contacts as well as the thermal resistance of the components of the actual cask body. Specific details of the contact of the copper conduction strips and basket support structure with the copper shell of the basket are proprietary information. While these details cannot be discussed, they were available for the thermal analysis. The thermal model was developed from as-built drawings, the results of a bench scale test conducted by REA, and other pertinent heat transfer data. Although the model is supported by this information, the contact thermal resistance is still not well known and is subject to local variations due to construction differences and thermal expansion.

Good contact of the copper shell of the basket with the stainless steel inner wall of the cask body was precluded by the design, which specified different radii of the mating surfaces. The basket is assembled in four quadrants that are placed in the cask and forced outward against the inner wall of the cask. The result is an irregular contact between the basket and cask body. Although there is undoubtedly some pressured contact between the basket and cask, most of the interface is potentially subject to this gap. The cask performance is computed on the basis of the average gap width. Using a feeler gauge having blades 30.5 cm (12 in.) long, the gap was measured at 28 circumferential locations around the top of the cask, the only access point. The gap varies in width from near zero to above 0.254 cm (0.100 in.). The average measured gap width is nearly equal to the average gap width computed from geometric analysis of the mating surfaces based on design dimensions. This gap width is 0.056 cm (0.022 in.) and was the gap width specified in the pretest analysis. Much of the data was obtained from quadrant 2 (see Figure 3.6) where the average measured gap width was 0.147 cm (0.058 in.). This is an upper bound for the specification of the gap width in the post-test analysis.

The lead gap in the cask body is anticipated to exist based on experience. When the molten lead is poured into the annulus formed by the stainless steel liners, it shrinks as it cools, leaving a gap on the outer surface. No measurements were made of the average gap; a value of 0.0501 cm (0.020 in.) was used in the pretest analysis. Based on experience that includes destructive testing, it is speculated that the gap may be as large as 0.127 cm (0.050 in.). Thus, a range of values is available for the post-test analysis.

Each of the above-mentioned gaps and contacts is not well defined, although realistic ranges in their values can be supported. An additional factor that makes their exact specification even more unlikely is thermal expansion effects. Thermal expansion may cause some gaps to close and others to open. In the basket, thermal expansion may cause warping of constrained components, thereby tightening some contacts and opening others. Thus, these gaps and contacts most likely result in significant local variations of thermal resistances.

An effective thermal conductivity is assigned to the neutron shield liquid. The conductivity is computed from Equation (5.5) of Section 5.1.2.2.

The conditions for which Equation (5.5) were developed are only approximated by the neutron shield; however, the associated small temperature difference is probably not significant.

At basket nodes 2J and 2E, the temperature gradients are relatively large, the thermocouples could not be attached to the basket, and the thermocouples could move laterally as a result of cask handling activities. The lack of precisely known lateral locations in regions of high temperature gradients introduces both uncertainty and scatter into the data. This problem does not exist for the centerline basket node where the temperature gradient should be near zero.

In spite of these uncertainties, comparisons of predicted and measured temperatures show some consistent trends that led to new specifications of some cask body parameters for the post-test analysis. The ratio of the predicted and measured cask body temperature difference is used to derive an improved description of the cask body heat transfer parameters discussed above. The product of this ratio and the overall radial thermal conductance used in the pretest analysis yields a new cask body radial thermal conductance that approximates the measured conditions. It is only a first approximation because of the temperature dependence of the conductance, and because a change in the radial conductance is arrived at without inclusion of the multidimensional nature of the cask and the cask model. None of the disagreement between predictions and data is assigned to the thermocouple location or the contact of the copper conduction strips and basket support structure with the copper shell of the basket. Furthermore, adjustment of parameters without cause cannot be justified. The values of any redefined cask parameters must fall within the range of measurements or experience.

There are seven runs (Figure 5.21) involving nitrogen backfill with the cask in the vertical orientation (1, 2, 6a, 6b, 7, 13, 14). For these runs, the average ratio of the predicted cask body temperature drop to the data is 0.75. For the five runs with helium backfill and the cask in the vertical orientation (5a, 5b, 11a, 11b, 12), the average ratio for all the data examined is 0.84. These average values are based on all the available data from the six basket TC locations identified above.

Computationally, the radial thermal resistance of the cask body includes the components identified in Figure 5.22. The radial thermal resistance is computed by summing the resistance of the various components as

$$R = \sum_i \left[\frac{\ln\{(r_{i+1})/r_i\}}{2\pi L k_i}\right] + \left[\frac{1}{2\pi L r_i h_i}\right] \tag{5.14}$$

where r is the radius, k is the thermal conductivity, h is the heat transfer coefficient, and L is the cask length.

To develop an improved description of the cask body parameters, this resistance was computed for both nitrogen and helium backfills. The resistance is independent of backfill gas except for the gap between the copper shell of the basket and the inner wall of the cask body. For nitrogen, the improved resistance, Ri, that should bring the predicted cask body temperature drop up to the measured temperature drop is $R_{i,N_2} = (1/0.75)\ R_{N_2}$ and for helium, $R_{i,He} = (1/0.84)\ R_{He}$. To satisfy both equations, the gap width between the copper shell and the stainless steel liner is redefined as 0.10 cm (0.040 in.) from 0.056 cm (0.022 in.). It is also necessary to consider adjustment of the common resistances of the lead gap and neutron shield. The equations are satisfied without changing the lead gap, and a value of 0.05 cm (0.020 in.)

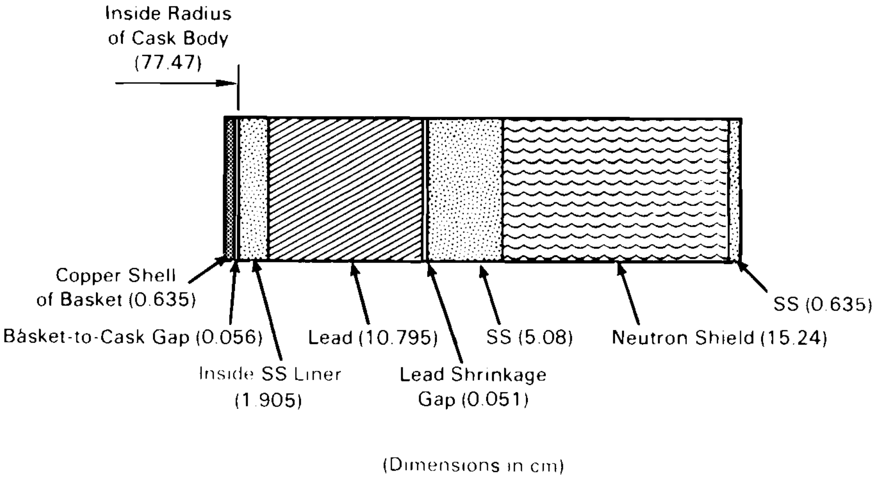

FIGURE 5.22. Components of Cask Body

was used for the lead gap in the post-test analysis. The effective conductivity of the neutron shield is reduced to 0.18 W/cm°C (10.4 Btu/hr/ft°C) from 0.20 W/cm°C (11.1 Btu/hr/ft°C) to be consistent with the predicted temperature drop and heat transfer through the body. These values are arrived at by comparisons of predictions to data and are justified because they fall well within previously suggested ranges.

5.1.3.1.4 Fuel Basket. Basket temperatures were measured at two elevations, 1.45 and 3.33 m above the bottom of the cask, in the interstices between fuel tubes on the diagonal of quadrant 2 (Figure 5.19). The evaluation of the heat transfer in the basket is based on comparisons of these measured temperatures with predicted temperatures at the same locations. Differences between temperatures in various basket nodes and temperatures in basket node 2E are compared. Basket node 2E temperatures are used as references because they are the lowest measured temperatures on the basket diagonal.

Temperature differences between basket node 2G and basket node 2E at an elevation of 1.45 m are shown in Figures 5.23 and 5.24. Figure 5.23 shows temperature differences on the same scale as Figure 5.5, thereby indicating the relative magnitude of temperature differences in the basket to total temperature differences. Figure 5.24 compares predicted and measured temperature differences with all values referenced to zero. These illustrations exemplify the information obtained from the two elevations in the various basket nodes.

The ratio of predicted and measured temperature differences between the basket nodes is an indication of how well the HYDRA models simulate the thermal resistance and the heat transfer throughout the basket matrix. For basket nodes 2G and 2E at an elevation of 1.45 m, the ratios lie between 0.87 (run 6b) and 1.38 (run 2). The average ratio at this location for all the vertical runs is 1.09. Comparisons of the temperature difference between the same interstitial locations, but at an elevation of 3.33 m, yield ratios of predicted-to-measured temperature differences that average 1.42. At this location, the ratios vary from 1.14 to 1.64. Greater disagreement at the higher elevation does not appear to be related to convection. The most severe disagreements are with helium backfill for which convection is of secondary importance. The fuel assembly orientation, which is somewhat random, would not consistently skew the

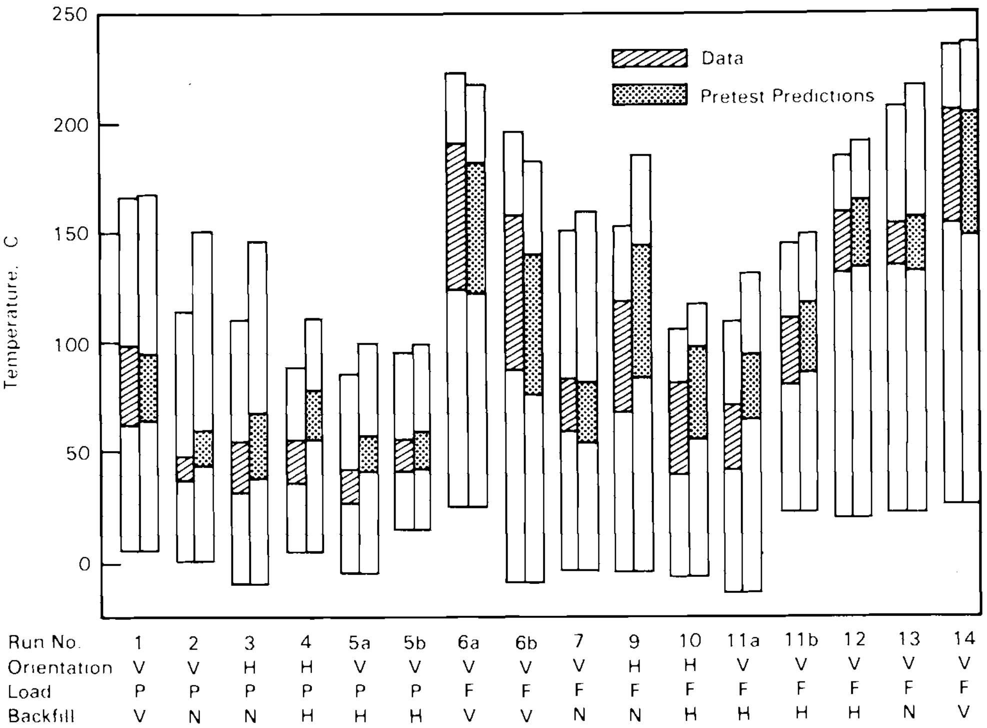

FIGURE 5.23. HYDRA Pretest Predictions of Temperature Differences from Basket Node 2G to 2E at 1.45 m Elevation Compared to Data and Peak-to-Ambient Temperature Differences

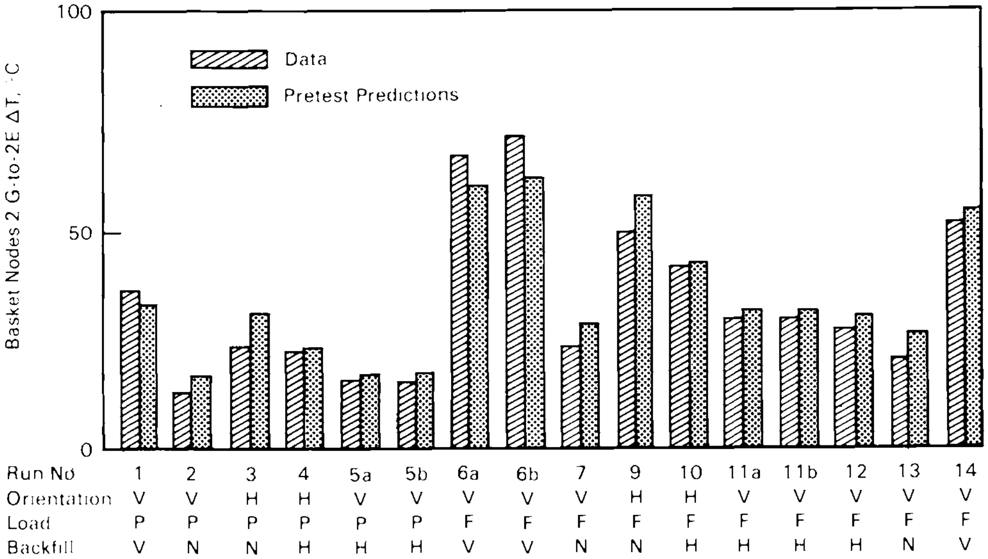

FIGURE 5.24. HYDRA Pretest Predictions of Temperature Differences from Basket Node 2G to 2E at 1.45 m Elevation Compared to Data

results in this fashion. A common adjustment of design parameters or emittances would not yield better agreement at both locations. Remaining possibilities that may lead to greater disagreements at the higher elevations are local variations in the basket construction and skewed positioning of the thermocouple in basket node 2G. Because the fuel tubes may not be precisely straight, the gap between adjacent tubes may vary with elevation.

Predicted and measured temperatures at other basket locations were compared. These comparisons involved temperature differences between the cask centerline and basket node 2E, and between basket nodes 2J and 2E (Figure 5.19). Again, the ratios of predicted and measured temperature differences were used to indicate the level of agreement. For the two elevations in the centerline and 2J basket nodes, the average ratio was 1.08. Of 46 data comparisons, 44 lie within a range of 0.73 to 1.33. The agreement here and at the lower elevation in basket node 2G (Figure 5.24) supports the conclusion that the disagreement at the higher elevation in basket node 2G is due to local uncertainties that cannot be addressed in the computational model. The uncertainties associated with the basket make accurate predictions of basket temperatures difficult as discussed below.

The contact or lack of contact between the components of the fuel basket is an important uncertainty in the basket matrix. When the fuel tubes are packed into the basket assembly, the contact between tubes may be extremely variable. A review of as-built drawings, including nominal dimensions of all components, suggests that for the fuel basket to occupy the inner cask cavity, the average separation of the fuel tubes is about 0.23 cm (0.091 in.). The fuel tubes have "beads" at regular axial intervals on the outside surface. These beads are elevated 0.13 cm (0.050 in.) and cover approximately 10% of the outer surface area of each fuel tube. The beads are staggered so that they cover about 20% of the area between adjacent fuel tubes. For this portion of the surface, the average separation of the fuel tubes is 0.10 cm (0.040 in.). Due to the tolerance on straightness and in consideration of the assembly technique that forces the quadrants of the basket outward against the inside surface of the cask body, there undoubtedly is some good contact between fuel tubes. Thus, the separation between surfaces in the basket may vary from near zero to values in excess of 0.23 cm (0.091 in.). While local variations may exist with regard to the actual basket heat transfer network, global agreement between predictions and data is obtained by using an average gap separating the adjacent basket components. The value used in the pretest analysis was 0.127 cm (0.050 in.) and the gap was modeled as a gas-filled gap with no contact of the adjacent components.

Typical junctions in the fuel basket matrix are shown in Figure 5.25. The heat transfer conductance through a junction is considerably less than that of the fuel tube. The added junction thermal resistance has a great influence on the heat transfer distribution through the basket. At the same time, there is some uncertainty about how these junctions should be modeled when only one computational cell is available per junction. Individual components of the junctions cannot be modeled; instead, composite thermal properties are required. The composite thermal resistance that is used to represent the junction accounts for the parallel/series thermal paths. But it also attempts to account for two-dimensional heat transfer around the corner of a fuel tube where a larger normal area for the heat transfer across the gap is available. This complexity makes accurate formulation of the junction models difficult.

In addition to these uncertainties of the basket model, accurate predictions of basket temperatures are affected by the predicted heat transfer distribution into and out of the basket. The fuel assemblies are modeled in the center of the fuel tubes. This establishes the predicted distribution of heat into the basket. The actual orientation of the fuel assemblies is, in general, noncentered and variable, and subject to change between runs. Therefore, the actual distribution of heat into the basket is not readily predictable.

A consistent adjustment to basket thermal resistances could not be justified because of the complexity of the basket matrix, and because of the uncertainty of the heat transfer distribution into the basket. Therefore, the post-test analysis was performed with the identical basket model used in the pretest analysis.

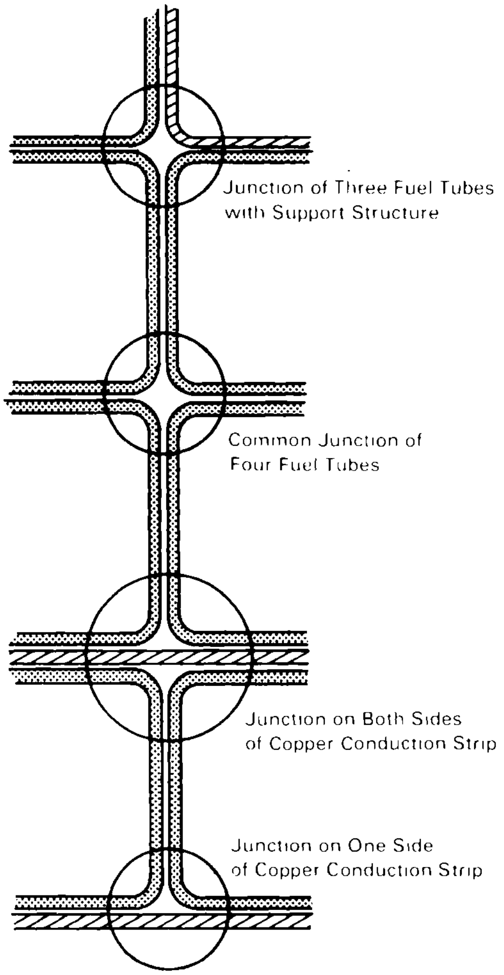

FIGURE 5.25. Typical Junctions in the Fuel Basket

5.1.3.1.5 Fuel Assembly. Fuel assembly heat transfer predictions were evaluated by considering heat transfer paths from center rods to adjacent basket nodes and center rods to outer rods. Temperature differences between the center rod of assembly 2G and basket node 2G (Figure 5.19) at an elevation of 1.45 m are shown in Figures 5.26 and 5.27. Figure 5.26 shows temperature differences on the same scale as Figure 5.5, thereby demonstrating the relative magnitude of local assembly temperature differences to total temperature differences. Figure 5.27 compares predicted and measured temperature differences with all values referenced to zero. Both figures exemplify the information obtained from other basket nodes and their respective fuel assembly center rod temperatures. Comparisons were also developed from data taken at the 3.33-m elevation.

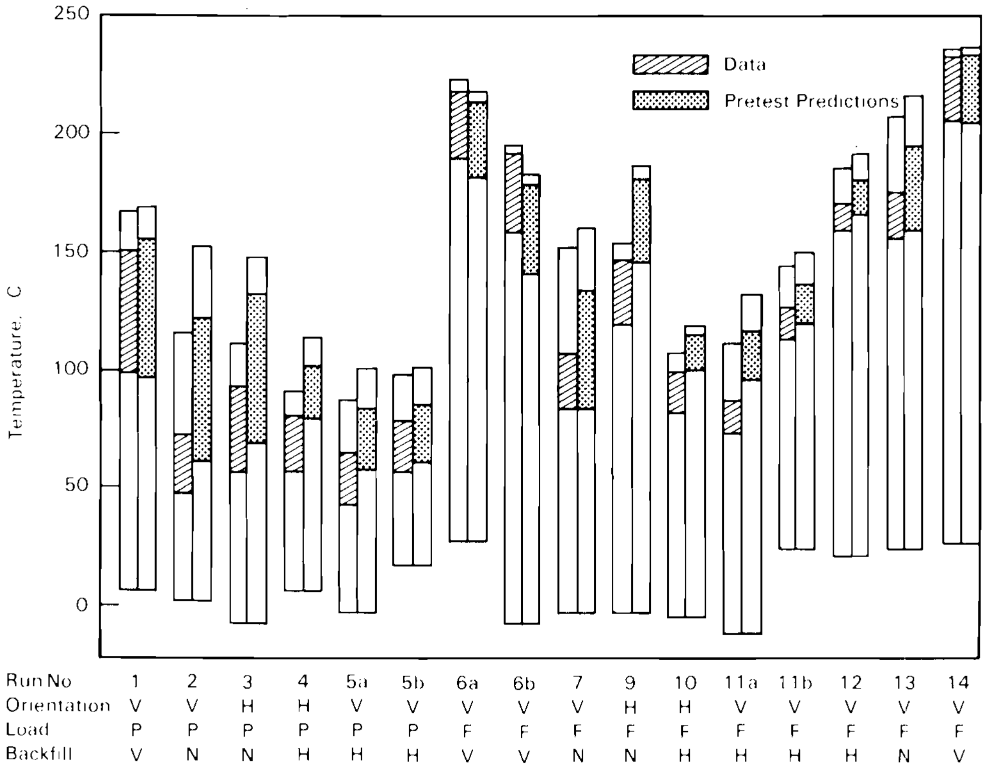

FIGURE 5.26. HYDRA Pretest Predictions of Temperature Differences from Assembly 2G Center Rod to Basket Node 2G at 1.45 m Elevation Compared to Data and Peak-to-Ambient Temperature Differences

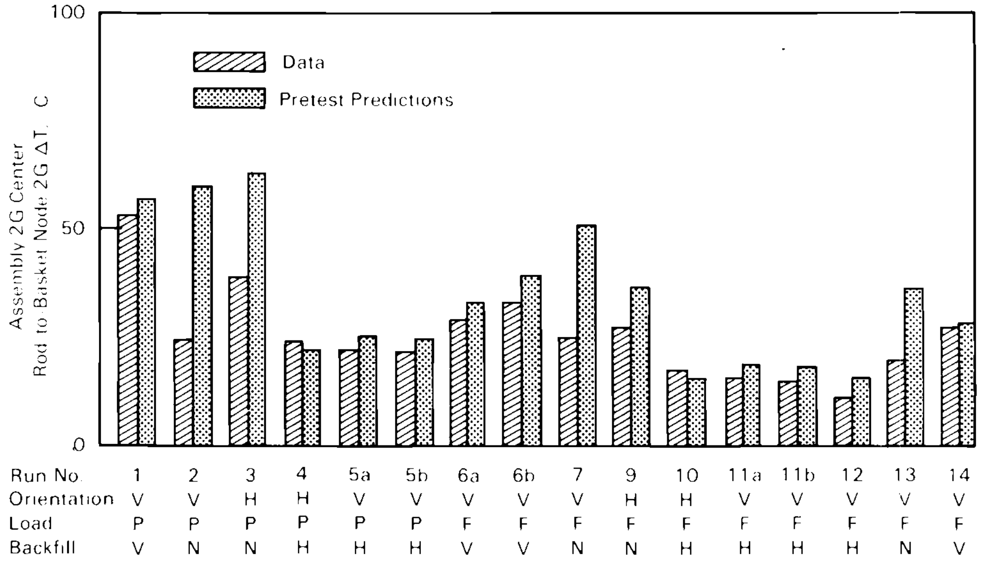

FIGURE 5.27. HYDRA Pretest Predictions of Temperature Differences from Assembly 2G Center Rod to Basket Node 2G at 1.45 m Elevation Compared to Data

Ratios of predicted to measured center rod-to-basket node temperature differences indicate how well the HYDRA model represents the thermal resistance and the heat transfer in the spent fuel assemblies. Because radiation is an important mode of heat transfer, the vacuum cases will be considered first. For the center rod and the basket node of assembly 2G, at an elevation of 1.45 m, ratios of predicted-to-measured temperature differences for the vacuum cases (runs 1, 6a, 6b, 14) average 1.11, with the range being 1.04 to 1.18. For all similar locations for which comparisons were made, the average ratio remained 1.11 and the range was 1.02 to 1.26.

These results suggest that enhancing the effective thermal conductance between these points by a factor of 1.11 is appropriate. If this is accomplished by the radiation component of heat transfer, the emittance would be increased for the rods and/or stainless steel fuel tube surfaces. Fuel rod emittances were assumed to be 0.8, and increasing this value is questionable. Emittances of the stainless steel fuel tubes were measured, and changing measured emittances to get predictions to match data is also questionable. The coarseness of the grid probably contributes the most to the disagreement. Because a change in emittances cannot be justified, and because it was not practical to refine the computational grid, the post-test analysis was conducted with the pretest radiation model and emittance values.

Disagreements between predictions and data for center to basket node temperature differences in the nitrogen runs (2, 3, 7, 9, 13) are obvious. These disagreements between the center rod and basket node temperatures are most likely due to the coarse grid and the use of a fuel tube model. Disagreements exist for both vertical and horizontal runs, but for different reasons. In the horizontal runs (3 and 9), the fuel assemblies rest against the fuel tubes. The actual thermal resistance between the outer rows of rods and fuel tubes is significantly less than the thermal resistance in the HYDRA model, which is based on a nominal gap of 0.56 cm (0.22 in.). Also, transverse convective circulation in the horizontal fuel tubes could contribute to an enhanced effective thermal conductance of the gas. The coarse grid precludes computation of this effect.

In the vertical orientation (runs 2, 7, and 13), the vertical flow resistance in the assembly is more than an order of magnitude greater than the vertical flow resistance in the nominal channel between the outer row of rods and the fuel tube wall, i.e., wall channel. A composite flow resistance is used in the HYDRA model. The fuel tube model used to define local fuel assembly temperatures included the assumption that the bulk axial flow splits between the assembly and the adjacent wall channels according to the ratio of flow resistances. This apparently is not the case because data comparisons suggest that the buoyancy-driven flow in the fuel assemblies is substantially greater than what is predicted by the flow split approach. In this application, the fact that the fuel tube model does not solve the momentum equations may be a significant shortcoming. Solution of the momentum equations would yield flows distributed in consideration of the forces driving the flow as well as flow resistance. Although the axial flow resistance of the assemblies is much greater than that of adjacent wall channels, the primary driver of the flow is the heat generated in the assemblies.

Shape of axial centerline temperature profiles predicted by HYDRA reasonably match shapes of distributions of axial assembly centerline temperature data for the nitrogen runs (Figures 5.7 and 5.9). This suggests that a significant axial mass flux exists within the assembly. Such a mass flux is approximated by the bulk flow. Therefore, the assumption of a uniformly distributed flow is applied to the fuel tube model in the post-test analysis. Although convection is less important in helium and vacuum runs, the uniform flow assumption in the fuel tube model is also applied to these cases in the post-test analysis.

In assemblies 1F and 2G, rod-to-rod temperature differences were measured. The outer rod thermocouples were placed so that, when the cask is horizontal, the outer rod thermocouples are on the side of the assemblies that is against the fuel tube walls. These thermocouples are at an elevation of 3.33 m. The outer rod thermocouple in assembly 1F is at an elevation of 3.63 m. The rods in question are shown in Figure 5.28, which portrays the quarter-symmetry view applicable to the vertical orientation. Figure 5.28a shows the relationship of the fuel tubes to the copper strips. Figure 5.28b

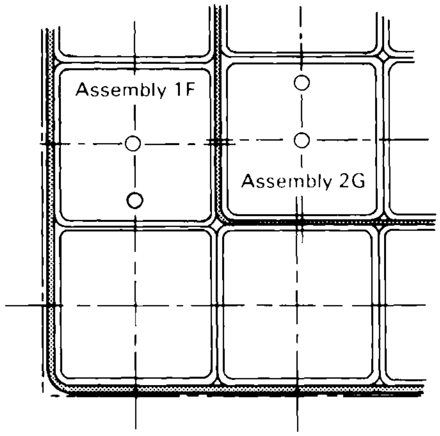

a. Instrumented Rods

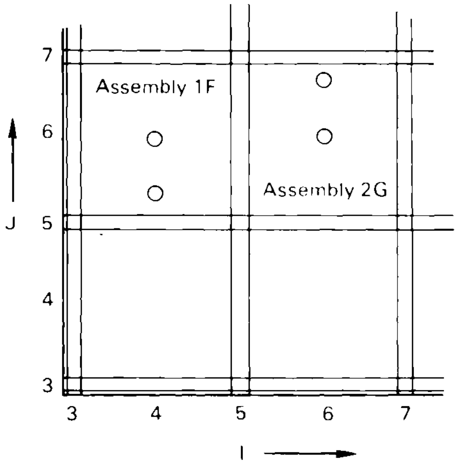

b. HYDRA Grid

FIGURE 5.28. Thermocouple Locations for Center Rod to Outer Rod Temperature Difference Measurements and Corresponding HYDRA Computational Grid

shows the HYDRA computational grid in this vicinity. Note that assemblies 1F and 2G are not actually adjacent to one another as shown in Figure 5.28. Although these are the actual assemblies in which the rod temperatures were measured, computationally there is no distinction between assemblies 1F and 2F or 1G and 2G in quarter symmetry.

Temperature differences from the center rods to the outer rods are shown in Figures 5.29 and 5.30. Agreement in a vacuum backfill is reasonably good. Disagreements between predicted and measured temperature differences in nitrogen and helium are seen to be quite large on a fractional basis for some of the

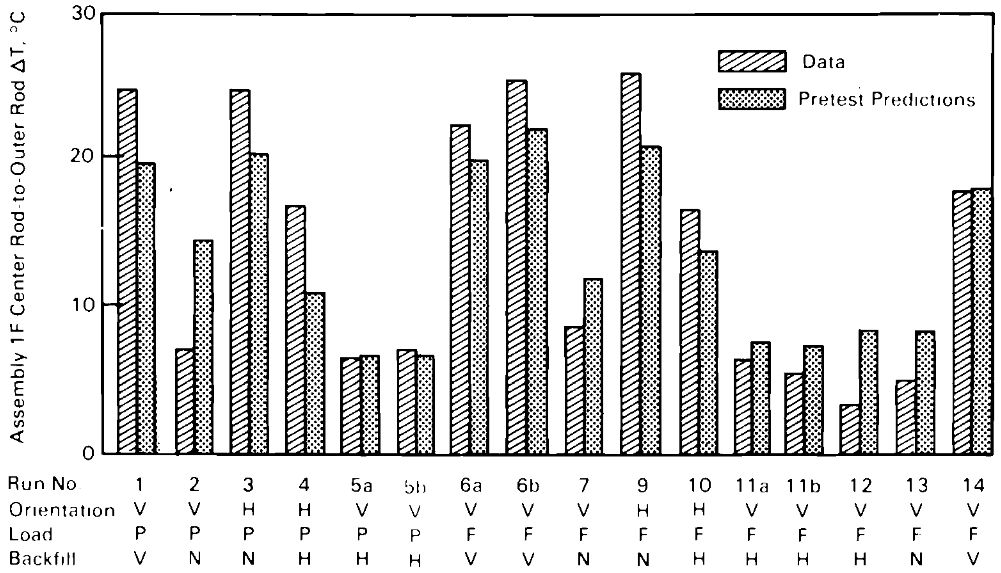

FIGURE 5.29. HYDRA Pretest Predictions of Temperature Differences from Center Rod-to-Outer Rod in Assembly 1F Compared to Data

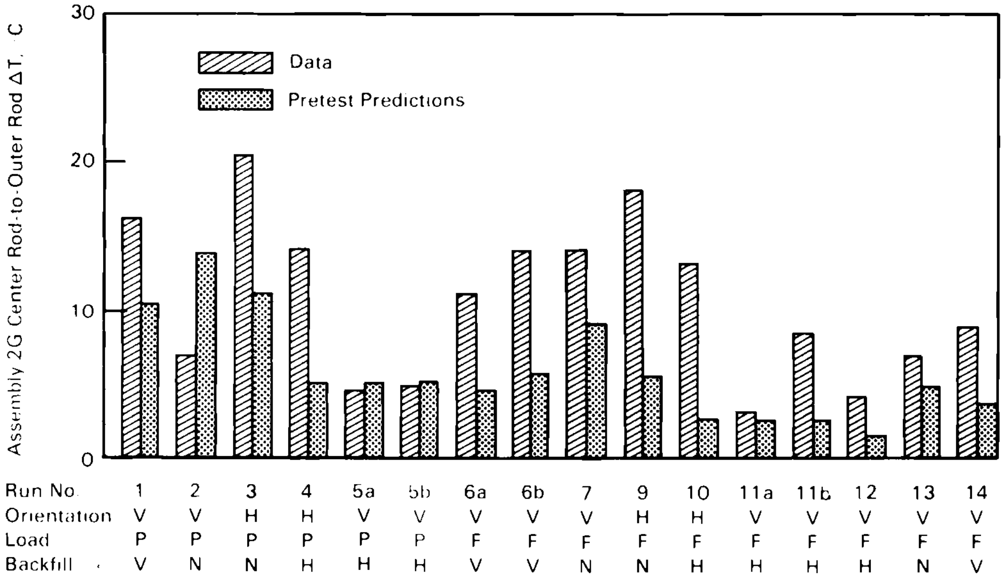

FIGURE 5.30. HYDRA Pretest Predictions of Temperature Differences from Center Rod-to-Outer Rod in Assembly 2G Compared to Data

cases. Disagreements are also quite variable, in that predicted temperature differences range from 0.24 to 2.50 times the measured temperature differences.

Some experimental conditions contribute to the disagreement between the predictions and the data for the temperature differences between the center rod and outer rod. The most pronounced problem may be the fuel assembly orientation. The fuel assembly orientation is not only unknown but also variable. Evidence of this is shown in the full load helium runs, 11a and 11b. The measured center rod-to-outer rod temperature difference in assembly 2G is greater for run 11b than for 11a (Figure 5.30). Because run 11a involves lower temperatures (outside run) than 11b (inside run), the opposite trend is expected. The measured values could result from a change in fuel assembly orientation. From run 10 the cask was lifted to the vertical position, and assembly 2G could have tipped away from the fuel tube wall. The reduced heat transfer from the exposed side of the assembly where the outer rod thermocouple is located would cause the measured temperature difference to drop as it did. Following run 11a, the rail car was pulled into the cask receiving area. The movement could have caused the assembly to tip back against the fuel tube wall. This would explain the larger measured temperature difference for run 11b. These data suggest how important fuel assembly orientation may be when comparing predictions and data on this scale. The cask was moved between runs 2 and 3; 4 and 5a; 5b and 6a; 6a and 6b; 7 and 9; 10 and 11a; and 11a and 11b. Each time it was moved, the fuel assembly orientations throughout the cask may have changed. This undoubtedly is responsible for much of the scatter seen in this and preceding data comparisons.

The coarseness of the HYDRA computational grid is probably the major contributor to the observed disagreement between predicted and measured temperature differences from the center rods to the outer rods. The grid appears coarse when focusing on rod-to-rod temperature differences that are essentially being defined from within the same HYDRA computational grid via the fuel tube model. The fuel tube wall temperatures defined by HYDRA are used as boundary temperatures in the fuel tube model. In the X-Y (or I,J) plane of the coarse grid, most of the fuel tube walls are represented by one cell and, therefore, by only one temperature. Any temperature gradient in the wall is not seen by the fuel tube model. In some cases, the neglect of the gradient in the boundary temperatures causes distortion and elevation of the predicted local temperatures within the fuel assembly.

Refer to Figure 5.28 to observe the effect of the temperature gradient in the fuel tube wall. For J = 7 and I = 5, 6, and 7, the predicted temperatures from HYDRA are generally related as in Figure 5.31. The fuel tube model for assembly 2G uses the temperature of (I,J) = (6,7) as a boundary condition. In effect, this boundary condition fails to account for the temperature gradient in the wall. Because the boundary temperature used by the fuel tube model is too high at every point except in the center of the wall, the heat transfer to the wall is artificially reduced. This is one of the reasons that predicted temperature differences from the center rod-to-outer rod in assembly 2G are, generally, well below the measured differences.

Failure to account for the temperature gradient in the wall should not have such an obviously negative impact on the prediction of local temperatures in every case. Consider the wall between assemblies 1F and 2G, i.e., at I = 5 and J = 5, 6, and 7 in Figure 5.28. This wall contains copper, so the temperature gradient is moderated. More important, the temperature gradient is somewhat uniform. Therefore, the wall temperature at (I,J) = (5,6) is very close to an average wall temperature as seen by the assembly. This temperature probably is a reasonable boundary condition for the fuel tube model.

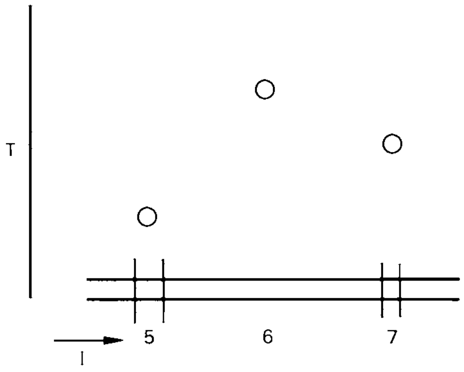

FIGURE 5.31. General Relationship Between Node Temperatures for J = 7 and I = 5, 6, 7

The same arguments apply to assembly 1F. In general, the temperature gradients in the walls perpendicular to the copper strips are more severe for assembly 1F. The axial temperature gradients in the walls are not large, and the gradients are uniform as in the copper. Therefore, the problems with the fuel tube model should not fully extend in the axial direction. In the vacuum and horizontal cases, predicted axial temperature differences are greater than predicted transverse temperature differences. If axial components of temperature differences are somewhat accurate and if the disagreement is largely due to problems in the transverse direction, the elevation difference of the thermocouples tends to moderate the apparent disagreement.

The distribution of acceptable and unacceptable boundary conditions in the fuel tube model moderates the final induced error that is due to failure to properly account for the temperature gradient in the wall. The heat transfer to some portions of the boundary is less than what it should be. The local temperatures are probably elevated only slightly to compensate for this. Nevertheless, future application of the fuel tube model should include temperature gradients in the walls.

A second element of the fuel tube model that needs to be addressed is radiation. Currently, the outer rod-to-fuel tube radiation is one-dimensional. A two-dimensional radiation model is essential to take advantage of any improvements in the boundary conditions.

5.1.3.2 HYDRA Post-Test Predictions

The post-test analysis is presented in two parts. In the first part, justifiable changes to various cask parameters are implemented universally in the input models for a select group of runs. For each of these runs a new temperature field is computed and the pretest and post-test temperature distributions are compared to data. Comparisons demonstrate improved overall predictions as well as improvements in predictions of local temperature differences. The second part of the post-test analysis is an investigation of specific problems that were identified by comparisons of pretest predictions with data. These problems were not sufficiently resolved such that they can be addressed universally in the post-test analysis. The problems are studied for selected runs to establish the magnitude of their contributions to differences between predicted and measured temperatures.

With unlimited manipulation of the input models, the disagreement between predictions and data could be minimized for every run. In general, this would require a unique cask description for each run. By using restraint in a willingness to assign new values to the cask description and by requiring that any change be adopted universally for every run, it will be seen that some disagreements are not completely resolved in the post-test analysis. This is a result of the fact that the input models for the various runs represent the best information available. Only in those cases where a change can be reasonably justified was the change actually implemented.

5.1.3.2.1 Universal Adjustment to Input Models. The relatively few changes implemented in the input models for the post-test analysis are reviewed, followed by comparisons of revised predictions to data.

For the post-test analysis, measured exterior surface temperatures of the cask are entered directly in the input models. This eliminates the need to provide correlations for heat transfer coefficients from the cask outer surface to the ambient, and facilitates comparisons in other regions of the cask. Although this action gives a correct surface temperature, there is one final note. Providing the measured surface temperatures as input is not the same as providing "correct" heat transfer coefficients. To accurately predict the surface temperatures, heat transfer coefficients and the cask thermal model both must be correct.

Comparisons of pretest predictions and data indicated that the modeled thermal resistance of the cask body needed to be increased. To accomplish this, the gap between the copper shell of the basket and the inside surface of the cask body was increased from 0.056 cm (0.022 in.) to 0.10 cm (0.039 in.). The gap due to lead shrinkage was rounded off from 0.051 cm (0.020 in.) to 0.05 cm (0.020 in.). The effective conductivity of the neutron shield was adjusted from 0.20 to 0.18 W/cm°C (11.6 to 10.4 Btu/hr/ft°F) to be consistent with the overall predicted temperature drop and heat transfer.

Two very general changes were made to the input model for the cask internals. The axial distribution of assembly decay heat generation used in the pretest analysis was a prediction based on core-average axial burnup. The axial distribution of gamma radiation was measured for a number of the test assemblies. The experimentally measured relative axial gamma distribution applied in the post-test analysis is shown in Figure 4.4 of Section 4.3.2.

The second change regarding the cask internals is very important. This change addresses the assumption of the flow split in the fuel tube model. Pretest predictions were based on the assumption that the bulk axial flow within a fuel tube predicted by the HYDRA model will divide between the assembly and the adjacent wall channels according to the relative axial flow resistance. For the nitrogen runs, this assumption yields predicted centerline axial temperature distributions that are in considerable disagreement with data. As a result of this observation, the flow split is removed for the post-test runs. This issue is one of the subjects of the next section in which special cases are evaluated.

The changes described above were implemented universally into the input models for five selected runs: 2, 6b, 9, 11a, and 13. Run 2 (partial load, vertical, nitrogen) was selected because the pretest predictions are in the greatest disagreement with data. Runs 6b (full load, vertical, vacuum), 11a (full load, vertical, helium), and 13 (full load, vertical, insulated, nitrogen) provide a representation of the three backfill media. Run 9 (full load, horizontal, nitrogen) represents the horizontal runs. Together, this selected group of runs is representative of the complete test matrix.

Axial and radial temperature profiles for post-test runs are shown in the figures of Appendix D. The results of the post-test analysis of these runs are summarized in Figure 5.32, where post-test predictions are compared to pretest predictions and the data. Temperature differences representing the four components of the heat transfer path from assembly 2G-to-ambient shown in Figure 5.19, along with temperature differences between assemblies 2J and 2G, are shown. Representative axial and radial temperature profiles are shown in Figures 5.33 and 5.34 for each backfill gas with the cask in a vertical orientation.

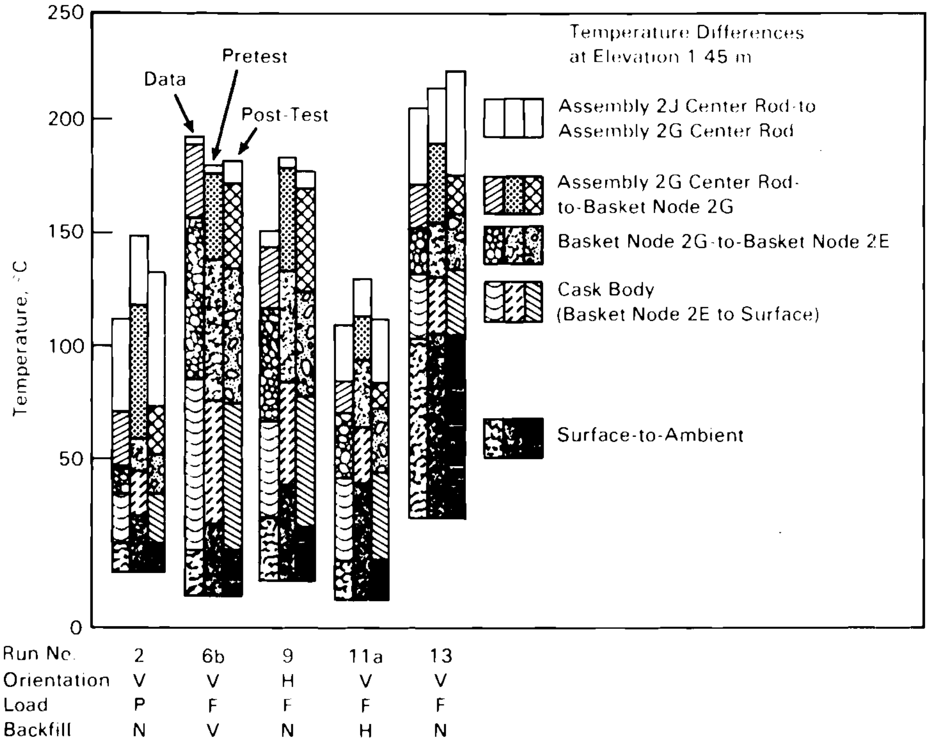

FIGURE 5.32. HYDRA Pretest and Post-Test Predictions of Overall and Component Temperature Differences at 1.45 m Elevation Compared to Data

The post-test predictions shown in Figure 5.32 demonstrate improved agreement with the data. The average ratio of the predicted-to-measured total temperature differences for the four vertical runs is 1.12 for the pretest predictions and 1.05 for the post-test runs. Local temperature differences are similarly improved.

There is still some disagreement between predictions and data for the two nitrogen runs (2 and 13) (Figure 5.32). This results in spite of the fact that the bulk flow is not divided in the fuel tube model. Although the prediction of the peak-to-ambient temperature difference is worse for run 13, local temperature differences are generally improved as seen by comparing the post-test axial profile of Figure 5.33 with that of the pretest axial profile of Figure 5.9 of Section 5.1.3. The biggest discrepancy occurs in the temperature difference between the assembly 2J centerline and adjacent basket node at elevation 3.33 m (Figure 5.34). The discussion of the fuel tube heat transfer in the next section looks further at this problem.

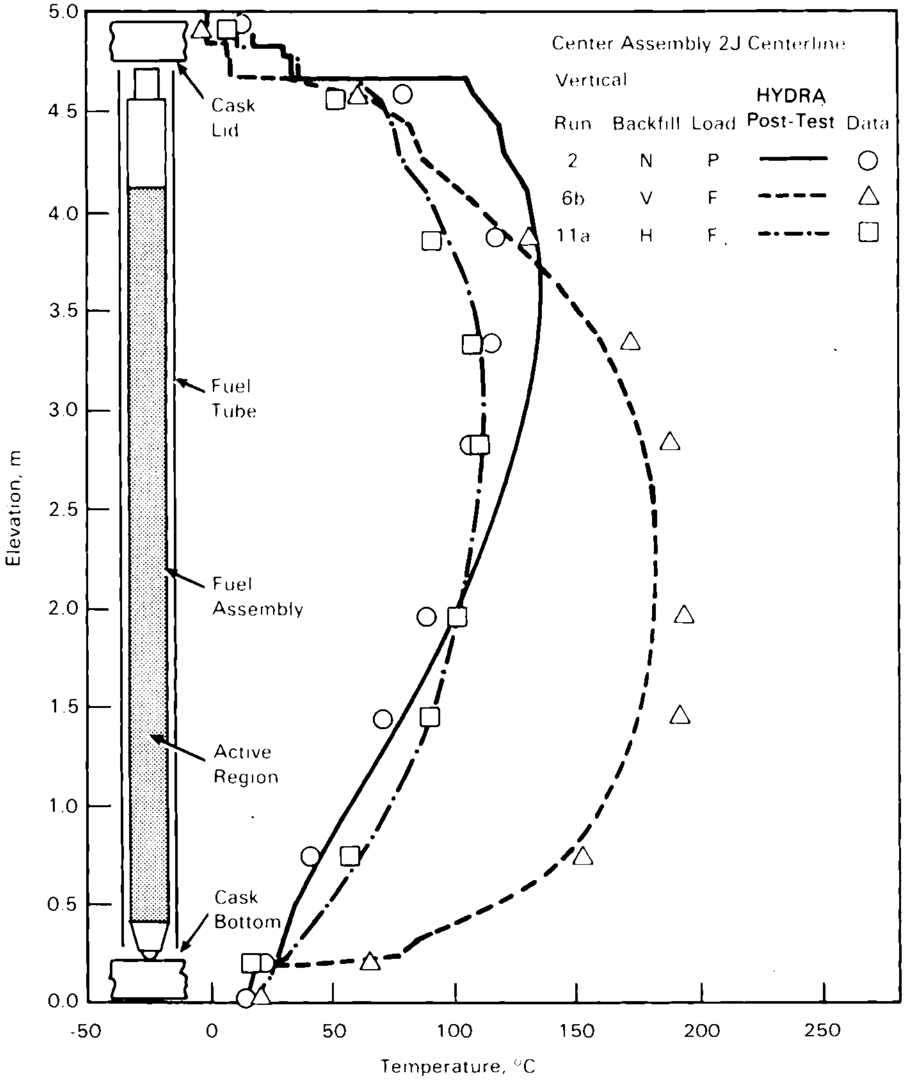

FIGURE 5.33. HYDRA Post-Test Predictions of Center Assembly 2J Centerline Axial Temperature Profiles Compared to Part and Full Load, Vertical, Vacuum, Nitrogen, and Helium Data

The results demonstrate a significant improvement in predictions of temperatures for the helium run (Figure 5.32). Only slight improvement is observed for the horizontal run. The eccentricity of the assemblies is still not modeled. This issue is also addressed in the next section.

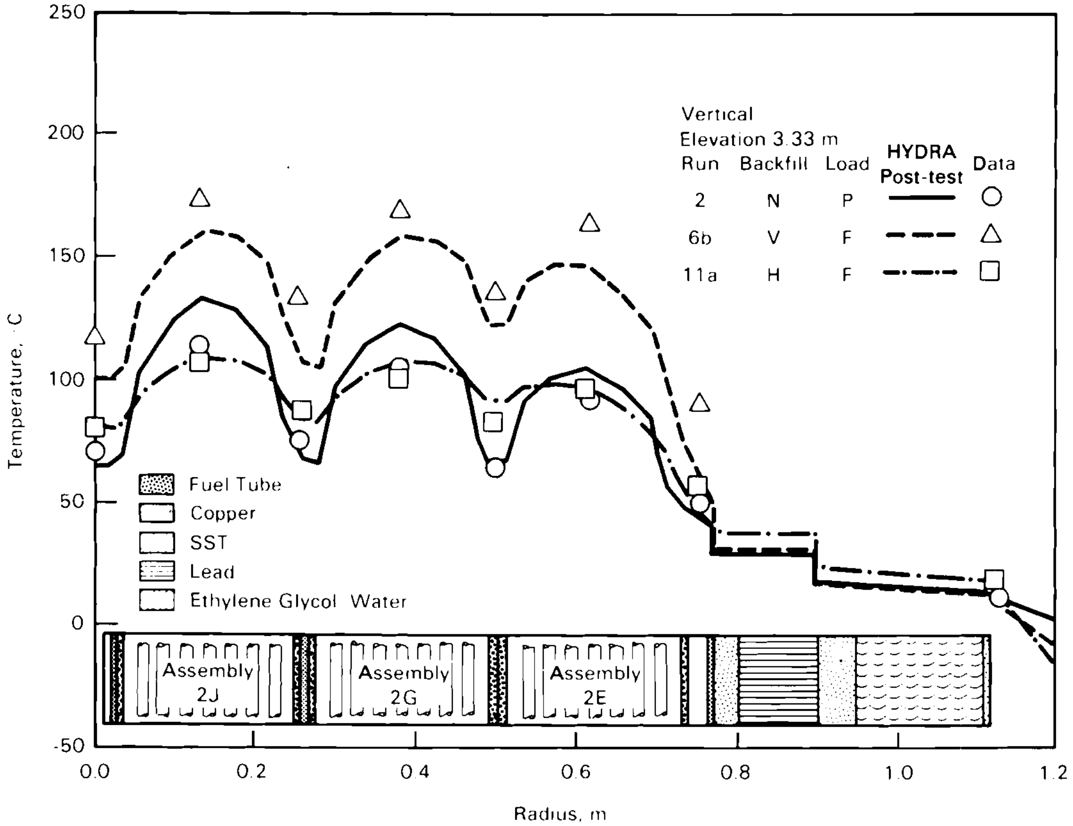

FIGURE 5.34. HYDRA Post-Test Predictions of Radial (Diagonal) Temperature Profiles Compared to Part and Full Load, Vertical, Vacuum, Nitrogen, and Helium Data at 3.33 m Elevation

The vacuum run, 6b, of Figure 5.32 also shows only slight overall improvement as a result of the post-test analysis. Predicted temperature differences through the basket and cask body are less than measured values. Several effects could lead to this result. The vacuum run is low-pressure (~1 mm Hg) nitrogen. It is assumed that the thermal conductivity of the gas is generally unaffected at this low pressure. It may be that in the narrowest gaps the conductivity is reduced. The radiation models may lead to some of the disagreement. Fuel assembly orientation may affect the amount of heat actually being transferred through the cask body on the diagonal of the quadrant. This third cause is a more likely source of the disagreement because the first two effects, conductivity and radiation, are not supported by the results for other vacuum runs in the pretest analysis.

5.1.3.2.2 Special Studies. In this section the results of some special studies are reviewed. In previous sections discussions are presented regarding certain features of the model. It was speculated that these features were involved significantly in the disagreement between the predictions and data. These special studies quantify possible effects. Specifically, these studies address the following model features:

- eccentricity of fuel assemblies in horizontal runs
- wall temperature gradients in the fuel tube model
- flow splits in the fuel tube model.

It has been pointed out previously that the fuel assemblies were modeled in the center of the fuel tube for the horizontal runs. Because there is nothing to support the assemblies, the assemblies will actually rest on the fuel tube wall when the cask is in the horizontal orientation. It was speculated that the disagreement between predictions and data for the horizontal runs was attributed to this difference between the model and the actual conditions.

A model was used that moved the assemblies against the bottom walls of fuel tubes with the cask in a horizontal orientation. The model provided no direct contact of the rods and walls. The composite transverse thermal conductance of an assembly, which is based on the rod pitch, is applied within the region occupied by the assembly, including the region adjacent to the wall. This computational displacement of an assembly removes the 0.56-cm (0.22-in.) gap between the outer surface of the assembly and lower fuel tube wall. This displacement requires the gap above the assembly to be increased to 1.12 cm (0.44 in.). The assembly is assumed to remain centered between the fuel tube side walls. These computational changes applied only to the thermal aspects of the model, i.e., energy equation only.

With the prescribed change of position of all the fuel assemblies, a new temperature field was predicted for run 9 (horizontal, full load, nitrogen). The results did not conform completely with expectations. The predicted peak temperature dropped by 10°C from the post-test prediction; however, the peak temperature is still overpredicted by 25°C. None of the measured asymmetry of temperatures in assemblies was predicted. These comparisons suggest that the thermal behavior of the cask in the horizontal orientation is influenced by some additional phenomena.

One possible cause of the asymmetry in the horizontal orientation is that the weight of the basket and assemblies forces at least partial closure of the gap between the copper shell of the basket and the inner wall of the cask along the lower supporting surface. The gap along the top surface would open as a result. This possible effect was quantified by implementing a circumferentially varying gap into the input model for run 9. The basket-to-inner wall gap was varied from 0.02 cm (0.008 in.) at the bottom to 0.18 cm (0.071 in.) at the top. The new predicted temperatures show a further reduction of the peak temperature and about 14°C asymmetry between assemblies 1A and 2A (see Figure 3.6 of Section 3.3 for assembly locations). These results identify this as a possible explanation of the disagreement between the pretest predictions and data, and agree with the experimental findings of McKinnon et al. (1986).

The failure of the fuel tube model to account for the lateral temperature gradient in the walls of the fuel tube was indicated in Section 5.1.3.1.5. It was speculated that this is a factor in the disagreement between predictions and data for center rod to outer rod temperature differences. To expediently evaluate the potential impact of the wall temperature gradient, a linear gradient was defined. Figure 5.31 is recreated in Figure 5.35 to compare an approximation of the actual wall temperature distribution with a linear temperature distribution. A linear gradient probably provides boundary temperatures that are too low because most of the temperature drop will actually occur at the junction. Therefore, application of the linear temperature distribution will overpredict the effect of the wall temperature gradient.

Test runs 2, 6b, and 7 were re-evaluated with the linear wall temperature gradient. The temperature change was on the order of -2°C for the peak. The effect on the predicted temperature difference between the center rod and the

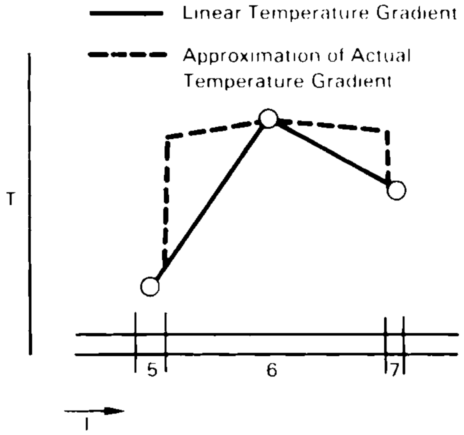

FIGURES 5.35. Approximate Wall Temperature Gradients for Nodes J = 7 and I = 5, 6, 7

outer rod was also quite small. Therefore, it appears that fuel tube temperature gradients are not of major importance in predicting assembly peak temperatures.

In the post-test analysis the assumption of the flow split was removed from the fuel tube model. The axial mass fluxes predicted by HYDRA were assigned to the assemblies and the adjacent wall channels. The post-test analysis results as reported in the previous section (Figure 5.33) indicate that, for the nitrogen runs, there is still some disagreement between predictions and data, primarily at the higher elevations in the fuel assembly. These remaining disagreements cannot be resolved without solution of the momentum equations in a fine mesh. The bulk flow predicted by HYDRA and the distribution of flow in the fuel tube model remain in question. Nevertheless, the following paragraphs refer to calculations that were performed to quantify effects that may contribute to the disagreement between the HYDRA post-test predictions and data.

Spacers were modeled in the fuel tube model to provide transverse mixing of the flow. Transverse flow and mixing would occur if gas were to flow around instead of through the spacers. This flow would carry heat outward from the central portion of the assembly, and heat would be given up to the fuel tube wall. The cooled gas would migrate back into the assembly above the spacer.

Although this process is merely speculated to occur, the potential effect on the heat transfer was quantified with the fuel tube model using the HYDRA predictions for run 2 (vertical, partial load, nitrogen). The spacers were modeled with an axial flow resistance that is ten times the flow resistance of the surroundings. The bulk flow was assigned to the remaining regions of the assemblies and adjacent channels. This causes the fuel tube model to define local mass fluxes that circumvent the spacers. In spite of this prescribed flow field, the axial location and the magnitude of the peak temperature were not significantly changed. The overall shape of the axial temperature profile was also unchanged. However, local peaks in the axial temperature profile occur where flow is reduced through the spacers.

The lack of response of the predicted temperatures to the modeling of the spacers may be due, in part, to the fact that, for the nitrogen runs, a large fraction of the temperature drop from the center rod to the fuel tube wall occurs in the gap between the assembly and the wall. Hence, the spacers were removed from the model and the thermal conductance across the gap was increased by a factor of 3. This reduced the predicted peak temperature for run 2 to 120°C compared to the pretest analysis, post-test analysis, and the measured value of 151, 134, and 115°C, respectively. Therefore, enhancement of the gap conductance reduced overprediction of the measured peak temperature to 5°C. However, at lower elevations the centerline temperature is overpredicted by as much as 10°C. This indicates that the bulk mass fluxes may be underpredicted by HYDRA, possibly due to inappropriate composite axial flow resistance or the coarseness of the computational grid.

To investigate the effect of the bulk mass flux on the peak temperature and the shape of the axial temperature profile, the composite axial flow resistance modeled in HYDRA was reduced. This action allowed the predicted mass flux to increase for run 2 by about 40%. The enhanced gap conductance was retained in the fuel tube model. With the additional bulk mass flux and enhanced gap conductance, very good agreement between the predictions and the data for the axial temperature profile was obtained except at the upper end of the assembly.

This evaluation of fuel tube/fuel assembly heat transfer has identified several contributing items that would have to be investigated further to establish a more reliable prediction of temperatures. These items include, but are not necessarily limited to:

- fuel tube wall temperature gradients
- fuel basket thermal model
- assembly-to-fuel tube radiation
- effect of noncentered fuel assemblies on both heat transfer and mass flux
- solution of the momentum equation in the fuel tube model
- low mixing due to spacers
- fuel tube bulk mass flux.

The above factors arise primarily because of the relatively coarse computational mesh employed and the use of a one-dimensional assembly-to-fuel tube radiation model. The recommended approach for future applications is to use an appropriately fine mesh and a two-dimensional assembly-to-fuel tube radiation model.

5.1.4 Parametric Analyses

In this section the results of two parametric analyses are presented. The analyses evaluate the sensitivity of the predicted temperatures in the cask to changes in fuel rod and fuel tube emittances and uniform fuel assembly heat generation rates.

5.1.4.1 Emittance Effects

Emittances of fuel rods and the fuel tube surface were changed to determine their effect on predicted temperatures. The analysis was performed using the input model for run 13 (insulated, vertical, full load, nitrogen). Effects on predicted temperatures of changes in emittances are an indication of how important thermal radiation is with nitrogen backfill gas.

The pretest and post-test analyses were performed with a fuel rod emittance of 0.8. The predicted peak temperature for run 13 in the post-test is 225°C. The fuel rod emittance was changed to 0.6 in the input model. With this single change, the new predicted peak temperature was 229°C. Predicted temperature profiles across center assembly 2J are shown in Figure 5.36. This represents a 12% increase in the temperature drop from the center rod to the wall node.

The other emittance that was changed is the fuel tube surface emittance. While the rod emittance was reset to 0.8, the fuel tube emittance was raised from 0.2 to 0.3 for all the fuel tube surfaces, both inside facing the assembly and outside facing adjacent fuel tubes and basket members. The fuel tube emittance was measured and found to be 0.2, but data scatter suggests that a higher value is possible. Also, subsequent cask testing conditions might cause the value to be above 0.2. With this single change to the input model for run 13, the new predicted peak temperature is 221°C. The predicted temperature profile across center assembly 2J at an elevation of 3.33 m is also shown in Figure 5.36. The response to this change in fuel tube emittance represents about a 12% decrease in the temperature drop between the center rod and the fuel tube wall.

In both cases, the effect of changing emittances is small compared to the total temperature drop from peak-to-ambient. This is due, in part, to the fact that the local temperature drop from the center rod to the fuel tube wall is only about 25% of the total temperature drop to the ambient. Because radiation contributes to the heat transfer in conjunction with convection and conduction, changing emittances affects only one component and, therefore, only a fraction of the total temperature drop. In general, with nitrogen backfill, heat is transferred from each assembly to the cask body by convection to basket members where it is conducted toward the cask body. Very little heat is transferred radially outward directly from one assembly to another. As a result, there is little or no compounding of the effect of changing fuel tube or rod emittances.

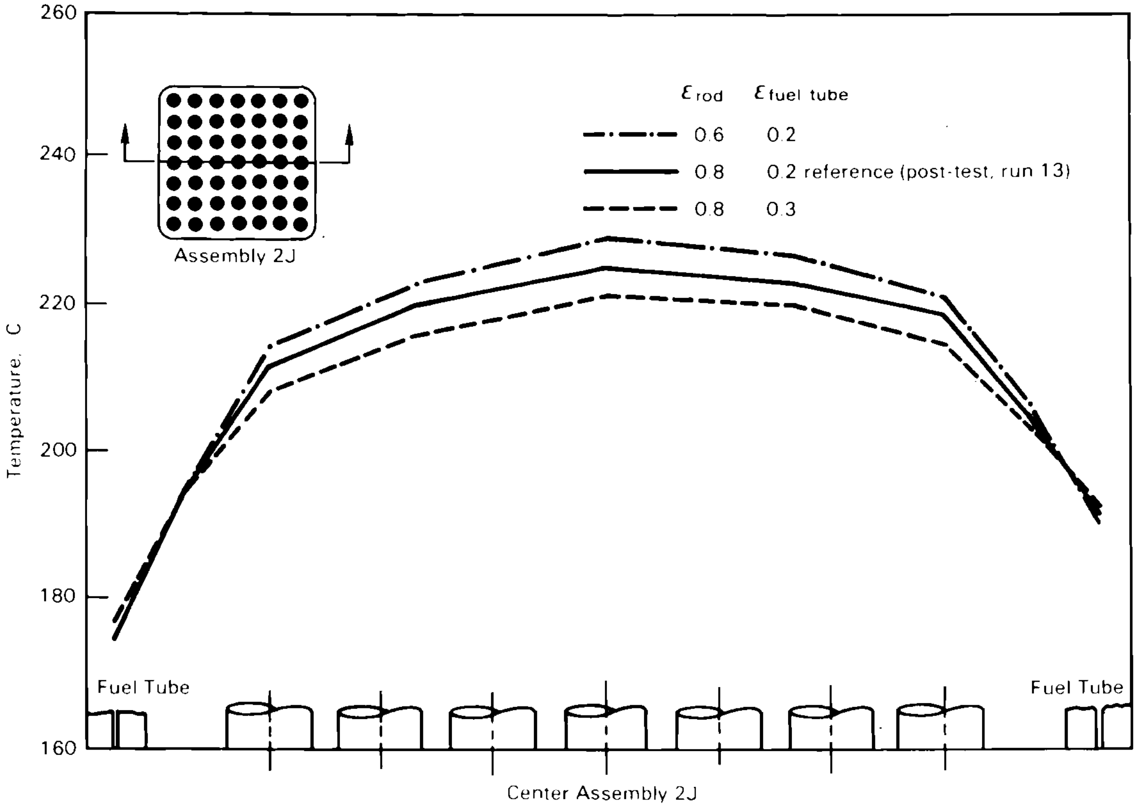

FIGURE 5.36. HYDRA Predictions of Center Assembly 2J Radial Temperature Profiles for Various Fuel Rod and Fuel Tube Emittances at 3.33 m Elevation

5.1.4.2 Predicted Maximum Cask Heat Load with Nitrogen

An analysis was performed to predict the maximum heat generation rate that could be dissipated by the REA cask. The predicted maximum heat load is determined subject to three constraints:

- 380°C allowable fuel temperature
- 327°C lead melting point
- 148°C [50 psia (3.40 atm)] saturation temperature of the ethylene glycol in the neutron shield.

The analysis used the same model described for the post-test runs with the following conditions:

- nitrogen backfill gas
- vertical orientation

- cavity pressure = 1.5 atm
- ambient temperature = 52°C
- natural convection from cask surface to ambient
- uniform assembly heat generation rates.

All of the constraints could be satisfied with a heat generation rate of 750 W per assembly. The predicted peak temperature is 383°C, which is the limiting condition. The temperature in the neutron shield is predicted to be as high as 145°C, which is also very near the saturation temperature at the 50-psig neutron shield design limit. However, predicted temperatures in the neutron shield vary from 120°C to 145°C, and mixing should reduce peak temperatures. Fluid mixing was not included in this analysis.

Axial and radial temperature profiles for the predicted maximum heat load of 750 W per assembly are shown in Figures 5.37 and 5.38. These results are compared to the post-test predictions and the data for run 13 (full load, vertical, nitrogen, insulated) for which the average assembly heat generation rate was 227 W. The comparison suggests that the results of the maximum heat rate prediction are conservative. In addition, pretest predictions showed that the heat transfer coefficients for natural convection on the exterior surface of the cask are conservative.

5.2 COBRA-SFS ANALYSIS

The COBRA-SFS (spent fuel storage) computer code was used to predict temperature and velocity distributions in the REA 2023 spent fuel storage cask. Results were obtained for cask operation with vacuum, nitrogen, and helium backfills in vertical and horizontal orientations. Descriptions of the COBRA-SFS code, its modeling capabilities, and the conservation equations are presented, along with comparisons of code predictions with test data.

5.2.1 COBRA-SFS Computer Code

The COBRA-SFS code is a steady-state, lumped-parameter, finite-difference computer code that predicts flow and temperature distributions in spent fuel storage systems and fuel assemblies under mixed and/or natural convection conditions. Derived from the COBRA family of codes (Stewart et al. 1977;

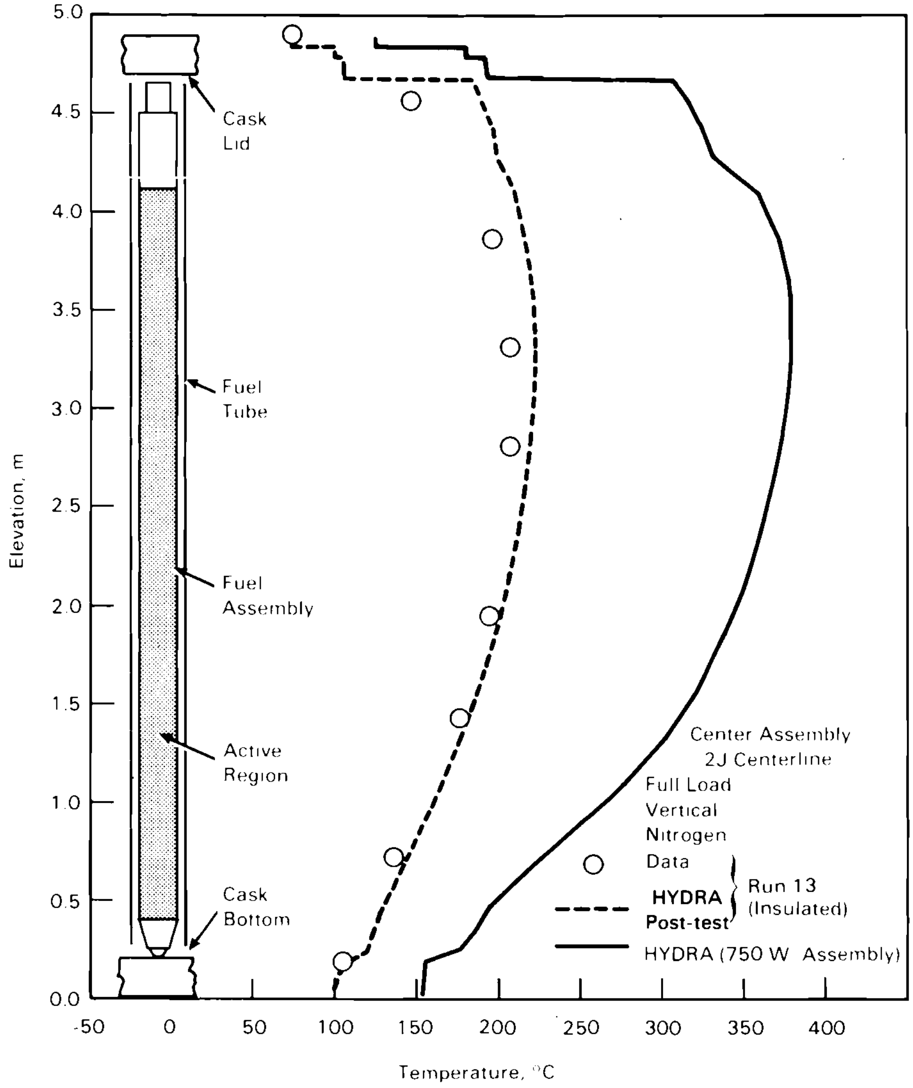

FIGURE 5.37. HYDRA Prediction of Center Assembly 2J Centerline Axial Temperature Profile for 750 W/Assembly Compared to Data and Prediction of Run 13 (Full Load, Vertical, Nitrogen, and Insulated)

George et al. 1980; Khan et al. 1981), which have been extensively evaluated against in-pile and out-of-pile data, COBRA-SFS retains all the important features of the COBRA codes and extends the range of application to problems with two-dimensional radiation and conduction heat transfer. This capability permits analyses of single and multiassembly spent fuel storage systems with unconsolidated or consolidated fuel, with a variety of fill media (Cuta, Rector, and Creer 1984).

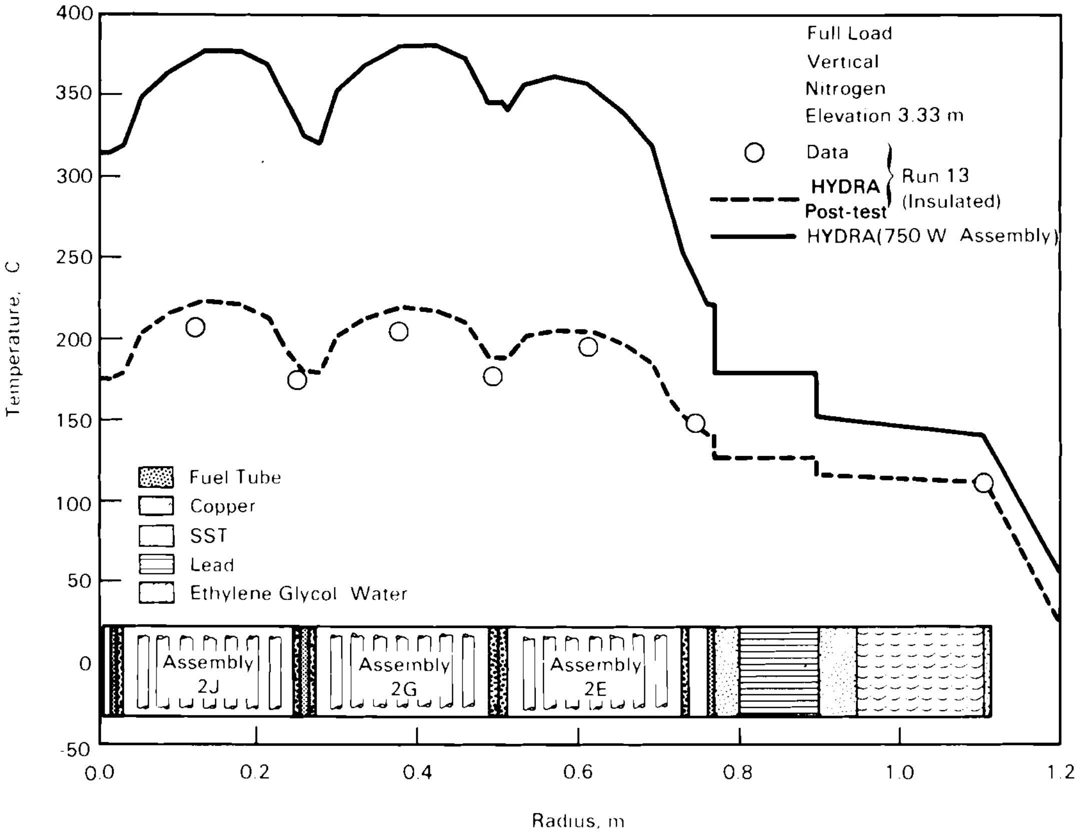

FIGURE 5.38. HYDRA Prediction of Radial (Diagonal) Temperature Profile for 750 W/Assembly Compared to Data and Prediction of Run 13 (Full Load, Vertical, Nitrogen, and Insulated)

COBRA-SFS provides finite-difference solutions to the equations governing mass, momentum, and energy conservation for incompressible flows. Analyses are conducted using a subchannel approach in which the flow areas of assemblies or storage systems are divided axially into discrete control volumes for which the conservation equations of mass, momentum, and energy are written. These equations are then solved using an iterative implicit method. The energy equations for the coolant, rod cladding, fuel, and structural members (walls) are solved implicitly by iteration, but simultaneously in a plane. Axial conduction in the structural members is modeled. A nonparticipating, gray body radiation heat transfer model also allows two-dimensional radiant heat exchange among all solid members in an enclosure and is iteratively coupled to the rod and wall energy equations.

The flow field may be either user-prescribed or internally calculated as a function of the gravitational and dynamic pressure losses. Specifications of heat losses from the boundary may vary circumferentially and axially, and can include both radiation and convection heat transfer. Axial heat transfer from the subchannel model to plenum regions (regions above and below the fuel assemblies) also can be modeled.

In the following sections, the COBRA-SFS modeling capabilities are outlined, and a brief description of the conservation equations is given.

5.2.1.1 Modeling Capabilities

COBRA-SFS allows simulations of a wide range of dry storage systems via input instructions. In addition to the multiassembly cask analysis described in this report, applications have included analyses of single assembly spent fuel storage systems under multiple orientations and fill media (Lombardo et al. 1986) and analyses of both single and multiassembly consolidated storage systems (Cuta, Rector, and Creer 1984). The code contains thermal-hydraulic models for pressure drop, turbulent mixing, diversion cross-flow, buoyancy-induced flow recirculation, and conduction and radiation heat transfer. A versatile fuel rod model allows simulation of consolidated fuel assemblies. The code's capabilities and limitations are outlined in Table 5.6.

5.2.1.2 Conservation Equations

The COBRA-SFS code solves the conservation equations of mass, momentum, and energy in a fuel assembly or fuel storage system using finite difference equations derived by performing suitable balances on finite control volumes. Empirical relationships are used where needed to close the set of equations.

The fluid control volume for continuity, axial momentum, and energy is characterized by a flow cross-sectional area, A; an axial length, Dx; and a gap width, S, for the connection between itself and adjacent control volumes. Figure 5.39 shows the relationship of a subchannel control volume to a fuel storage system; a typical subchannel control volume is also displayed. Any series of control volumes connected axially is considered a subchannel. In the

TABLE 5.6. COBRA-SFS Capabilities and Limitations

Modeling Capabilities	Lumped parameter	Multiple flow regions
	Steady state	Fluid conduction and turbulent mixing
	Triangular, square, or consolidated rod arrays	Pressure drop model (network and subchannel)
	Recirculating flows	Variable property rod model
	Zero net flow solution	Variable boundary heat transfer
	Interassembly and intra-assembly heat transfer	Prescribed heat flux
	Nonparticipating radiation (planar)	Plenum heat loss model
	Mixed geometry	Use of specified or prescribed flow regions
	Variable axial grid spacing	Variable fluid properties
Program and I/O Control	Constant prescribed flow	
	Zero net flow	
	Restart and post-processing dump	
	Decoupled hydrodynamics (no buoyancy)	
	Fully coupled hydrodynamics	
	Echoed input	
	Result execution and time monitoring	
	Variable/constant fluid properties	
	Pressure drop initialization scheme	
	Data "roll" option for large problems	
Limitations & Assumptions	Incompressible flow	
	Lumped parameter approach	
	No free-field capability	
	One-dimensional boundary heat transfer	

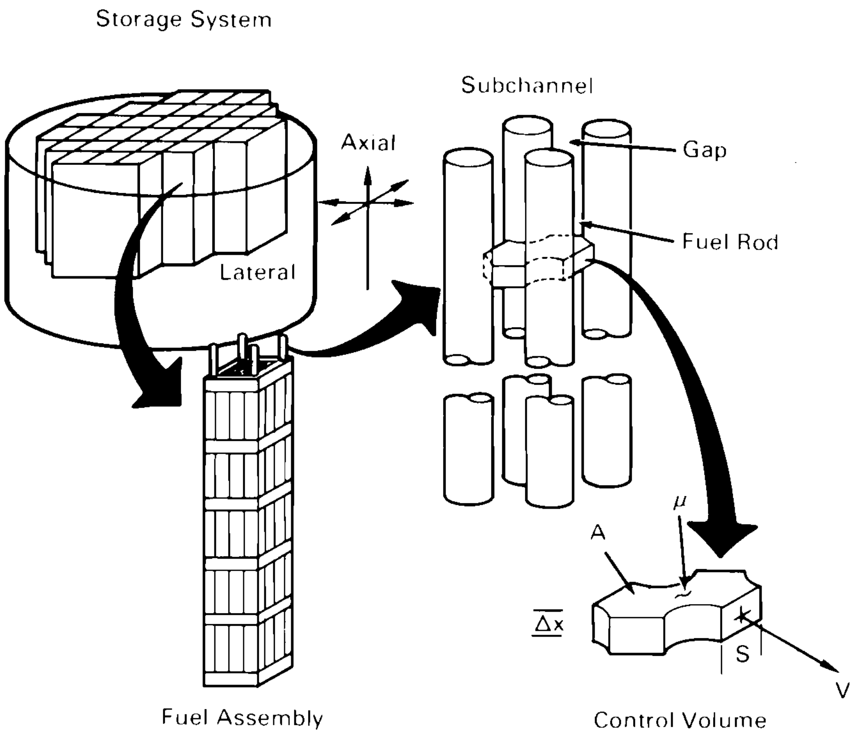

FIGURE 5.39. Subchannel Definition

following equations, the finite-difference terms are presented with the corresponding word definitions given in brackets immediately below each equation. The list of symbols in the Nomenclature section of this document should be referred to for explanation of the notation.

Continuity Equation (for subchannel i)

$$\bar{A}\,\frac{\rho - \rho^n}{\Delta t}\,j = \left(\frac{v_{j-1}A_{j-1}\rho^*_{j-1}}{\Delta x_j} - \frac{v_j A_j \rho^*_j}{\Delta x_j}\right) + \sum_{k\,\varepsilon\,\Psi_i} e_k\left(u_k S_k \rho^*_k\right)_j \tag{5.15}$$

$$\begin{bmatrix}\text{mass}\\ \text{storage}\end{bmatrix} = \begin{bmatrix}\text{mass transported}\\ \text{axially}\end{bmatrix} + \begin{bmatrix}\text{mass transported}\\ \text{laterally}\end{bmatrix}$$

The asterisk denotes that donor cell values are convected by the velocity v.

Fluid Energy Equation (for channel i)

$$\bar{A}\,\frac{\rho h - (\rho h)^n}{\Delta t}\,j = \left(\frac{v_{j-1}A_{j-1}\rho^*_{j-1}h^*_{j-1}}{\Delta x_j} - \frac{v_j A_j \rho^*_j h^*_j}{\Delta x_j}\right) + \sum_{k\,\varepsilon\,\Psi_i} e_k \left(u_k S_k \rho^*_k h^*_k\right)_j$$

$$\begin{bmatrix}\text{energy}\\ \text{storage}\end{bmatrix} = \begin{bmatrix}\text{energy transported}\\ \text{axially}\end{bmatrix} + \begin{bmatrix}\text{energy transported}\\ \text{laterally}\end{bmatrix}$$

$$+ \sum_{n\,\varepsilon\,\lambda_i} \frac{A_{HTR}H_R}{\Delta x_j}\left(T_{c_n} - T\right) + \sum_{m\,\varepsilon\,\tau_i} \frac{A_{HTW}H_W}{\Delta x_j}\left(T_{w_m} - T\right)$$

$$+ \left[\text{rod heat flux}\right] \qquad + \left[\text{wall heat flux}\right]$$

$$+ \sum_{k\,\varepsilon\,\Psi_i} e_k S_k K_k \frac{T_{II} - T_{JJ}}{\ell_k Z_k} + \sum_{k\,\varepsilon\,\Psi_i} \frac{e_k w_T}{\Delta x_j}\left(h_{II} - h_{JJ}\right)$$

$$+ \begin{bmatrix}\text{conductive heat}\\ \text{transfer laterally}\end{bmatrix} + \begin{bmatrix}\text{turbulent}\\ \text{energy exchange}\end{bmatrix} \qquad (5.16)$$

All other forms of energy transport that are not explicitly represented in Equation (5.16) (e.g., potential and kinetic energy) have been neglected.

Axial Momentum Equation (for channel i)

$$\bar{A}\,\frac{\rho v - (\rho v)^n}{\Delta t}\,j = \left(\frac{A_{j-1}v_{j-1}v^*_{j-1}\rho^*_{j-1}}{\Delta x_j} - \frac{A_j v_j v^*_j \rho^*_j}{\Delta x_j}\right) + \sum_{k\,\varepsilon\,\Psi_i} e_k \left(u_k S_k V^*_k \rho^*_k\right)_j$$

$$\begin{bmatrix}\text{axial}\\ \text{momentum}\\ \text{storage}\end{bmatrix} = \begin{bmatrix}\text{axial momentum}\\ \text{transported}\\ \text{axially}\end{bmatrix} + \begin{bmatrix}\text{axial momentum}\\ \text{transported}\\ \text{laterally}\end{bmatrix}$$

$$+ \bar{A}_j \frac{P_{j-1} - P_j}{\Delta x_j} \qquad + \sum_{k \varepsilon \Psi_i} \frac{e_k w_T}{\Delta x} (v_{II} - V_{JJ})$$

$$+ \left[\begin{array}{l}\text{pressure}\\ \text{gradient}\end{array}\right] \qquad + \left[\begin{array}{l}\text{turbulent momentum}\\ \text{exchange}\end{array}\right]$$

$$- \frac{1}{2}\left(\frac{f}{D_h} + \frac{C_f}{\Delta x_j}\right) \rho_j v_j |v_j| A_j \qquad - A \rho g \cos \theta$$

$$- \left[\begin{array}{l}\text{irreversible friction}\\ \text{and form losses}\end{array}\right] \qquad - \left[\begin{array}{l}\text{gravitational}\\ \text{head}\end{array}\right] \qquad (5.17)$$

In the derivation of the axial momentum equation, it is assumed that all irreversible losses can be obtained by use of suitable friction factors and loss coefficients applied to the bulk velocity. Also, it is assumed that pressure changes linearly along the control volume, and the shear stress terms due to flow in the adjacent subchannels can be neglected.

Transverse Momentum Equation

The momentum control volume length, ℓ, and gap width, S, define a transverse momentum control volume as shown in Figure 5.40. Inside this control volume, the transverse velocity is normal to the transverse gap; the flow is assumed to have no transverse component outside the transverse momentum control volume.

$$S\Delta x_j \frac{\rho^* u - (\rho^* u)^n}{\Delta x} k = S_k v_{j-1} (\rho u)^*_{k,j-1} - S_k v_j (pu)^*_{k,j}$$

$$\left[\begin{array}{l}\text{lateral}\\ \text{momentum}\\ \text{storage}\end{array}\right] = \left[\begin{array}{l}\text{transverse momentum}\\ \text{transported axially}\end{array}\right]$$

$$+ (P_{II} - P_{JJ})_{j-1} \frac{S_k \Delta x_j}{\ell_k} - C_T u_k u_k \frac{\rho S \Delta x_j}{2\ell_k}$$

$$[\text{pressure gradient}] \qquad - \left[\begin{array}{l}\text{irreversible form}\\ \text{and friction loss}\end{array}\right] \qquad (5.18)$$

A further assumption in the transverse momentum equation is that there are no applied body forces in the transverse direction.

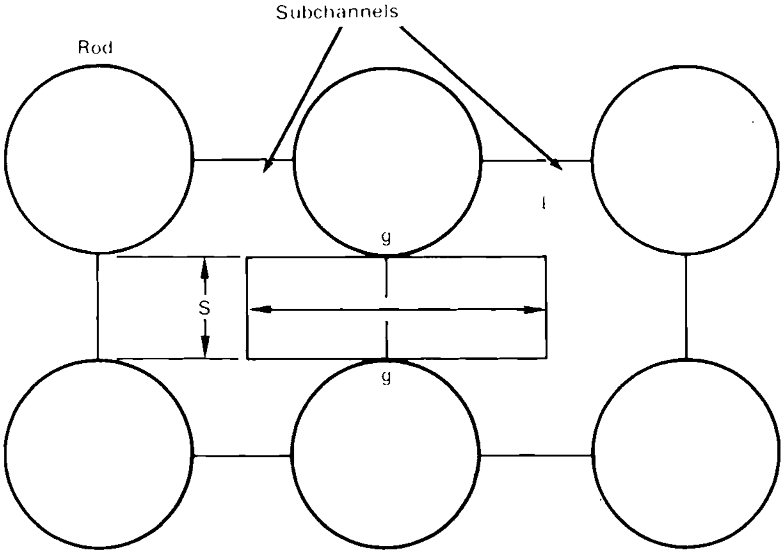

FIGURE 5.40. Transverse Momentum Control Volume

Fuel Rod and Cladding Energy Equations

By assuming that 1) there is no heat transfer axially, 2) the heat is generated uniformly throughout the fuel at a given axial location, and 3) the fuel properties do not vary with the radial variation in temperature, the cladding temperature is obtained by performing a lumped energy balance on the cladding material at each axial level. The finite-difference form of the equation used is presented in Equation (5.19).

$$y_c \rho_c c_c \frac{T_c - T_c^{\,n}}{\Delta t} = H_R \sum_{i \varepsilon \gamma_i} \phi_i \left(T_{c_n} - T\right) + H_g \frac{R_f}{R_c}\left(T_{fs} - T_c\right)$$

$$\begin{bmatrix}\text{energy}\\ \text{storage}\end{bmatrix} = \begin{bmatrix}\text{convective}\\ \text{transfer to}\\ \text{the fluid}\end{bmatrix} + \begin{bmatrix}\text{heat transfer}\\ \text{from fuel}\end{bmatrix}$$

$$+ \sigma \sum_{n \varepsilon \zeta_n} F_{in}\left(T_c^{\,4} - T_{c_n}^{\,4}\right) + \sigma \sum_{m \varepsilon \beta_m} F_{im}\left(T_c^{\,4} - T_{w_m}^{\,4}\right)$$

$$\begin{bmatrix}\text{radiation heat}\\ \text{transfer from}\\ \text{rods}\end{bmatrix} + \begin{bmatrix}\text{radiation heat}\\ \text{transfer from}\\ \text{walls}\end{bmatrix} \qquad (5.19)$$

In the above, it is assumed that the temperature is uniform around the circumference of the cladding. The film coefficient, HR, is given by user-specified correlations, and the gap conductance between fuel pellet and cladding, Hg, is assumed constant. F_{in} and F_{im} are gray body radiation exchange factors that account for multiple reflections within an enclosure. F_{in} is a coefficient for rod-to-rod heat transfer, while F_{im} is a coefficient for rod-to-wall heat transfer. Both are derived by assuming constant surface emissivity. The gray body exchange factors can be user-prescribed or calculated internally by specifying black body view factors and surface emissivity values.

Energy Equations

$$\rho_w c_w t_w \frac{T_w - T_w^n}{\Delta t} = \sum_{i \epsilon \xi_i} U\left(T - T_w\right) + \sigma \sum_{m \epsilon \sigma_m} F_{im}\left(T_w^4 - T_{w_m}^4\right)$$

$$\begin{bmatrix}\text{energy}\\ \text{storage}\end{bmatrix} = \begin{bmatrix}\text{heat transfer}\\ \text{from adjacent}\\ \text{channels}\end{bmatrix} + \begin{bmatrix}\text{radiation heat}\\ \text{transfer from}\\ \text{walls}\end{bmatrix}$$

$$+ \left[\sigma \sum_{n \epsilon K_n} F_{in}\left(T_w^4 - T_{c_n}^4\right)\right] + q'''$$

$$+ \begin{bmatrix}\text{radiation heat}\\ \text{transfer from rods}\end{bmatrix} + \begin{bmatrix}\text{heat}\\ \text{generation}\end{bmatrix}$$

$$+ U_{j-1}\left(T_w - T_{w_{j-1}}\right) + U_j\left(T_w - T_{w_{j+1}}\right) + \sum_{m \epsilon \alpha_m} U\left(T_w - T_{w_m}\right)$$

$$+ \begin{bmatrix}\text{axial conduction}\\ \text{heat transfer}\end{bmatrix} + \begin{bmatrix}\text{heat transfer}\\ \text{from adjacent}\\ \text{walls}\end{bmatrix} \qquad (5.20)$$

As before, F_{im} and F_{in} are the gray body exchange factors from wall node i to wall node m and rod node n, respectively. Axial heat transfer from the walls to a plenum region can be included at the end axial levels.

5.2.2 COBRA-SFS Computational Model

A three-dimensional, one-eighth section model of the REA cask was developed for the COBRA-SFS analysis. Descriptions of the model, material properties, and correlations are provided, along with a discussion of the modeling uncertainties.

5.2.2.1 Nodal Representation

The REA spent fuel storage cask is presented in Figure 3.1 in Section 3.1. A brief description of the cask is provided here to allow a better understanding of the computational model; for a detailed description of the cask geometry and components, the reader is referred to Section 3.1 and Volume I of this report (McKinnon et al. 1986a).

The two main components of the cask are the basket and the cask body. The basket contains the spent fuel assemblies within the cask, and is composed of stainless-steel-clad Boral fuel tubes for criticality control, copper plates to transfer heat from the cask interior, and stainless steel spacers for structural integrity. The basket consists of four individually fabricated quadrants, which are inserted into the cavity formed by the cask body. The cask body (sides and bottom) is an annulus of stainless steel in which molten lead was poured and allowed to solidify for gamma shielding. Exterior to this annulus is a second annulus filled with a solution of ethylene glycol and water for neutron shielding. To seal the cask and ensure integrity, a dual lid system was employed. As with the cask body, the cask primary seal is a sandwich of lead and stainless steel. A dead air space separates the primary lid from the secondary stainless steel cover. A cross section of a cask quadrant perpendicular to the longitudinal axis is shown schematically in Figure 3.3 of Section 3.1, which details the basket and cask body geometry.

A three-dimensional model of the REA cask was developed for this analysis. By assuming symmetry of the cask geometry and fuel loading, the cask was simulated with a one-eighth section model; a cross section of the computational cell arrangement perpendicular to the longitudinal axis is presented in Figure 5.41. The subchannel noding used in modeling the spent fuel assemblies is illustrated in Figure 5.41 along with the wall noding employed for the cask

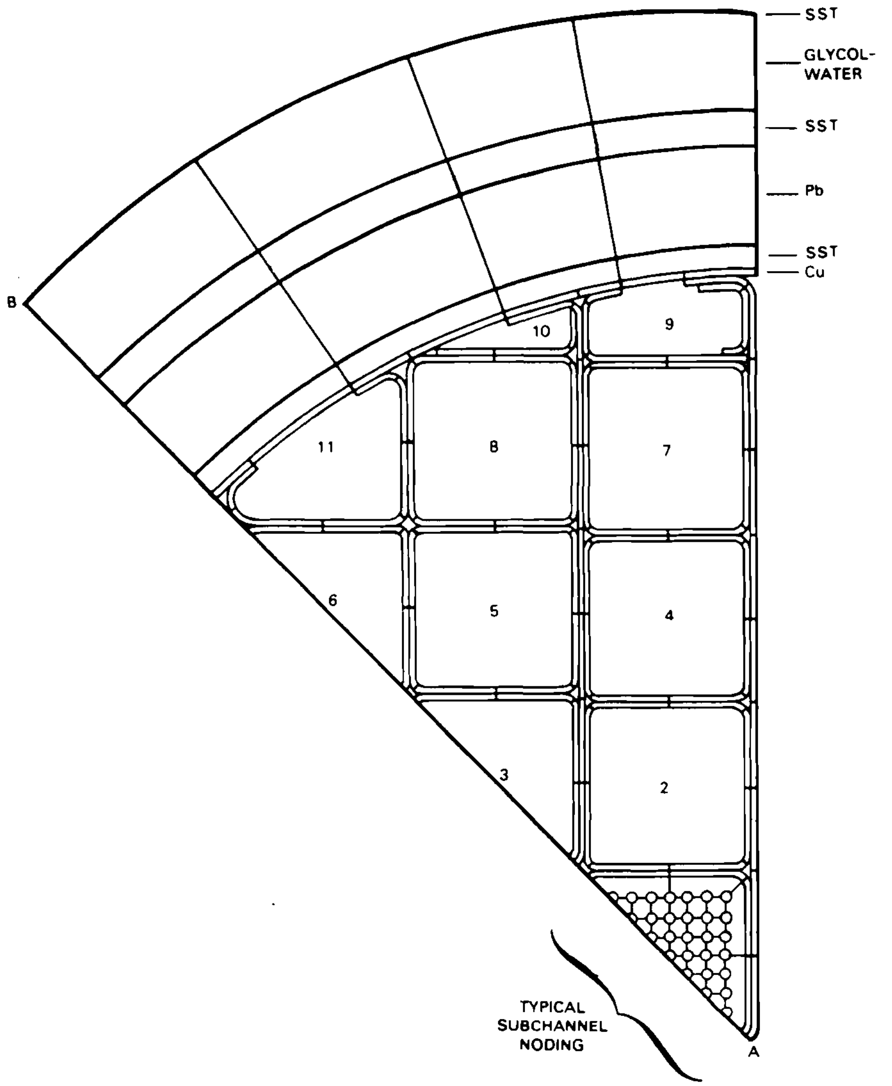

FIGURE 5.41. COBRA-SFS One-Eighth Cross Section Model of REA Cask

structural members. A total of 24 uniform nodes were used in the axial direction, as shown schematically in Figure 5.42. Approximately 300 fluid subchannels were used to describe the flow paths at each axial level for the fully loaded cask. For the partially loaded cask, flow areas of empty fuel tubes were modeled as single subchannels. Flow areas created by basket spacers were also treated as single subchannels.

To describe the cask and basket structural members at each axial level, 106 wall nodes were used. Radiation and/or conduction heat transfer between

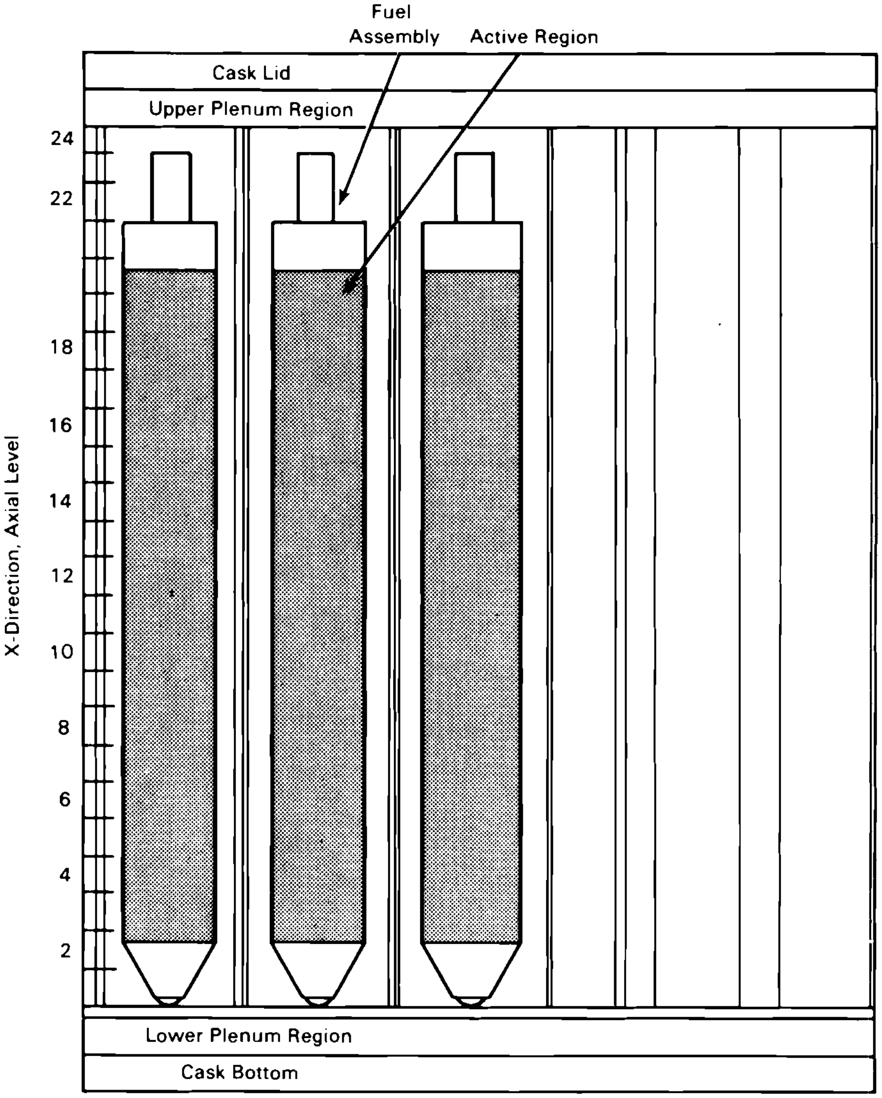

FIGURE 5.42. COBRA-SFS Axial Computational Cell Arrangement of REA Cask

wall nodes were included within a plane by specifying the appropriate thermal conductance terms. Wall axial conduction along with fluid-to-fluid conduction between adjacent fluid subchannels was also accounted for. The fuel tube walls and adjacent heat conduction strips were split into two circumferential nodes. For the complex geometry of the basket-cask interface, finer noding was employed to allow more complete modeling of conduction and radiant heat exchange within this region. Coarser noding was employed within the relatively simple geometry of the cask body.

Each rod in each fuel assembly was individually modeled; a total of 329 rods were used in the fully loaded cask model. Each fuel rod consisted of five radial nodes: four for the fuel and a single node for the cladding. Circumferential noding was not used in the rods. The heat generation rates were based on spent fuel calorimetry data presented in Figure 3.6 of Section 3.3, and in Volume 1 (McKinnon et al. 1986a) and in Section 4.0 of this report. The values used reflected the elapsed time from the calorimeter measurements to the steady-state test time (decay heat rate of change values were obtained from ORIGEN-2 predictions). The loading patterns, assembly heat rates, and daily decay rates for the partially and fully loaded cask are also presented in Figure 3.6 of Section 3.3. The fuel assembly numbering scheme also is shown in Figure 3.6.

Decay heat values used in the one-eighth sector model represent the average loading for cask quadrant 2, and ranged from 0.28 kW to 0.38 kW per assembly. The axial decay heat profile displayed in Figure 4.4 of Section 4.3 was applied to all assemblies. A uniform radial power distribution within a fuel assembly was assumed.

The radiant heat exchange between rods and fuel tube walls was computed from prescribed, gray body exchange factors based on one-quarter rod surface segments. All gaseous fill media were considered nonparticipating.

The computational model described above extends into the cask body, terminating at the inner boundary of the ethylene glycol/water chamber. Within this region, the mass, momentum, and energy conservation equations are solved to predict velocity and temperature distributions. Heat transfer from the glycol inner boundary to the ambient is calculated using a boundary heat transfer model that solves a one-dimensional energy equation. Heat transfer between the boundary region can include radiation and natural or forced convection heat transfer. Four radial nodes were employed: a single node each for the inner neutron shield liner, the outer neutron shield liner, the ethylene glycol/mixture, and the ambient air. Solar insolation was neglected in the calculations (see Section 5.1.3.1.2).

An optional plenum model was used to describe the heat transfer from the recirculating fluid-to-ambient in the regions immediately above and below the fuel tubes/assemblies. As with the boundary region model, only one-dimensional energy equations are solved. The upper lid was modeled with 10 nodes; five nodes apiece for the axial and radial directions. For the bottom of the cask, only five nodes were used, because the bottom surface of the cask was assumed to be adiabatic. The overall heat transfer from the lid and bottom was modeled by specifying the thermal resistance between plenum nodes. Conduction heat transfer between the basket and cask body to the lid and to the cask bottom is also simulated via the plenum model.

5.2.2.2 Material Properties and Correlations

The material properties used in the model, with the exception of emittances, were well defined. Fluid properties were input as functions of temperature and continuously updated during the simulations; property values for the solids and for the ethylene glycol/water mixture (Curme and Johnston 1952) remained constant and were evaluated based on a preliminary predicted cask temperature distribution. Wall heat transfer in the radial and circumferential directions was modeled by specifying appropriate thermal resistances. The input value of resistance for a composite of materials is a combination of parallel and/or series paths. The resistances were obtained as functions of temperature, but remained constant during the simulation. As-measured emissivity values were provided for the fuel tube and the high-emissivity paint used to coat the outer surface of the neutron shield (Taylor 1983, 1984). A wide range of emittances is possible for the other cask components; these emittances are dependent on fabrication technique, temperature, and oxidation buildup. A tabulation of the emittances used in the analysis is presented in Table 5.7; emittances not experimentally determined are assumed values.

Heat transfer from the rods and walls to the gas coolant was prescribed using a film coefficient of the form $Nu = 4.364$ (Kays and Crawford 1980). This value is a solution of the energy equation for a constant heat rate and fully developed velocity and temperature profiles in a circular tube. The film coefficient was evaluated as a function of temperature at each location.

The overall contribution of convective heat transfer is dependent on the flow field established. For these simulations the flow field is obtained by

TABLE 5.7. Material Emittance Values

Component	Emittance
Fuel rods	0.8
Fuel tubes (stainless steel)	0.2 (measured)
Other stainless steel surfaces	0.2
Copper	0.5
Lead	0.6
High emissivity paint	0.78 (measured)
Cask surface (stainless steel)	0.3

adjusting the total pressure drop until 1) the pressure drop across all subchannels is equal and 2) the total net flow rate is approximately zero. Thus, the flow resistance of the cask becomes an important convection parameter. The overall cask flow resistance is assumed to be a combination of:

- rod and wall surface drag
- spacer losses
- fuel tube inlet and exit losses
- fuel assembly inlet and outlet losses.

Rod and wall friction were modeled using an analytical solution for fully developed laminar flow along cylinders arranged in a square array, $f = 100/Re$ (Sparrow and Loeffler 1959). Spacer and fuel assembly inlet and outlet losses were included by specification of a pressure loss coefficient of 1.0. The major source of uncertainty, however, was the fuel tube inlet and outlet flow resistances. Loss coefficients for the fuel tube inlet and outlet were obtained from a handbook of hydraulic resistance (Idel'Chik 1966); uniform values of $K = 9$ and $K = 3$ were assigned for the fuel tube inlets and outlets, respectively.

Heat transfer from the subchannel model to the boundary requires specification of the heat transfer across the glycol/water annulus, and from the cask surface to the ambient. Heat transfer from natural convection in the partitioned glycol/water annulus was modeled as a function of the temperature difference across the annulus using

$$\mathrm{Nu} = 0.22A^{-1/4}\left(\frac{\mathrm{Pr}}{0.2 + \mathrm{Pr}}\ \mathrm{Pr}\ \mathrm{Gr}\right)^{0.28} \tag{5.21}$$

where Pr is the Prandtl number, Gr the Grashof number, and A the annulus aspect ratio, L/D (Catton 1978). Because of uncertainties associated with application of this correlation to the neutron shield, Equation (5.21) was assumed to apply with the cask oriented either horizontally or vertically.

Heat transfer from the cask surface to the ambient included both radiation and convection components. During testing, the cask was located either indoors or outdoors. For the indoor runs, natural convection correlations were used to prescribe the cask surface heat transfer. For the outdoor runs with a nonzero wind speed, the cask surface heat transfer was computed from forced convection correlations. In situations where the cask was positioned outdoors with a reported wind speed of 0 mph, natural convection correlations were used. The natural and forced convection correlations employed are described below.

Forced convection heat transfer from the vertical cask surface to the ambient was likened to a cylinder in crossflow; because the direction of crossflow was not constant throughout the test, an average film coefficient was required. An empirical relationship developed by McAdams (1954) of the form

$$\mathrm{Nu} = B\ (\mathrm{Re})^{N} \tag{5.22}$$

where B = 0.0239 and N = 0.805 for the REA cask, was chosen since it provides an estimate of the average convection heat transfer coefficient about a cylindrical cask body (Welty, Wicks, and Wilson 1969). For horizontal surfaces exposed to crossflow, specifically the cask lid, Reynolds' analogy was applied, enabling the convective heat transfer coefficient to be evaluated from estimates of the frictional drag as

$$h = C_f \rho V_\infty C_p \tag{5.23}$$

where h is the average film coefficient, C_f the frictional drag, and V_∞ the free-stream (wind) velocity. Using a local skin friction coefficient computed from the Blasius shear stress relationship (Welty, Wicks, and Wilson 1969) results in

$$C_f = \frac{0.0576}{Re_x^{\,0.2}} \tag{5.24}$$

where Re_x is the local Reynolds number. Integrating Equation (5.24) over the length of the lid gives a correlation of the form

$$Nu = 0.036\ PrRe^{0.8} \tag{5.25}$$

The cask surface natural convection film coefficients were evaluated from an expression obtained for vertical cylinders and horizontal plates in air at atmospheric conditions, $Nu = C(Gr\ Pr)^{0.33}$, where $C = 0.13$ for vertical surfaces, and $C = 0.14$ for horizontal surfaces (Lindeburge 1981). The forced and natural convection coefficients listed above were calculated using wind data at the time of steady state for each run. The effects of cask orientation on the outer surface convection were ignored because Equations (5.22) and (5.24) give similar results regardless of orientation. The bottom of the cask was assumed adiabatic because the plywood sheet on which the cask rested resulted in a high thermal resistance.

In addition to the indoor and outdoor cask test runs, three runs were made in which an insulation layer was applied over the outer surface of the neutron shield. For these cases (runs 12, 13, and 14, Table 5.4, Section 5.1), heat transfer from the cask surface to the ambient was no longer modeled; instead, the measured cask surface temperatures were directly applied via input.

Radiation heat transfer to the ambient was included in addition to the natural/forced convection component described above. The radiation component was based on radiative heat exchange between gray bodies and was determined as a function of heat transfer area and cask emissivity. Two cask surface emissivities were used: 0.78, an as-measured value of the high-emissivity paint used to cover the surface of the neutron shield (Taylor 1984), and 0.3, the assumed emissivity for the unpainted stainless steel cask surfaces. The ambient was assumed to be a black body ($\varepsilon = 1.0$).

5.2.2.3 Modeling Uncertainties

The computational model developed for this analysis is based on design drawings supplied by REA, predicted and measured assembly heat generation rates, and predicted and measured axial heat generation profiles. In developing the model, uncertainties associated with five important heat transfer and fluid flow parameters were encountered:

- contact resistances
- material emissivities
- surface-to-ambient thermal resistance
- ambient conditions
- flow resistances.

Contact heat transfer was assumed to be a function of material type, gap size, surface finish, contact pressure, and the effective contact area. Areas not in contact transfer heat through a gap via radiation and conduction through the fluid. In cases where partial contact is assumed, the relatively low thermal resistance of the contact path dominates the parallel thermal resistance term, making the uncertainty in gap size relatively insignificant. Thus, uncertainties in the contact heat transfer are primarily a function of the materials in contact and the effective contact area.

The cask basket components subject to large uncertainties in contact heat transfer are 1) fuel tubes, 2) basket spacers, 3) conduction strips, and 4) fuel assemblies. Fuel tube contact heat transfer (fuel tube-to-fuel tube, fuel tube-to-basket spacer, and fuel tube-to-conduction strip) is possible only from the fuel tube bead surface area. Because the bead surface is a small fraction of the total fuel tube surface area, no contact between the fuel tubes was assumed.

Contact heat transfer for the basket spacers (spacer-to-spacer and spacer-to-basket) is ensured by use of special proprietary fasteners. Measurement of the contact conductance for a similar fastened joint was experimentally determined and reported in a REA proprietary document. Because it is unlikely that the conductances in the cask will be as high as those measured on a benchtop model, the conductance used in this analysis was arbitrarily taken to be 80% of the as-measured value. Contact heat transfer for the conduction strips (strip-to-basket and strip-to-basket spacer) also is ensured with fasteners. Again, the conductance used was assumed to be 80% of the as-measured value.

For this analysis, it was assumed that fuel assemblies are centered within the fuel tubes so that no contact exists between fuel rods and fuel tubes. This assumption will result in conservatively high cladding tempertures, especially when the cask is horizontally oriented.

Other regions where contact heat transfer is subject to large uncertainties are 1) basket-cask interface and 2) lead-stainless steel interface. Basket-cask contact heat transfer uncertainty is due to the fabrication techniques employed; contact is not ensured because of the differing basket and cask radii of curvature. In determining the contact conductance, an average of the measurements of the as-built gaps was used. No contact was assumed along the basket-cask interface.

The uncertainty in the geometry of the lead within the stainless steel annulus of the cask body again results from the fabrication technique. Molten lead is poured and allowed to solidify in place; during cooling, contraction of the lead from the outer stainless steel shell is expected. Thus, no contact was assumed; an estimated value of the lead-stainless steel gap was provided by the lead pourer, E. L. Manufacturing, Peebles, Ohio.

As-measured emissivity values were provided for the fuel tubes and for the high emissivity paint used to coat the outer surface of the neutron shield (Taylor 1983, 1984). A wide range of emissivity values was found in the literature for other cask structures (e.g., strips, spacers, fuel). The values were found to be dependent upon fabrication technique, oxidation buildup, and temperature. Thus, a large degree of uncertainty exists in the emissivity values. However, the uncertainty in the fuel rod emissivity has been shown to have little effect on the radial temperature distribution in an enclosed assembly, as indicated in Section 5.2.4.

Heat transfer from the outer cask surface includes radiation and convection components. For the indoor runs or runs in which the ambient air was considered "stagnant", only natural convection was included, and it was assumed that this natural convection component was eliminated with a nonzero wind speed. In this situation, a forced convection correlation was substituted. The cask geometry, however, suggests that large Grashof numbers will result from the large vertical height of the cylinder, and that free convection will continue to play an important role in the overall heat transfer; i.e., both free and forced convection should be considered simultaneously. Additionally, studies have shown significant increases in Nu with increased turbulent intensities. Thus, the lack of turbulence data and a means to correlate the data, plus the difficulty in defining a method for correlating the combined convection effects, results in a large uncertainty in the cask surface heat transfer coefficient. Definition of the cask surface heat transfer is complicated also by the ambient weather conditions, i.e., insolation, rain, and snow. No attempts were made to model the effect of these natural phenomena on the cask thermal response.

The major uncertainty in flow resistance comes from the contribution of the fuel tube inlet and outlet flow losses. This uncertainty is due in part to the slight bowing of the as-built cask bottom, which results in inlet flow area variations from fuel tube to fuel tube.

5.2.3 COBRA-SFS Predictions Compared to Data

The COBRA-SFS computer code was used to predict the temperature and velocity distributions within the REA dry storage cask. In this section, comparisons of pretest predictions to measured test data are presented. Following pretest data comparisons, justified improvements in the computational model are recommended, and their effects are demonstrated in selected post-test simulations. An assessment of the code's predictive capabilities is also provided for the pre- and post-test simulations. The evaluation procedure is outlined below.

To properly evaluate code predictions, several comparisons of code predictions to data must be made. The most obvious comparisons to be made are of peak cladding temperatures; however, comparisons of temperature drops between components of the cask and comparisons of axial and radial temperature profiles add substance to the evaluation. Pretest comparisons of peak temperatures may be used to assess the code's blind predictive capabilities. However, the pretest comparisons are directly affected by the accuracy, reliability, and completeness of the cask description provided to the modelers, as well as the accuracy of the test data.

5.2.3.1 COBRA-SFS Pretest Predictions

In the pretest analysis, 16 of the 17 experimental runs listed in Table 5.4 of Section 5.1 were simulated. To make pretest predictions, boundary condition data were supplied for each run. The data consisted of cask internal pressure, ambient temperature, wind speed, and insolation. Additional information supplied included the cask loading pattern and fuel assembly heat generation rates.

The overall ability of the code to predict the thermal performance of the cask without having access to the performance data is represented in bar graph form in Figure 5.43. How well do the code predictions match the data? Four of the 12 vertical runs fall within the estimated scatter of the data, determined to be ±3% of the measured peak-to-ambient temperature difference (see Section 5.1.3.1). Furthermore, 7 of the 12 vertical runs fall within ±6% of the measured temperature differences. Expressed in terms of absolute temperatures, 4 of the 12 predictions were within 10°C of the data, 8 within 20°C, and 11 within 30°C of measured peak temperatures. Generally speaking, the agreement between predicted and measured peak temperatures is good.

Before a true evaluation of the code can be undertaken, the uncertainties associated with the cask description and the data need to be reduced (total elimination of these uncertainties is not considered reasonable). Toward this end, comparisons of the temperature drop between key components, essentially a measure of thermal resistance, are used to reduce the uncertainties associated with the cask description and various code input models. Analysis of the test data to uncover the scatter and repeatability of the data was also undertaken to evaluate its reliability. Modifications of the cask description inferred from the comparisons of predictions and data were incorporated into the computational model for the post-test analysis. The subsequent post-test

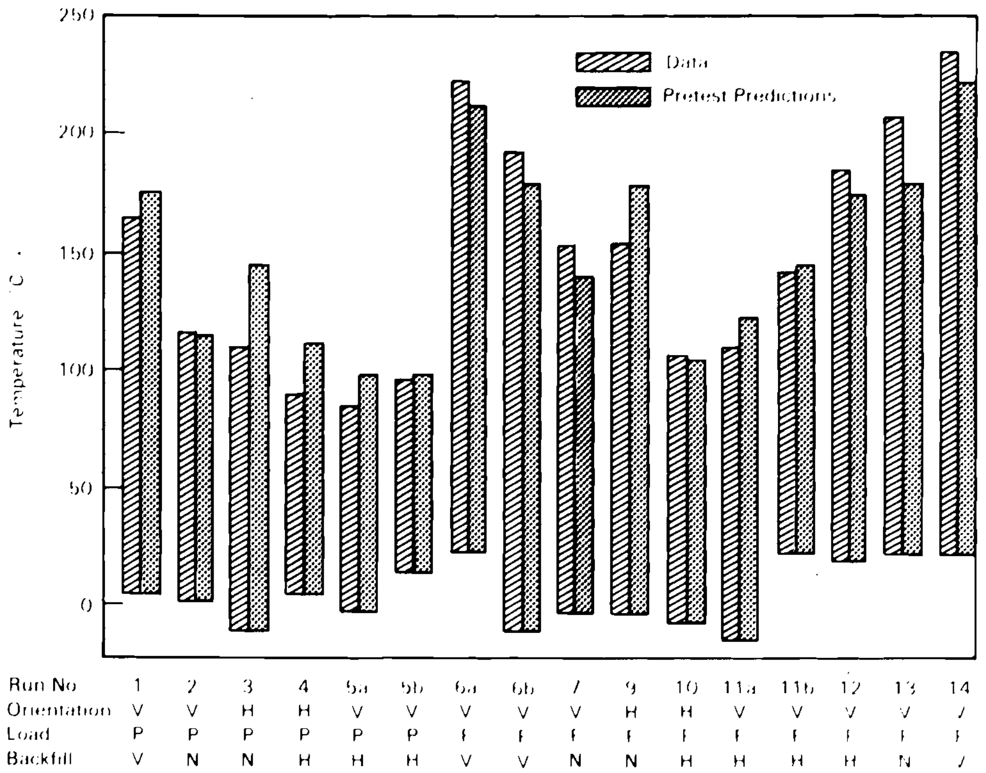

FIGURE 5.43. COBRA-SFS Pretest Predictions of Peak Temperatures and Overall Temperature Differences Compared to Data

predictions still show some disagreement with data, but offer a much better representation of the code's predictive capabilities than do the pretest comparisons.

In the next section, a more detailed review of several important runs examines the effects of cask orientation, loading, and backfill media on the cask thermal response. Results for additional cases are presented in Appendix E in the form of axial and radial temperature profiles.

5.2.3.1.1 General Observations. Seven of the 16 test cases were selected to examine the separate effects of cask orientation, fuel loading, and fill media on the predicted versus measured cask thermal response. Comparisons of axial and radial temperature profiles demonstrating these effects are displayed in Figures 5.44 through 5.51. The axial profiles are for the centerline of assembly 2J, and the radial profiles are along the diagonal of quadrant 2 from the center of the cask to the ambient, at an elevation 3.33 m above the cask bottom (see Figure 5.19 of Section 5.1).

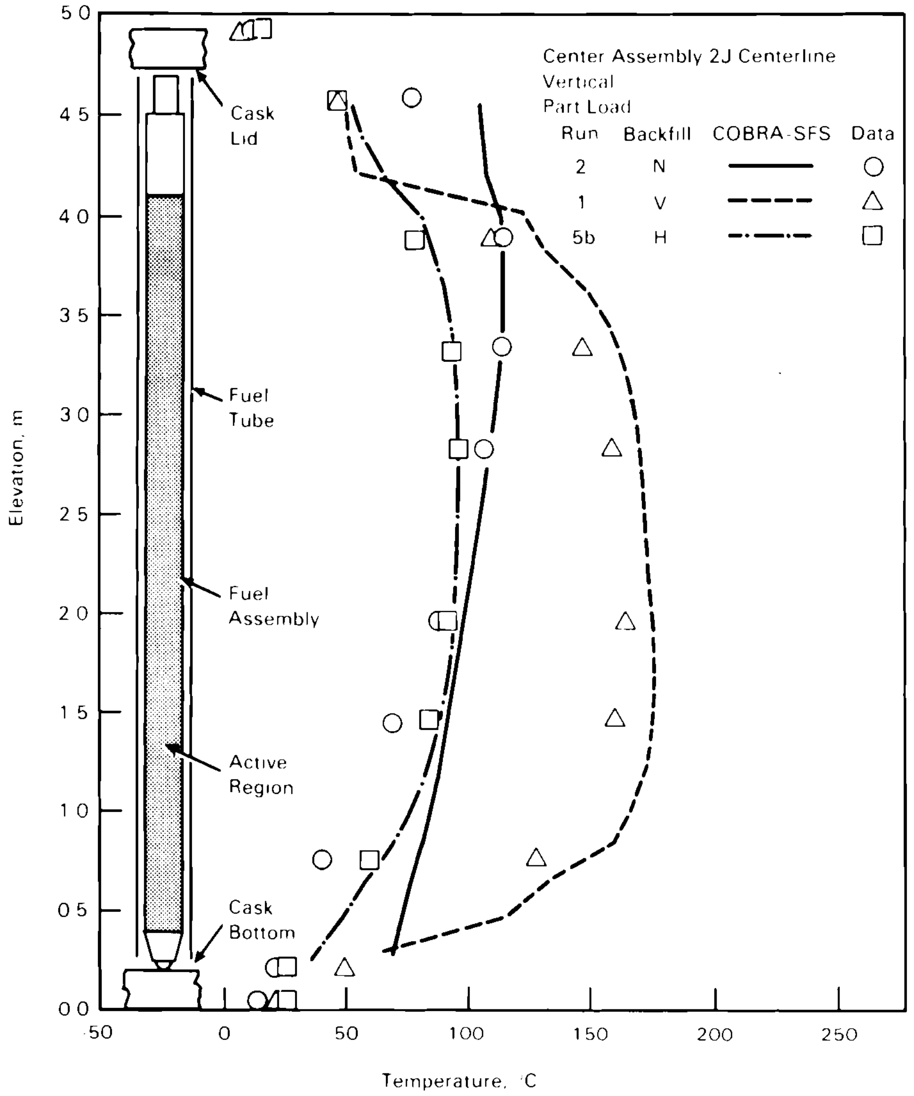

FIGURE 5.44. COBRA-SFS Pretest Predictions of Center Assembly 2J Centerline Axial Temperature Profiles Compared to Part Load, Vertical, Vacuum, Nitrogen, and Helium Data

Some interpretation of the code predictions and data displayed in these figures is in order. For the axial profiles, the data points above 4.5 and below 0.5 do not represent cladding surface temperature measurements, but measurements of gas temperatures. However, predictions given represent the cladding surface temperatures and, thus, should read higher than data at these locations. For the radial profiles, the lateral locations of the thermocouples

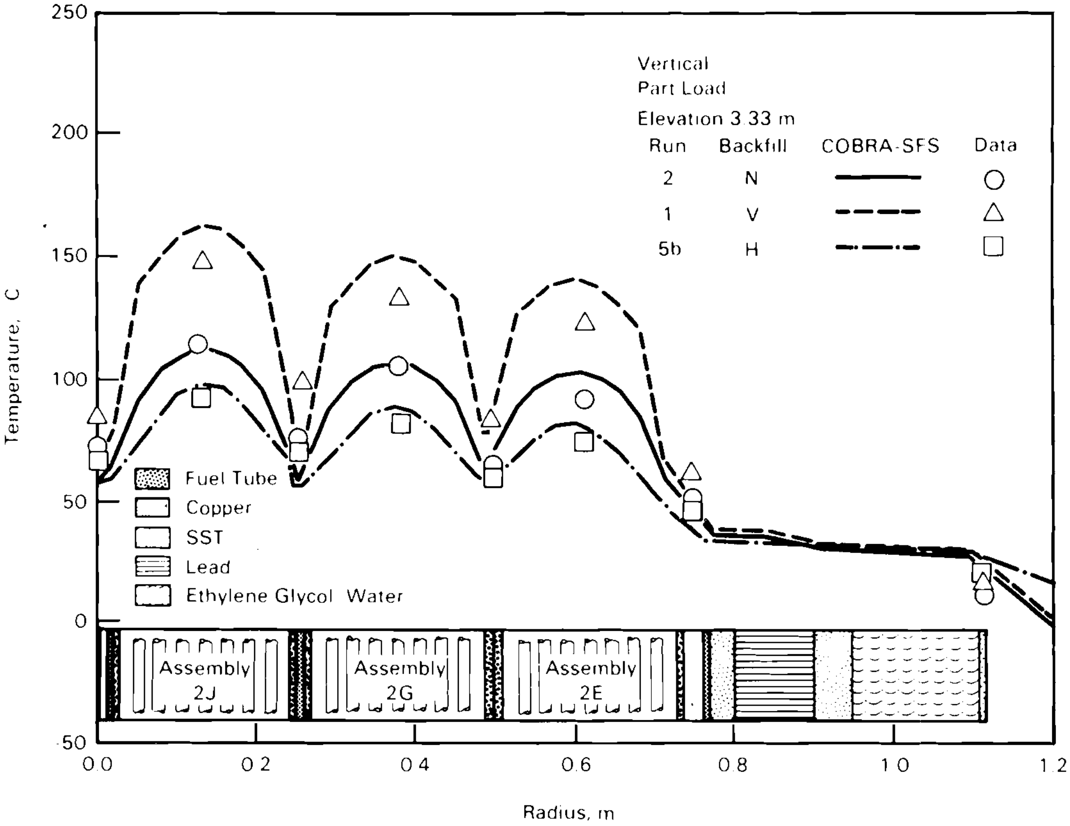

FIGURE 5.45. COBRA-SFS Pretest Predictions of Radial (Diagonal) Temperature Profiles Compared to Part Load, Vertical Vacuum, Nitrogen, and Helium Data at 3.33 m Elevation

within the interstitial regions of the basket junctions were not exactly known. This uncertainty significantly affects the data comparison where the radial temperature gradient is severe, i.e., basket node 2E (see Figure 5.19 of Section 5.1). Because basket thermocouples were designed to remain suspended within basket junctions, any contact of thermocouples with surrounding walls biases measured temperatures. For lack of alternative information, the data was assumed to measure the interstitial gas temperature, which represents an average temperature of the exposed junction surfaces. The calculated results, on the other hand, are given for the copper strips along the diagonal of the basket junctions, which, because of their high thermal conductivity and connection to the low temperature of the cask exterior, are at substantially lower temperatures than the surrounding junction walls. As a result, the code

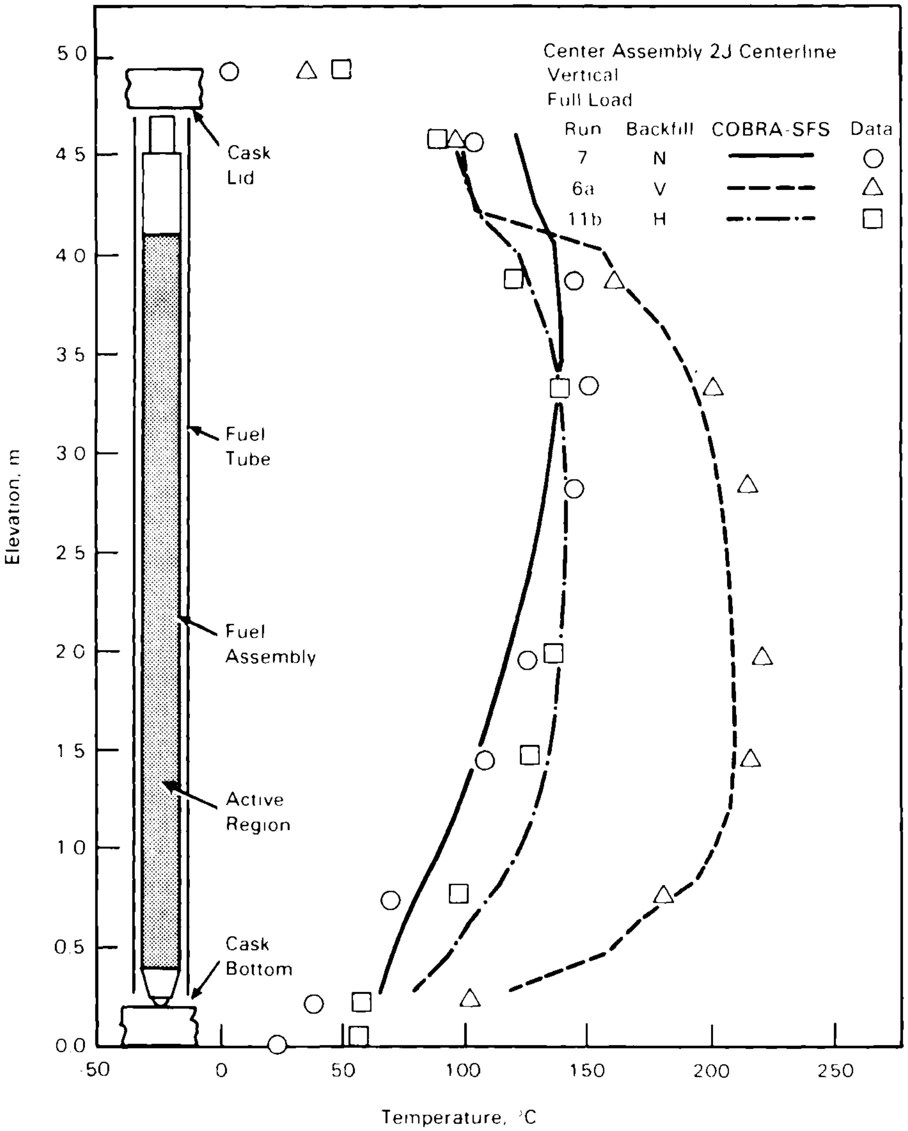

FIGURE 5.46. COBRA-SFS Pretest Predictions of Center Assembly 2J Centerline Axial Temperature Profiles Compared to Full Load, Vertical, Vacuum, Nitrogen, and Helium Data

predictions fall consistently below the data at the basket locations as they should. This makes a direct comparison of predicted and measured basket temperatures difficult.

Figures 5.44 through 5.51 show that both locations and magnitudes of peak cladding temperatures were satisfactorily predicted in all cases, with the greatest disagreement in peak temperatures occurring in the full load,

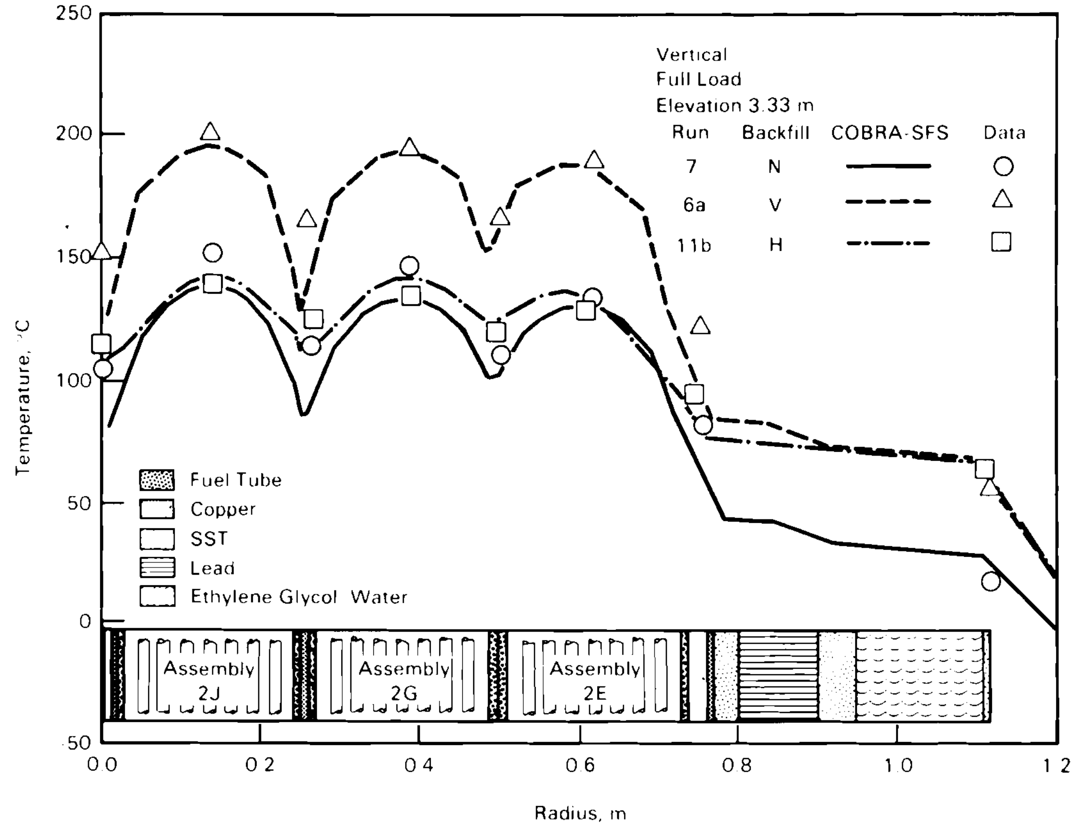

FIGURE 5.47. COBRA-SFS Pretest Predictions of Radial (Diagonal) Temperature Profiles Compared to Full Load, Vertical, Vacuum, Nitrogen, and Helium Data at 3.33 m Elevation

horizontal, nitrogen case (run 9 in Figure 5.50). The ability to satisfactorily predict both magnitudes and locations of peak temperatures suggests that, generally speaking, the important physical phenomena occurring within the cask are properly modeled by COBRA-SFS. However, the radial temperature profiles (Figures 5.45, 5.47, 5.49, and 5.51) illustrate greater local temperature differences that exist within the cask and suggest where improvements to the cask description or computational model may be made. For example, the cask surface temperatures are consistently overpredicted in all cases, suggesting a deficiency in the cask surface convective heat transfer correlations. Comparisons of temperatures within the cask interior are complicated by this difference in predicted and measured surface temperatures. For more meaningful

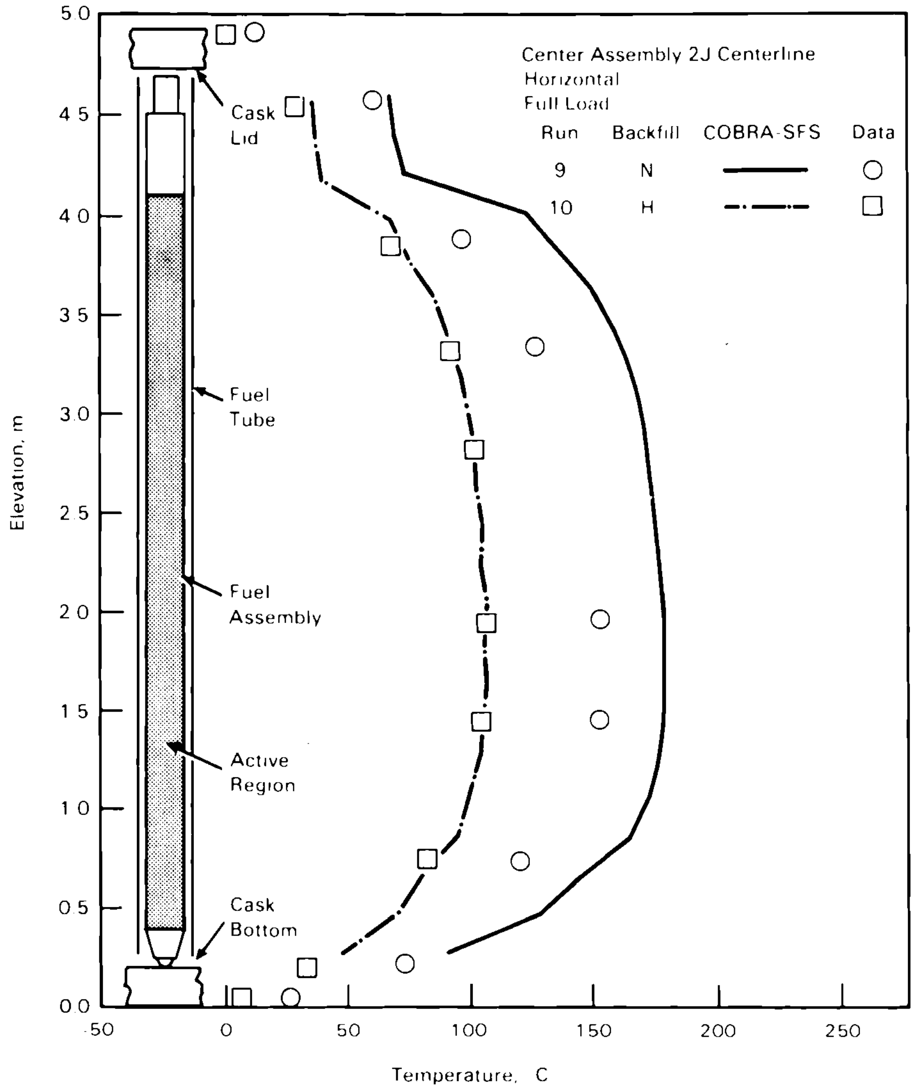

FIGURE 5.48. COBRA-SFS Pretest Predictions of Center Assembly 2J Centerline Axial Temperature Profiles Compared to Full Load, Horizontal, Nitrogen, and Helium Data

comparisons of predicted and measured thermal response of the different cask components, predictions and data are compared using lateral temperature differences across the cask components.

Effects of backfill media on temperature distributions are shown in Figures 5.46 and 5.47 for a fully loaded, upright cask, and in Figures 5.44 and 5.45 for a partially loaded, upright cask. The results for the nonconvective

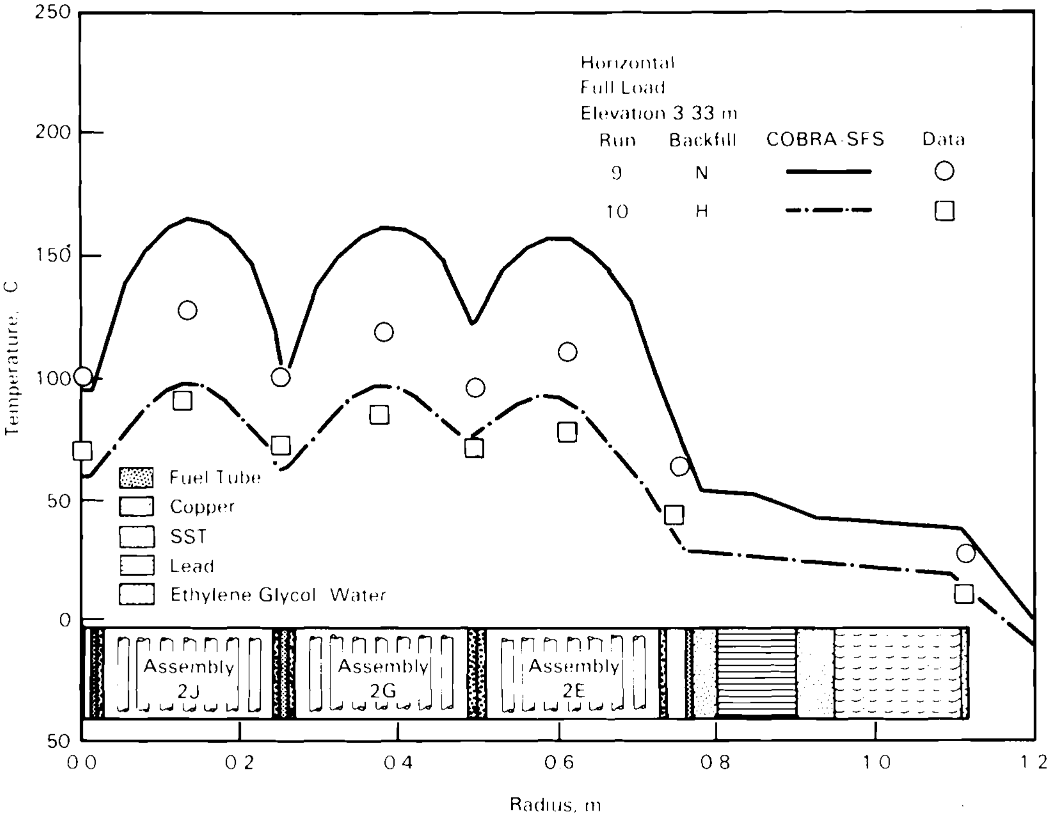

FIGURE 5.49. COBRA-SFS Pretest Predictions of Radial (Diagonal) Temperature Profiles Compared to Full Load, Horizontal, Nitrogen, and Helium Data at 3.33 m Elevation

cases (helium, vacuum) closely match the axial and radial profiles. The good agreement for both backfills in the shape of the profiles suggests that the radiation and conduction heat transfer models are performing adequately. For the helium runs, the successful predictions can be attributed in part to the low molecular weight and high thermal conductivity of helium. The low molecular weight precludes the development of large density differences; thus, discrepancies in the computational treatment of convection are minimized. The high thermal conductivity of helium lessens the influence of gap width uncertainties on temperature distributions and effectively reduces the uncertainty in the cask model. The enhanced conductivity also lessens the impact of the radiative heat transfer component on the overall cask heat transfer.

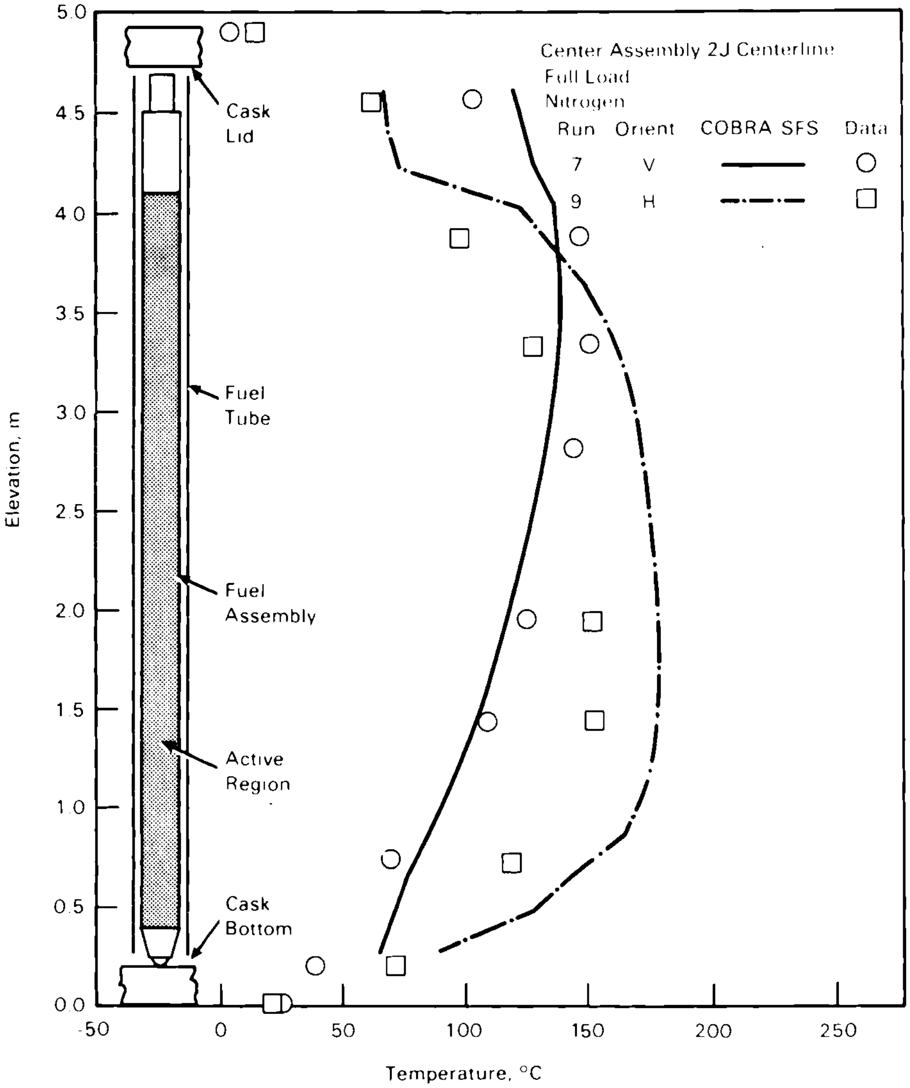

FIGURE 5.50. COBRA-SFS Pretest Predictions of Center Assembly 2J Centerline Axial Temperature Profiles Compared to Full Load, Vertical and Horizontal, Nitrogen Data

As with the helium runs, the low pressures and correspondingly low densities of the vacuum cases (purged nitrogen) minimize the establishment of natural convection, and, therefore, eliminate a possible source of uncertainty. The good agreement in the shape of the axial and radial profiles for the radiation-dominated vacuum runs indicates that the detailed gray body radiation exchange package employed in COBRA-SFS is performing adequately.

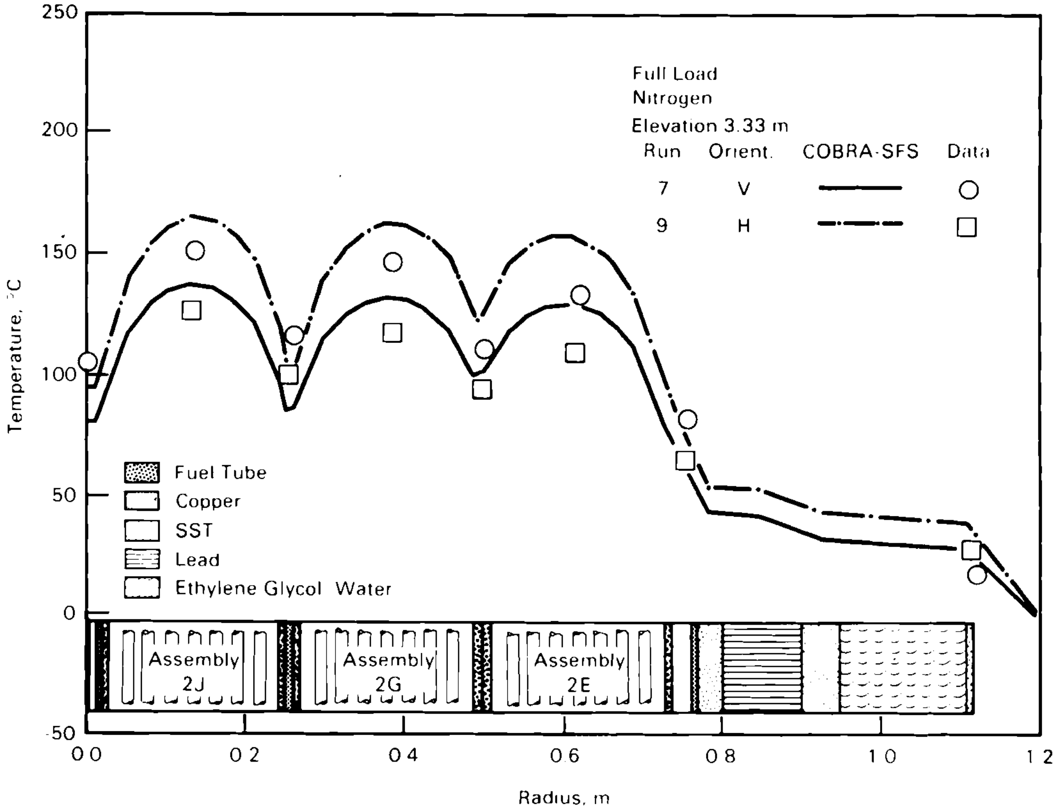

FIGURE 5.51. COBRA-SFS Pretest Predictions of Radial (Diagonal) Temperature Profiles Compared to Full Load, Vertical and Horizontal, Nitrogen Data at 3.33 m Elevation

For the nitrogen backfill runs, both the calculations and the measured data show skewed temperature profiles, with peak temperatures located toward the top of the active fuel region. These temperature distributions result from natural convection within the cask. From this it is concluded that the code models convection within a cask. However, comparisons between the predicted and measured profiles show that the predicted shape is flatter and that this difference is accentuated in the partial load case (Run 2). This difference suggests that the code is overpredicting the magnitude of the natural convection flow rate, but because of the lack of data regarding the cask flow field, it is impossible to make a definitive judgment. The calculated average velocities within the assemblies are summarized in Table 5.8.

TABLE 5.8. COBRA-SFS Velocity Predictions (Elevation 1.97 m)

Run Number	Run Parameters	Velocity, m/sec	
		Center Assembly	Outer Assembly
2	P,N,V	+0.3810	-0.8717
5a	P,He,V	+0.0899	+0.1295
5b	P,He,V	+0.0893	+0.1256
7	F,N,V	+0.1341	+0.0817
11a	F,He,V	+0.0933	+0.0692
11b	F,He,V	+0.0735	+0.0555
12	F,He,V,Ins	+0.0704	+0.0582
13	F,Nl,V,Ins	+0.1588	+0.1116

P = Partial Load; F = Full Load; N = Nitrogen; He = Helium;
V = Vertical;
Ins = Insulated

Predicted natural convection flow rates can be large because the difference in the gravitational head between the upflow and downflow regions is overpredicted, and/or because the overall flow resistance is underpredicted. There is little data from this experiment that would help in quantifying either of these effects. However, close inspection of predictions and data in the lower elevations reveals two important and related trends: 1) the predicted inlet (plenum) temperatures consistently exceed the data, and 2) the measured inlet temperatures vary as a function of radial position. Over-predicted plenum temperatures can result from 1) modeling differences in the heat transfer of the fluid returning to the lower plenum as it flows along the peripheral downcomer channels and 2) differences in the heat transfer of the recirculating fluid as it flows across the cask bottom.

The underpredicted heat transfer in the downcomers can be attributed to the inability to correctly define all the necessary heat transfer and fluid flow parameters, including the as-built geometry. However, the inability to correctly predict the plenum temperatures can be attributed in part to the simplified heat transfer model employed in this region--a one-dimensional energy equation that assumes the cask bottom is isothermal, and fuel tube inlet temperatures based on the bulk mixed mean temperature of the entire lower plenum. In addition, the flow field in the plenums is not computed. Therefore, a plenum film heat transfer coefficient must be accurately specified. Because only a single, bulk temperature is computed for the plenum regions, the radial variation in fuel tube inlet temperatures seen in the data was not modeled [this phenomenon can be readily observed from the data and can vary as much as 25°C from the interior and exterior assembly positions (see full load, vertical, nitrogen figure in Appendix E)]. Together, the use of a common inlet temperature, isothermal cask bottom, and unknown flow field complicates the ability to correctly predict plenum cooling.

To better understand how the plenum heat transfer affects the overall predicted cask thermal response, the plenum bulk-to-film heat transfer coefficient was reduced by an order of magnitude in a numerical study performed for the data evaluation. In this simulation, the peak cladding temperature for the full load, vertical, nitrogen case was increased by 10°C. Thus, this heat transfer parameter is important in determining the thermal performance of the REA cask. To lessen the importance of this parameter on future analyses, it is suggested that 1) the current plenum model be revised to include radially varying inlet conditions; 2) multidimensional heat transfer in the solid components be modeled; and 3) more detailed data, including information on the plenum velocity distributions, be obtained for future evaluation of the plenum heat transfer.

Before the modeling revisions suggested above are implemented, a more complete separate effects study is needed. In light of the large uncertainties associated with both the plenum computational model and heat transfer, and the lack of detailed data in this region, the assumed thermal plenum resistance was modified in the post-test simulations.

An additional test of the code's convective capabilities is the ability to predict the resulting flow field in a partially loaded cask (Figure 5.44). Although not verified by test data, predictions indicate that much larger flows result with the partially loaded cask. The empty fuel tubes that surround the concentration of spent fuel assemblies located in the center of the cask (see Figure 3.6 in Section 3.3) are believed to enhance the cooling of the fluid such that a greater net gravitational head is established between the hot and cold channels in the cask. As a result, assembly flows are generally predicted to increase.

The effect of backfill media on the predicted and actual thermal response is shown in Figures 5.48 and 5.49 for a fully loaded, horizontal cask. As expected, the temperatures are overpredicted, with the greatest disagreement observed for the nitrogen run. Little axial convection is observed to occur from inspection of the axial temperature profiles. Again, this trend was correctly modeled by COBRA-SFS. The reasons behind the anticipated over-predictions for the horizontal runs are presented below.

The computational model used for the horizontal simulations incorporates two simplifying, conservative assumptions: 1) fuel assemblies are concentrically oriented within fuel tubes and 2) there are no buoyancy effects. The consequences of these assumptions were expected to be revealed in the pretest data comparison. Although contact of fuel assemblies with fuel tubes could be expected, the type of contact, i.e., point, line, or plane, was not defined. Thus, assemblies were assumed centered. A previous study has shown that assembly-wall contact reduces temperatures within the assembly and provides superior heat transfer to the contacting surfaces (Cuta, Rector, and Creer 1984). This analytic study showed a reduction in peak fuel rod-to-fuel tube temperatures of 6°C for a 1-kW PWR fuel assembly in air. Although difficult to determine for the lower power BWR fuel assemblies incorporated into a multi-assembly cask, some thermal benefit was expected. The magnitude of this effect can be inferred from comparisons of measured peak-to-ambient temperature differences for the vertical and horizontal nitrogen runs shown in Figure 5.43. Temperature differences for these two runs are roughly the same, indicating that the thermal benefit of assembly/fuel tube contact for horizontal runs is similar to that of natural convection in vertical runs. Thus, fuel assembly/tube contact is effective in reducing fuel temperatures in a dry storage cask.

The second simplifying assumption employed in horizontal runs was the elimination of buoyancy-induced effects--natural convection and thermal stratification. This assumption was mandated by the current models in COBRA-SFS, which do not allow buoyancy effects in the transverse direction.

5.2.3.1.2 Individual Component Evaluations. In the following sections, evaluations of the predicted thermal performance in the major cask components are made. From these comparisons, a better understanding of the computational models and cask description can be expected. The major cask components examined are:

- surface (surface-to-ambient)
- cask body
- fuel basket
- fuel assembly.

The predicted thermal response of each component is discussed below.

Surface

Heat transfer from the cask surface-to-ambient included both convection (natural or forced) and radiation components. To examine the differences in the predicted to measured thermal resistance in this region, the cask surface-to-ambient temperature differences for 13 of the 16 simulated test cases are presented in Figures 5.52 and 5.53. Relative magnitudes of surface-to-ambient temperature differences are compared to total cask temperature drops (peak-to-ambient) in bar graph form in Figure 5.52; absolute temperature differences from surface-to-ambient are displayed in Figure 5.53. Results for insulated runs (12, 13, and 14), in which measured surface temperatures were used on boundary conditions, are not included.

In all cases, predicted surface temperatures exceeded data, indicating that the cask surface heat transfer was underpredicted. Because the cask surface emissivity was experimentally determined, it was expected that the radiative heat transfer component was well defined. The convective component may not have been so well defined.

Correlations used in determining cask convective heat transfer were discussed in Section 5.2.2.2. Development of these correlations was based on ideal conditions--steady, free streams, with little or no turbulence, directed uniformly at infinitely long cylinders or flat plates with defined leading edges. Testing of the cask outdoors and near other structures subjected it to conditions in which the free stream varied in intensity and direction.

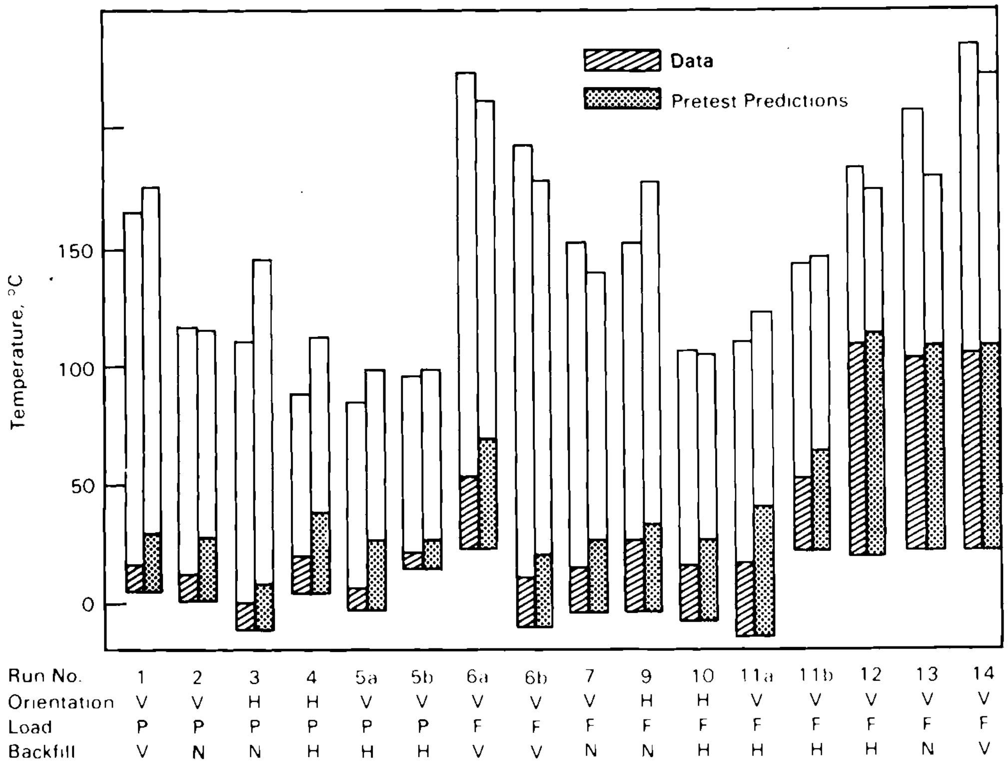

FIGURE 5.52. COBRA-SFS Pretest Predictions of Cask Outer Surface-to-Ambient Temperature Differences Compared to Data Peak Rod-to-Ambient Temperature Differences

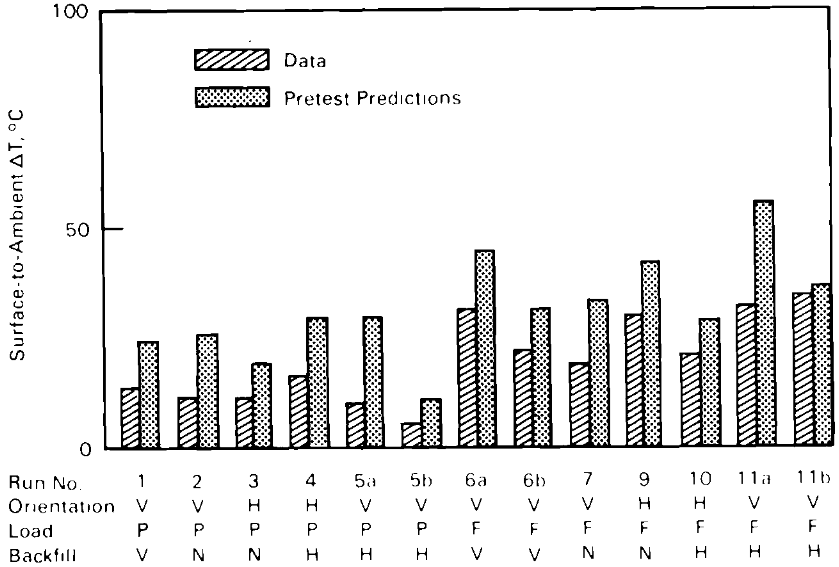

FIGURE 5.53. COBRA-SFS Pretest Predictions of Cask Outer Surface-to-Ambient Temperature Differences Compared to Data

Additionally, the validity of the correlations outside the intended range of applicability is also questionable (e.g., L = 4.9 m, 16 ft). Because it is believed that the radiative component is relatively accurate, it is concluded that the surface-to-ambient heat transfer is not accurately modeled by conventional forced or natural convection correlations.

Two major deficiencies in the convective correlations can be identified: 1) the correlations were developed for either forced or natural convection only, and 2) ncreased free-stream turbulence from structures near the test station are not taken into account. The large vertical height of the cask is such that large Grashof numbers ($>10^{10}$) can develop. Large Grashof numbers suggest that free convection may be occurring in combination with forced convection. Specifically, evaluation of the Richardson number, a criterion for determining the mechanism of convection, defined as $Ri = Gr/Re^2$, lies in the range where combined convection should be considered, i.e., $0.1 \leq Ri \leq 10$ (Morgan 1975; Clausing, Wagner, and Skarda 1984).

A significant departure from ideal test conditions used in developing the convection correlations is in the steadiness and uniformity of the free stream. The presence of the cask test stand (rail car) and other test site structures was expected to induce additional free-stream turbulence in the vicinity of the cask. Increased turbulence has been shown to enhance the convective heat transfer from cylinders up to 50% (Kestin and Maeder 1957); however, no general method for correlating higher turbulence intensity with heat transfer has gained wide acceptance. Because of the difficulty in correlating the turbulence effects and the lack of turbulence data for the cask site, the effects of free-stream turbulence were ignored. The large disagreement with the predictions and data suggests that free-stream turbulence must be included when determining cask surface heat transfer.

Other factors that may have influenced cask surface heat transfer include natural phenomena--precipitation and insolation. These effects were ignored in all simulations. Because periods of precipitation were generally shorter than the cask thermal time constant, elimination of this phenomenon appears appropriate. To examine the possible influence of the insolation, the ratio of predicted to measured surface temperature differences was plotted as a function of solar gain (see Figure 5.18 of Section 5.1). No correlation between the prediction error and insolation was observed; thus, exclusion of the solar gain in the computational model is also appropriate.

Cask Body

The cask body heat transfer model is evaluated from temperatures obtained along the cask body diagonal. The temperature data locations and nomenclature are displayed in Figure 5.22 of Section 5.1; data obtained at the junctions of fuel tubes and/or conduction strips are referred to as basket nodes. The primary evaluation of the cask body thermal resistance model is obtained from comparisons of the predicted versus measured temperature differences from basket node 2E to the surface. The open area of basket node 2E, as depicted, is somewhat misleading; many of the structural details in this region have been eliminated due to their proprietary nature. Basket node 2E, however, has the largest interstitial area and, thus, the largest uncertainty in its position--an unfortunate situation in that the temperature gradient in this region is quite severe. Although comparisons of other basket nodes to the surface will also indicate cask body resistance (e.g., 2G, 2J to surface) these internal comparisons include portions of the basket thermal resistance and, therefore, provide somewhat misleading information. Thus, in spite of the relatively large uncertainties associated with the temperature represented by basket node 2E, a more meaningful evaluation of the cask body resistance is obtained.

Temperature differences between basket node 2E and the surface at an elevation of 1.45 m above the cask bottom are presented in Figure 5.54. These temperature differences are highlighted against total peak cladding-to-ambient temperature drops. The same data is displayed in Figure 5.55, with all values referenced to zero. For all vertical runs, temperature drops through the cask body were underpredicted, and the average difference between predicted and measured values is 40%. Comparisons of temperature drops from other internal basket nodes to the surface underpredicted the data as well. Potential causes of the underpredictions are discussed below.

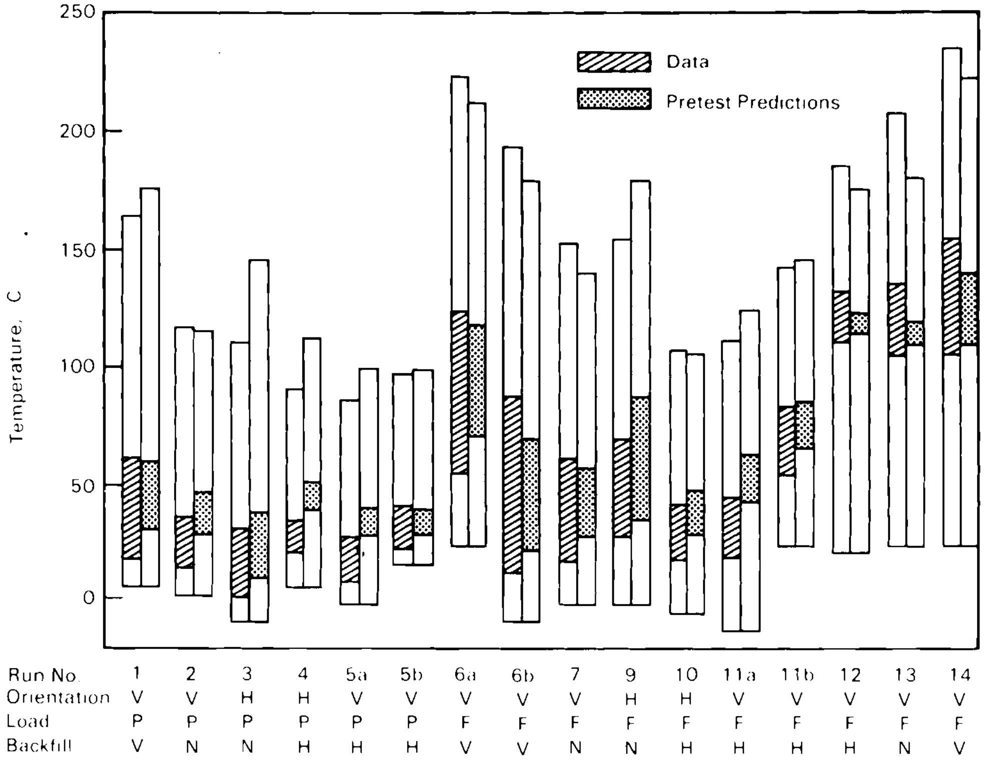

FIGURE 5.54. COBRA-SFS Pretest Predictions of Temperature Differences from Basket Node 2E to Cask Outer Surface at 1.45 m Elevation Compared to Data and Peak-to-Ambient Temperature Differences

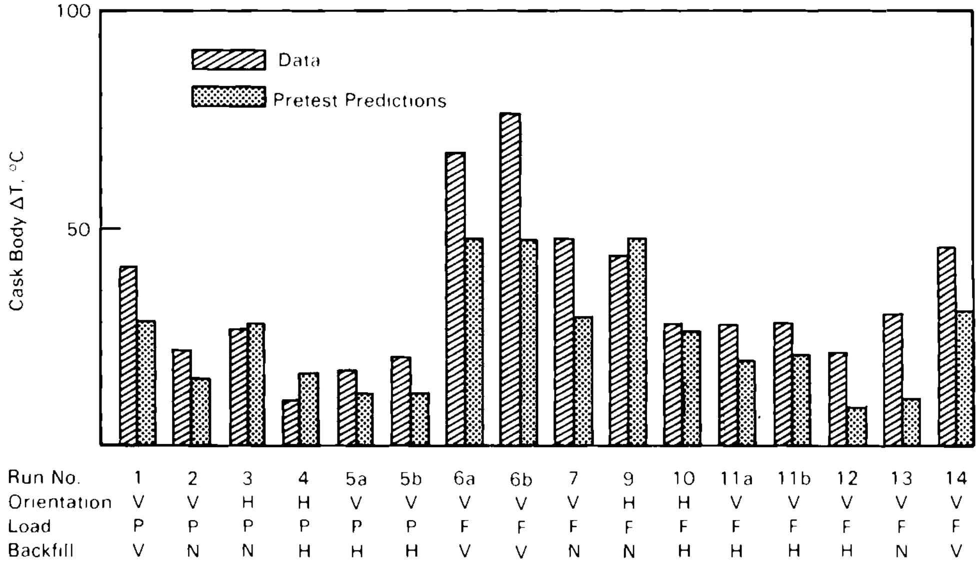

FIGURE 5.55. COBRA-SFS Pretest Predictions of Temperature Differences from Basket Node 2E to Cask Outer Surface at 1.45 m Elevation Compared to Data

The major uncertainties in the heat transfer path from node 2E to the surface are:

- conduction strip-to-basket contact resistance
- basket-to-cask contact resistance
- gamma shield gap(s) resistance
- neutron shield conductance.

Although contact of the conduction strips to the basket support structure occurs within the basket region, its effect is included in the cask body resistance because of the location of the basket node 2E thermocouple. The value of the surface contact conductance used for the pretest simulation was 0.56 W/cm^2°C (1000 Btu/hrft^2°F). This value was derived from data supplied by REA, who obtained the data from measurements on a bench-top test model of a prototypic fastened joint. The value measured is proprietary and cannot be reported. However, the value used was less than that measured because it is doubtful that the prototypic joints have as good a conductance as that of a bench-top model.

The uncertainty in the basket-to-cask contact resistance results from the different radii of curvature of the basket and the interior of the cask cavity. Some contact of the basket and cask body is ensured because the four basket sections are forced against the cask body inner wall. However, irregular, non-uniform contact between the basket and cask exists. To obtain an estimate of the contact region and the existing gap, as-built basket-to-cask gap measurements were obtained at 28 circumferential locations, 30 cm (12 in.) below the top of the cask (accessibility precluded measurements of this gap at other elevations). The gap width was found to vary from near zero to greater than 0.254 cm (0.100 in.). An average gap size computed from the measured data for all quadrants is 0.056 cm (0.022 in.), a value nearly equal to the average gap width computed from a geometric analysis of the component designs. Gap width data for the quadrant represented by the COBRA-SFS model (quadrant 2) averaged 0.147 cm (0.055 in.). The potential for basket movement during cask handling, especially with a shift in cask orientation, is great; thus, the validity of these as-measured gap values for all runs, and for all orientations, is questionable. Therefore, a uniform 0.056-cm (0.022-in.) gap was used throughout pretest simulation analysis. Variations in the gap width as a function of elevation were ignored.

The gap that exists in the lead gamma shield shrinks from the outer annulus wall as the lead cools. The size of the gap is dependent upon the radial temperature gradient in the lead and the rate of cooling. No data on the expected gap size for this cask was available; however, based on experience of lead pourers, an upper bound of 0.127 cm (0.050 in.) was assumed. The gap size will be less than the upper limit; therefore, an arbitrary gap size of 0.051 cm (0.020 in.) was selected for the pretest simulations. Because this gap represents a significant portion of the cask body thermal resistance, it was expected that this value would be modified in the post-test analysis.

The resistance of the ethylene glycol/water neutron shield was determined from a correlation based on the temperature difference across the annulus boundaries. It is expected that this correlation will provide the correct order of magnitude of thermal resistance for this naturally convecting region.

In each of the above heat transfer paths, the existing gaps and contacts are not well defined, although realistic ranges in their values can be determined. The situation is complicated by the possibility of shifting components and thermal expansion effects. Thus, while an assumed set of values may appear to be appropriate for some tests, they may be inappropriate for others. The inability to define the local gap and contact conditions on a run-by-run basis dictates that average values be employed.

Fuel Basket

The fuel basket heat transfer model was evaluated from temperature differences obtained along the cask diagonal between basket nodes 2G and 2E (Figure 5.22 of Section 5.1) at an elevation of 1.45 m above the cask bottom. Fuel basket temperature differences are presented in Figure 5.56 relative to total cask temperature differences. Identical data are displayed in Figure 5.57, with all values referenced to zero. Generally speaking, basket temperature differences were well predicted, with an average predicted-to-measured temperature difference ratio of 0.86 (vertical runs only).

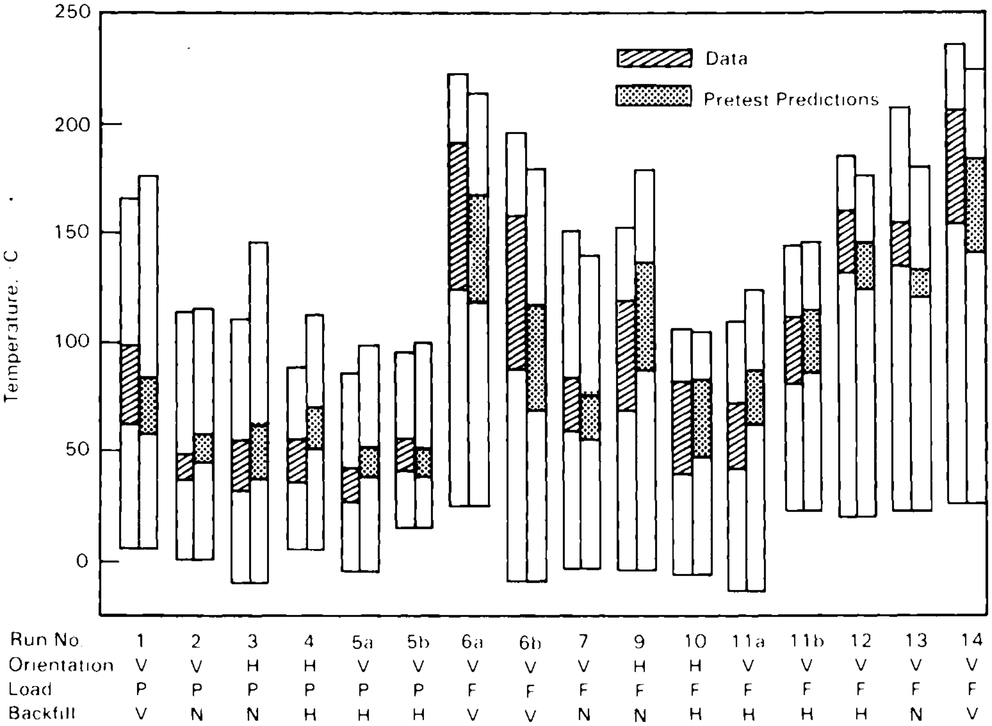

FIGURE 5.56. COBRA-SFS Pretest Predictions of Temperature Differences from Basket Node 2G to 2E at 1.45 m Elevation Compared to Data and Peak-to-Ambient Temperature Differences

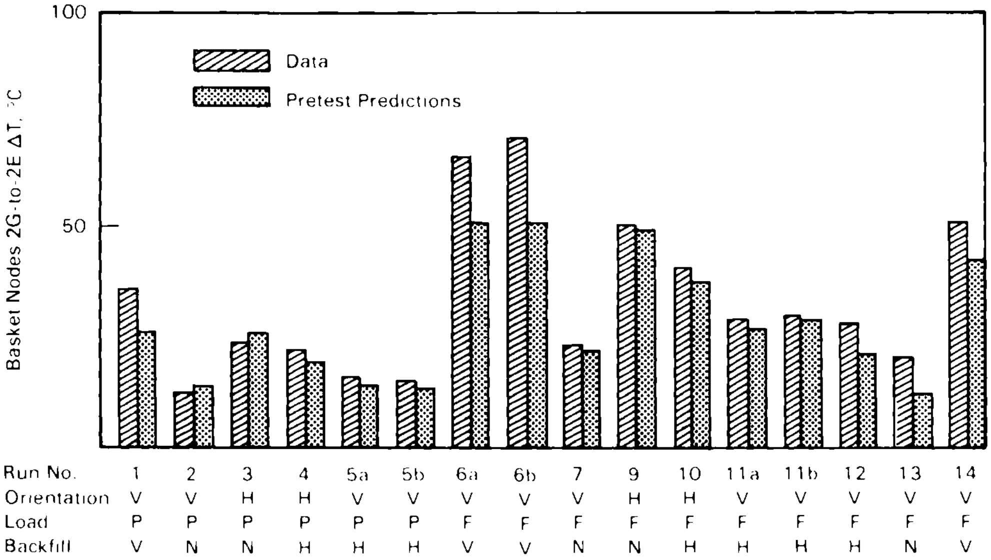

FIGURE 5.57. COBRA-SFS Pretest Predictions of Temperature Differences from Basket Node 2G to 2E at 1.45 m Elevation Compared to Data

The contact or lack of contact of the fuel tubes with each other or other basket components is an important uncertainty in modeling basket heat transfer. Fuel tube-to-plate or fuel tube-to-fuel tube gaps were determined to have an average width of 0.23 cm (0.090 in.) from as-built drawings (using nominal dimensions). Accounting for tolerances on straightness and fabrication technique, the separation between surfaces in the basket may vary from zero to in excess of the nominal 0.23-cm (0.090-in.) value. Because no information is available on the actual space surrounding each fuel tube in the as-built cask, it was universally modeled as a nominal 0.11-cm (0.004-in.) gap. The general agreement of temperature distributions in the cask interior and in predicted to measured temperature difference ratios for the data comparisons suggests that this approach provides a reasonable estimate of basket thermal resistance.

The conduction strips and spacers that contact the basket periphery are a major means of removing heat from the basket interior, a conclusion readily supported by the relatively low temperatures of these components observed in the data. The conduction strips that bisect the basket interior act as heat transfer pathways, establishing parallel path heat transfer network from the basket interior to exterior. Temperatures within the basket are strongly influenced by these pathways. The major resistance along these pathways is in the contact of the strips with the basket radial support structure, contact which is neither well defined nor uniform. Differences in the assumed versus actual contact resistance for these components cause temperature differences in the interior basket locations. Differences in predicted-to-measured temperature drops in the basket indicate that the predicted heat distribution along the parallel conduction path network is not entirely accurate.

The final factor influencing basket temperatures is the fuel rod-to-fuel tube resistance. As discussed earlier, fuel assembly eccentricity and fuel tube contact can significantly affect the heat flux distribution within a fuel tube and, therefore, the heat transfer into the basket conduction heat transfer network. Because the orientation of the fuel assemblies is unknown and subject to change, the actual heat transfer distribution to the fuel tube walls is not easily predicted. Also influencing the basket resistance is the axial heat removal by convection and the ability to correctly model the radiation heat transfer occurring within enclosed fuel tubes. As discussed in the next section describing fuel assembly heat transfer, the radiation model appears to correctly model the rod-to-rod and rod-to-wall radiation exchange occurring within a fuel tube. Thus, the largest uncertainty in fuel assembly-to-fuel tube resistance exists in the fuel assembly orientation. Changes to the computational model or input parameters cannot be expected to reduce this uncertainty.

In summary, the disagreement between predicted and measured temperatures in the basket cannot be attributed to a specific cause, but rather to a complicated interaction of effects, which, in total, produce the discrepancies observed in the comparisons of predictions with data. Because there appear to be no major errors in the parameters or models that define the basket temperature distribution, there was little justification for revisions. As such, the post-test analysis was performed with the same basket model employed in the pretest analysis.

Fuel Assembly

The fuel assembly heat transfer model is evaluated primarily from center rod-to-edge rod temperature differences obtained in assemblies 1F and 2G at an elevation of 3.33 m above the cask bottom(a) (see Figure 5.28 of Section 5.1). Although center rod-to-basket node temperature differences also could be used to evaluate the fuel assembly resistance, these values reflect some basket resistance uncertainties and are therefore less desirable. Comparison of rod-to-rod temperatures is believed to provide more meaningful information on the effects of conduction, radiation, and convection occurring within an assembly. It was therefore used in evaluating predicted assembly resistances.

The predicted and measured center-to-edge rod temperature differences for assemblies 1F and 2G are shown in Figures 5.58 and 5.59, respectively. In reviewing the vertical runs only, the temperature drop in assembly 1F was constantly overpredicted, with the greatest disagreement observed in the helium runs. More important, the best agreement was observed for the vacuum runs,

---

(a) Temperature data for edge rod in assembly 1F was taken 3.63 m above the cask bottom.

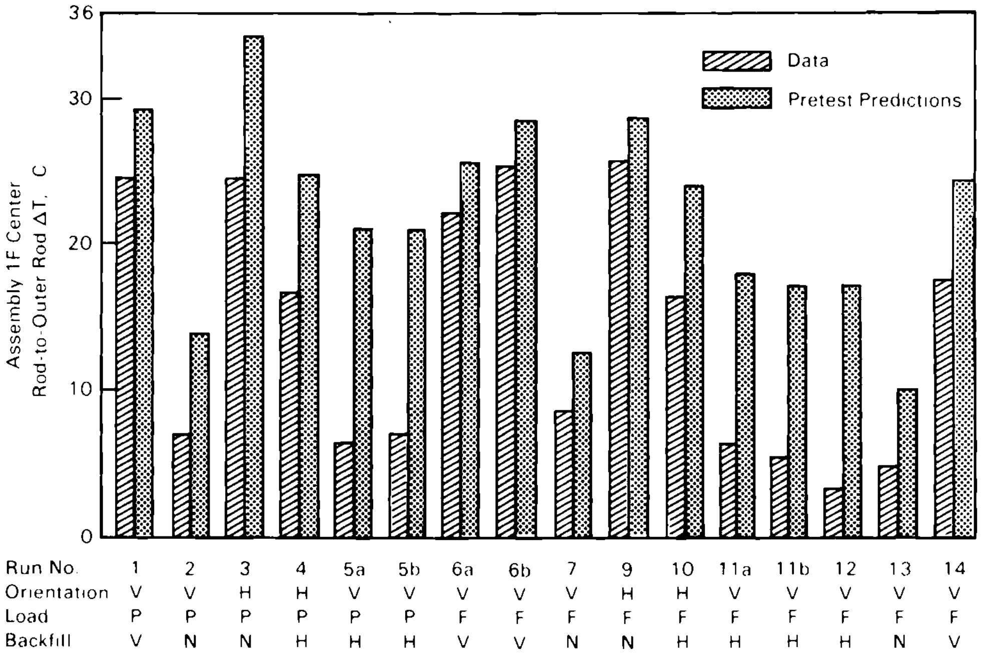

FIGURE 5.58. COBRA-SFS Pretest Predictions of Temperature Differences from Assembly 1F Center Rod-to-Outer Rod Compared to Data

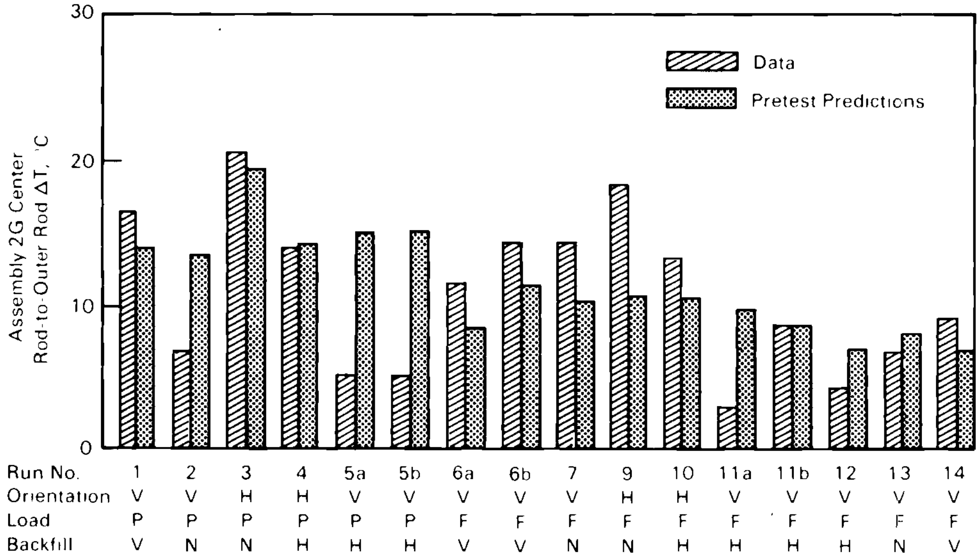

FIGURE 5.59. COBRA-SFS Pretest Predictions of Temperature Differences from Assembly 2G Center Rod-to-Outer Rod Compared to Data

cases that depend strongly on a description of the radiation heat transfer. Similar trends can be observed in the rod-to-rod temperature differences for assembly 2G as well; however, the data is not as consistently overpredicted. The generally good agreement between the rod-to-rod temperature differences for the vacuum and nitrogen runs suggests that the radiation model is performing adequately. The discrepancies observed in the helium cases are discussed below.

The greater disagreement in the helium backfill cases is related directly to modeling heat transfer from the isothermal rod surface to the gas. In the pretest analysis, the heat transfer from a rod to an adjacent subchannel was based on the average temperature of all surrounding subchannels. This approach, which assumes uniform rod heat flux, is valid for some applications, but fails in situations where the fluid conduction is a significant means of heat removal. The assumption of uniform rod heat flux provides reduced overall rod heat transfer to the fluid. This results in an apparent increase in the fuel assembly resistance. In the nitrogen cases, the error in the rod-to-fluid heat transfer is offset effectively by the more dominant radiation heat transfer. In helium, where conduction through the fluid becomes an important means of heat removal, the error in the fluid heat transfer is more noticeable. As a result of these data comparisons, the rod-to-fluid heat transfer model was modified in the post-test analysis to include the effect of asymmetric rod heat flux. The result of this modification on a helium case was examined in the post-test analysis and was found to significantly lessen some of the uncertainties associated with describing the fuel assembly thermal resistance.

The rod-to-rod temperature data sheds some light on the effect of fuel assembly orientation. Rod-to-rod temperature differences for assembly 2G were observed to be approximately two-thirds of those for assembly 1F in all vacuum runs except run 11B, in which this ratio increased to 1.5. Because runs 11A and 11B were identical except for the boundary conditions, the shift observed in the assembly rod temperature differences is believed to result from a shift in fuel assembly position. This conclusion is supported by the fact that the cask orientation was changed from horizontal to vertical for the start of run 11A, and was subsequently moved indoors for run 11B. Undoubtedly, the effect of changing fuel assembly orientation is responsible for most of the scatter in the rod-to-rod temperature data, which, when compared to small overall measured rod temperature differences, can become significant.

The difficulty of differentiating between effects of fuel assembly orientation and problems in the basket heat transfer model on the fuel assembly resistance makes other revisions of the fuel assembly model difficult. However, the change in the rod-to-fluid heat transfer model to include asymmetric rod heat transfer was found to improve the agreement in the post-test simulations. This was the only modification made to the fuel assembly model in the post-test analysis.

5.2.3.1.3 Summary of Pretest Prediction Results. Comparisons of pretest predicted peak temperatures and component temperature differences with test data showed that, in spite of some significant uncertainties in the cask description and physical models, the thermal performance of a multiassembly dry storage cask can be predicted satisfactorily using COBRA-SFS under a variety of operating conditions. Comparisons also showed where improvements could be made in the code's formulations and in the input description of the REA cask.

5.2.3.2 COBRA-SFS Post-Test Predictions

In this section, the modifications recommended from the pretest data comparisons are evaluated for several significant cask test cases. The runs chosen for the post-test analysis were selected to show the effect of these changes under different loading, backfill media, and orientation conditions. The recommended modifications include changes in the assumed cask description and changes in the modeling approach. Pretest and post-test simulations for the overall peak-to-ambient and four key components of the cask (surface-to-ambient, cask body, basket, and fuel assembly) are presented and compared to data to demonstrate the improved predictive capabilities.

Evaluations of predicted versus measured surface-to-ambient temperature differences showed a consistent overprediction of the data under forced convection or stagnant ambient conditions, suggesting deficiencies in the convective heat transfer correlations applied to the cask outer surface. The underpredicted convective heat transfer observed in the pretest comparisons was attributed to the inability to correctly specify combined natural and forced convection and the assumed dependence of convective heat transfer on free-stream turbulence. To account for differences in surface temperature, the cask surface heat transfer coefficient was increased to provide an approximate match of predicted and measured surface temperatures. No attempt was made to define a new heat transfer correlation from these new film coefficients, as this was beyond the intended scope of the data comparisons. Only an agreement in surface temperature was sought. As a result of this agreement, evaluations of other cask component temperature differences was greatly simplified. An adequate agreement in cask surface temperature was achieved in all cases using this approach.

Comparisons of cask body interior and exterior temperatures showed an underestimated thermal resistance. To increase the cask body resistance, the assumed width of the basket-to-cask gap was increased 50% from 0.056 cm (0.022 in.) to 0.012 cm (0.036 in.), well within the measured upper bounds for this parameter (0.254 cm, 0.100 in.). Additionally, the contact conductance assumed for the conduction strip-to-basket contact was reduced 50% from the pretest value of 0.56 w/cm^2°C (1000 Btu/hrft^2°F) to 0.28 W/cm^2°C (500 Btu/hrft^2°F) for the nonevacuated tests. This contact conductance was reduced even further to 0.056 W/cm^2°C (10 Btu/hrft^2°F) for the vacuum cases to account for gap widths that may be less than the mean-free molecular path of low pressure nitrogen. No other modifications in the cask body model or description were made.

Disagreements between predicted and measured temperatures in the basket region were not attributed to a specific cause, but rather to a complicated interaction of effects, which, in total, produced discrepancies observed in the data comparisons. As such, the post-test simulations were performed with the same basket model used in the pretest analysis.

Modifications made in the fuel assembly resistance included changes in the code models and changes in the input (film heat transfer coefficient). Disagreements in the fuel assembly resistance were observed as differences between the predicted and measured center-to-edge rod temperature differences in the helium backfill cases. This discrepancy was attributed to the symmetric rod-to-fluid heat transfer model, in which conduction through the high conductivity helium gas is inhibited by the assumed uniform distribution of heat from the rod into the surrounding fluid. An asymmetric rod heat flux model was incorporated for the post-test simulations, which considerably improved the predicted helium-to-fuel assembly thermal resistance. Little change in the vacuum and nitrogen radial profiles was seen as a result of this model refinement.

The second modification to the fuel assembly model was in the fuel assembly heat transfer coefficient. The axial surface temperature profiles were found to more closely represent a constant-surface temperature condition for fully developed flow in a pipe, rather than the earlier assumed constant heat flux condition. This was especially so for the nitrogen case. As a result, a new heat transfer correlation was chosen. The new expression, developed for constant surface temperature conditions, reduced the film heat transfer coefficient by 16%, from Nu = 4.36 to Nu = 3.66. This modification has little effect on the predicted fuel assembly temperature distributions in this cask, but it was made to be consistent with recommendations made in single assembly data comparisons (Lombardo et al. 1986).

The final modification to the fuel assembly model was in the axial power profile. A measured gamma flux axial distribution was available for the post-test analysis and was uniformly incorporated into the computational model. This experimentally measured gamma profile is shown in Figure 4.4 of Section 4.3.

The final revision to the input for the post-test simulations was in the plenum regions. A great deal of uncertainty is associated with modeling these regions due to the simplified momentum and heat transfer models employed in COBRA-SFS and in the complex flow paths and flow resistances of these regions. A significant trend not predicted by the current plenum model was the radial variation in assembly inlet temperatures. A mini parameter study on the input heat transfer coefficient for the upper and lower plenum showed that if other parameters were held constant, the variation in inlet temperature could be improved by reducing the plenum heat transfer coefficient. Therefore, the pretest plenum film heat transfer coefficient was decreased by an order of magnitude in the post-test analysis.

The refinements described above were used to perform post-test simulations of five selected runs: 2, 6b, 9, 11a, and 13. Run 2 (vertical, nitrogen, partial load) was selected because it was anticipated that flow recirculation in the partially loaded cask would be the most difficult to predict accurately. Runs 6b (vertical, vacuum, full load), 11a (vertical, helium, full load), and 13 (vertical, nitrogen, full load, insulated) provide a representation of the three backfill media. Run 9 (horizontal, nitrogen, full load) represents effects of these modifications in the horizontal orientation.

The results of the post-test predictions are again summarized in bar graph form in Figure 5.60. Overall peak-to-ambient temperature differences, as well as temperature differences through the four major cask components, are shown. To indicate the improvement offered by the post-test predictions, pretest and post-test results are shown with test data. As seen in Figure 5.60, the post-test predictions demonstrate an improved agreement with the data. In addition to improved overall temperature predictions, predictions of the four component temperature differences are similarly improved.

To further demonstrate the improvements, axial and radial post-test profiles for the three different fill media are presented in Figures 5.61 and 5.62, respectively. Although improvements were obtained, some disagreement between predictions and data still exist. Specifically, the predicted axial temperature profile (Figure 5.61) for the nitrogen case shows different trends at the lower elevations. Differences in the predicted and measured axial profiles for the convective cases result from several interrelated effects: the simplified one-dimensional plenum model, the unknown downcomer and fuel assembly film heat transfer, and unknown cask flow resistances. To improve the nitrogen post-test predictions, the plenum model would need to be revised to account for radially varying pressure and temperature distributions.

Peak cladding temperatures are underpredicted in the helium case (run 11a of Figure 5.60). A comparison of the component temperature drops in Figures 5.60 and 5.62 for the helium case shows that the major portion of the difference is in the cask body. Also, comparisons of pretest predictions with

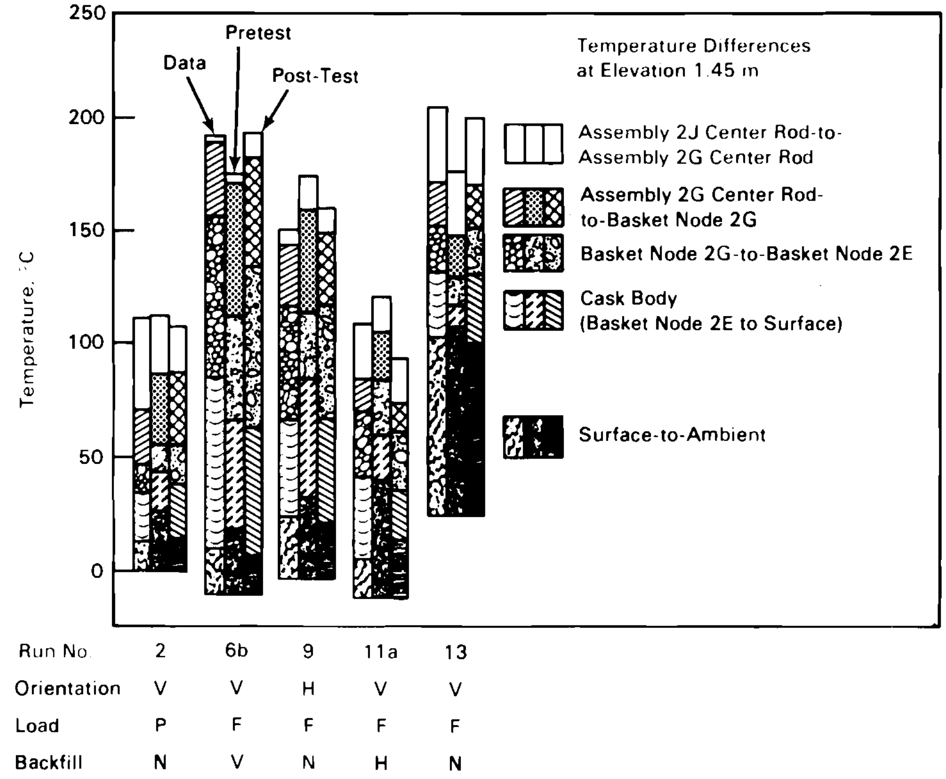

FIGURE 5.60. COBRA-SFS Pretest and Post-Test Predictions of Overall and Component Temperature Differences at 1.45 m Elevation Compared to Data

post-test predictions in Figure 5.60 show that modifications made to the cask body model have little effect on calculated cask temperature differences for the helium.

5.2.4 Parametric Studies

This section describes two separate parametic studies. In the first study, the overall sensitivity of the predicted results to fuel tube and fuel rod emissivity values is investigated. The best-estimate maximum cask decay heat loading with helium backfill is presented in the second study.

5.2.4.1 Fuel Assembly and Fuel Tube Emittances

Uncertainties of the assumed fuel rod and fuel tube emittances on the overall predicted cask heat transfer were investigated in two separate effects simulations. The sensitivity of these parameters was investigated for the full load, vertical, helium run (run 11a) by separately varying the fuel rod emittance from 0.8 to 0.6 and subsequently modifying the fuel tube emittance from 0.2 to 0.3. In each case, only a single value of emittance was changed at a time; the other emittance remained at its nominal value. Both revisions are

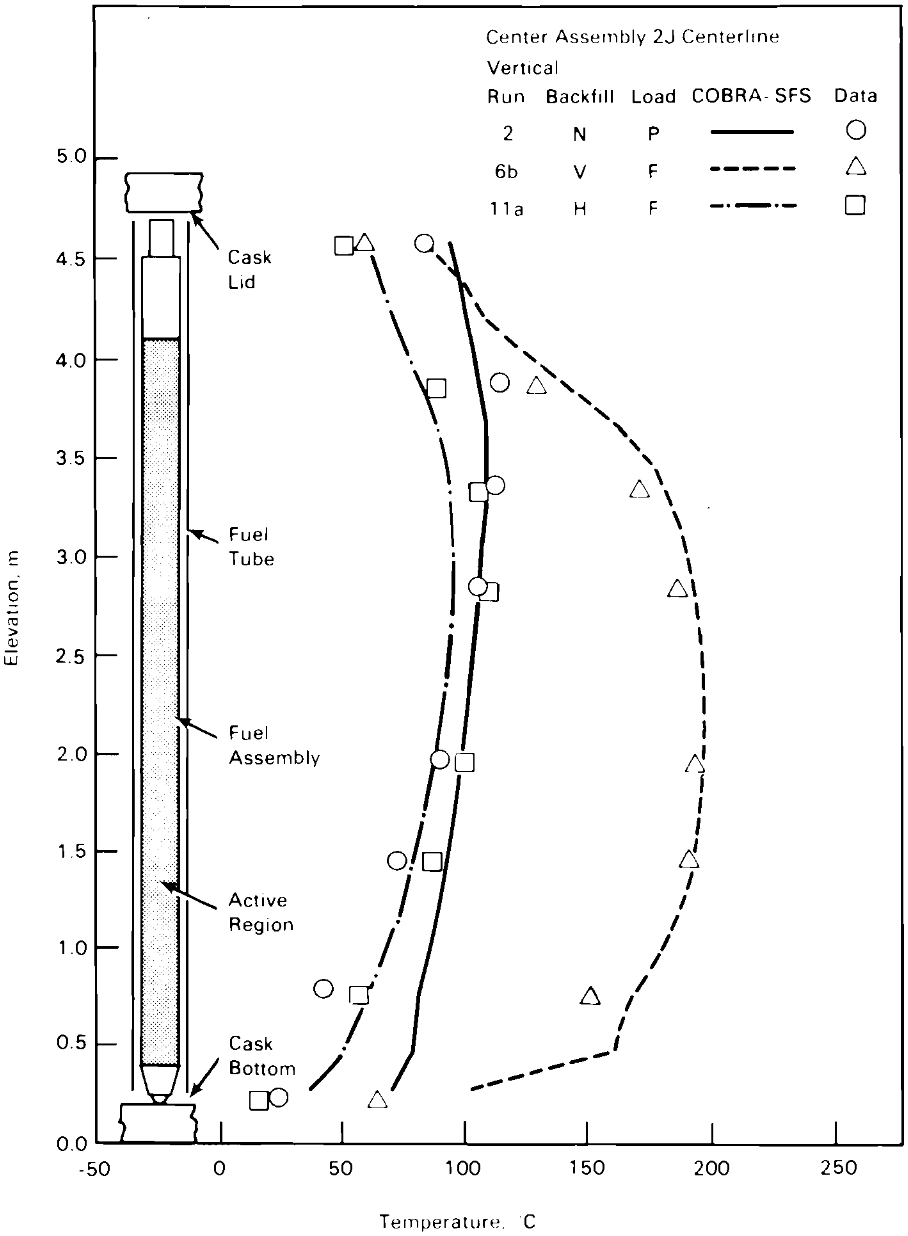

FIGURE 5.61. COBRA-SFS Post-Test Predictions of Center Assembly 2J Centerline Axial Temperature Profiles Compared to Part and Full Load, Vertical, Vacuum, Nitrogen, and Helium Data

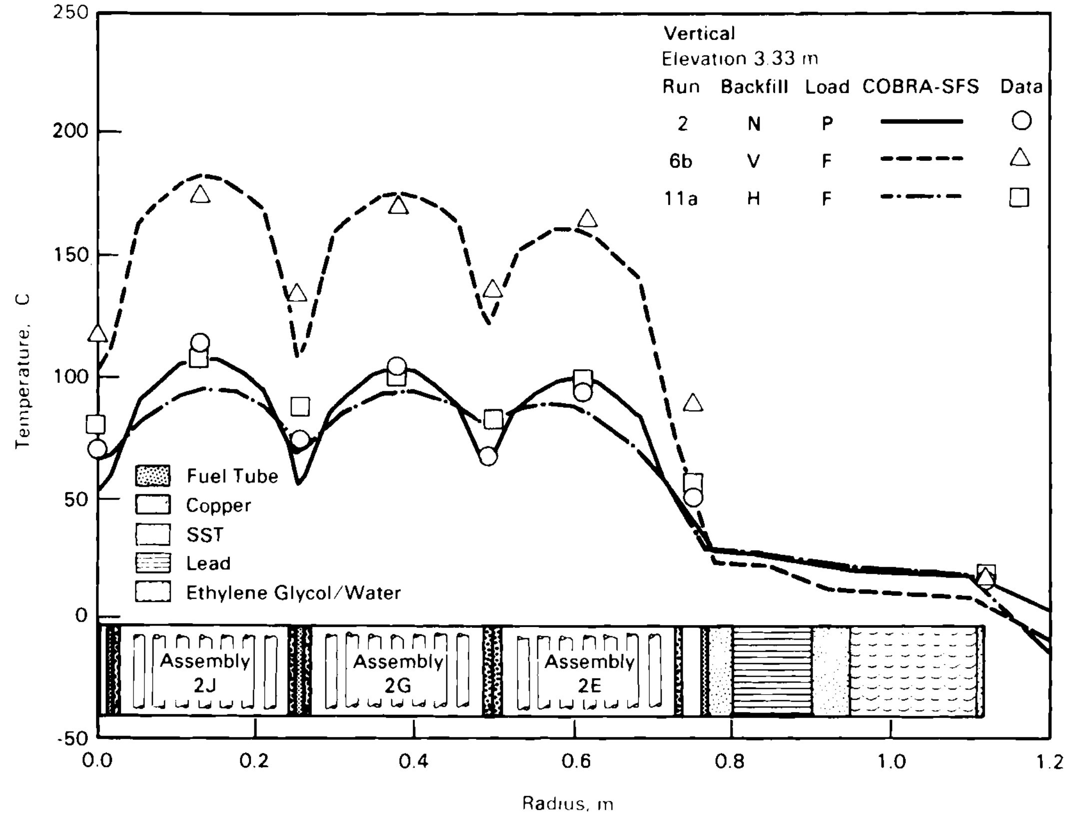

FIGURE 5.62. COBRA-SFS Post-Test Predictions of Radial (Diagonal) Temperature Profiles Compared to Part and Full Load, Vertical, Vacuum, Nitrogen, and Helium Data at 3.33 m Elevation

expected to lie within the range of emittance values for these two components and therefore can be expected to provide important information on the impact of radiation heat transfer in a helium backfill. An ambient temperature of 52°C with stagnant atmospheric conditions was assumed in this study.

The predicted radial temperature profiles for assembly 2J are presented in Figure 5.63 for the two revised sets of fuel rod/fuel tube emittance values. As can be seen, a 25% decrease in fuel rod emittance and a 50% increase in fuel tube emittance does little (13°C) to change the predicted peak cladding temperature. This is expected because the thermal resistance of the fuel assembly is small compared to the overall cask resistance.

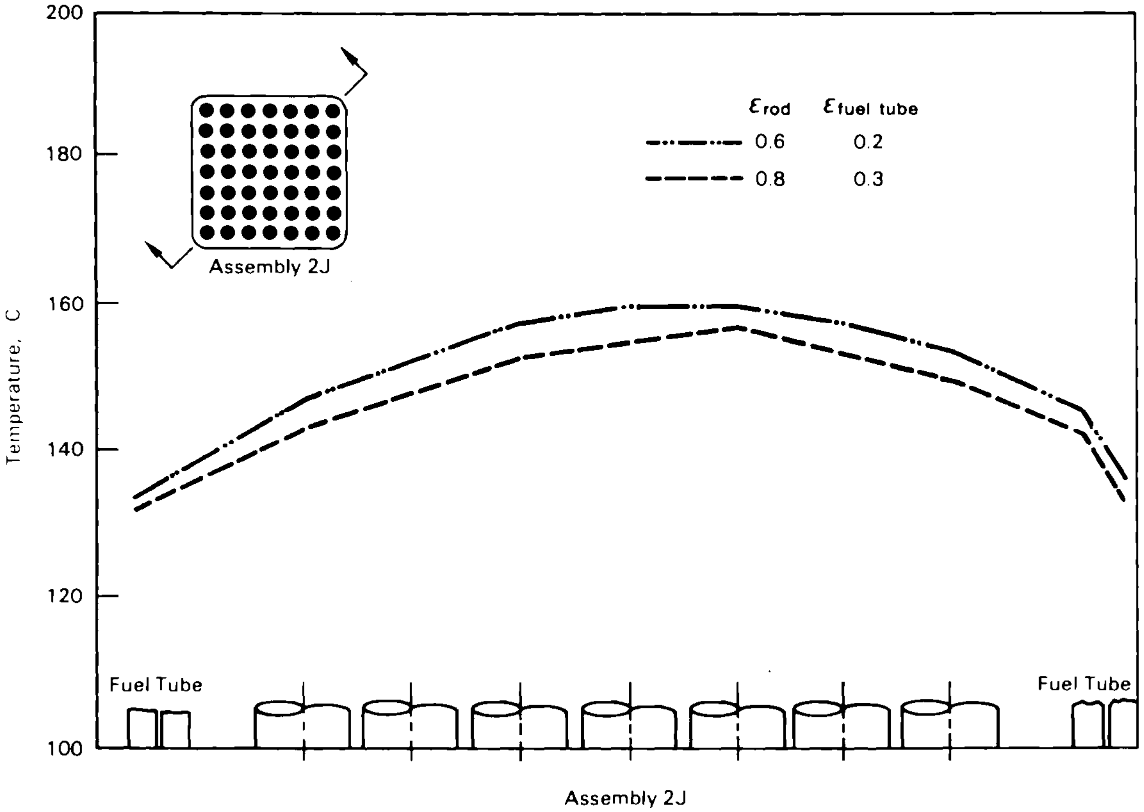

FIGURE 5.63. COBRA-SFS Predictions of Assembly 2J Radial Temperature Profiles for Various Fuel Rod and Fuel Tube Emittances at 3.33 m Elevation

5.2.4.2 Best-Estimate Maximum Cask Heat Load in Helium

The maximum cask decay heat load under licensing conditions with a helium backfill was investigated for a vertically oriented cask, again with the post-test code input and computational model refinements. The maximum heat load in the cask is limited by three constraints on the fuel and cask component temperatures:

- 380°C maximum fuel temperature
- 327°C maximum gamma shield (lead) temperature
- 148°C maximum neutron shield temperature.

The fuel temperature limit is a constraint dictated by current information regarding fuel rod cladding integrity (Johnson and Gilbert 1983). The constraint on the gamma shield is dictated by the lead melting point, 327°C. The limit on the neutron shield temperature occurs with boiling of the ethylene glycol/water mixture; the 148°C limit represents the saturation temperature of the glycol/water mixture at 50 psia (3.63 atm), the design pressure for the neutron shield.

Knowing the above temperature limits, the maximum heat rate was determined using the following conditions:

- vertical orientation
- helium backfill (P = 1.5 atm)
- uniform assembly decay heat rates
- 52°C ambient temperature
- stagnant ambient conditions.

After some iteration, the neutron shield temperature was identified as the limiting condition. A maximum, uniform heat rate of 750 W per assembly was found to approach the limit on the neutron shield temperature, but resulted in a peak fuel temperature of only 296°C. The fuel temperature limit was not reached because of the exceptional conductance of the basket with a helium backfill. Axial and radial temperature profiles for the maximum predicted heat load of 750 W per assembly are shown in Figures 5.64 and 5.65, respectively. For reference, the predictions and data for run 11a, a vertical helium case with an average loading of 290 W/assembly located outdoors, are presented with the maximum heat rate predictions. It is interesting to note that the maximum predicted heat load for helium and nitrogen backfills were identical (see Section 5.1.4.2). The added thermal benefit of a helium backfill was not observed in this study because of the thermal limit reached on neutron shield temperature. Elimination of this constraint would allow a higher heat loading with helium, as would be expected.

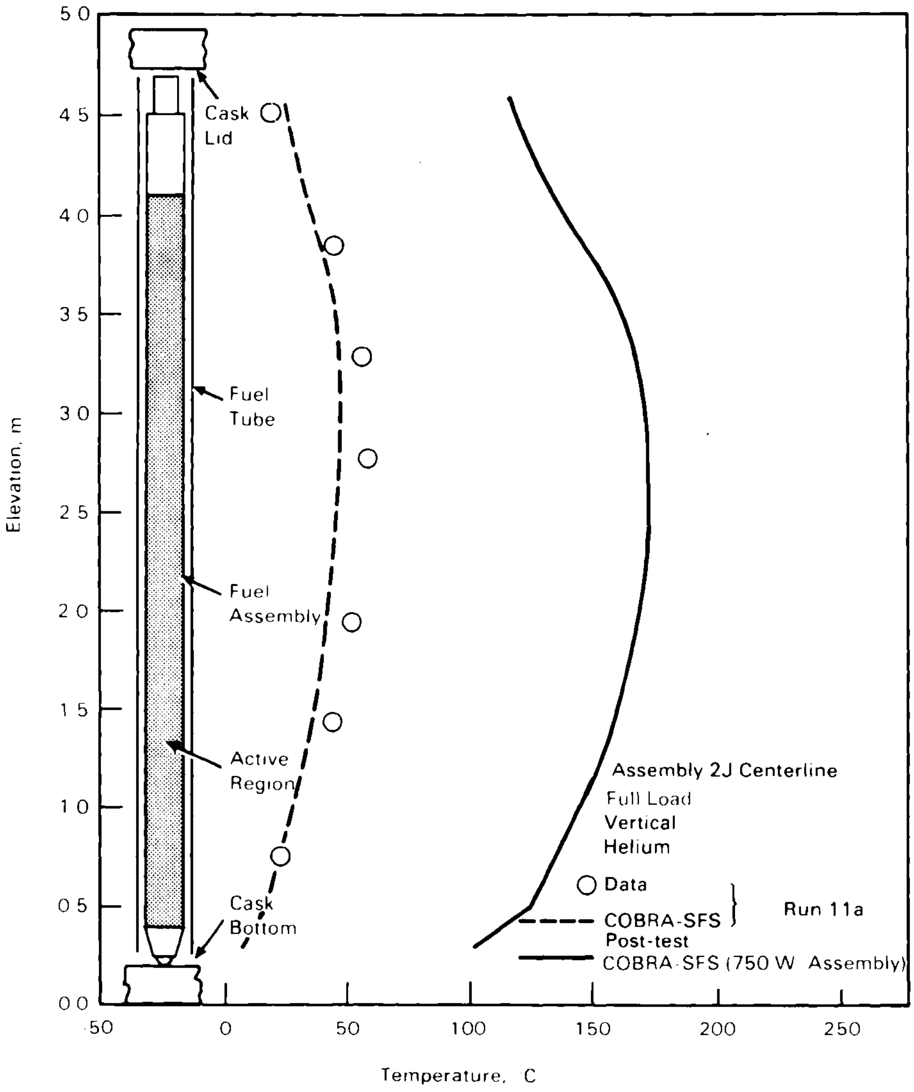

FIGURE 5.64. COBRA-SFS Prediction of Center Assembly 2J Centerline Axial Temperature Profile for 750 W/Assembly Compared to Data and Prediction of Run 11a (Full Load, Vertical, Helium)

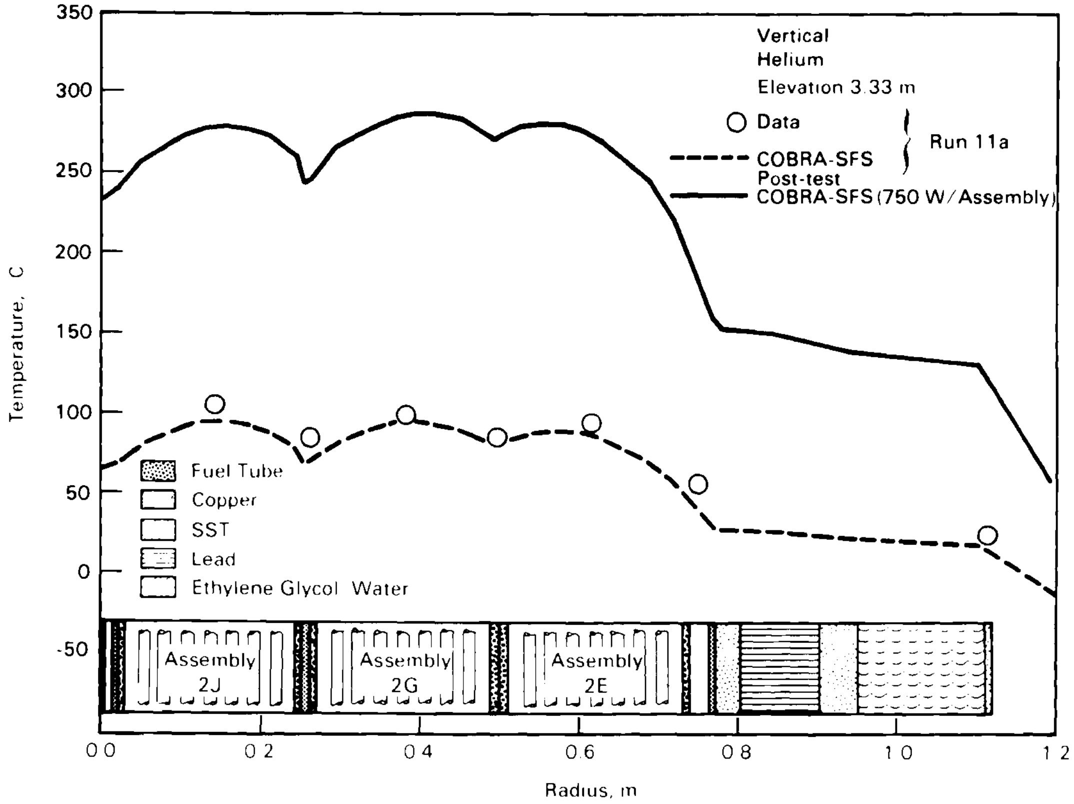

FIGURE 5.65. COBRA-SFS Prediction of Radial (Diagonal) Temperature Profile for 750 W/Assembly Compared to Data and Prediction of Run 11a (Full Load, Vertical, Helium) at 3.33 m Elevation

6.0 SHIELDING ANALYSES

In this section, shielding predictions are compared with experimental dose rate data obtained on the exterior surface of the REA 2023 cask. Included are discussions of the QAD and DOT computer codes used to perform the "pre-look" shielding analyses. The codes and their models and input are described. Because the "pre-look" predictions were in satisfactory agreement with data, no post-test analyses were performed.

6.1 QAD ANALYSIS

The QAD code was used to calculate gamma-ray dose rates on the REA cask outer surface. The code itself, along with the models and input used to describe the cask, are discussed in the following sections.

6.1.1 QAD Computer Code

The QAD-CG code (Malenfant 1967; ORNL 1977) was used to calculate gamma-ray radiation dose rates on the outer surface of the cask. The code calculates the fast-neutron and gamma-ray penetrations through various shielding configurations using the point-kernel method. The point-kernel method involves representing the source volume by a number of point isotropic sources and computing the line-of-sight distance from each of these source points to the detector points. From the distances through the shielding regions and the attenuating characteristics of the shielding materials, geometric attenuation and material attenuation are determined.

The QAD code has evolved through several stages to the version used for this analysis, QAD-CG (ORNL 1977). It contains the MORSE (Straker et al. 1970) combinatorial geometry subroutines, which permit accurate descriptions of the systems.

6.1.2 QAD Models and Input

Several models of the cask were developed during the analysis. The first model simplified the cavity volumes. The fuel assemblies were homogenized with the structural materials and the voids. This model was used for scoping predictions.

In the "best estimate" cask model, the fuel assemblies, voids, and basket structure were represented as specific regions in one quadrant of the cask. A plan view of the basket is shown in Figure 6.1. Detailed structural material was included in the model but is not shown in Figure 6.1 because it is proprietary. Two fuel tubes and some structural material adjacent to the quadrant were modeled in detail because of possible contribution to some of the radiation dose values. The fuel assemblies were assumed to be centered within each fuel tube. In the model, there was no gap between the fuel assembly and the fuel tube wall. Within each fuel assembly, the fuel pins were homogenized with the space between the pins.

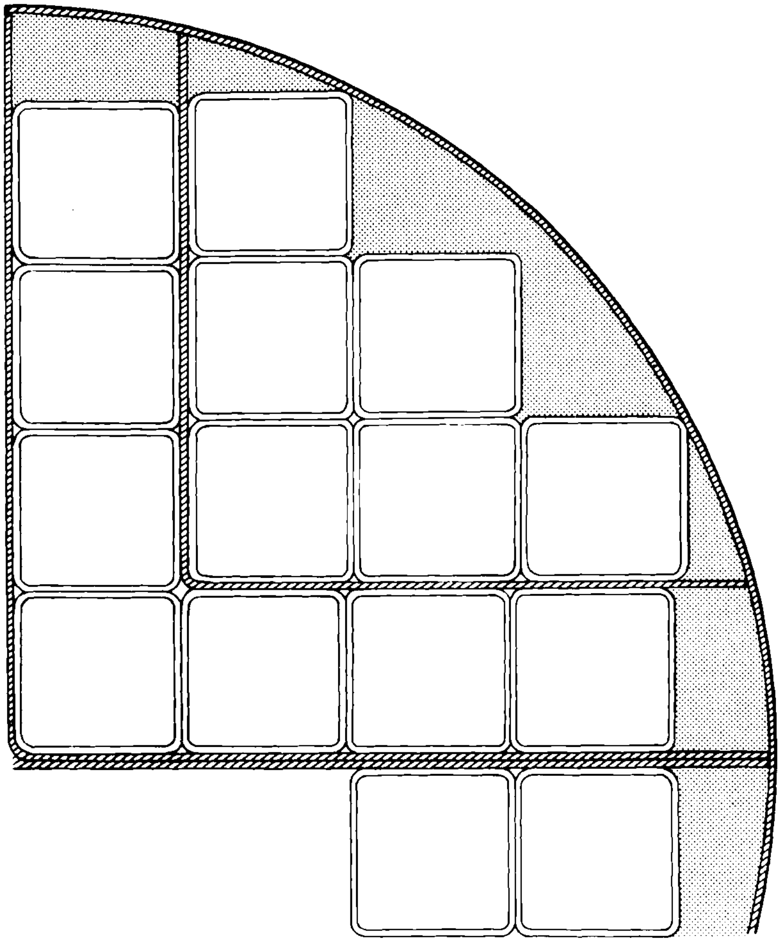

FIGURE 6.1. Detailed QAD Basket Model

In the other quadrants of the cask, 37 assemblies were represented as uniform regions of fuel, end fittings, plenum, tie plates, and lifting bails. The structural material was omitted. The R-Z model of the cask showing the axial position of these materials is shown in Figure 6.2. Gaps within the cask were ignored, as were protrusions on the surface. It was assumed that the bottom section (expansion chamber) of the neutron shield contained air. Basic cask material elemental densities are given in Table 6.1.

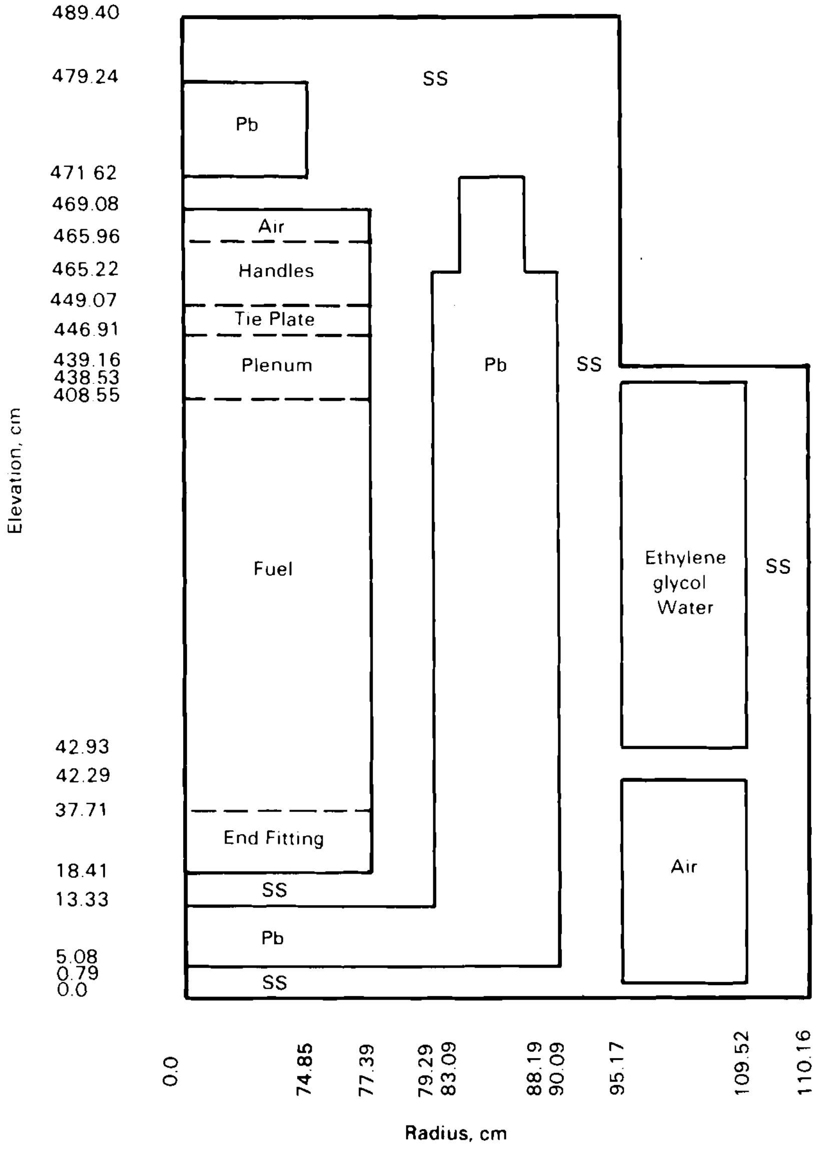

FIGURE 6.2. QAD Axial Cask Model

TABLE 6.1. QAD Material Elemental Densities, gm/cm^3

Element	Neutron Shield	Lead	Stainless Steel	Handles	Tie Plate	Plenum	End Fitting	Fuel	Copper
H	0.109								
C	0.212					0.0002		0.00035	
N			0.0104	0.0002	0.0035	0.0002	0.0013	0.00023	
O	0.732							0.2978	
Al								0.00138	
Si			0.0802	0.0014	0.0270	0.0018	0.0097		
Cr			1.5238	0.0271	0.5138	0.0395	0.1850	0.0196	
Mn			0.1604	0.0029	0.0541	0.0036	0.0195	0.0020	
Fe			5.5298	0.0983	1.8647	0.1265	0.6710	0.0699	
Ni			0.7154	0.0127	0.2412	0.0299	0.0868	0.0093	
Cu									8.92
Zr						0.9239		0.5488	
Sn						0.0150		0.0090	
Gd								0.0035	
Pb		11.34							
U								2.2118	

The description of the fuel assemblies was obtained from GE. It was assumed that the stainless steel contained 800 ppm of cobalt and the Inconel 718 contained 4694 ppm of cobalt. Densities for the fuel assemblies were specified in Section 4.0. It was assumed that each assembly contained 190.5 kg of uranium. The elemental densities used in the QAD model are also given in Table 6.1.

Neutron and photon source terms for the fuel were based on ORIGEN2 predictions (Section 4.0). Core average axial exposures from the Cooper BWR reactor were obtained for end-of-cycle 6 and 7 (EOC6 and EOC7) from GE. Average exposures for 24 equally-spaced axial nodes were provided. The relative axial exposure distribution was normalized and averaged for the two cycles to produce the composite axial burnup distribution shown in Figure 6.3. This distribution was used to determine the burnup input to ORIGEN2 in order to calculate the neutron and photon source terms in the axial direction.

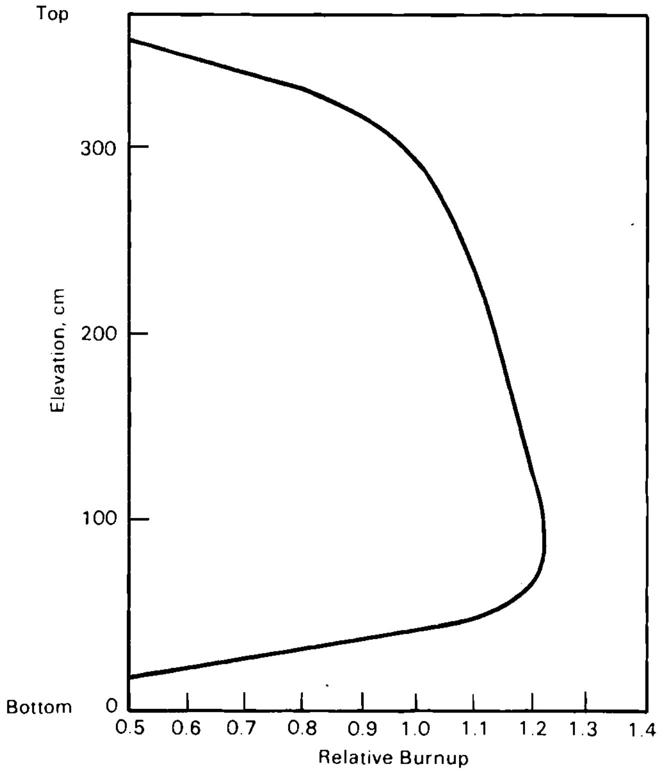

FIGURE 6.3. Cooper Fuel Assembly Average Axial Burnup Profile (Cycles 6 and 7)

The average exposure of the fuel assemblies expected to be loaded into the cask was 26,512 MWd/MTU. Assembly CZ460 had an exposure of 26,511 MWd/MTU, so the source terms calculated for it were used as an average for the cask. Photon source term values for the most important energy groups are given in Table 6.2. The shape of the source distribution in the X and Y directions was based on the assembly exposure as a function of position and is given in Table 6.3. The axial 2.25-MeV source distribution is shown in Figure 6.4 and was used as input to QAD. The specific source values used in QAD are given in Table 6.4.

In addition to the gamma rays from the fuel, there were gamma rays produced in the stainless steel and Inconel structural materials because of the

TABLE 6.2. QAD Photon Source Terms

Energy, MeV	Photons/sec/MTU	Photons/sec/Assembly
0.85	9.602 + 14	1.829 + 14
1.25	2.017 + 14	3.842 + 13
1.75	9.475 + 12	1.805 + 12
2.25	8.083 + 12	1.540 + 12
2.75	2.121 + 11	4.041 + 10
3.50	2.693 + 10	5.130 + 09

TABLE 6.3. QAD X- and Y-Direction Photon Profile

Distance from Cask Centerline, cm	Relative Value
0.0	1.04
5.0	1.04
9.0	1.03
13.0	1.02
17.0	1.01
21.0	1.00
25.0	0.99
29.0	0.98
32.8	0.98

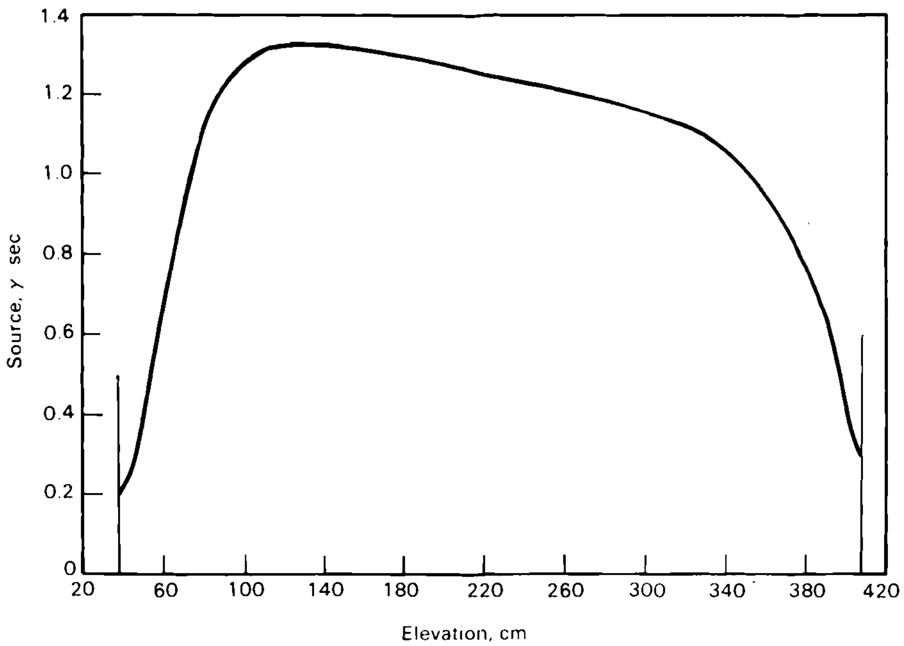

FIGURE 6.4. Fuel Assembly Axial Gamma-Ray Source Profile

TABLE 6.4. QAD Z-Direction Photon Profile

Distance from Cask Bottom, cm	Relative Value
37.71	0.22
45.0	0.31
60.0	0.68
80.0	1.10
100.0	1.27
120.0	1.32
140.0	1.32
160.0	1.30
180.0	1.29
200.0	1.27
220.0	1.24
240.0	1.22
260.0	1.21
280.0	1.19
300.0	1.16
320.0	1.12
340.0	1.05
360.0	0.95
380.0	0.78
390.0	0.64
400.0	0.42
405.0	0.32
408.55	0.28

presence of cobalt. During irradiation, neutron captures by ^{59}Co produce ^{60}Co, which has a half-life of 5.272 years. Each ^{60}Co decay results in two photons, one with an energy of 1.332 MeV and the other with an energy of 1.173 MeV.

The ^{60}Co activity was calculated with XSDRN (ORNL 1969) by modeling the fuel and the regions above and below the fuel as slab regions. Perpendicular to the slab regions is the axial direction of the core. The steam void fraction influences the neutron spectrum and, hence, the top fitting activation. The steam void fraction for the XSDRN prediction was estimated using the axial burnup distribution shown in Figure 6.3. It was assumed that the axial burnup distribution was an accurate reflection of the cycle-averaged axial power distribution. Table 6.5 shows the assumed relative power, enthalpy rise factor, and the resulting nodal average steam void fractions. The assumed inlet enthalpy was 535 Btu/lb and the assumed inlet subcooling was 30 Btu/lb, giving an average void fraction of 0.39. Above the fuel, the void fraction was assumed to be 0.742 as shown in Table 6.5.

The cobalt activations in each region of a fuel assembly are given in Table 6.6 for an exposure of 26,512 MWd/MTU. The source term is determined from the activations assuming a dose rate measurement date of September 30,

TABLE 6.5. Assumed Axial Steam Void Distribution

Node		Relative Power	Enthalphy Rise Factor	Steam Void Fraction
Bottom	1	0.420	0.035	0.00
	2	1.072	0.124	0.050
	3	1.221	0.226	0.130
	4	1.221	0.328	0.211
	5	1.192	0.427	0.289
	6	1.165	0.524	0.366
	7	1.131	0.618	0.440
	8	1.111	0.711	0.513
	9	1.072	0.800	0.584
	10	1.013	0.885	0.651
	11	0.859	0.956	0.707
Top	12	0.523	1.000	0.742

Inlet Enthalpy: 535 Btu/lb
Inlet Subcooling: 30 Btu/lb
Average Steam Void Fraction: 0.390

1984. With a half-life of 5.272 years, a significant amount of the ^{60}Co has decayed away by the measurement date. The photon source for each of the two energies is given in Table 6.6.

Activation rates as a function of axial position within each region were also calculated with XSDRN. Normalized values used in QAD are given in Table 6.7. Assembly exposures vary by only 16% from the minimum to the maximum (8% in the first quadrant). Because the gamma-ray sources are nearly linear with exposure, the variation among assemblies is about 15%. To simplify modeling the system, a flat source distribution was used in the X-Y plane.

TABLE 6.6. Cobalt Activation Photon Sources

Region	^{60}Co Activation per kg of SS and Inconel	Partial Cask Source, γ/sec	Full Cask Source, γ/sec
End fittings	8.2 + 19	1.66 + 13	3.09 + 13
Plenum	7.0 + 20	5.8 + 13	1.07 + 14
Tie plate	1.7 + 20	1.09 + 13	2.03 + 13
Handles	1.3 + 20	3.32 + 12	6.18 + 12

TABLE 6.7. QAD Axial Photon Source Profiles

Plenum		Tie Plate	
Elevation, cm	Relative Value	Elevation, cm	Relative Value
408.55	1.23	446.91	1.10
413.00	1.306	447.99	1.00
420.00	1.23	449.07	0.90
430.00	0.99		
440.00	0.72		
446.91	0.52		

Handles		End Fitting	
Elevation, cm	Relative Value	Elevation, cm	Relative Value
449.07	1.31	18.41	0.14
452.00	1.26	25.00	0.43
456.00	1.07	30.00	1.00
460.00	0.88	34.00	1.82
463.00	0.75	37.71	2.62
465.96	0.65		

6.2 DOT ANALYSIS

The DOT code was used to calculate neutron dose rates on the cask outer surface. DOT and the models and input used to describe the cask are discussed in the following sections.

6.2.1 DOT Computer Code

The DOT code (Rhoades and Childs 1982) calculates neutron and photon particle fluxes in two dimensions using the method of discrete ordinates to solve the Boltzmann transport equation. Balance equations are solved for the flow of particles moving in a set of discrete directions in each cell of a space mesh and in each group of a multigroup energy structure. Mesh spacings and discrete directions are selected by the user. Anisotropic cross sections can be expressed in a Legendre expansion of arbitrary order.

The DLC-85 library (Ford et al. 1980) was used for this cask analysis. It is a coupled neutron/photon library with P3 cross sections. The neutron cross sections are represented in 22 energy groups; the photon cross sections are represented in 21 energy groups.

6.2.2 DOT Models and Input

The cask was modeled using R-Z geometry. Because of the large number of cells needed to describe the cask in the axial direction, the top half and the bottom half of the cask were set up as two separate problems as shown in Figures 6.5 and 6.6, respectively. The fuel and structural material were modeled as a homogeneous mixture. Likewise, the end fitting, plenum, tie plate, and lifting bail regions were modeled as homogeneous mixtures with the structural material.

The expansion chamber of the neutron shield was assumed to contain air rather than ethylene glycol/water. An air region of thickness 5.08 cm (2 in.) surrounding the cask was included in the model so the dose could be obtained

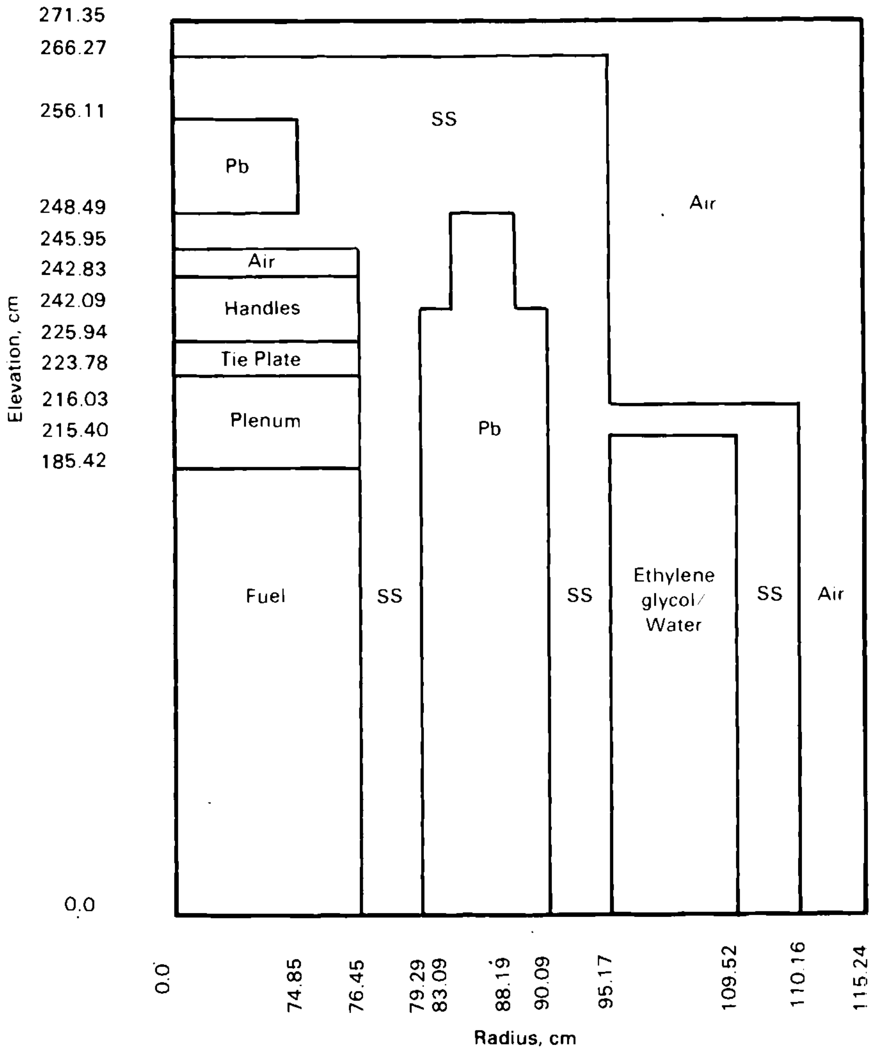

FIGURE 6.5. DOT Axial Cask Model (Top Half)

2.54 cm (1 in.) from the cask. The material atom densities or volume fractions are given in Table 6.8, depending on whether microscopic or macroscopic cross sections were used from the DLC-85 library.

To model the partially loaded cask, the fuel region was subdivided into annuli as shown in Figure 6.7. The first annulus (innermost) represents

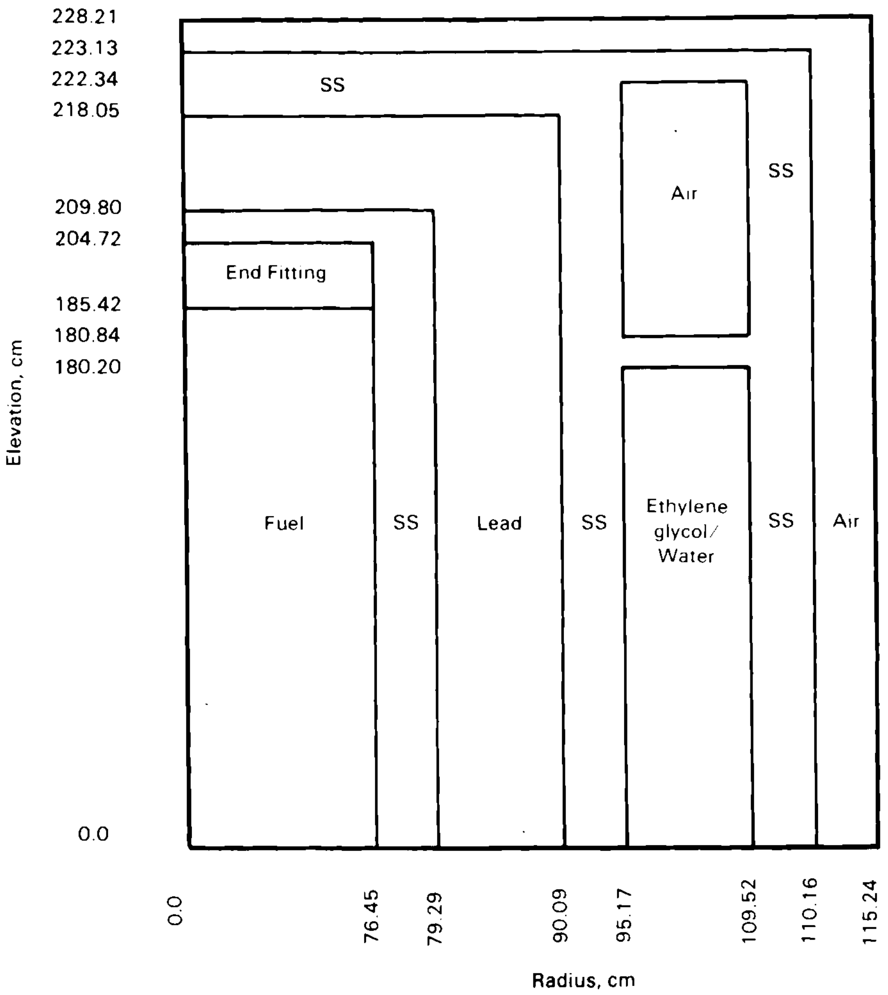

FIGURE 6.6. DOT Axial Cask Model (Bottom Half)

16 fuel assemblies. The second annulus represents 12 empty fuel tubes. The third annulus represents 12 fuel assemblies, and the fourth annulus represents 12 empty fuel tubes.

The flux-to-dose rate (mrem/hr per particle/cm^2/sec) conversion factors (ANSI 1977) were calculated with the DOSE code, which is a module in the AMPX

TABLE 6.8. DOT Material Atom Densities or Volume Fractions

Region Description	Material	Atom Density, a/b-cm	Volume Fraction
Fuel	UO_2		0.1506
	SS		0.1624
	Zr	2.135 -3	
Ethylene glycol/water	C	1.019 -2	
	O	2.640 -2	
	H	6.300 -2	
Plenum	Zr	4.072 -3	
	SS		0.1789
Tie plate	SS		0.3842
Handles	SS		0.1741
Lead	Pb	3.296 -2	
End fitting	Zr	7.82 -4	
	SS		0.2422
Empty tubes	SS		0.1624

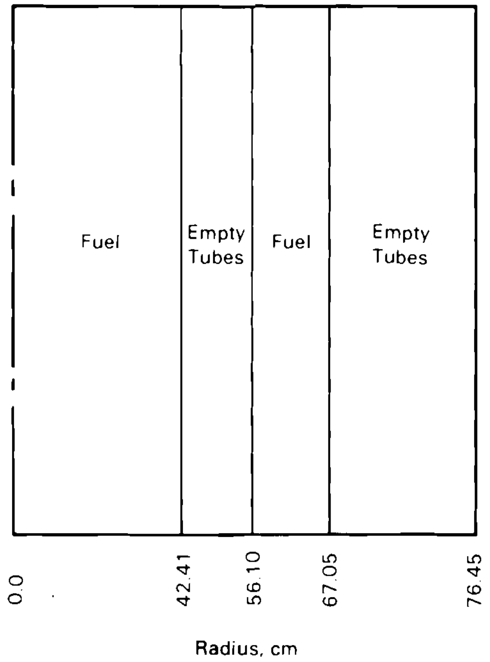

FIGURE 6.7. DOT Radial Geometry Model for Partially Loaded Cask

system (ORNL 1978). The code calculates conversion factors based on ANS Standard 6.1.1-1977. Values for the 22 neutron groups and 21 gamma ray groups are shown in Table 6.9.

Neutron source strength and spatial distributions were based on ORIGEN2 predictions of axial burnup distributions shown in Figure 6.3. The source strength increases rapidly with exposure as shown in Figure 6.8. Consequently, axial neutron source distributions are much more peaked than are exposure distributions. The relative axial distribution for assembly CZ346 is shown in Figure 6.9. Although CZ346 was the highest exposure assembly, axial distributions for all the assemblies were assumed to be the same. The input to DOT was based on assembly CZ346.

TABLE 6.9. DOT Flux-to-Dose Rate Conversion Factors

Neutrons		Gamma Rays	
Group No.	Factor	Group No.	Factor
1	0.19706	23	1.1020 -2
2	0.15977	24	8.7716 -3
3	0.14706	25	7.6626 -3
4	0.14769	26	6.9265 -3
5	0.15334	27	6.1909 -3
6	0.15069	28	5.4136 -3
7	0.13896	29	4.6221 -3
8	0.12849	30	3.9596 -3
9	0.12527	31	3.4686 -3
10	0.12633	32	2.9270 -3
11	0.12895	33	2.3156 -3
12	0.11681	34	1.7536 -3
13	0.065235	35	1.3082 -3
14	0.0091964	36	9.2798 -4
15	0.0037133	37	5.6676 -4
16	0.0040083	38	3.2767 -4
17	0.0042943	39	2.6816 -4
18	0.0044729	40	2.7185 -4
19	0.0045658	41	4.1154 -4
20	0.0044782	42	8.2668 -4
21	0.0042781	43	2.1439 -3
22	0.0037142		

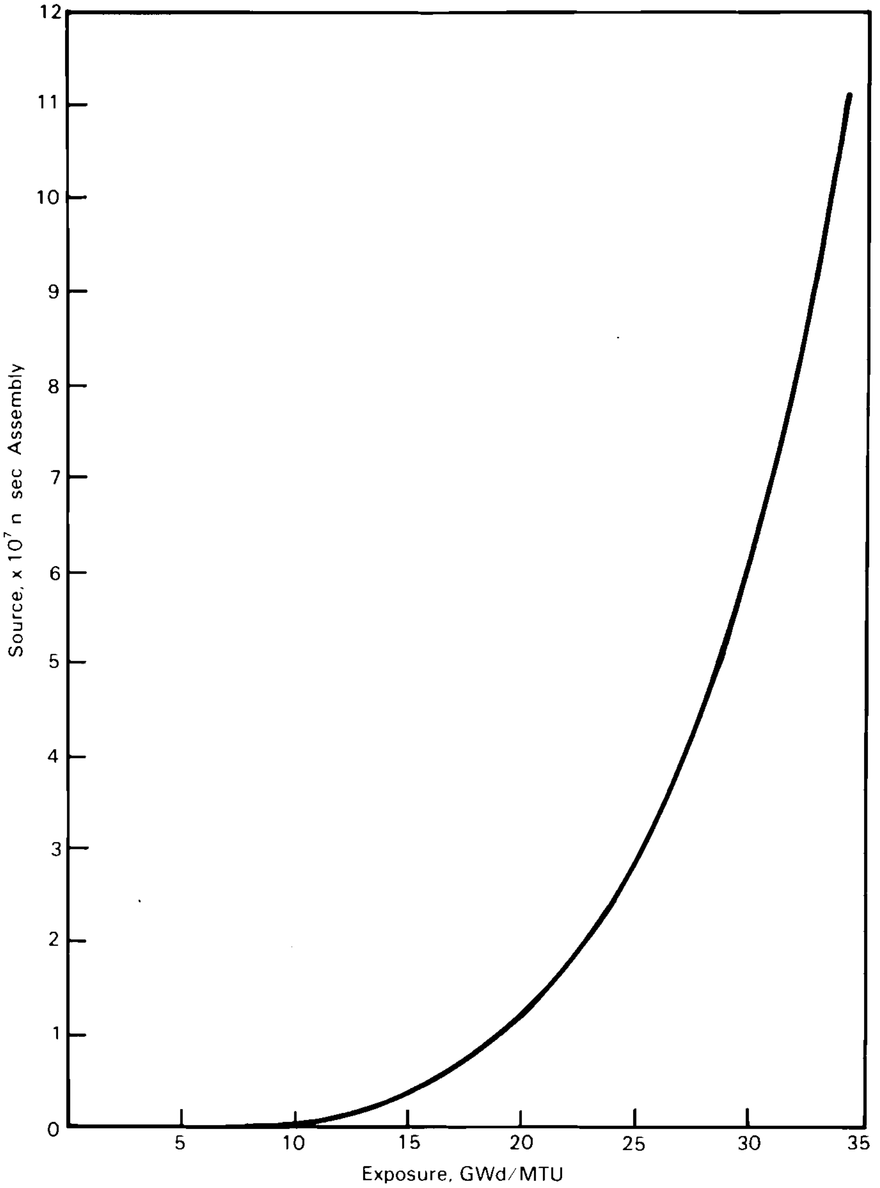

FIGURE 6.8. Fuel Assembly Neutron Source Strength as a Function of Exposure

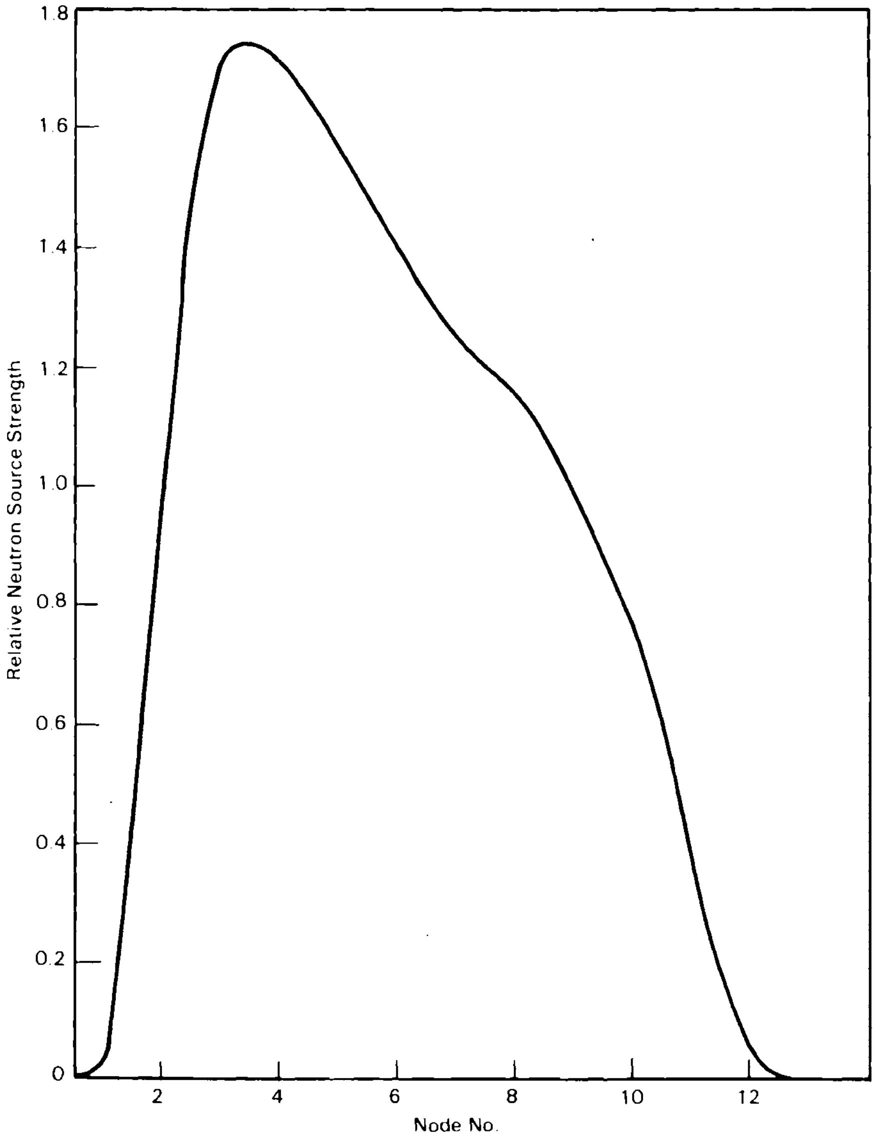

FIGURE 6.9. Fuel Assembly Relative Axial Neutron Distribution

The radial neutron source shape was based on a curve drawn through the assembly source strengths plotted as a function of distance from the center of the cask. The unnormalized curve is shown in Figure 6.10.

The absolute neutron source strength for each DOT prediction was based on ORIGEN2 values calculated for each assembly in the cask as shown in Table 6.10, and on the fraction of neutrons in each half of the assembly as determined by the ORIGEN2 axial runs for assembly CZ346. The value of the fraction of neutrons for the top half of the cask is 0.383. For the bottom half of the cask the fraction is 0.617. The neutron source strengths for the four DOT predictions are summarized in Table 6.11.

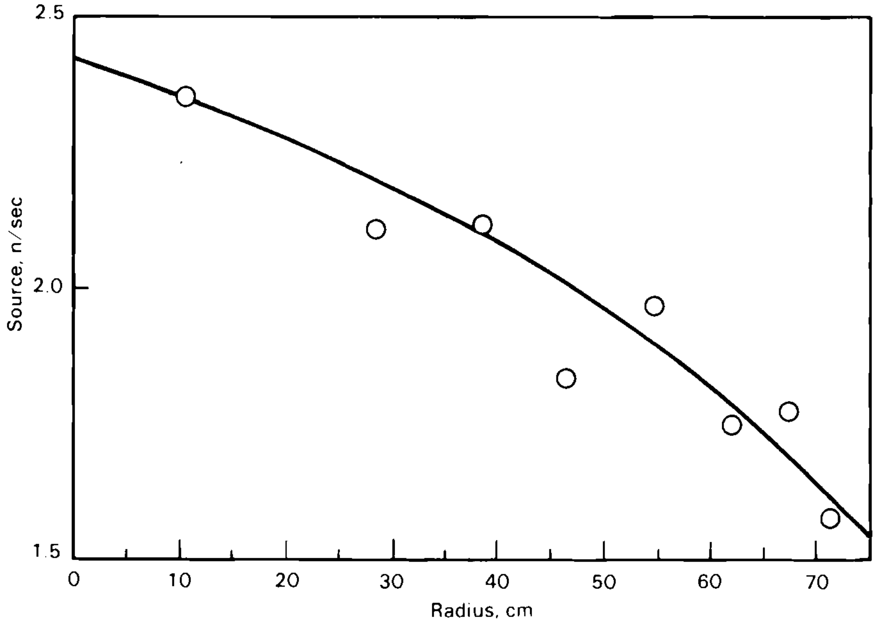

FIGURE 6.10. Cask Radial Neutron Source Profile

TABLE 6.10. Cooper Fuel Assembly Neutron Source Terms (July 1, 1984)

First Quadrant		Second Quadrant		Third Quadrant		Fourth Quadrant	
Assembly	n/sec/MTU	Assembly	n/sec/MTU	Assembly	n/sec/MTU	Assembly	n/sec/MTU
CZ209(a)	1.566 +8	CZ346(a)	2.500 +8	CZ302(a)	1.810 +8	CZ264(a)	1.762 +8
CZ296(a)	1.744 +8	CZ182(a)	2.047 +8	CZ222(a)	2.030 +8	CZ308(a)	1.694 +8
CZ398(a)	2.296 +8	CZ211(a)	1.823 +8	CZ526(a)	2.322 +8	CZ369(a)	1.994 +8
CZ531(a)	2.018 +8	CZ337(a)	2.038 +8	CZ416(a)	2.244 +8	CZ430(a)	2.055 +8
CZ246(a)	2.276 +8	CZ311(a)	2.205 +8	CZ348(a)	2.279 +8	CZ148(a)	1.713 +8
CZ498(a)	1.964 +8	CZ355(a)	1.964 +8	CZ379(a)	1.710 +8	CZ239(a)	2.191 +8
CZ259(a)	1.752 +8	CZ277(a)	1.756 +8	CZ147(a)	1.832 +8	CZ429(a)	2.346 +8
CZ433	1.630 +8	CZ318	1.898 +8	CZ508	1.890 +8	CZ372	1.593 +8
CZ351	1.684 +8	CZ315	2.045 +8	CZ197	1.152 +8	CZ286	2.129 +8
CZ542	1.965 +8	CZ415	1.597 +8	CZ472	1.798 +8	CZ545	1.937 +8
CZ357	2.125 +8	CZ460	1.907 +8	CZ468	1.991 +8	CZ536	1.808 +8
CZ515	1.563 +8	CZ342	2.106 +8	CZ466	1.760 +8	CZ205	1.625 +8
CZ225	1.720 +8	CZ528	1.557 +8	CZ195	1.731 +8	CZ473	1.885 +8

(a) These assemblies were used in the partial cask loading.

TABLE 6.11. Neutron Source Strengths

Position	Source, n/sec	
	Partial Load	Full Load
Top Half	3.94 +8	7.08 +8
Bottom Half	6.34 +8	11.41 +8

6.3 SHIELDING PREDICTIONS COMPARED TO DATA

QAD and DOT dose rate "pre-look" predictions are compared to experimental data in the following sections. Because "pre-look" predictions compared favorably with the data, no post-test predictions were performed.

6.3.1 Neutron Dose Rates

Neutron dose rate measurements made by PNL and GE with portable instruments for the partially loaded cask are given in Volume I of this report

(McKinnon et al. 1986a). Predicted neutron dose rates for the partially loaded cask are compared to the measured data in Figures 6.11 through 6.13. On the top of the cask (Figure 6.11), predicted dose rates are a factor of 2 higher than the PNL measurement, but somewhat lower than GE measurements. At a radius of 96 cm, the predicted value is a factor of 3 lower than the GE measurement. On the bottom of the partially loaded cask, predicted dose rates are a factor

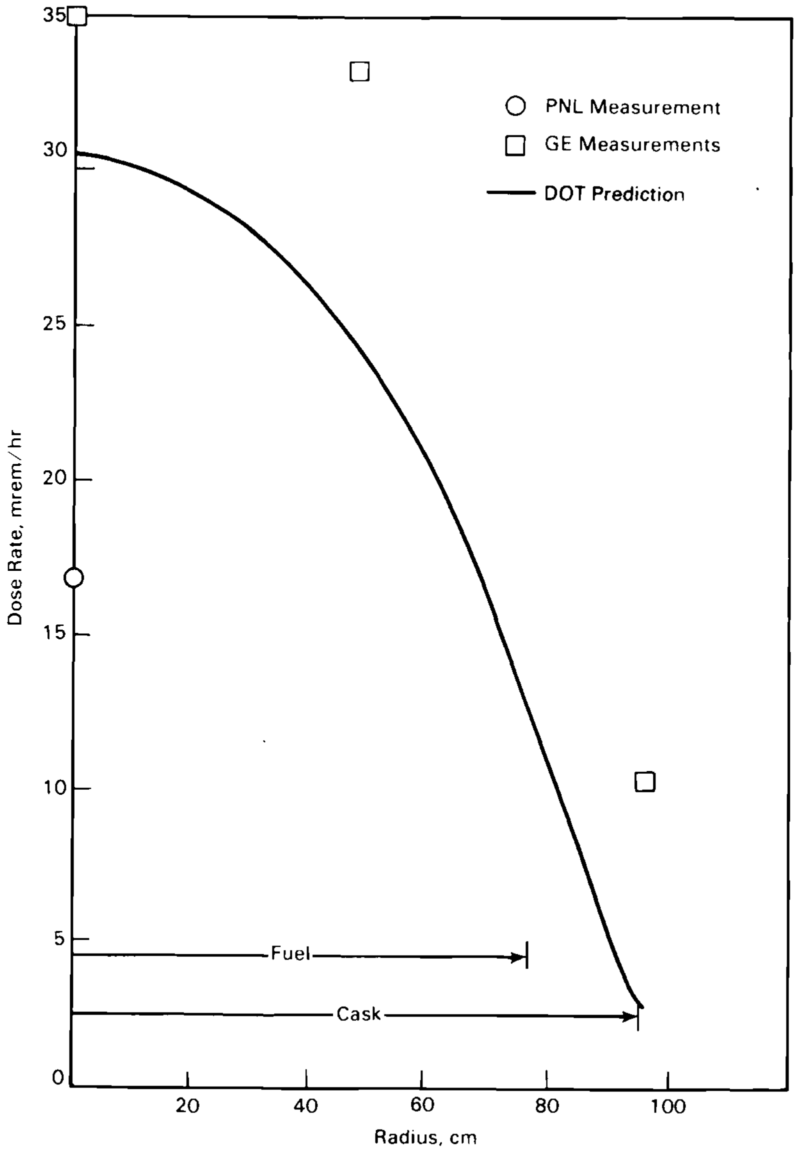

FIGURE 6.11. Neutron Dose Rates on Top of Partially Loaded Cask

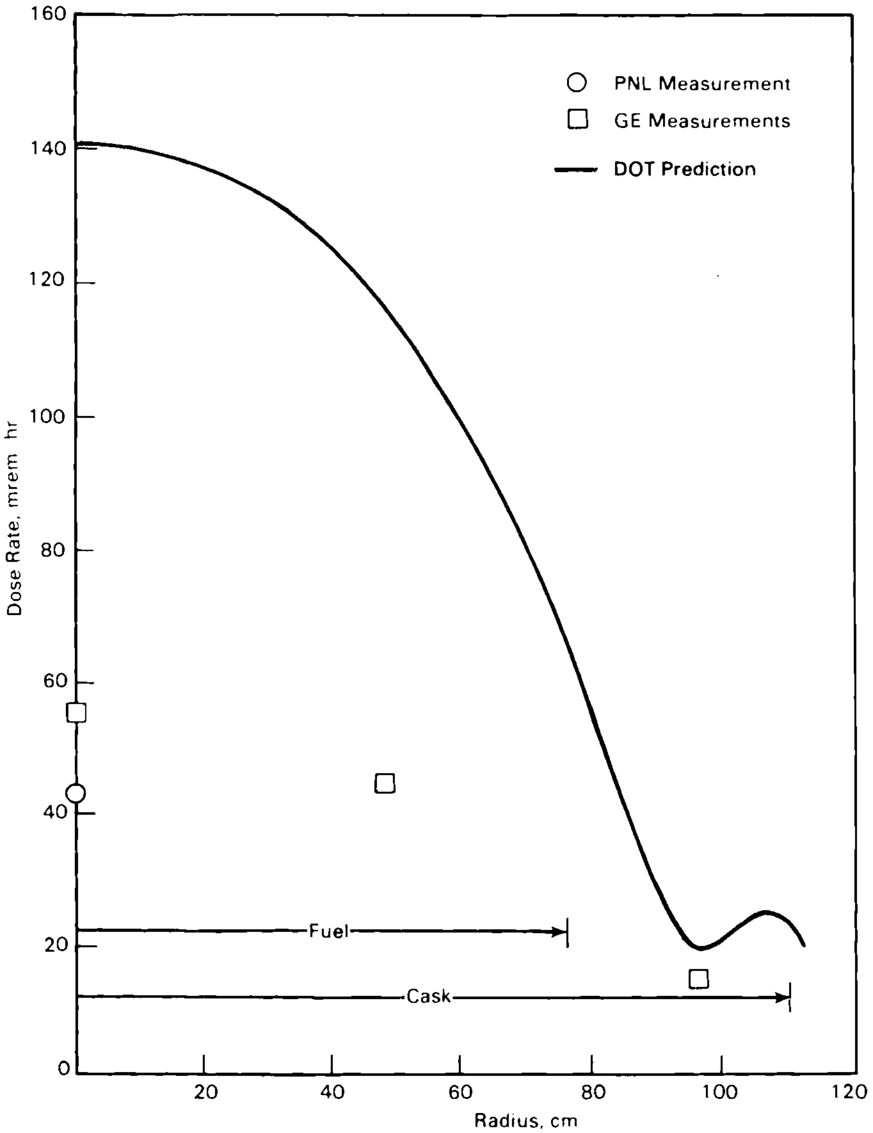

FIGURE 6.12. Neutron Dose Rates on Bottom of Partially Loaded Cask

of 3 higher than measured data directly below the fuel assemblies (Figure 6.12). At a radius of 96 cm, predicted values agree reasonably well with measured data.

Dose rates on the side of the partially loaded cask peak just above and just below the neutron shield (Figure 6.13). Above the neutron shield, calculated dose rates are a factor of 3 higher than experimental data. Below the

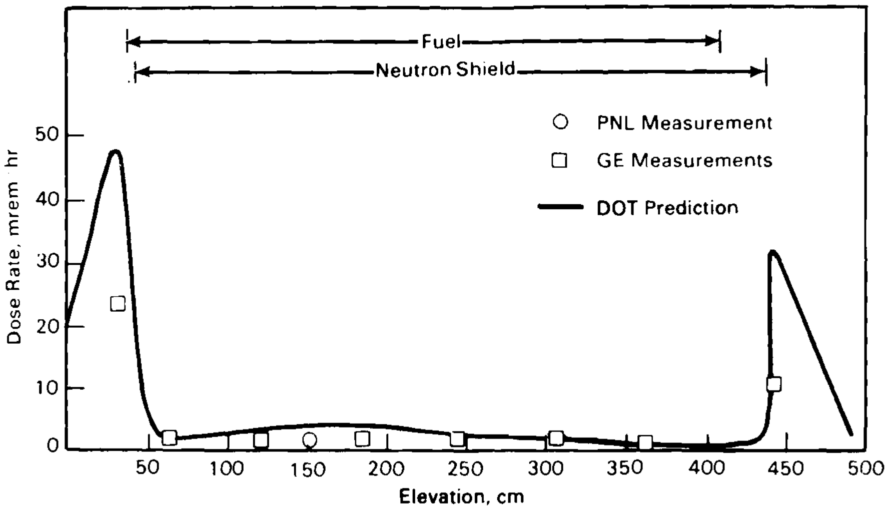

FIGURE 6.13. Neutron Dose Rates on Side of Partially Loaded Cask

shield expansion chamber. Predicted dose rates through the neutron shield are high over the bottom half of the fuel, but are in good agreement over the top half of the fuel. This effect would suggest that the axial neutron source profile used in DOT may be incorrect.

Predicted dose rates on top of the fully loaded REA cask are compared with measured values from Volume I (McKinnon et al. 1986a) in Figure 6.14. Predicted dose rates agree quite well with GE measurements directly above the fuel. At the edge of the cask, predicted dose rates are in good agreement with PNL measurements. In general, predicted dose rates decrease along the radius more than the PNL or GE measurements indicate.

Comparisons of results on the bottom of the cask are shown in Figure 6.15. PNL and GE measurements are in good agreement with each other. Predicted dose rates are a factor of 3 or 4 higher than measurements.

Figure 6.16 shows comparisons of results on the side of the cask. The predicted dose rate peaks are a factor of 3 higher than the measurements. neutron shield, predicted dose rates are a factor of 2 higher than data; however, it is unknown how much ethylene glycol/water there was in the neutron

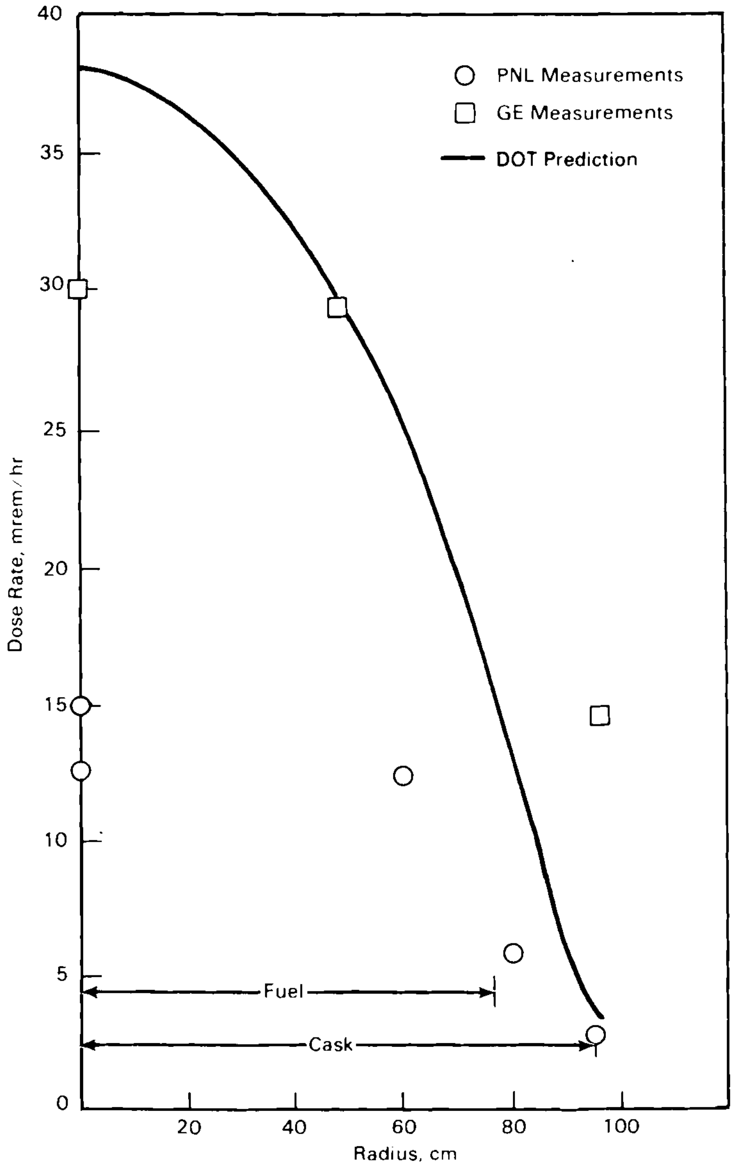

FIGURE 6.14. Neutron Dose Rates on Top of Fully Loaded Cask

Within the major peaks at each end of the neutron shield, there appear to be secondary peaks. These secondary peaks are not predicted by DOT. At the bottom of the fuel, predicted dose rates are a factor of 3 higher than the data. At the top of the fuel, predicted dose rates are in agreement with measured data. Again, this effect may be due to an inaccurate axial neutron source distribution.

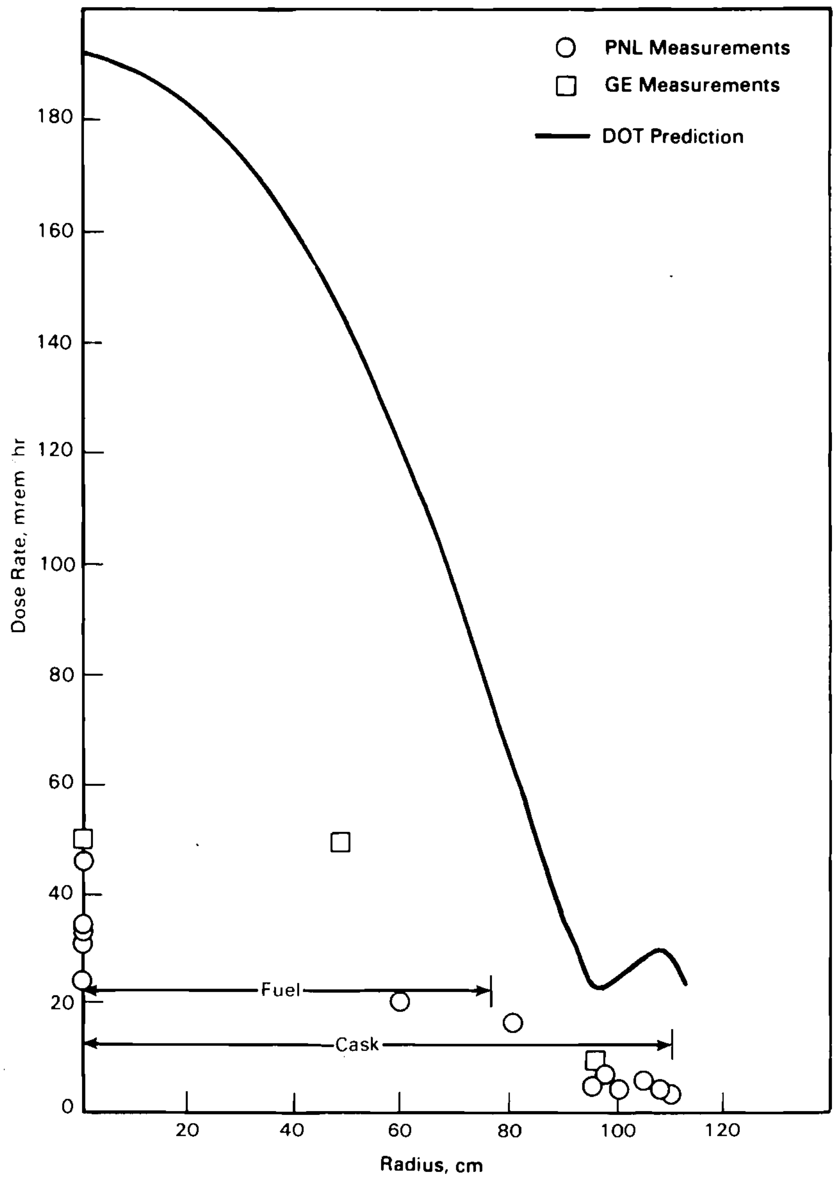

FIGURE 6.15. Neutron Dose Rates on Bottom of Fully Loaded Cask

Comparisons of DOT dose rate predictions with measured dose rates on a fully loaded cask are summarized in Table 6.12. On the side of the cask, the average difference between predictions and measurements is +15.8 mrem/hr (predictions were greater than measurements) with a standard deviation of ±13.1 mrem/hr. Predictions were, on the average, approximately four times

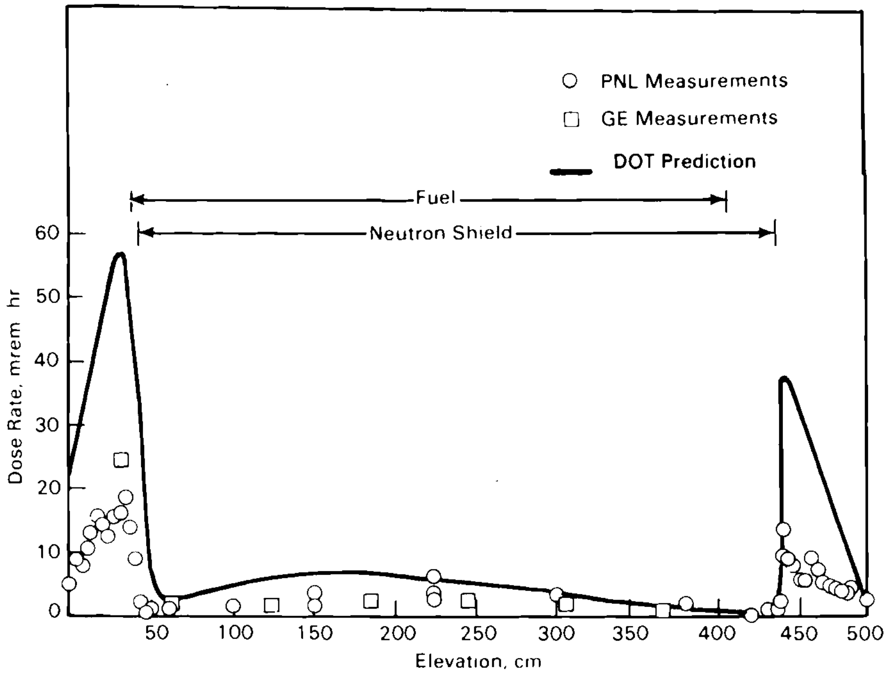

FIGURE 6.16. Neutron Dose Rates on Side of Fully Loaded Cask

higher than measured values. On the top of the cask, the average difference is +11.6 mrem/hr with a standard deviation of ±9.0 mrem/hr. Predicted neutron dose rates averaged approximately two times higher than data. On the bottom of the cask, the average difference is +75.1 mrem/hr with a standard deviation of ±66.2 mrem/hr, and predictions were approximately six times measurements. Overall, the average difference between predicted and measured dose rates is +26.6 mrem/hr with a standard deviation of ±30.8 mrem/hr. Also, predictions were, on the average, four times higher than data.

In summary, predicted neutron dose rates on the ends of the fully loaded cask and the side of the cask where there is no neutron shield are a factor of approximately 2 to 6 higher than experimental data. On the side of the cask where there is neutron shielding, calculated neutron dose rates are approximately a factor of 2 higher than data. Differences between calculated and measured neutron dose rates could be due to any or all of the following three items: 1) inaccurate modeling of the cask; 2) incorrect neutron cross

TABLE 6.12. Comparisons of Predicted Neutron Dose Rates with Data for Fully Loaded Cask

Elevation, cm	Angle, degrees	Side of Cask, mrem/hr Measured	Predicted	Pred-Meas	Pred/Meas
0.00	26.5	5.0	24.7	19.7	4.9
3.33	26.5	8.8	28.5	19.7	3.2
6.67	26.5	7.7	32.0	24.3	4.2
10.00	26.5	10.7	34.5	23.8	3.2
13.33	26.5	12.8	38.5	25.7	3.0
16.67	26.5	15.0	43.0	28.0	2.9
20.00	26.5	14.3	47.0	32.7	3.3
23.33	26.5	12.5	51.0	38.5	4.1
26.67	26.5	15.6	55.0	39.4	3.5
30.00	26.5	16.2	56.6	40.4	3.5
33.33	26.5	18.7	57.0	38.3	3.0
36.67	26.5	14.2	50.0	35.8	3.5
40.00	26.5	9.2	37.0	27.8	4.0
43.33	26.5	2.1	29.0	26.9	13.8
46.67	26.5	0.4	11.0	10.6	27.5
50.00	26.5	1.2	6.5	5.3	5.4
60.00	26.5	1.5	3.0	1.5	2.0
100.00	26.5	1.5	5.0	3.5	3.3
150.00	26.5	3.4	6.8	3.4	2.0
223.10	0.0	3.8	6.0	2.2	1.6
223.10	4.0	3.6	6.0	2.4	1.7
223.10	26.5	6.2	6.0	-0.2	1.0
223.10	41.0	2.8	6.0	3.2	2.1
223.10	45.0	2.6	6.0	3.4	2.3
300.00	26.5	3.2	4.1	0.9	1.3
380.00	26.5	1.7	1.2	-0.5	0.7
420.00	26.5	0.6	0.6	0.0	1.0
430.00	26.5	0.9	1.2	0.3	1.3
433.33	26.5	0.9	1.9	1.0	2.1
436.67	26.5	1.5	5.0	3.5	3.3
440.00	26.5	9.3	36.8	27.5	4.0
443.33	26.5	8.8	37.0	28.2	4.2
446.67	26.5	7.9	34.5	26.6	4.4
450.00	26.5	6.0	32.2	26.2	5.4
453.33	26.5	6.0	29.8	23.8	5.0
456.67	26.5	8.7	27.0	18.3	3.1
460.00	26.5	7.0	24.3	17.3	3.5
463.33	26.5	5.1	22.0	16.9	4.3
466.67	26.5	4.8	19.2	14.4	4.0
470.00	26.5	4.3	16.5	12.2	3.8
473.33	26.5	3.9	14.0	10.1	3.6
476.67	26.5	3.4	11.5	8.1	3.4
480.00	26.5	4.6	9.0	4.4	2.0
490.00	26.5	2.1	2.5	0.4	1.2
			Average:	+15.8	3.9
			Standard Deviation:	±13.1	±4.1

TABLE 6.12. (contd)

Elevation, cm	Angle, degrees	Top of Cask, mrem/hr			Pred/Meas
		Measured	Predicted	Pred-Meas	
0.0	45	12.6	38.1	25.5	3.0
60.0	45	12.3	25.1	12.8	2.0
80.0	45	5.8	12.9	7.1	2.2
95.0	45	2.7	3.7	1.0	1.4
			Average:	+11.6	2.2
			Standard Deviation:	±9.0	±0.6

Elevation, cm	Angle, degrees	Bottom of Cask, mrem/hr			Pred/Meas
		Measured	Predicted	Pred-Meas	
0.0	45	32.8	192.0	159.2	5.9
0.0	135	29.8	192.0	162.2	6.4
0.0	225	34.2	192.0	157.8	5.6
0.0	315	23.7	192.0	168.3	8.1
80.0	45	15.5	65.0	49.5	4.2
95.0	45	4.5	23.3	18.8	5.2
97.5	45	6.0	22.6	16.6	3.8
100.0	45	4.0	24.2	20.2	6.1
105.0	45	5.3	28.0	22.7	5.3
107.5	45	3.6	29.0	25.4	8.1
110.0	45	2.6	27.5	24.9	10.6
			Average:	+75.1	6.3
			Standard Deviation:	±66.2	±1.9
			Overall Average:	+26.6	4.2
			Overall Standard Deviation:	±30.8	±3.7

sections; and/or 3) incorrect axial neutron source strength profiles. The last item is probably responsible for the greatest part of the difference between predictions and measurements.

6.3.2 Gamma-Ray Dose Rates

Gamma-ray dose rate measurements on the partially loaded cask obtained by PNL with thermoluminescent dosimeters (TLDs) and by PNL and GE with portable gamma meters are provided in Volume I of this report (McKinnon et al. 1986a). Predicted dose rates are compared to measured values in Figures 6.17 through 6.19. Dose rates shown in Figure 6.17 are directly above the fuel assemblies, i.e., centered above each assembly on the lid of the cask. Predicted dose rates decrease with distance from the center of the cask while measured dose

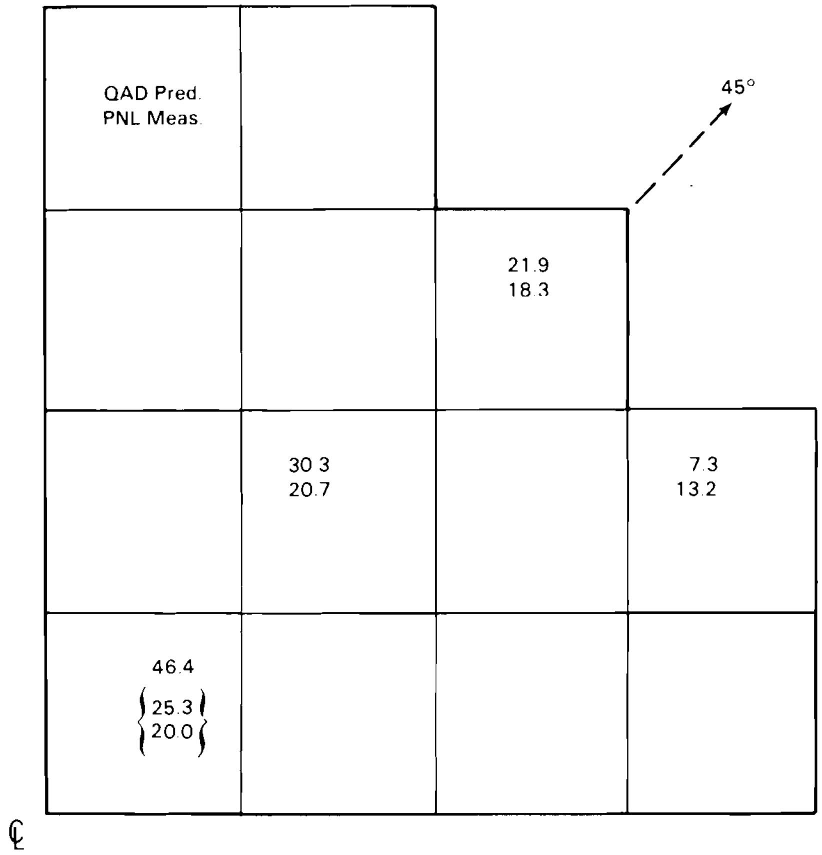

FIGURE 6.17. Gamma-Ray Dose Rates (mrem/hr) on Top of Partially Loaded Cask

rates are relatively uniform. This would imply that measured values result solely from the assembly directly below the location of the measurement while predicted values have appreciable contributions from adjacent assemblies. Additional predicted dose rates are compared to measured values in Figure 6.18. On the cask centerline, predicted dose rates are a factor of 2 higher than measurements; near the edge of the cask they are a factor of 4 lower.

On the bottom centerline of the partially loaded cask, a predicted dose rate of 76.1 mrem/hr resulted in an agreement with measured values of 69 and 78 mrem/hr from Volume I.

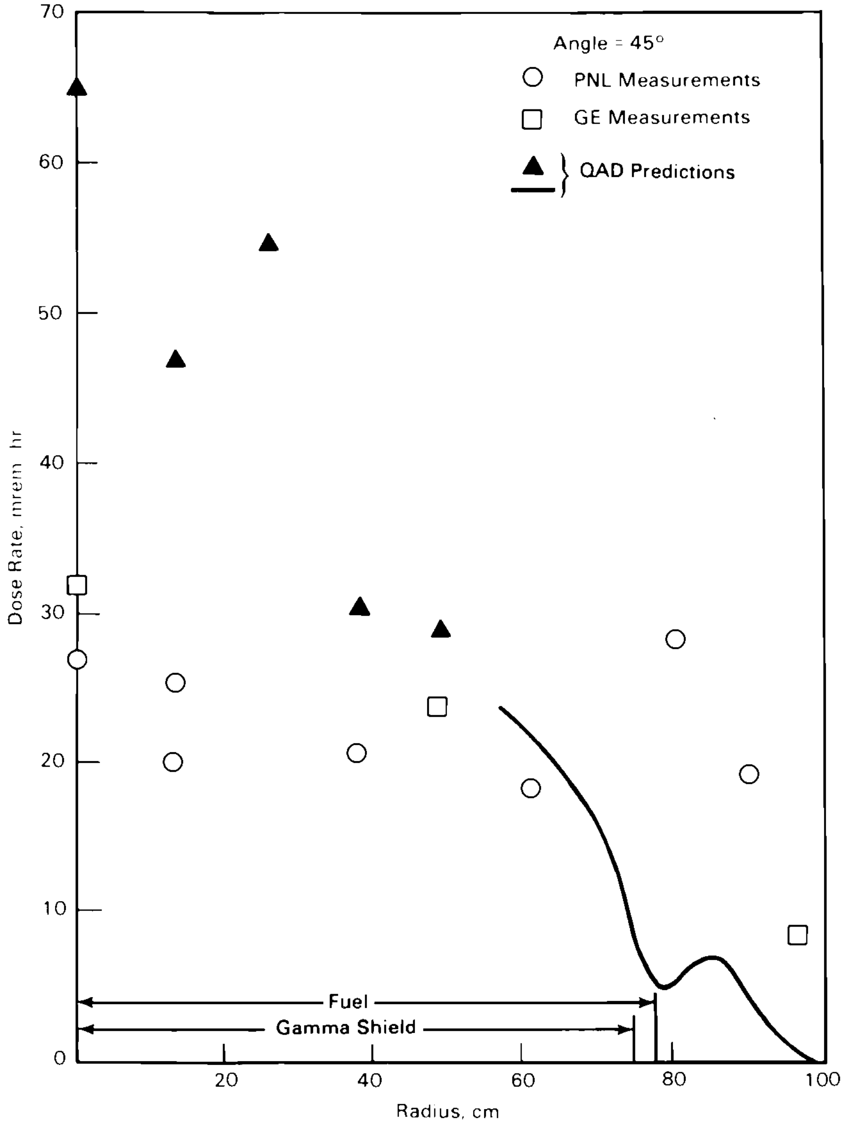

FIGURE 6.18. Gamma-Ray Dose Rates on Top of Partially Loaded Cask

Figure 6.19 shows gamma-ray dose rates on the side of the partially loaded cask. From 50 cm to 460 cm, predicted dose rates are in good agreement with measured values. This may be fortuitous because 60% of the dose rate is due to secondary gamma rays. If the neutron source strength is reduced by a factor of 3, the predicted gamma-ray dose rate will be reduced by 40%, giving predicted values that are one-half to two-thirds of the measured values. Near the ends of the cask, dose rate peaks are underpredicted by a factor of 2. This could

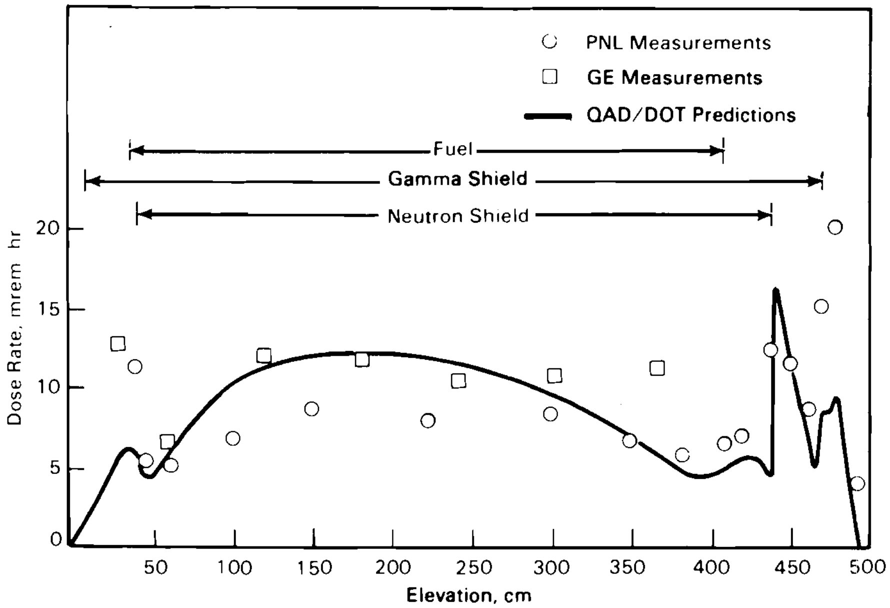

FIGURE 6.19. Gamma-Ray Dose Rates on Side of Partially Loaded Cask

easily be accounted for by the ^{59}Co content in stainless steel. The predicted dose rate peak at 440 cm agrees very well with the measurement.

Comparisons of gamma-ray dose rate predictions with measured values for a partially loaded cask are summarized in Table 6.13. On the side of the cask, the average difference between predictions and measurements is -0.8 mrem/hr (predictions were slightly less than measurements). The standard deviation of the differences is ±3.7 mrem/hr. On the average, predictions are less than measurements by approximately 6%. On the top of the cask, differences between predictions and measurements average -1.2 mrem/hr, but the standard deviation on the differences is a relatively high ±20.1 mrem/hr. Predictions are, on the average, 8% less than measurements. The prediction of the centerline dose rate on the bottom of the cask differed from the measurement by 7.5 mrem/hr and is 11% higher than the measurement. Overall, the average difference between predictions and measurements is -0.6 mrem/hr, and the standard deviation of the differences is ±12.1 mrem/hr. Predictions of all measurements average 6% less than the measurements.

TABLE 6.13. Comparisons of Predicted Gamma Dose Rates with Data for Partially Loaded Cask

Elevation, cm	Side (45°) Dose Rates, mrem/hr			
	Measured	Predicted	Pred-Meas	Pred/Meas
40.0	11.5	5.6	-5.8	0.49
46.0	5.2	4.4	-0.8	0.85
60.0	5.3	5.8	0.4	1.08
100.0	6.7	10.1	3.4	1.51
150.0	8.5	11.9	3.4	1.40
223.1	8.0	11.9	3.9	1.49
300.0	8.3	9.6	1.3	1.15
350.0	6.6	6.9	0.3	1.04
380.0	5.5	4.8	-0.7	0.87
408.5	6.3	4.8	-1.5	0.76
420.0	6.8	5.4	-1.5	0.79
440.0	12.2	16.1	4.0	1.33
450.0	11.3	11.5	0.3	1.02
460.0	8.3	7.0	-1.3	0.85
470.0	14.8	8.2	-6.5	0.56
480.0	19.4	9.3	-10.1	0.48
490.0	3.8	1.3	-2.5	0.35
		Average:	-0.8	0.94
		Standard Deviation:	±3.7	±0.35

Radius, cm	Angle, degrees	Top Dose Rates, mrem/hr			
		Measured	Predicted	Pred-Meas	Pred/Meas
0.0	0	26.8	64.9	38.1	2.42
13.0	45	25.3	46.4	21.1	1.83
37.6	45	20.7	30.3	9.6	1.47
61.0	45	18.3	21.9	3.6	1.19
64.5	24.5	13.2	7.3	-5.9	0.55
80.0	26.5	31.1	4.9	-26.2	0.16
80.0	45	28.4	5.2	-23.2	0.18
90.0	26.5	16.4	3.2	-13.2	0.20
90.0	45	19.3	4.5	-14.8	0.23
			Average:	-1.2	0.92
			Standard Deviation:	±20.1	±0.80

Radius, cm	Angle, degrees	Bottom Dose Rates, mrem/hr			
		Measured	Predicted	Pred-Meas	Pred/Meas
0.0	0	68.6	76.1	7.5	1.11
			Overall Average:	-0.6	0.94
			Overall Standard Deviation:	±12.1	±0.58

Comparisons of calculated dose rates to measured values for the fully loaded cask are given in Figures 6.20 through 6.22. Directly above the fuel assemblies on the cask lid (Figure 6.20), comparisons are similar to those for the partially loaded cask; i.e., near the cask centerline the calculated dose rates are higher than data, but on the periphery agreement is good. The overall comparisons for the top of the cask are shown on Figure 6.21. The peak at about 80 cm, just beyond the lead shield in the cask lid, is underpredicted by a factor of 4.

On the bottom of the fully loaded cask, the predicted centerline dose rate of 72.1 mrem/hr agrees very well with measured values of 70 and 68 mrem/hr from Volume I (McKinnon et al. 1986a). At a radius of 61 cm, the predicted dose rate of 37.2 mrem/hr is a factor of 2 lower than PNL measurements (83 mrem/hr).

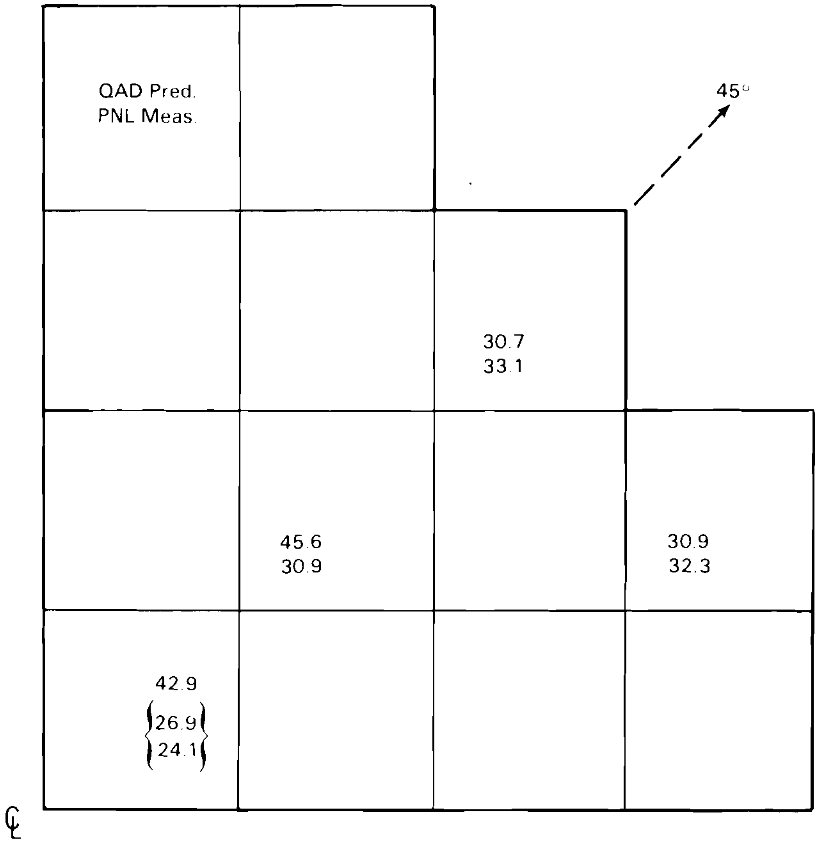

FIGURE 6.20. Gamma-Ray Dose Rates (mrem/hr) on Top of Fully Loaded Cask

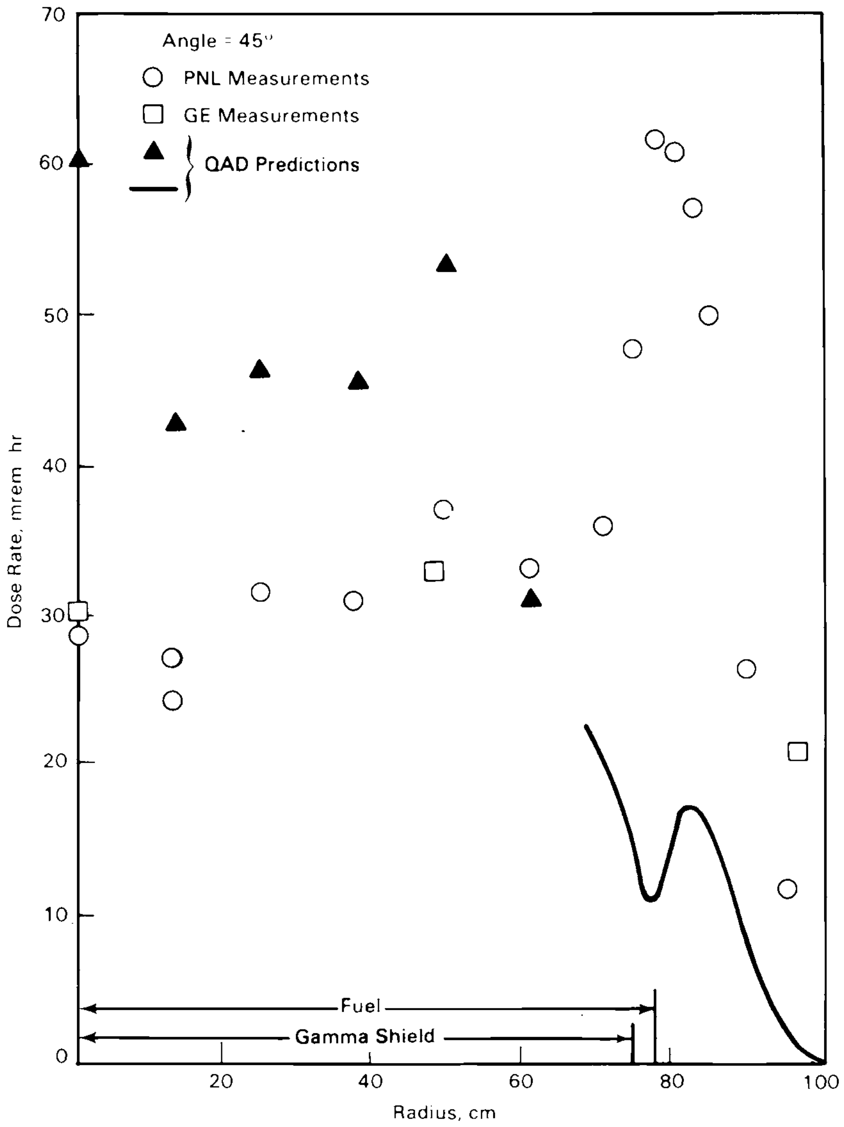

FIGURE 6.21. Gamma-Ray Dose Rates on Top of Fully Loaded Cask

Figure 6.22 shows comparisons of predicted dose rates on the side of the fully loaded cask with measured values. Most of the measurements were taken at an angle of 26.5 degrees, while the predictions were made for an angle of 45 degrees (Figure 3.6 of Section 3.3). Comparisons of 26.5-degree predictions with 45-degree predictions suggest the 26.5-degree curve shown in Figure 6.22 can be used for comparisons with 45-degree measured values. From 100 cm to

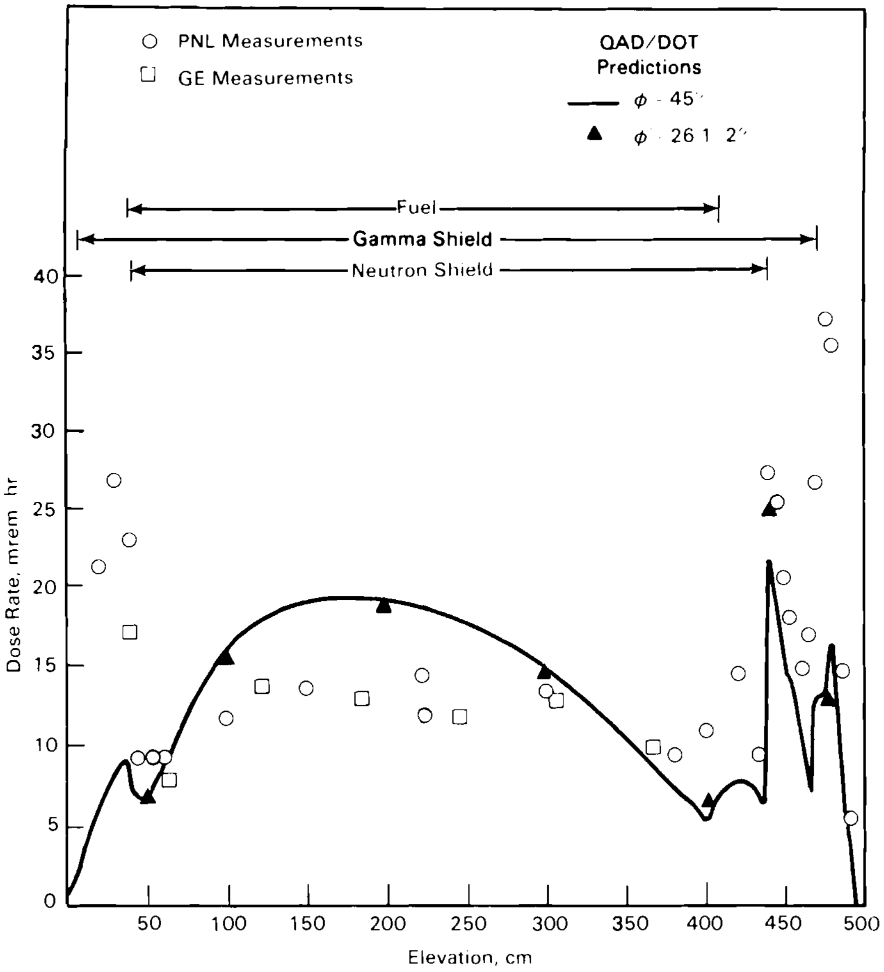

FIGURE 6.22. Gamma-Ray Dose Rates on Side of Fully Loaded Cask

250 cm, calculated dose rates are high by ~40%. At the peaks near the ends of the cask, calculated dose rates are low by a factor of 2 to 3. These differences are similar to those of the partially loaded cask.

Comparisons of gamma-ray dose rate predictions with measured values for a fully loaded cask are summarized in Table 6.14. On the side of the cask, the average difference between predictions and measurements is -3 mrem/hr (predictions were slightly less than measurements). The standard deviation of the differences is ±10 mrem/hr. On the average, predictions are less than

TABLE 6.14. Comparisons of Predicted Gamma Dose Rates with Data for Fully Loaded Cask

Elevation, cm	Angle, degrees	Dose Rates on Side of Cask, mrem/hr			Pred/Meas
		Measured	Predicted	Pred-Meas	
100.0	26.5	11.7	15.5	3.8	1.33
223.1	45.0	11.6	18.6	7.0	1.60
300.0	26.5	13.4	14.6	1.3	1.10
400.0	26.5	10.8	6.3	-4.4	0.59
440.0	26.5	26.6	24.6	-2.1	0.92
475.0	26.5	36.8	13.1	-23.7	0.36
			Average:	-3.0	0.98
			Standard Deviation:	±10.0	±0.42

Radius, cm	Angle, degrees	Dose Rates on Top of Cask, mrem/hr			Pred/Meas
		Measured	Predicted	Pred-Meas	
0.0	0	28.6	60.5	31.8	2.11
13.0	45	26.9	42.9	16.0	1.59
25.3	45	31.5	46.0	14.5	1.46
37.6	45	30.9	45.6	14.7	1.48
49.3	45	37.3	53.5	16.2	1.44
61.0	45	33.1	30.7	-2.4	0.93
63.5	24.5	32.3	30.8	-1.5	0.95
71.0	45	35.9	20.0	-15.9	0.56
75.0	45	47.9	13.7	-34.1	0.29
77.5	45	61.6	10.3	-51.3	0.17
80.0	45	60.7	14.6	-46.1	0.24
82.5	45	57.0	17.4	-39.6	0.31
85.0	45	49.9	15.4	-34.5	0.31
90.0	26.5	29.9	8.5	-21.4	0.28
90.0	45	26.4	7.9	-18.5	0.30
95.0	45	11.6	2.6	-9.1	0.22
			Average:	-11.3	0.79
			Standard Deviation:	±24.7	±0.62

Radius, cm	Angle, degrees	Dose Rates on Bottom of Cask, mrem/hr			Pred/Meas
		Measured	Predicted	Pred-Meas	
0.0	0	69.7	72.1	2.4	1.03
61.0	45	83.2	37.2	-46.0	0.45
			Average:	-21.8	0.74
			Standard Deviation:	±24.2	0.29
			Overall Average:	-10.1	0.83
			Overall Standard Deviation:	±21.9	±0.56

measurements by approximately 2%. On the top of the cask, differences between predictions and measurements average -11.3 mrem/hr, and the standard deviation on the differences was ±24.7 mrem/hr. Predictions are, on the average, 21% less than measurements. Predictions of dose rates on the bottom of the cask differed from measurements by -21.8 mrem/hr and were 26% lower than the measurements. On an overall basis, the average difference between predictions and measurements is -10.1 mrem/hr, and the standard deviation of the differences is ±21.9 mrem/hr. Predictions of all measurements average 17% less than the measurements.

In summary, calculated peak gamma-ray dose rates are underestimated by a factor of 2 to 3. Dose rates on the side of the cask between 50 and 450 cm are calculated reasonably well (~±50%). Overall, the predictions of both neutron and gamma-ray dose rates are considered to be satisfactory. Considering that the cask must attenuate a difficult to determine radiation source several orders of magnitude (usually more than three), and reduce the level to a relatively low value, agreement between predictions and data within a factor of two or three times is relatively good.

REFERENCES

ANSI. 1977. "Neutron and Gamma-Ray Flux-to-Dose Rate Factors." ANSI/ANS-6.1.1-1977, (N666), American National Standards Institute, New York, New York.

Barry, R. F. 1963. *LEOPARD - A Spectrum Dependent Non-Spatial Depletion Code for the IBM-7094.* WCAP-3269-26, Westinghouse Electric Corporation, Pittsburgh, Pennsylvania.

Catton, I. 1978. "Natural Convection in Enclosures." In *Proceedings, Sixth International Heat Transfer Conference*, Vol. 6, pp. 13-31.

Clausing, A. M., K. C. Wagner and J. R. Skarda. 1984. "An Experimental Investigation of Combined Convection from a Short Verical Cylinder in a Crossflow." *Journal of Heat Transfer*. 106.

Creer, J. M. 1984. "Decay Heat and Heat Transfer Predictions for Spent Fuel Storage Systems." In *Proceedings Second International Workshop on Irradiated Fuel Storage: Operating Experience and Development Programs*, pp. 157-209. Ontario Hydro, Toronto Ontario, Canada.

Croff, A. G. 1980a. *A User's Manual for the ORIGEN2 Computer Code*. ORNL/TM-7175, Oak Ridge National Laboratory, Oak Ridge, Tennessee.

Croff, A. G. 1980b. *ORIGEN2--A Revised and Updated Version of the Oak Ridge Isotpe Generation and Depletion Code*. ORNL-5621, Oak Ridge National Laboratory, Oak Ridge, Tennessee.

Croff, A. G., M. A. Bjerke, J. W. Morrison and L. M. Petrie. 1978. *Revised Uranium-Plutonium Cycle PWR and BWR Models for the ORIGEN Computer Code*. ORNL/TMP-6051, Oak ridge National Laboratory, Oak Ridge, Tennessee.

Curme, G. O., and F. Johnston. 1952. *Glycols*. Waverly Press.

Cuta, J. M., D. R. Rector and J. M. Creer. 1984. *Thermal-Hydraulic Analysis of Consolidated Spent PWR Fuel Rods*. NP-3764, Electric Power Research Institute, Palo Alto, California.

DOE. 1985. *Spent Fuel Storage Requirements*. DOE/RL-85-2, U.S. Department of Energy, Richland Operations Office, Richland, Washington.

Ford, W. E., III, C. C. Webster, B. R. Diggs, R. E. Pevey and A. G .Croff. 1980. *FCXSEC: Multigroup Cross-Section Libraries for Nuclear Fuel Cycle Shielding Calculations*. ORNL/TM-7038, Oak Ridge National Laboratory, Oak Ridge, Tennessee.

George, T. L., K. L. Basehore, C. L. Wheeler, W. A. Prather and R. E. Masterson. 1980. *COBRA-WC: A Version of COBRA for Single-Phase*

Multiassembly Thermal-Hydraulic Transient Analysis. PNL-3259, Pacific Northwest Laboratory, Richland, Washington.

Halbig, J. K., and J. C. Caine. 1985. ION-1 Technical Manual. LA-10433-M, Los Alamos National Laboratory, Los Alamos, New Mexico.

Idel'Chik, I. E. 1966. Handbook of Hydraulic Resistance, Coefficients of Local Resistance and of Friction. AEC-TR-6630, U.S. Atomic Energy Commission and the National Science Foundation, Washington.

Johnson, A. B., Jr., and E. R. Gilbert. 1983. Technical Basis for Storage of Zircaloy-Clad Spent Fuel in Inert Gases. PNL-4835, Pacific Northwest Laboratory, Richland, Washington.

Kays, W. M., and M. E. Crawford. 1980. Convection Heat and Mass Transfer. McGraw-Hill, Inc., New York, New York.

Kestin, J., and P. F. Maeder. 1957. "Influence of Turbulence on Heat from Cylinders." Technical Note 4018, National Advisory Committee for Aeronautics, Washington, D.C.

Khan, E. U., W. A. Prather, T. L. George and J. M. Bates. 1981. A Validation Study of the COBRA-WC Computer Program for LMFBR Thermal-Hydraulic Analysis. PNL-4128, Pacific Northwest Laboratory, Richland, Washington.

Leung, R. K. G. 1975. Combined Convection Heat Transfer from Vertical Bodies in a Horizontal Stream. M.S. thesis, Queen's University at Kingston, Ontario, Canada.

Lindeburge, M. R. 1981. Mechanical Engineering Review Manual. 6th ed. The Professional Engineering Program, San Carlos, California.

Lombardo, N. J., T. E. Michener, C. L. Wheeler, and D. R. Rector. 1986. COBRA-SFS Predictions of Single Assembly Spent Fuel Heat Transfer Data. PNL-5781, Pacific Northwest Laboratory, Richland, Washington.

Malenfant, R. E. 1967. QAD: A Series of Point-Kernel General Purpose Shielding Programs. LA-3572, Los Alamos National Laboratory, Los Alamos, New Mexico.

McAdams, W. H. 1954. Heat Transmission. 3rd ed. McGraw-Hill, New York, New York.

McKinnon, M. A., J. W. Doman, J. E. Tanner, R. J. Guenther, J. M. Creer and C. E. King. 1986a. BWR Spent Fuel Storage Cask Performance Test, Volume I: Cask Handling Experience and Decay Heat, Heat Transfer, and Shielding Data. PNL-5777 Vol. I, Pacific Northwest Laboratory, Richland, Washington.

McKinnon, M. A., J. W. Doman, C. M. Heeb and J. M. Creer. 1986b. Decay Heat Measurements and Predictions of BWR Spent Fuel. NP-4269, Electric Power Research Institute, Palo Alto, California.

Morgan, V. T. 1975. "The Overall Convective Heat Transfer for Smooth Cylinders." Advances in Heat Transfer. II:199-264.

Oosthuizen, P. H., and R. K. G. Leung. 1978. "Combined Convection Heat Transfer from Vertical Cylinders in a Horizontal Flow." ASME Paper No. 78-WA/HT-45, American Society of Mechanical Engineers, New York, New York.

ORNL. 1969. XSDRN: A Discrete Ordinates Spectral Averaging Code. CCC-123, Radiation Shielding Information Center, Oak Ridge National Laboratory, Oak Ridge, Tennessee.

ORNL. 1977. QAD-CG: A Combinatorial Geometry Version of QAD-P5A, a Point-Kernel Code for Neutron and Gamma-Ray Shielding Calculations. CCC-307, Radiation Shielding Information Center, Oak Ridge National Laboratory, Oak Ridge, Tennessee.

ORNL. 1978. AMPX-II: Modular Code System for Generating Coupled Multigroup Neutron-Gamma-Ray Cross-Section Libraries from Data in ENDF Format. PSR-63, Radiation Shielding Information Center, Oak Ridge National Laboratory, Oak Ridge, Tennessee.

REA. 1983. REA 2023 Dry Storage Cask for BWR Spent Fuel, Docket M33. Ridihalgh, Eggers & Associates, Inc., Columbus, Ohio.

Rhoades, W. A., and R. L. Childs. 1982. An Updated Version of the DOT-4 One- and Two-Dimensional Neutron/Photon Transport Code. ORNL-5851, Oak Ridge National Laboratory, Oak Ridge, Tennessee.

Schmittroth, F. 1984. ORIGEN2 Calculations of PWR Spent Fuel Decay Heat Compared with Calorimeter Data. HEDL-TME-83-32, Hanford Engineering Development Laboratory, Richland, Washington.

Sissom, L. E., and D. R. Pitts. 1972. Elements of Transport Phenomena. McGraw-Hill, New York, New York.

Sparrow, E. M., and A. L. Loeffler, Jr. 1959. "Longitudinal Laminar Flow Between Cylinders Arranged in Regular Array." AIChE Journal. 5(3):325-330.

Stewart, C. W., C. L. Wheeler, R. J. Cena, C. A. McMonagle, J. M. Cuta and D. S. Trent. 1977. COBRA-IV: The Model and the Method. BNWL-2214, Pacific Northwest Laboratory, Richland, Washington.

Straker, E. A., P. N. Stevens, D. C. Irving and V. R. Cain. 1970. The Morse Code - A Multigroup Neutron and Gamma-Ray Monte Carlo Transport Code. ORNL-4585, Oak Ridge National Laboratory, Oak Ridge, Tennessee.

Taylor, R. E. 1983. Hemispherical Total Emissivity of Stainless Steel. TPRL 324, School of Mechanical Engineering, Purdue University, Lafayette, Indiana.

Taylor, R. E. 1984. Hemispherical Total Emissivity of Painted Stainless Steel. TPRL-364, School of Mechanical Engineering, Purdue University, Lafayette, Indiana.

Touloukian, Y. S., and C. Y. Ho. 1970. Thermophysical Properties of Matter. Thermophysical Properties Research Center (TPRL), Purdue University, Lafayette, Indiana.

Welty, J. R., C. E. Wicks and R. E. Wilson. 1969. Fundamentals of Momentum, Heat, and Mass Transfer. J. Wiley and Sons, New York, New York.

APPENDIX A

COOPER NUCLEAR STATION OPERATING HISTORY

TABLE A.1. Cooper Nuclear Station Operation History

Cycle	Date	Days from Startup	Core Average Power, MW/MTU	Cycle	Date	Days from Startup	Core Average Power, MW/MTU
1	07-03-74	0	0				
1	07-22-74	19	12.15				
1	07-30-74	27	0				
1	10-01-74	90	11.04	4	05-05-78	1402	0
1	12-07-74	157	17.67	4	06-12-78	1440	16.57
1	12-24-74	174	0	4	09-13-78	1533	19.88
1	01-01-75	182	11.04	4	11-25-78	1606	17.68
1	02-03-75	215	19.88	4	02-15-79	1688	20.76
1	02-13-75	225	0	4	04-17-79	1749	18.78
1	04-25-75	296	20.99				
1	09-27-75	451	11.04	5	05-10-79	1772	0
1	11-01-75	486	0	5	05-21-79	1783	14.36
1	11-20-75	505	11.04	5	05-30-79	1792	0
1	12-10-75	525	19.88	5	06-12-79	1805	17.67
1	12-17-75	532	0	5	11-11-79	1957	19.88
1	01-08-76	554	17.67	5	11-24-79	1970	0
1	01-20-76	566	0	5	03-01-80	2068	19.88
1	03-15-76	621	17.67				
1	05-07-76	674	15.46	6	06-07-80	2166	0
1	05-26-76	693	0	6	06-30-80	2189	19.88
1	06-20-76	718	15.46	6	07-25-80	2214	22.09
1	09-17-76	807	17.67	6	08-08-80	2228	11.04
				6	01-14-80	2326	20.99
2	11-15-76	866	0	6	11-23-80	2335	0
2	11-29-76	880	15.46	6	01-04-81	2377	20.99
2	12-23-76	904	20.98	6	01-20-81	2393	22.09
2	01-07-77	919	11.04	6	03-20-81	2452	20.99
2	02-02-77	945	20.99	6	04-20-81	2483	19.88
2	02-10-77	953	0	7	06-07-81	2531	0
2	03-25-77	996	20.99	7	06-15-81	2539	8.84
2	03-30-77	1001	8.84	7	06-24-81	2548	17.67
2	04-15-77	1017	20.99	7	09-11-81	2627	21.64
2	04-20-77	1022	0	7	11-11-81	2688	0
2	05-12-77	1044	19.88	7	01-05-82	2743	21.64
2	06-20-77	1083	13.25	7	03-20-82	2817	20.99
2	09-17-77	1172	17.67	7	03-25-82	2822	0
3	10-18-77	1203	0	7	04-25-82	2853	19.88
3	03-31-78	1367	15.46	7	05-21-82	2879	17.67

APPENDIX B

SAMPLE ORIGEN2 INPUT FOR ASSEMBLY CZ205

TABLE B.1. Sample ORIGEN2 Input for Assembly CZ205

```
-1
-1
-1
TIT     CZ205
BAS     METRIC TON
LIP     0  0  0
LIB     0  1  2  3  251  252  253  9  3  0  1  4
PHO     101   102   103  10
INP     1  1 -1 -1  1  1
RDA     BURNUP TO25344.  MWD/MT
BUP
IRP       90.00      9.81   1   2   4   1
IRP      157.00     16.86   2   3   4   0
DEC      174.00             3   4   4   0
IRP      225.00     13.92   4   5   4   0
IRP      296.00     20.01   5   6   4   0
IRP      451.00     10.52   6   7   4   0
DEC      486.00             7   8   4   0
IRP      674.00     14.13   8   9   4   0
DEC      693.00             9  10   4   0
IRP      807.00     16.38  10  11   4   0
DEC      866.00            11   1   4   0
IRP      880.00     21.87   1   2   4   0
IRP      904.00     29.68   2   3   4   0
IRP      919.00     15.62   3   4   4   0
IRP      945.00     29.69   4   5   4   0
DEC      953.00             5   6   4   0
IRP      996.00     29.69   6   7   4   0
IRP     1001.00     12.51   7   8   4   0
IRP     1017.00     26.69   8   9   4   0
DEC     1022.00             8  10   4   0
IRP     1044.00     28.12  10  11   4   0
IRP     1083.00     18.74  11   1   4   0
IRP     1172.00     25.00   1   2   4   0
DEC     1203.00             2   3   4   0
IRP     1367.00     18.21   3   4   4   0
DEC     2166.00             5   4   4   0
IRP     2189.00      5.87   5   6   4   0
IRP     2214.00      6.52   6   7   4   0
IRP     2228.00      3.26   7   8   4   0
IRP     2326.00      6.20   8   9   4   0
DEC     2335.00             9  10   4   0
IRP     2377.00      6.20  10  11   4   0
IRP     2393.00      6.52  11   1   4   0
IRP     2452.00      6.20   1   2   4   0
IRP     2483.00      5.87   2   3   4   0
DEC     2531.00             3   4   4   0
IRP     2539.00      4.27   4   5   4   0
IRP     2548.00      8.53   5   6   4   0
IRP     2627.00     10.45   6   7   4   0
DEC     2688.00             7   8   4   0
IRP     2743.00     10.45   8   9   4   0
IRP     2817.00     10.13   9  10   4   0
```

TABLE B.1. (contd)

```
DEC       2822.00           10  11   4   0
IRP       2853.00     9.60  11   1   4   0
IRP       2879.00     8.53   1   2   4   0
BUP
MOV        2  1  0  1.0
DEC      650.    1  2  4  1
DEC      681.    2  3  4  0
Dec      711.    3  4  4  0
DEC      742.    4  5  4  0
DEC      772.    5  6  4  0
DEC      803.    6  7  4  0
DEC      834.    7  8  4  0
DEC      864.    8  9  4  0
DEC      895.    9 10  4  0
DEC      925.   10 11  4  0
HED     1 DISCHARGE
HED     2 MAR 1, 84
HED     3 APR 1, 84
HED     4 MAY 1, 84
HED     5 JUN 1, 84
HED     6 JUL 1, 84
HED     7 AUG 1, 84
HED     8 SEP 1, 84
HED     9 OCT 1, 84
HED    10 NOV 1, 84
HED    11 DEC 1, 84
OPTA    8 8 8 8 7 8 8 8 7 8 8 8 8 8 8 8 8 8 8 8 8 8 8 8
OPTL    8 8 8 8 8 8 8 8 7 8 8 8 8 8 8 8 8 8 8 8 8 8 8 8
OPTF    8 8 8 8 7 8 8 8 7 8 8 8 8 8 8 8 8 8 8 8 8 8 8 8
OUT    11    1    0   -1
STP     4
4       1000     4.3     50000 11.1          60000 156.0        70000 104.0
4       80000 134695.0   90000 10.7          110000 150.0       120000 2.0
4       130000 475.8     140000 12.1         150000 55.4        160000 22.5
4       170000 5.3       180000 2.0          220000 6.1         230000 8.1
4       240000 8864.0    250000 913.0        260000 31584.0     270000 39.8
4       280000 4191.0    290000 6.1          400000 248140.0    420000 10.0
4       470000 0.1       480000 25.1         490000 2.0         500000 4056.8
4       640000 1573.0    720000 19.8         740000 7.1         820000 1.0
2       922350 25000.    922380 975000.      0       0.0
0
END
```

APPENDIX C

COMPARISONS OF PREDICTED DECAY HEAT RATES WITH MEASUREMENTS

TABLE C.1. Comparisons of Predicted With Measured Decay Heat Rates

Fuel Assembly	Burnup, GWd/MTU	Decay Time, days	Date	Meas., W	Pred., W	P-M, W	(P-M)/M, %
CZ147	26.71	1294	04-Nov-84	276.7	296.4	-19.7	-7.1
CZ148	26.31	1283	23-Oct-84	273.5	293.6	-20.1	-7.3
CZ182	26.82	860	27-Sep-84	342.6	364.9	-22.3	-6.5
CZ195	26.39	1289	30-Oct-84	255.5	289.6	-34.1	-13.3
CZ205(a)	25.34	857	24-Sep-84	324.0	331.7	-7.7	-2.4
CZ205(a)	25.34	868	05-Oct-84	368.0	328.3	39.7	10.8
CZ205(a)	25.34	871	08-Oct-84	343.5	327.4	16.1	4.7
CZ205(a)	25.34	872	09-Oct-84	352.9	327.1	25.8	7.3
CZ205(a)	25.34	886	23-Oct-84	331.7	322.8	8.9	2.7
CZ205(a)	25.34	887	24-Oct-84	338.6	322.5	16.1	4.8
CZ205(a)	25.34	892	29-Oct-84	327.4	321.0	6.4	2.0
CZ205(a)	25.34	896	02-Nov-84	313.5	320.0	-6.5	-2.1
CZ205(a)	25.34	899	05-Nov-84	311.3	319.2	-7.9	-2.5
CZ205(a)	25.34	900	06-Nov-84	314.0	313.8	0.2	0.1
CZ205(a)	25.34	936	12-Dec-84	331.0	315.5	15.5	4.7
CZ205(a)	25.34	946	22-Dec-84	317.2	318.2	-1.0	-0.3
CZ205(a)	25.34	1089	14-May-85	289.7	276.0	13.7	4.7
CZ205(a)	25.34	1103	28-May-85	308.0	273.6	34.4	11.2
CZ209(a)	25.38	891	28-Oct-84	279.5	289.3	-9.8	-3.5
CZ211	26.68	1261	02-Oct-84	296.0	302.7	-6.7	-2.3
CZ211	26.68	1491	20-May-85	240.3	266.6	-26.3	-10.9
CZ222	26.69	898	04-Nov-84	355.7	346.2	9.5	2.7
CZ225	25.80	835	02-Oct-84	333.5	321.4	12.1	3.6
CZ239	27.25	893	30-Oct-84	366.5	358.8	7.7	2.1
CZ246	27.36	896	02-Nov-84	320.9	364.4	-43.5	-13.6
CZ246	27.36	899	05-Nov-84	341.7	363.4	-21.7	-6.4
CZ259(a)	26.47	1288	29-Oct-84	247.6	290.9	-43.3	-17.5
CZ259(a)	26.47	1340	20-Dec-84	288.5	281.7	6.8	2.4
CZ259(a)	26.47	1485	14-May-84	254.1	260.0	-5.9	-2.3
CZ264	26.50	1282	23-Oct-84	263.8	292.6	-28.8	-10.9
CZ277	26.48	1287	28-Oct-84	262.7	290.9	-28.2	-10.7
CZ277	26.48	1497	26-May-85	243.0	261.2	-18.2	-7.5
CZ286	27.14	930	06-Dec-84	278.4	326.8	-48.4	-17.4
CZ286	27.14	1104	29-May-85	284.2	290.8	-6.6	-2.3
CZ296	26.39	1293	03-Nov-84	256.7	297.0	-40.3	-15.7
CZ296	26.39	1492	21-May-85	251.9	266.0	-14.1	-5.6
CZ302	26.59	1283	24-Oct-84	285.6	290.8	-5.2	-1.8
CZ308	25.82	895	01-Nov-84	269.7	298.7	-29.0	-10.8
CZ311	27.39	890	27-Oct-84	356.9	340.1	16.8	4.7

(a) EPRI-sponsored.

TABLE C.1. (contd)

Fuel Assembly	Burnup, GWd/MTU	Decay Time, days	Date	Meas., W	Pred., W	P-M, W	(P-M)/M, %
CZ315	26.88	932	08-Dec-84	328.0	317.2	10.8	3.3
CZ318	26.57	931	07-Dec-84	277.6	297.9	-20.3	-7.3
CZ337	26.72	891	01-Nov-84	347.7	346.4	1.3	0.4
CZ337	26.72	1095	24-May-85	300.4	295.5	4.9	1.6
CZ342	27.07	931	07-Dec-84	280.1	320.1	-40.0	-14.3
CZ342	27.07	1101	26-May-85	300.0	286.1	13.9	4.6
CZ346	28.05	890	27-Oct-84	388.7	376.5	12.2	3.1
CZ348	27.48	894	31-Oct-84	342.8	355.5	-12.7	-3.7
CZ351	25.75	931	10-Dec-84	313.8	297.1	16.7	5.3
CZ355	25.42	891	28-Oct-84	290.5	293.0	-2.5	-0.9
CZ357	27.14	932	08-Dec-84	320.3	326.3	-6.0	-1.9
CZ369(a)	26.58	858	25-Oct-84	347.7	343.3	4.4	1.3
CZ370	26.34	1257	28-Sep-84	293.6	292.4	1.2	0.4
CZ372	25.85	1256	27-Sep-84	294.3	286.3	8.0	2.7
CZ379	25.93	898	04-Nov-84	287.4	296.9	-9.5	-3.3
CZ398	27.48	890	27-Oct-84	372.0	361.0	11.0	3.0
CZ415	25.86	1255	26-Sep-84	289.3	286.7	2.6	0.9
CZ416	27.46	894	31-Oct-84	319.8	339.1	-19.3	-6.0
CZ429(a)	27.64	889	26-Oct-84	385.6	370.3	15.3	4.0
CZ430	26.82	894	31-Oct-84	353.3	344.2	9.1	2.6
CZ433	25.98	1255	26-Sep-84	287.4	281.6	5.8	2.0
CZ433	25.98	1492	21-May-85	256.7	252.7	4.0	1.6
CZ460	26.51	933	09-Dec-84	313.5	308.9	4.6	1.5
CZ466	26.08	861	28-Sep-84	302.1	309.4	-7.3	-2.4
CZ468	26.76	935	11-Dec-84	325.3	317.9	7.4	2.3
CZ472	25.96	859	26-Sep-84	325.0	321.2	3.8	1.2
CZ473	26.52	934	10-Dec-84	293.2	297.6	-4.4	-1.5
CZ498	26.48	888	25-Oct-84	359.4	345.0	14.4	4.0
CZ508	26.36	933	09-Dec-84	310.0	309.6	0.4	0.1
CZ515(a)	25.74	1254	25-Sep-84	294.0	285.0	9.0	3.1
CZ515(a)	25.74	1285	26-Oct-84	296.0	279.2	16.8	5.7
CZ526(a)	27.60	864	01-Oct-84	397.0	378.9	18.1	4.6
CZ526(a)	27.60	1097	22-May-85	321.8	323.1	-1.3	-0.4
CZ528(a)	25.72	1284	25-Oct-84	297.6	279.0	18.6	6.3
CZ531	26.70	893	30-Oct-84	347.2	343.2	4.0	1.2
CZ536	26.59	1256	27-Sep-84	295.2	296.1	-0.9	-0.3
CZ542	26.69	932	08-Dec-84	311.9	312.4	-0.5	-0.2
CZ545	26.67	935	11-Dec-84	295.2	300.6	-5.4	-1.8

(a) EPRI-sponsored.

APPENDIX D

ADDITIONAL HYDRA PREDICTIONS COMPARED TO DATA

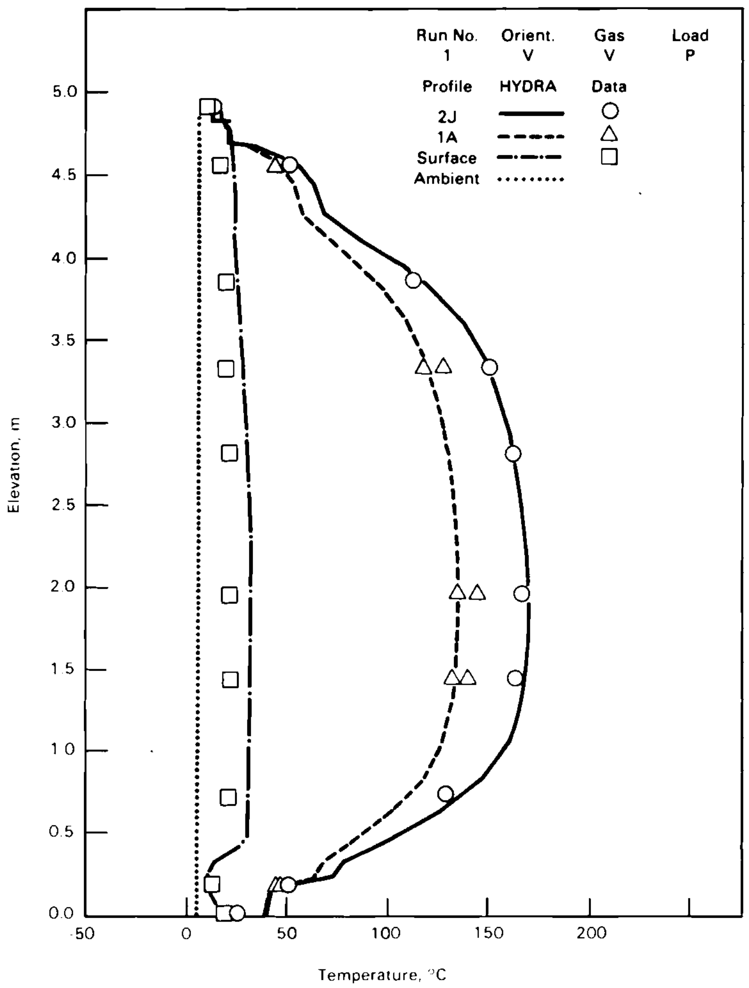
Run No.
1
Orient.
V
Gas
V
Load
P
Profile
HYDRA
Data
2J
1A
Surface
Ambient
Elevation, m
5.0
4.5
4.0
3.5
3.0
2.5
2.0
1.5
1.0
0.5
0.0
-50
0
50
100
150
200
Temperature, °C

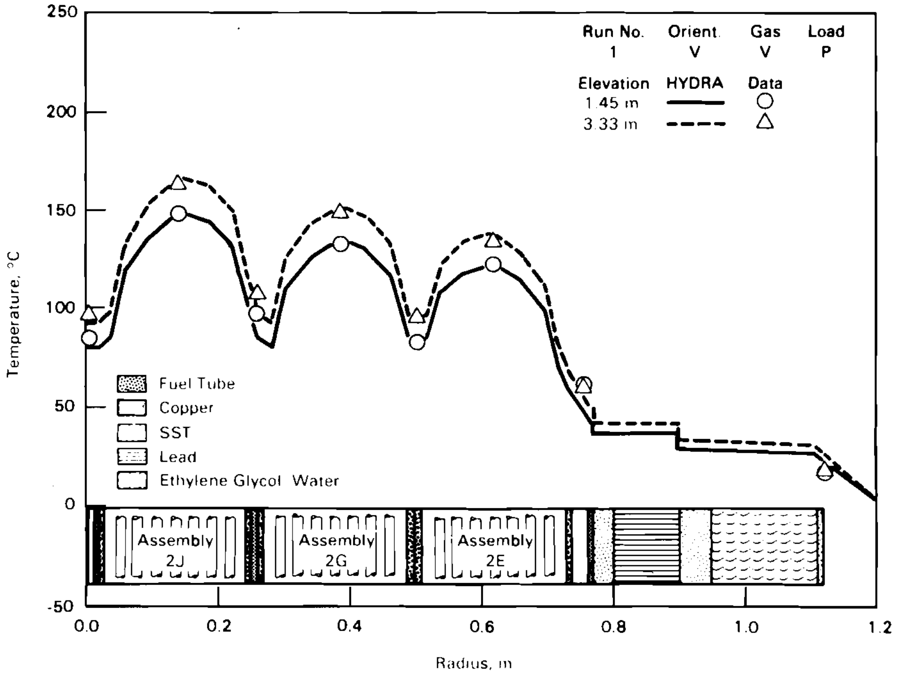
Run No.
1
Orient.
V
Gas
V
Load
P
Elevation
HYDRA
Data
1.45 m
3.33 m
Fuel Tube
Copper
SST
Lead
Ethylene Glycol Water
Assembly 2J
Assembly 2G
Assembly 2E
Temperature, °C
250
200
150
100
50
0
-50
0.0
0.2
0.4
0.6
0.8
1.0
1.2
Radius, m

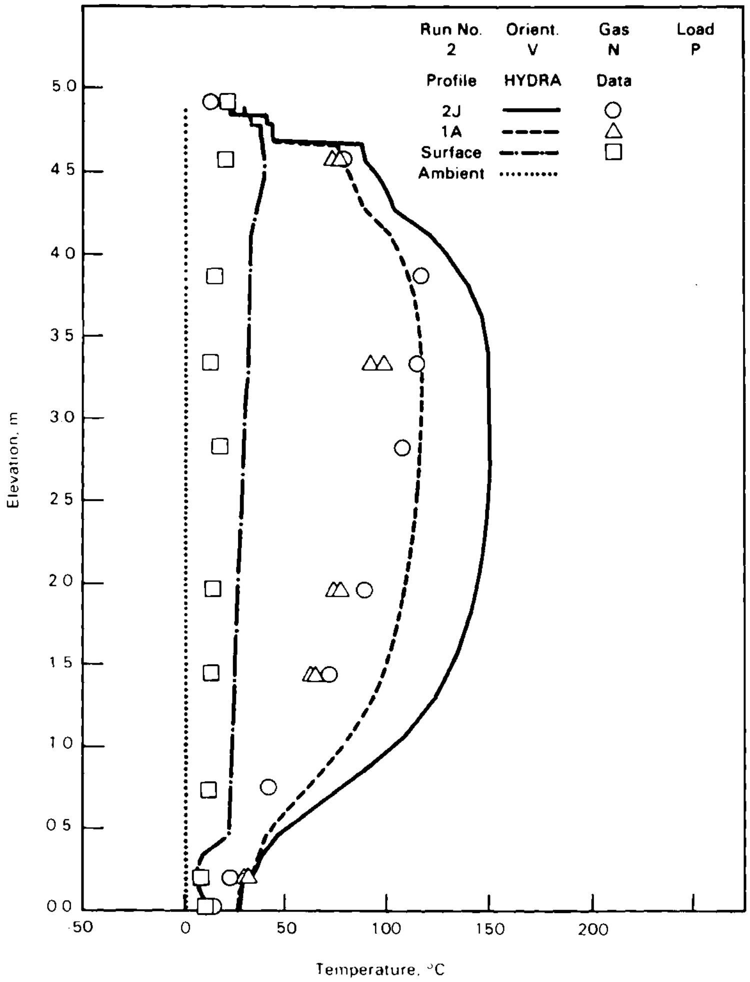

Run No. 2
Orient. V
Gas N
Load P
Profile
HYDRA
Data
2J
1A
Surface
Ambient
Elevation, m
0.0
0.5
1.0
1.5
2.0
2.5
3.0
3.5
4.0
4.5
5.0
-50
0
50
100
150
200
Temperature, °C

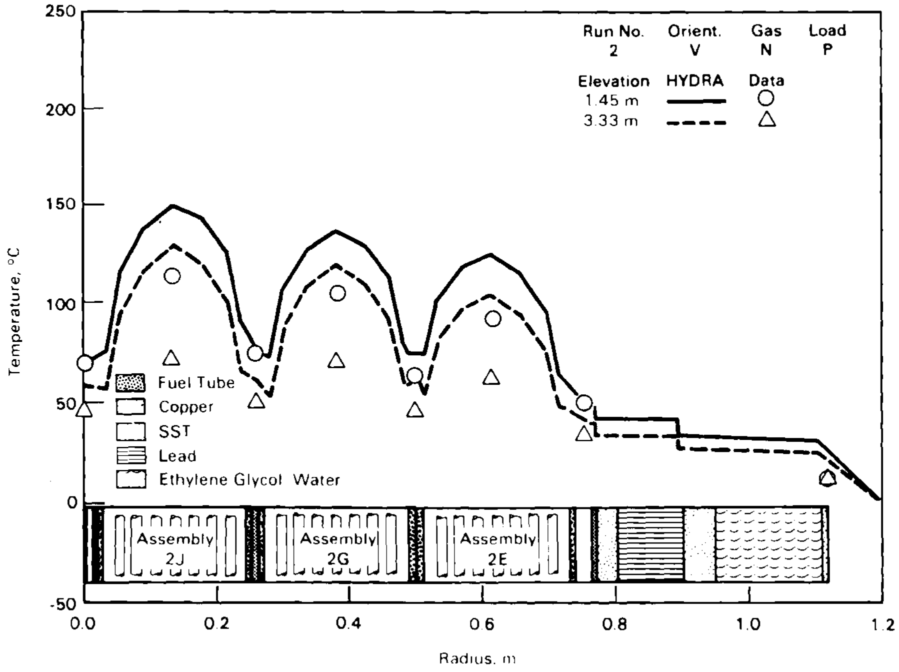

Run No. 2
Orient. V
Gas N
Load P
Elevation
HYDRA
Data
1.45 m
3.33 m
Fuel Tube
Copper
SST
Lead
Ethylene Glycol Water
Assembly 2J
Assembly 2G
Assembly 2E
Temperature, °C
250
200
150
100
50
0
-50
0.0
0.2
0.4
0.6
0.8
1.0
1.2
Radius, m

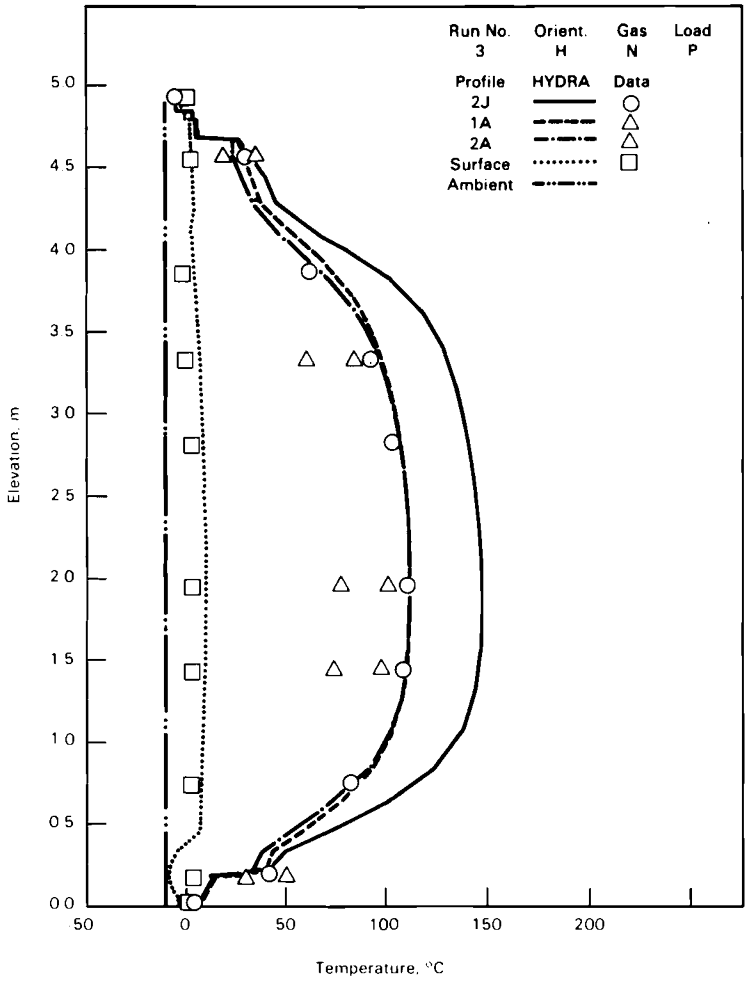

Run No. 3
Orient. H
Gas N
Load P
Profile
HYDRA
Data
2J
1A
2A
Surface
Ambient
Elevation, m
Temperature, °C
0.0
0.5
1.0
1.5
2.0
2.5
3.0
3.5
4.0
4.5
5.0
50
0
50
100
150
200

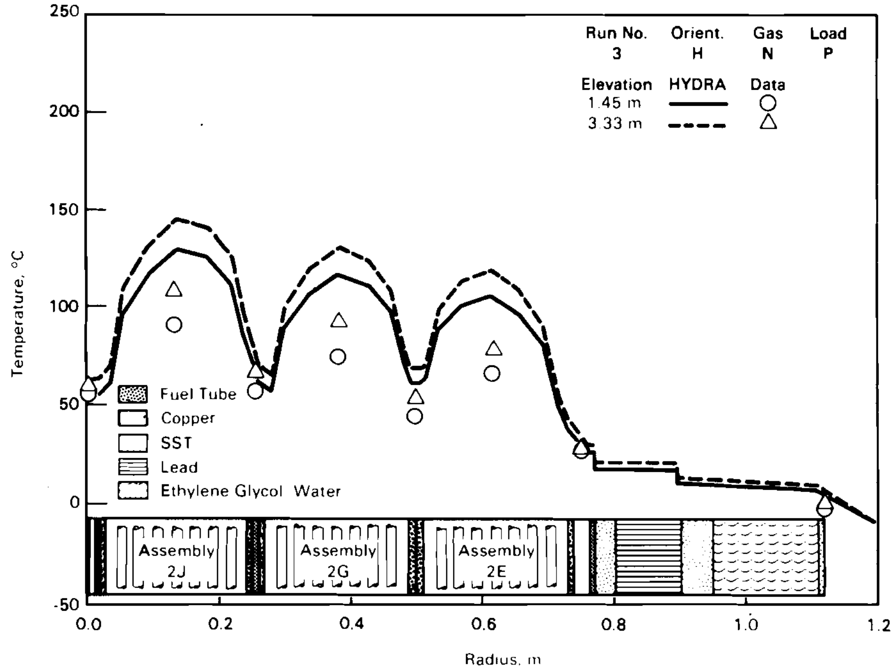

Run No. 3
Orient. H
Gas N
Load P
Elevation
HYDRA
Data
1.45 m
3.33 m
Fuel Tube
Copper
SST
Lead
Ethylene Glycol Water
Assembly 2J
Assembly 2G
Assembly 2E
Temperature, °C
Radius, m
250
200
150
100
50
0
-50
0.0
0.2
0.4
0.6
0.8
1.0
1.2

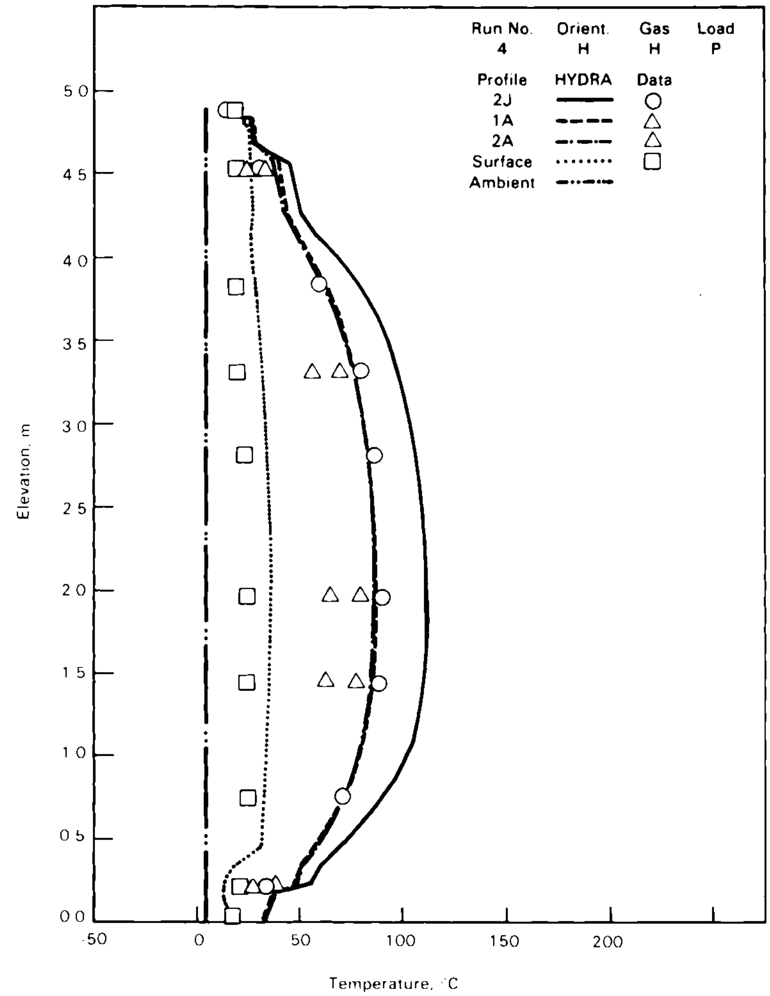
Run No.
4
Orient.
H
Gas
H
Load
P
Profile
HYDRA
Data
2J
1A
2A
Surface
Ambient
Elevation, m
0.0
0.5
1.0
1.5
2.0
2.5
3.0
3.5
4.0
4.5
5.0
-50
0
50
100
150
200
Temperature, °C

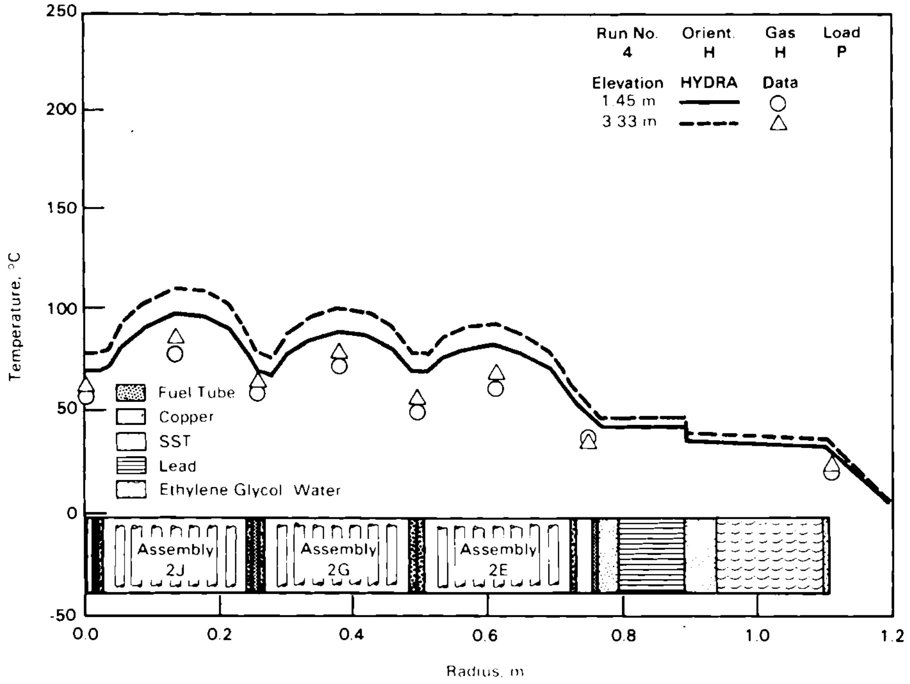
Run No.
4
Orient.
H
Gas
H
Load
P
Elevation
HYDRA
Data
1.45 m
3.33 m
Fuel Tube
Copper
SST
Lead
Ethylene Glycol Water
Assembly 2J
Assembly 2G
Assembly 2E
Temperature, °C
250
200
150
100
50
0
-50
0.0
0.2
0.4
0.6
0.8
1.0
1.2
Radius, m

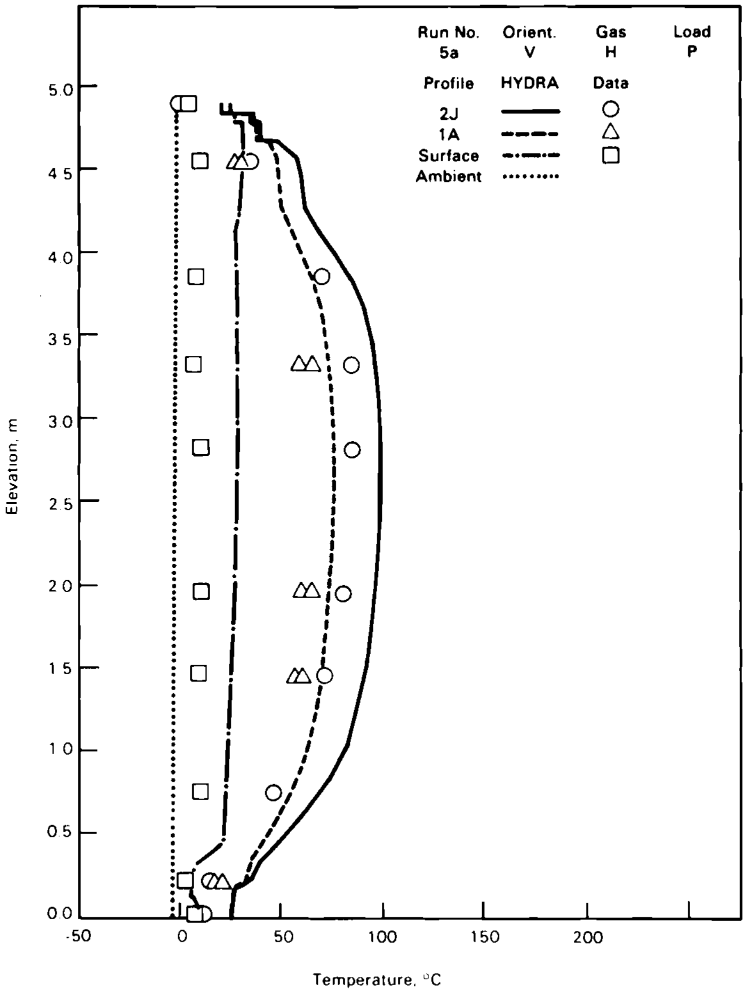
Run No.
5a
Orient.
V
Gas
H
Load
P
Profile
HYDRA
Data
2J
1A
Surface
Ambient
5.0
4.5
4.0
3.5
3.0
2.5
2.0
1.5
1.0
0.5
0.0
Elevation, m
-50
0
50
100
150
200
Temperature, °C

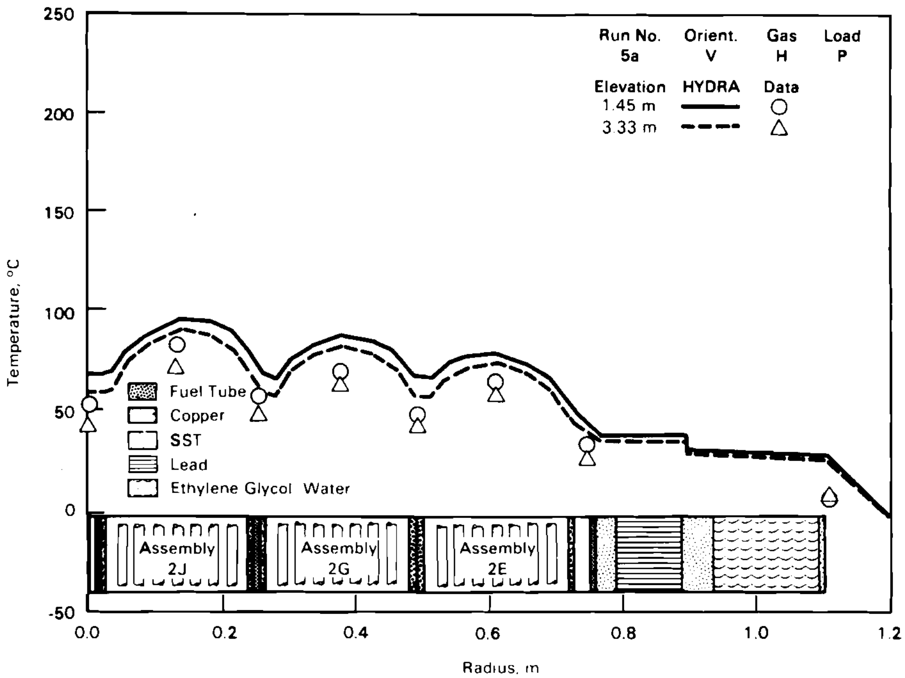
Run No.
5a
Orient.
V
Gas
H
Load
P
Elevation
HYDRA
Data
1.45 m
3.33 m
Fuel Tube
Copper
SST
Lead
Ethylene Glycol Water
Assembly 2J
Assembly 2G
Assembly 2E
250
200
150
100
50
0
-50
Temperature, °C
0.0
0.2
0.4
0.6
0.8
1.0
1.2
Radius, m

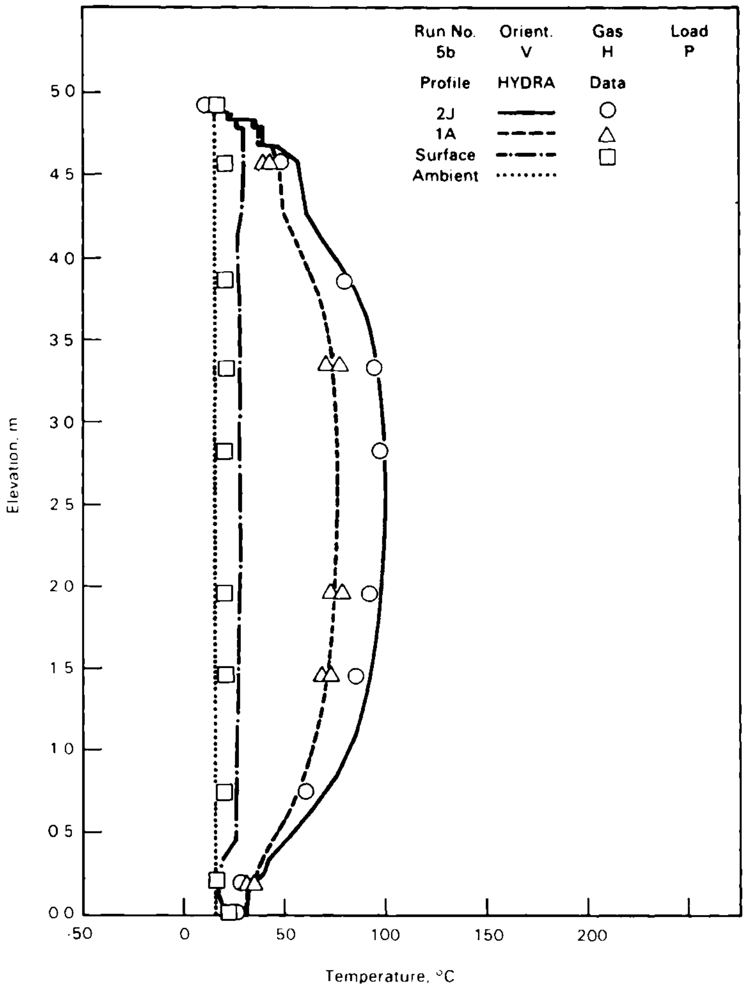
Run No. 5b
Orient. V
Gas H
Load P
Profile
HYDRA
Data
2J
1A
Surface
Ambient
5.0
4.5
4.0
3.5
3.0
2.5
2.0
1.5
1.0
0.5
0.0
Elevation, m
-50
0
50
100
150
200
Temperature, °C

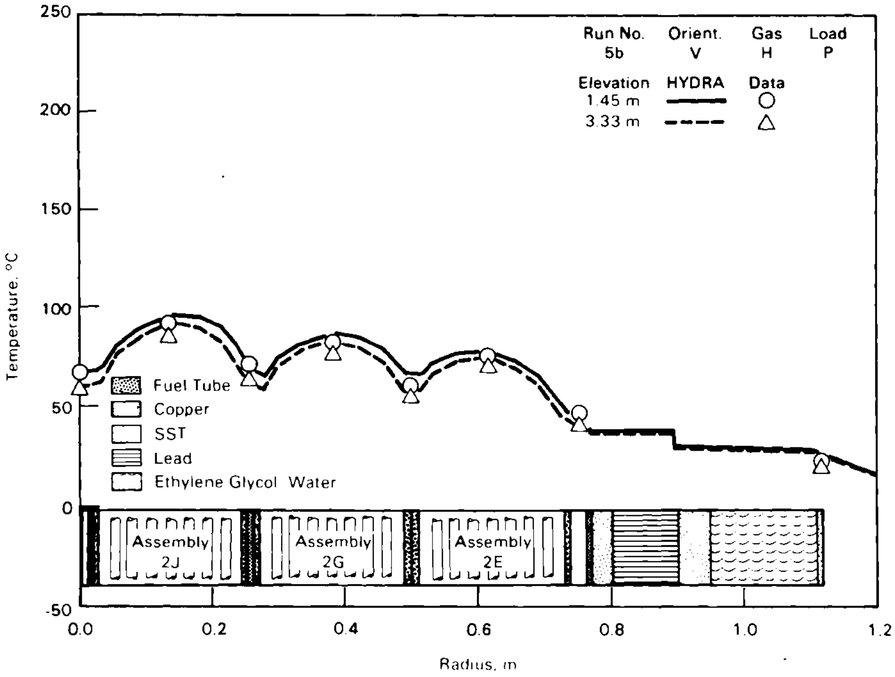
Run No. 5b
Orient. V
Gas H
Load P
Elevation
HYDRA
Data
1.45 m
3.33 m
250
200
150
100
50
0
-50
Temperature, °C
Fuel Tube
Copper
SST
Lead
Ethylene Glycol Water
Assembly 2J
Assembly 2G
Assembly 2E
0.0
0.2
0.4
0.6
0.8
1.0
1.2
Radius, m

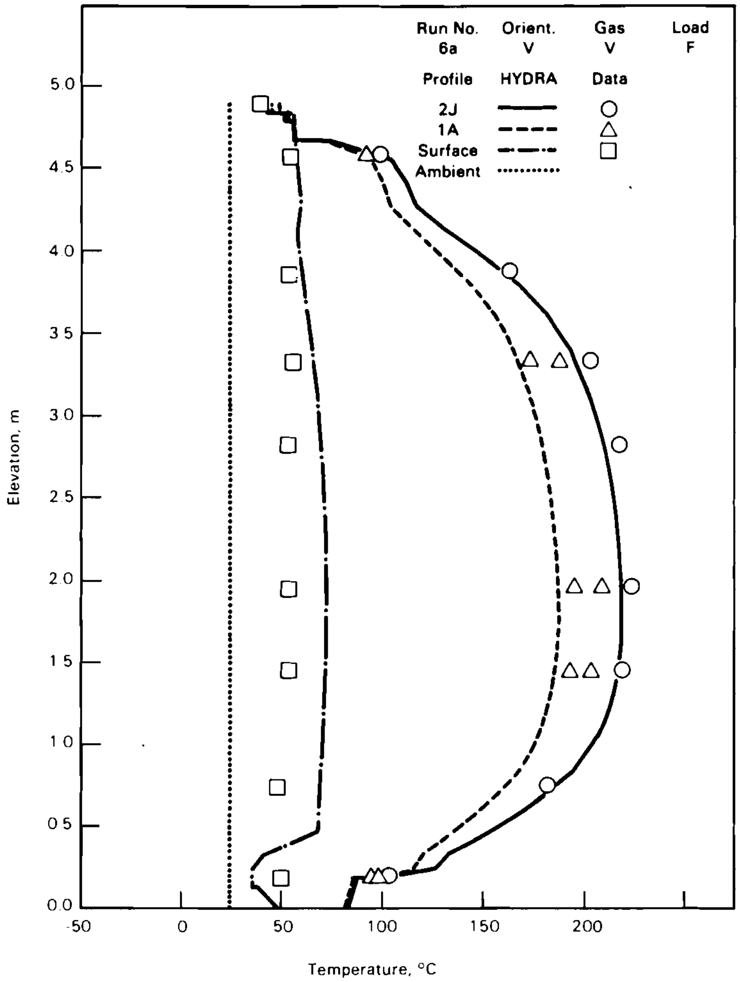
Run No. 6a
Orient. V
Gas V
Load F
Profile
HYDRA
Data
2J
1A
Surface
Ambient
Elevation, m
0.0
0.5
1.0
1.5
2.0
2.5
3.0
3.5
4.0
4.5
5.0
-50
0
50
100
150
200
Temperature, °C

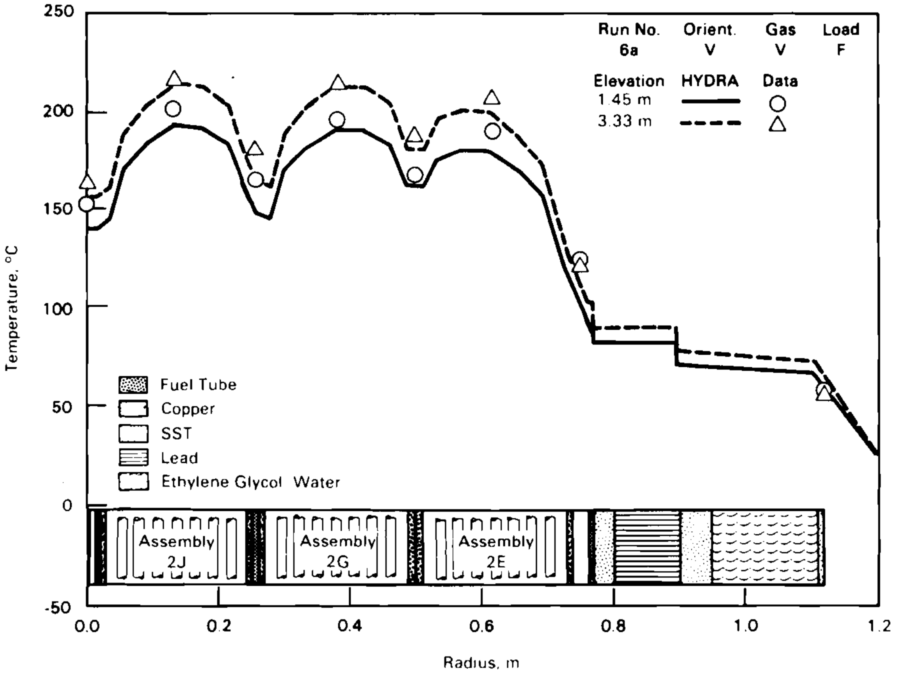
Run No. 6a
Orient. V
Gas V
Load F
Elevation
HYDRA
Data
1.45 m
3.33 m
Fuel Tube
Copper
SST
Lead
Ethylene Glycol Water
Assembly 2J
Assembly 2G
Assembly 2E
Temperature, °C
-50
0
50
100
150
200
250
0.0
0.2
0.4
0.6
0.8
1.0
1.2
Radius, m

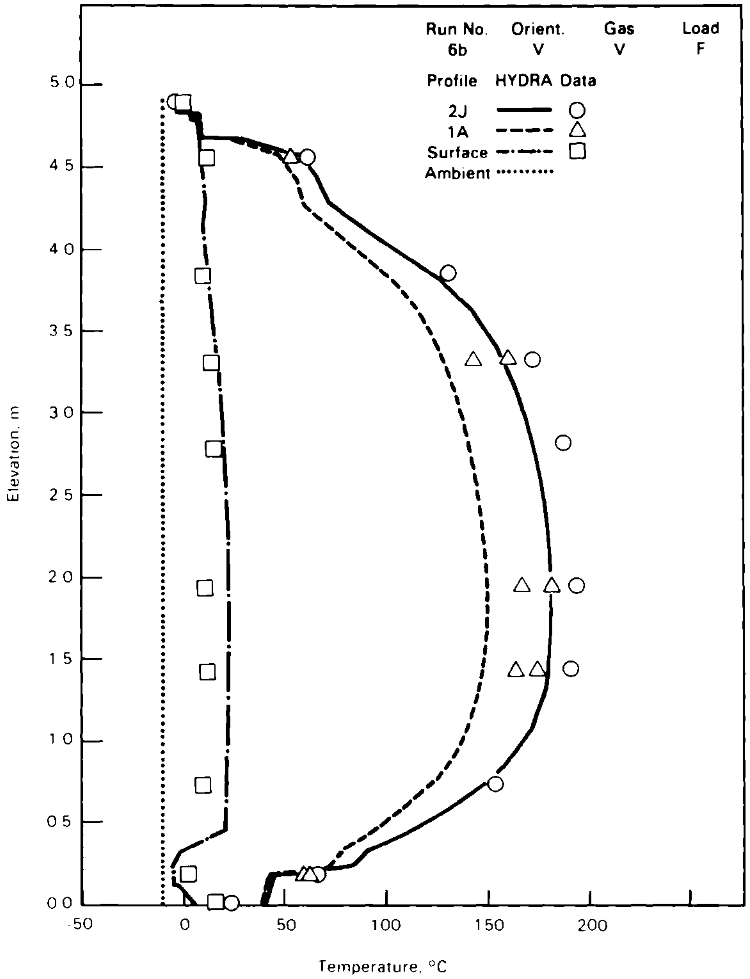
Run No. 6b
Orient. V
Gas V
Load F
Profile HYDRA Data
2J
1A
Surface
Ambient
Elevation, m
5.0
4.5
4.0
3.5
3.0
2.5
2.0
1.5
1.0
0.5
0.0
-50
0
50
100
150
200
Temperature, °C

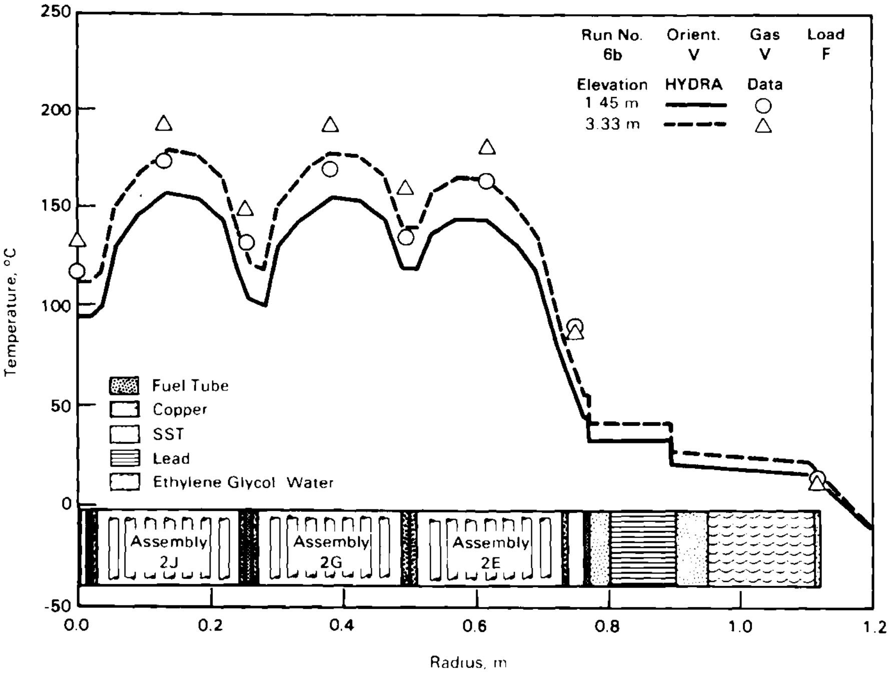
Run No. 6b
Orient. V
Gas V
Load F
Elevation HYDRA Data
1.45 m
3.33 m
Fuel Tube
Copper
SST
Lead
Ethylene Glycol Water
Assembly 2J
Assembly 2G
Assembly 2E
Temperature, °C
250
200
150
100
50
0
-50
0.0
0.2
0.4
0.6
0.8
1.0
1.2
Radius, m

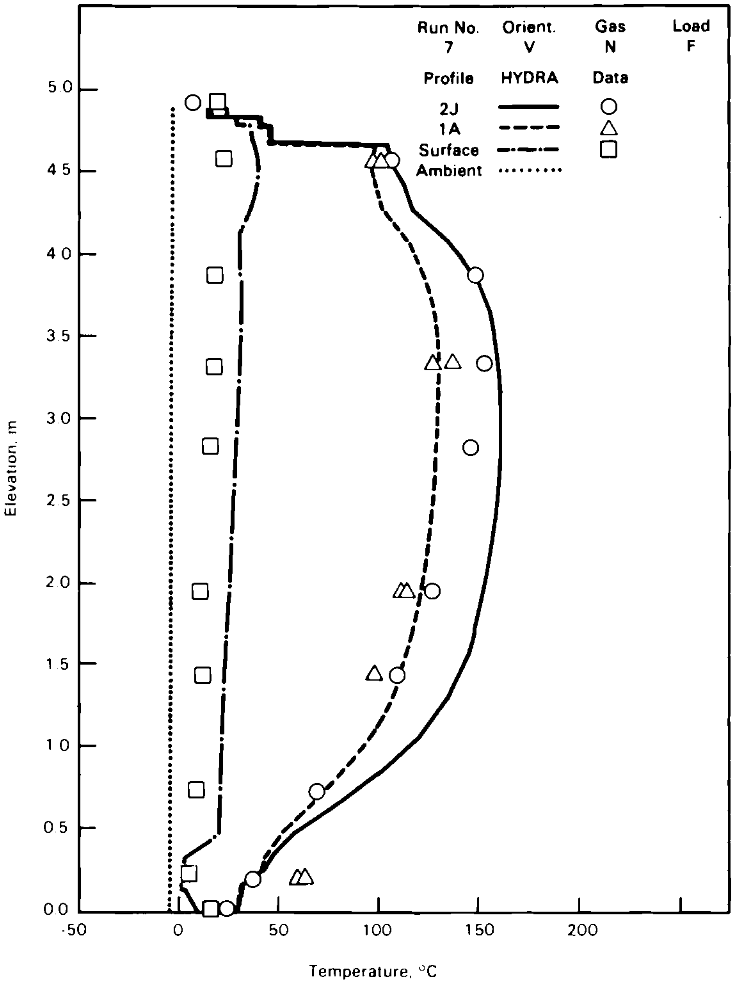
Run No.
7
Orient.
V
Gas
N
Load
F
Profile
HYDRA
Data
2J
1A
Surface
Ambient
5.0
4.5
4.0
3.5
3.0
2.5
2.0
1.5
1.0
0.5
0.0
Elevation, m
-50
0
50
100
150
200
Temperature, °C

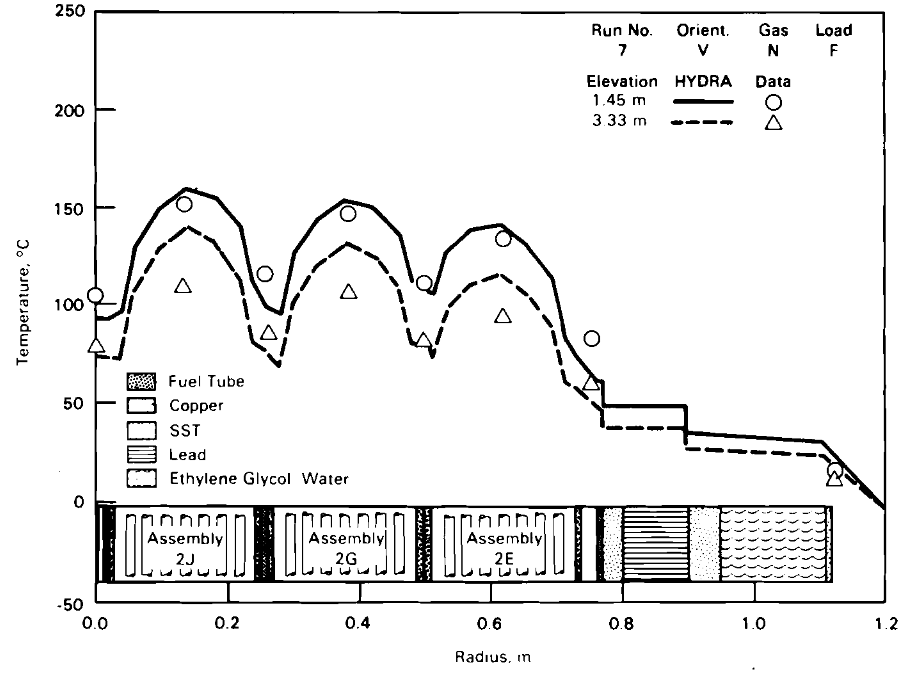
Run No.
7
Orient.
V
Gas
N
Load
F
Elevation
1.45 m
3.33 m
HYDRA
Data
Fuel Tube
Copper
SST
Lead
Ethylene Glycol Water
Assembly 2J
Assembly 2G
Assembly 2E
250
200
150
100
50
0
-50
Temperature, °C
0.0
0.2
0.4
0.6
0.8
1.0
1.2
Radius, m

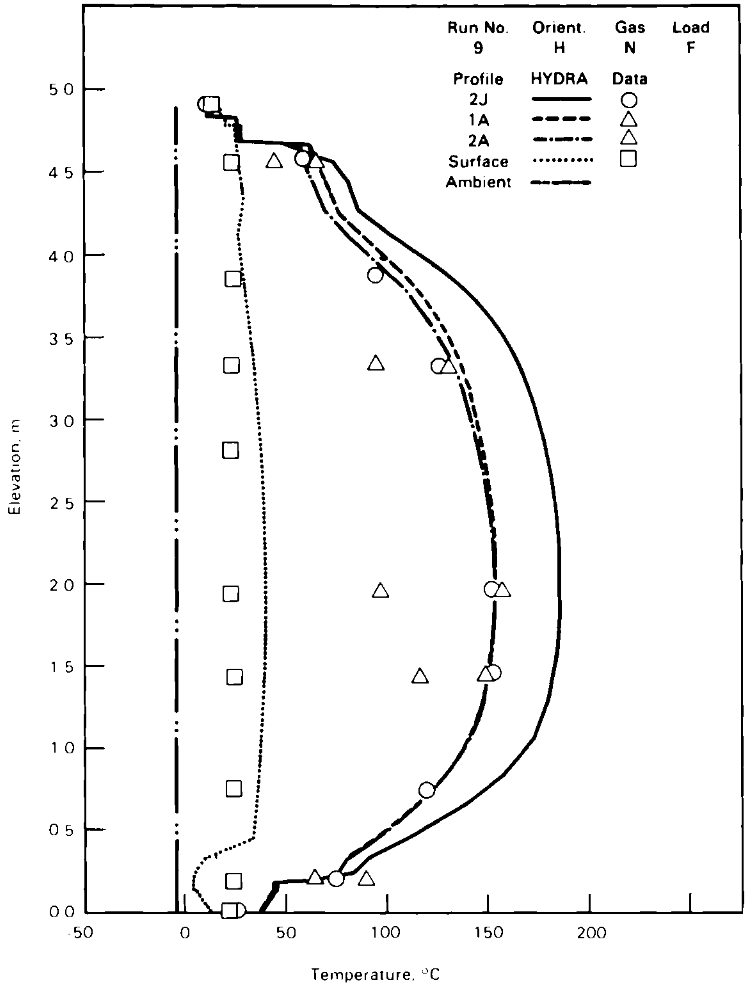

Run No. 9
Orient. H
Gas N
Load F
Profile
HYDRA
Data
2J
1A
2A
Surface
Ambient
Elevation, m
Temperature, °C
0.0
0.5
1.0
1.5
2.0
2.5
3.0
3.5
4.0
4.5
5.0
-50
0
50
100
150
200

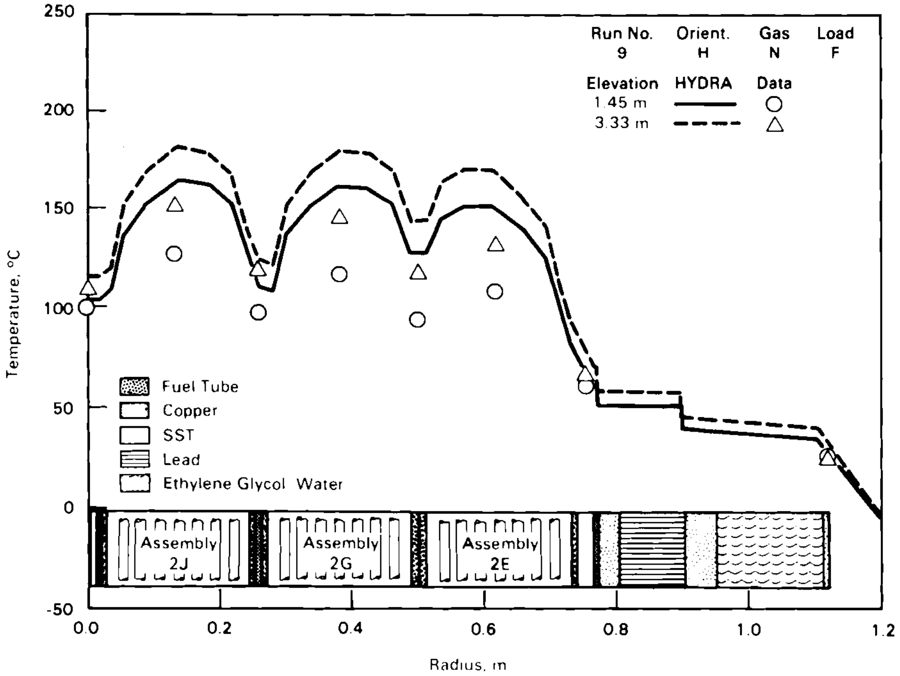

Run No. 9
Orient. H
Gas N
Load F
Elevation
HYDRA
Data
1.45 m
3.33 m
Fuel Tube
Copper
SST
Lead
Ethylene Glycol Water
Assembly 2J
Assembly 2G
Assembly 2E
Temperature, °C
Radius, m
250
200
150
100
50
0
-50
0.0
0.2
0.4
0.6
0.8
1.0
1.2

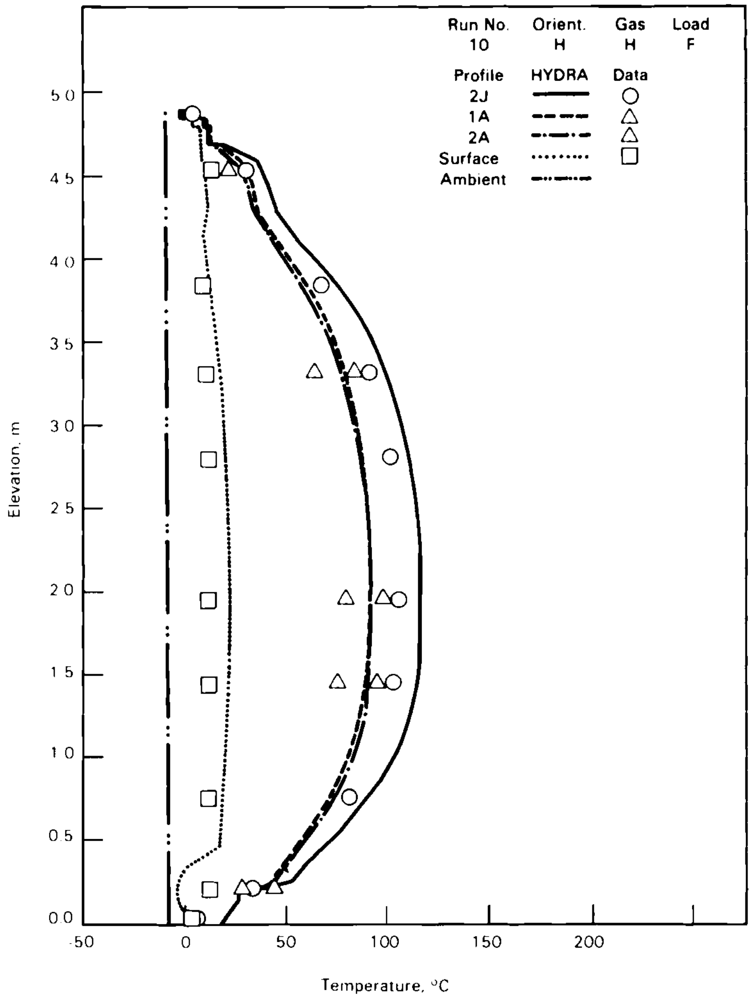

Run No. 10
Orient. H
Gas H
Load F
Profile
HYDRA
Data
2J
1A
2A
Surface
Ambient
Elevation, m
0.0
0.5
1.0
1.5
2.0
2.5
3.0
3.5
4.0
4.5
5.0
Temperature, °C
-50
0
50
100
150
200

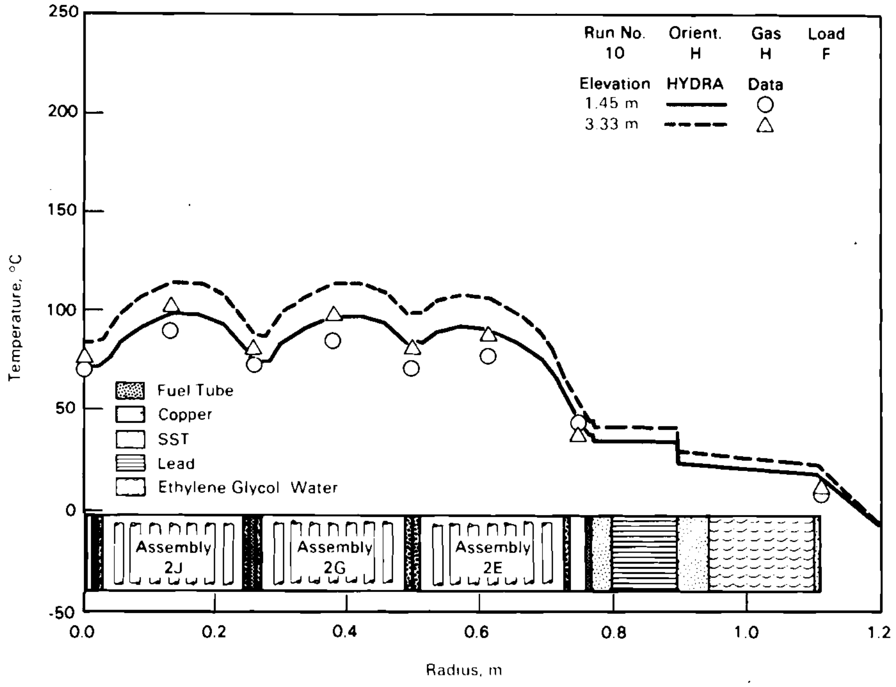

Run No. 10
Orient. H
Gas H
Load F
Elevation
HYDRA
Data
1.45 m
3.33 m
Fuel Tube
Copper
SST
Lead
Ethylene Glycol Water
Assembly 2J
Assembly 2G
Assembly 2E
Temperature, °C
-50
0
50
100
150
200
250
Radius, m
0.0
0.2
0.4
0.6
0.8
1.0
1.2

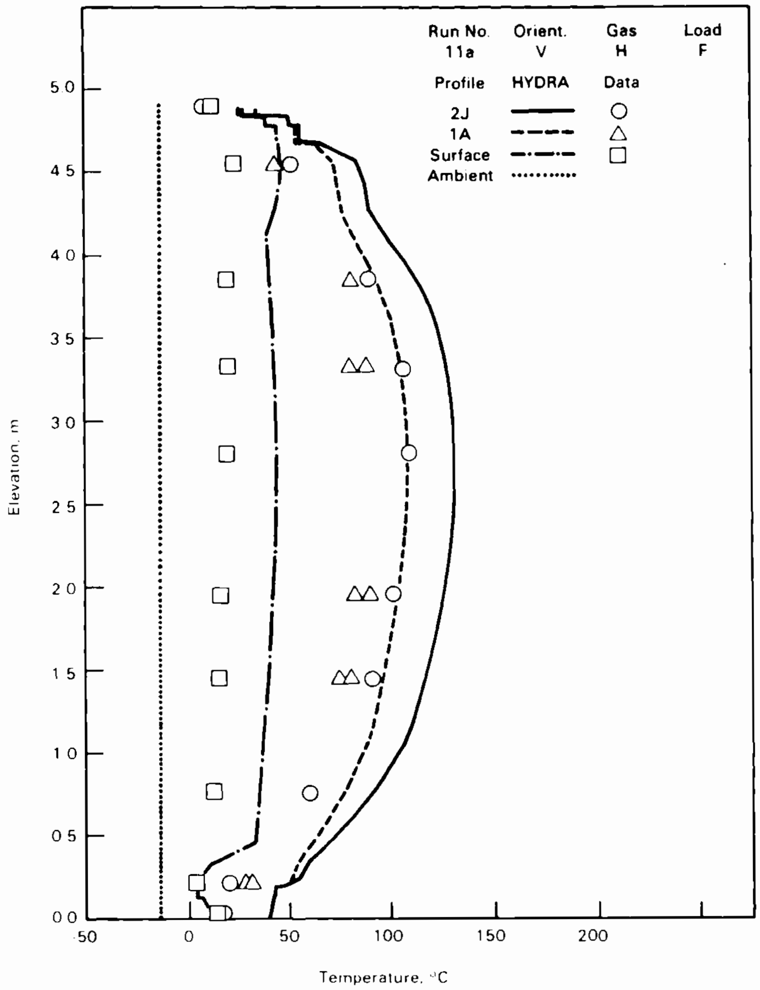
Run No. 11a
Orient. V
Gas H
Load F
Profile
HYDRA
Data
2J
1A
Surface
Ambient
Elevation, m
0 0
0 5
1 0
1 5
2 0
2 5
3 0
3 5
4 0
4 5
5 0
Temperature, °C
-50
0
50
100
150
200

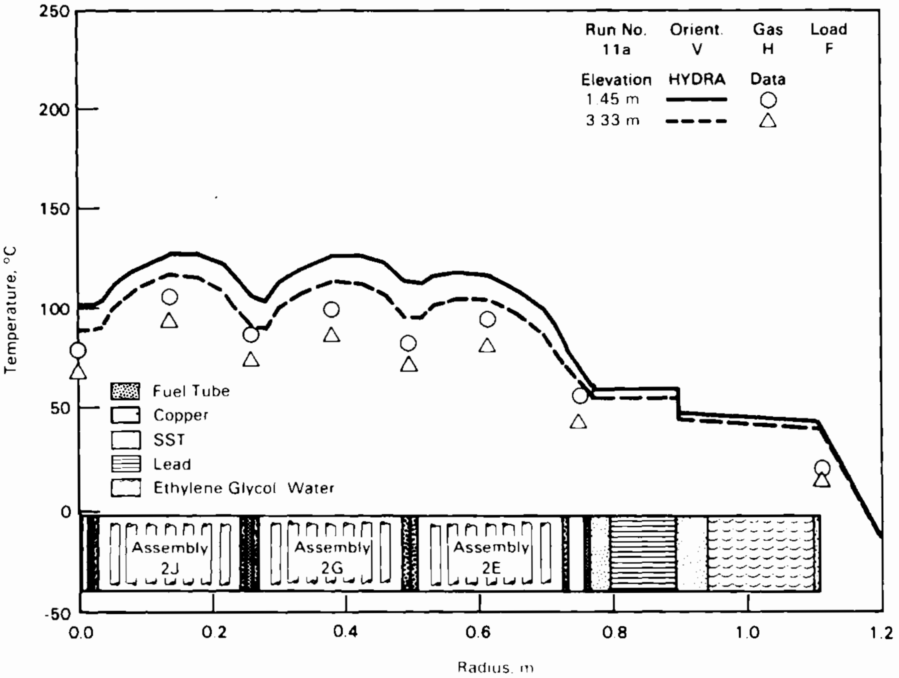
Run No. 11a
Orient. V
Gas H
Load F
Elevation
HYDRA
Data
1 45 m
3 33 m
Fuel Tube
Copper
SST
Lead
Ethylene Glycol Water
Assembly 2J
Assembly 2G
Assembly 2E
Temperature, °C
-50
0
50
100
150
200
250
Radius, m
0.0
0.2
0.4
0.6
0.8
1.0
1.2

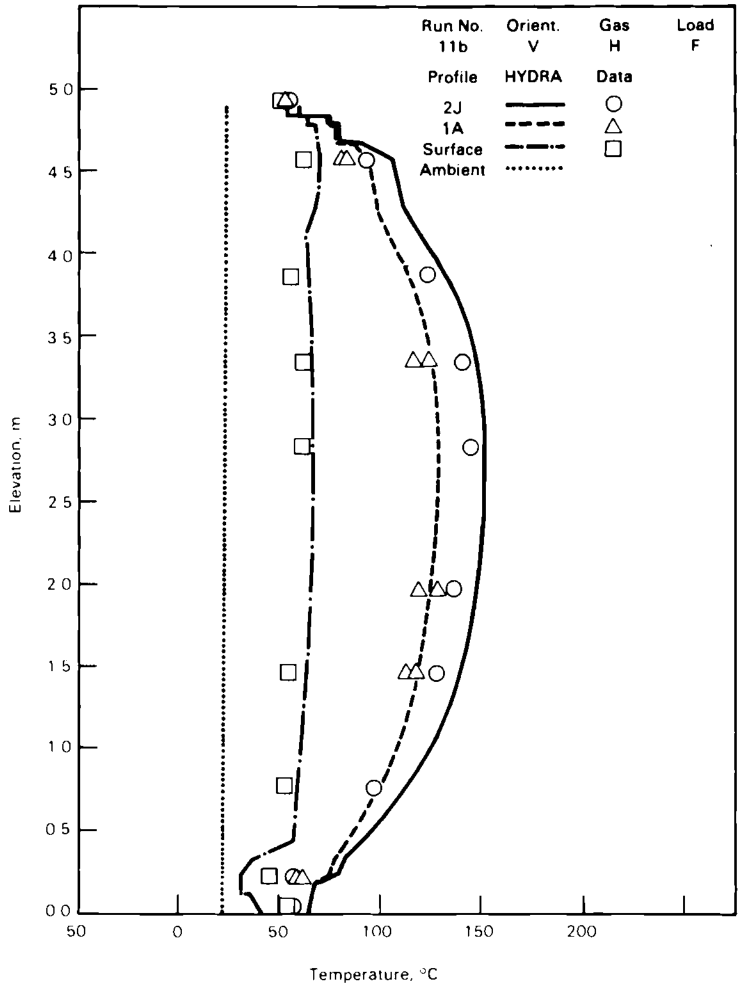
Run No.
11b
Orient.
V
Gas
H
Load
F
Profile
HYDRA
Data
2J
1A
Surface
Ambient
Elevation, m
5.0
4.5
4.0
3.5
3.0
2.5
2.0
1.5
1.0
0.5
0.0
50
0
50
100
150
200
Temperature, °C

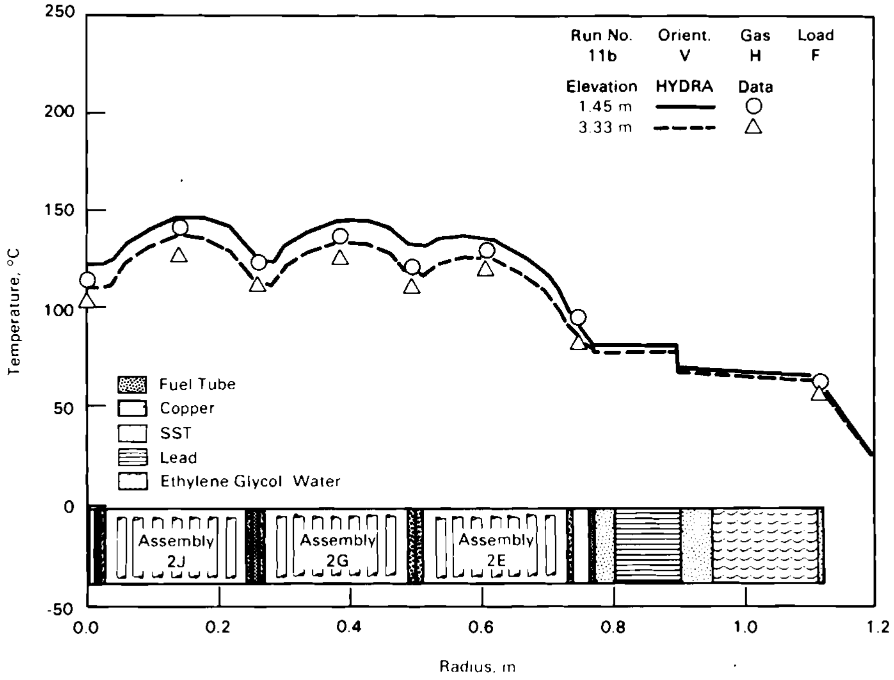
Run No.
11b
Orient.
V
Gas
H
Load
F
Elevation
HYDRA
Data
1.45 m
3.33 m
Fuel Tube
Copper
SST
Lead
Ethylene Glycol Water
Assembly 2J
Assembly 2G
Assembly 2E
Temperature, °C
250
200
150
100
50
0
-50
0.0
0.2
0.4
0.6
0.8
1.0
1.2
Radius, m

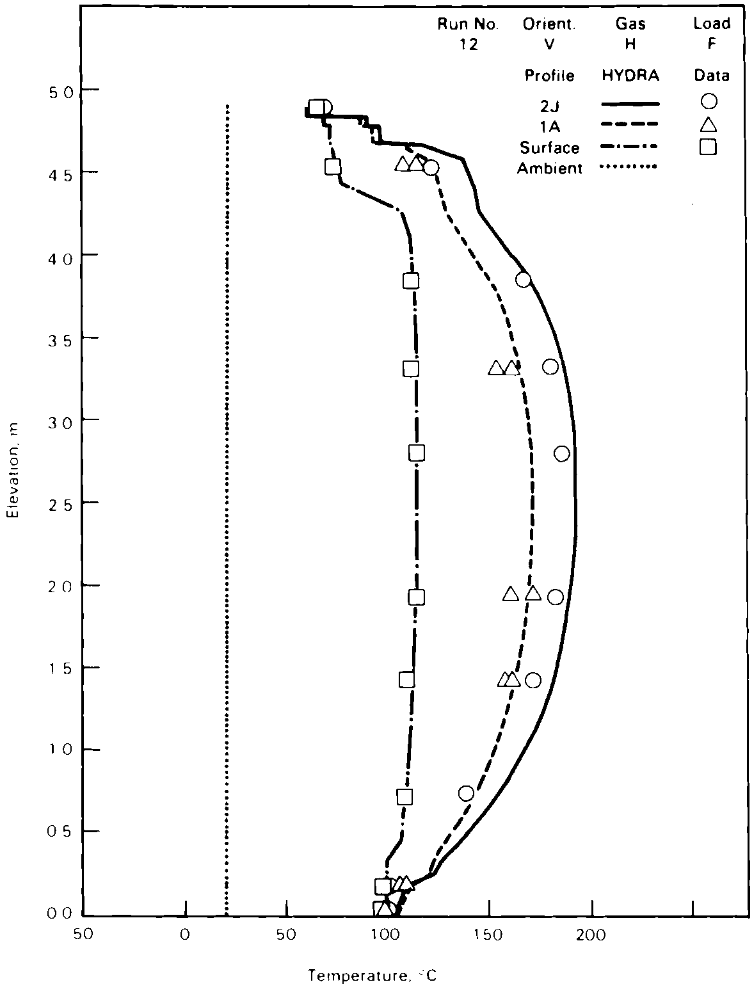
Run No.
12
Orient.
V
Gas
H
Load
F
Profile
HYDRA
Data
2J
1A
Surface
Ambient
Elevation, m
5.0
4.5
4.0
3.5
3.0
2.5
2.0
1.5
1.0
0.5
0.0
50
0
50
100
150
200
Temperature, °C

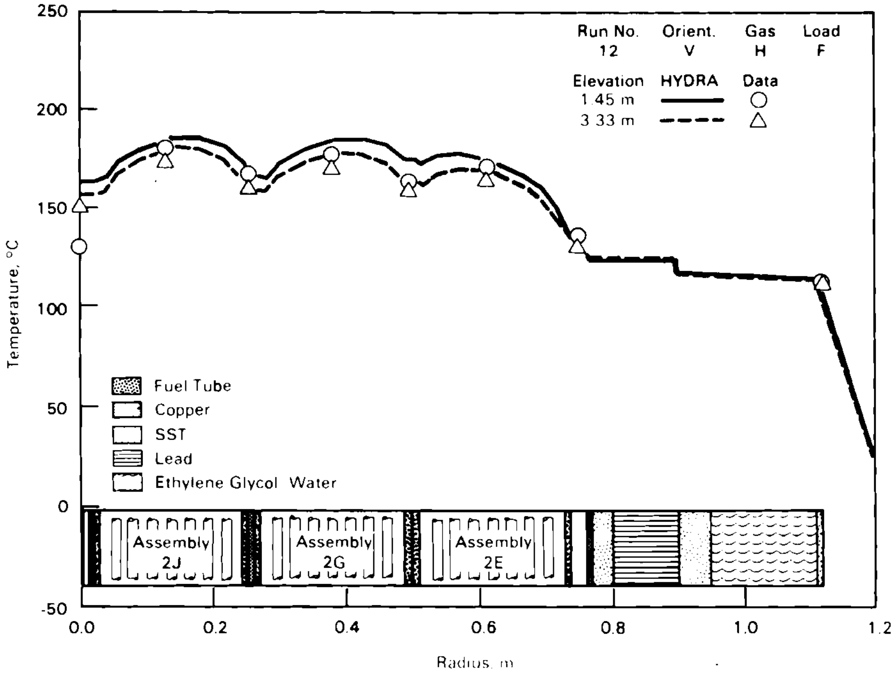
250
200
150
100
50
0
-50
Temperature, °C
Run No.
12
Orient.
V
Gas
H
Load
F
Elevation
HYDRA
Data
1.45 m
3.33 m
Fuel Tube
Copper
SST
Lead
Ethylene Glycol Water
Assembly
2J
Assembly
2G
Assembly
2E
0.0
0.2
0.4
0.6
0.8
1.0
1.2
Radius, m

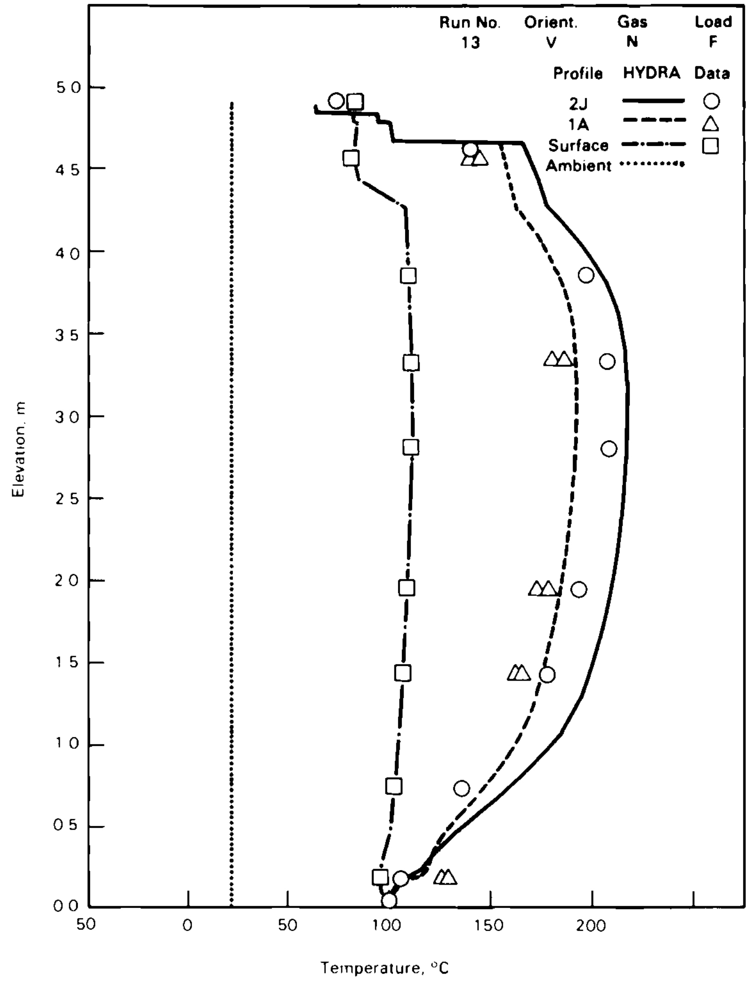
Run No. 13
Orient. V
Gas N
Load F
Profile
HYDRA
Data
2J
1A
Surface
Ambient
Elevation, m
0.0
0.5
1.0
1.5
2.0
2.5
3.0
3.5
4.0
4.5
5.0
Temperature, °C
50
0
50
100
150
200

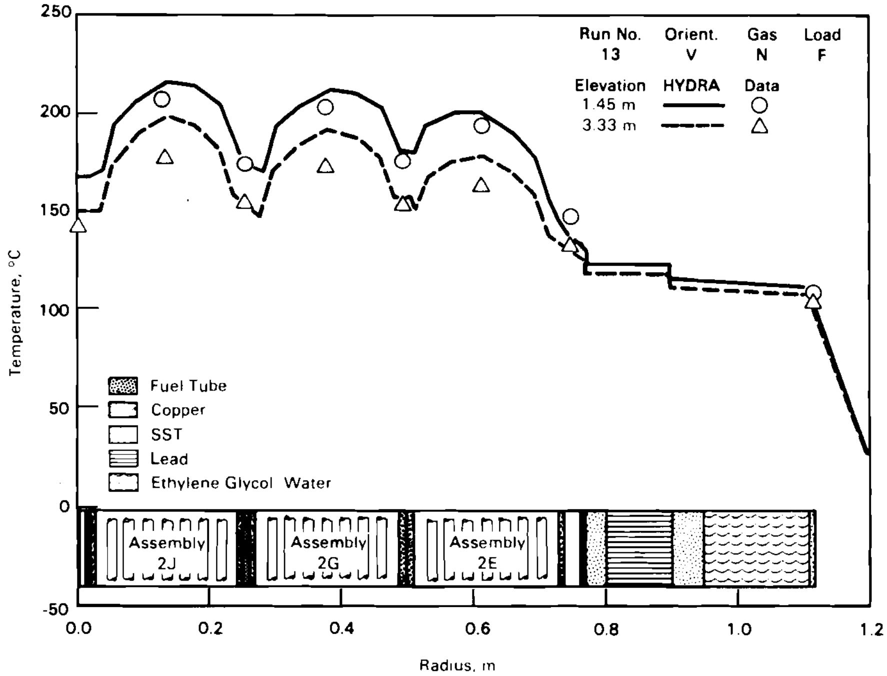
Run No. 13
Orient. V
Gas N
Load F
Elevation
HYDRA
Data
1.45 m
3.33 m
Fuel Tube
Copper
SST
Lead
Ethylene Glycol Water
Assembly 2J
Assembly 2G
Assembly 2E
Temperature, °C
250
200
150
100
50
0
-50
Radius, m
0.0
0.2
0.4
0.6
0.8
1.0
1.2

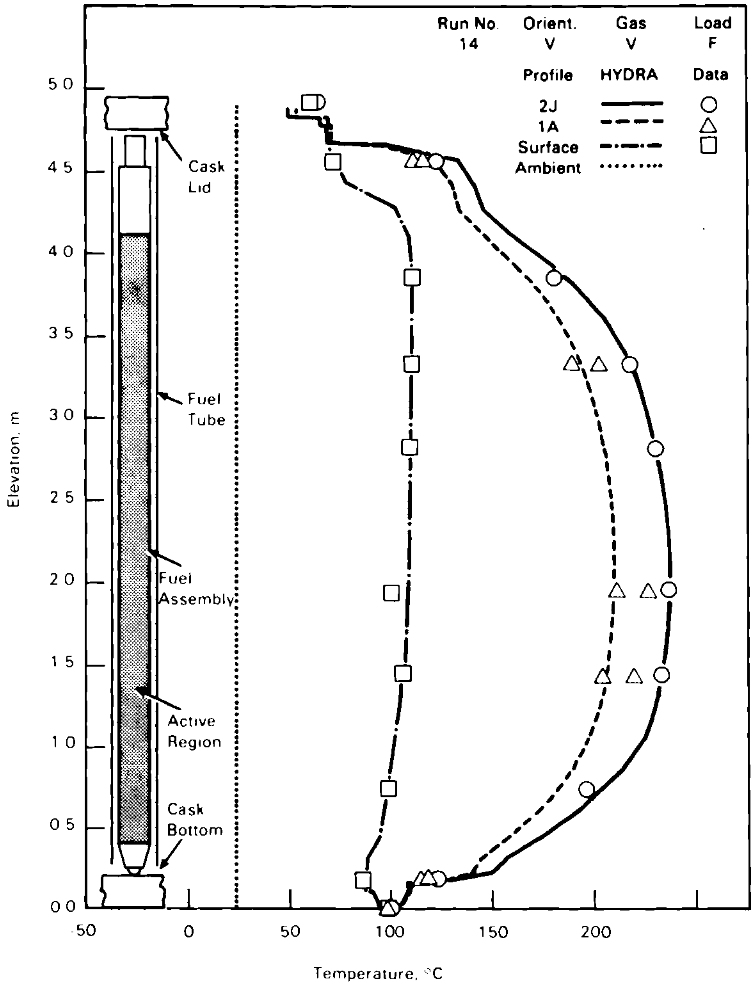
Run No. 14
Orient. V
Gas V
Load F
Profile
HYDRA
Data
2J
1A
Surface
Ambient
Cask Lid
Fuel Tube
Fuel Assembly
Active Region
Cask Bottom
Elevation, m
5.0
4.5
4.0
3.5
3.0
2.5
2.0
1.5
1.0
0.5
0.0
-50
0
50
100
150
200
Temperature, °C

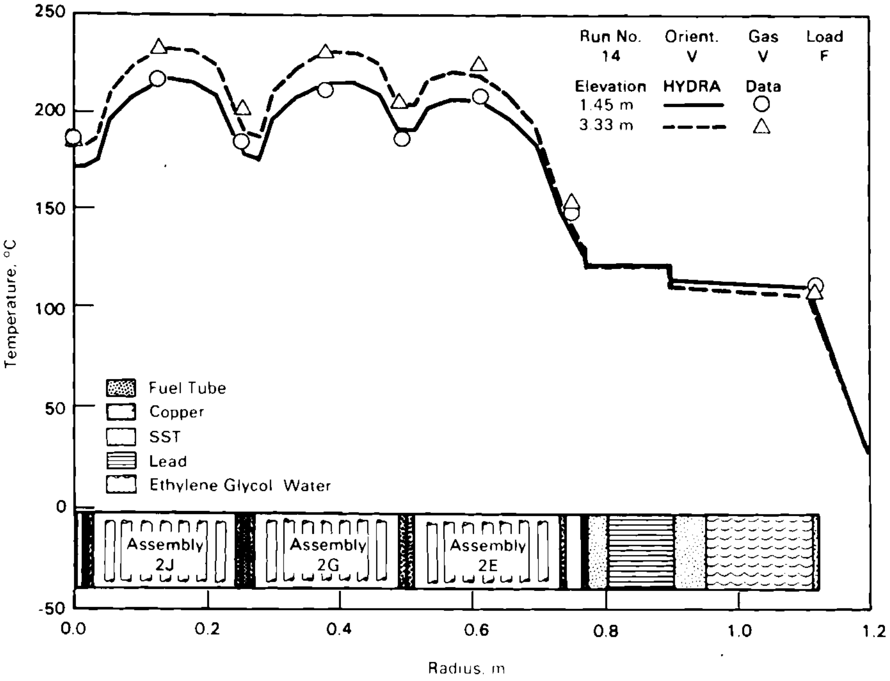
Run No. 14
Orient. V
Gas V
Load F
Elevation
HYDRA
Data
1.45 m
3.33 m
Fuel Tube
Copper
SST
Lead
Ethylene Glycol Water
Assembly 2J
Assembly 2G
Assembly 2E
Temperature, °C
250
200
150
100
50
0
-50
0.0
0.2
0.4
0.6
0.8
1.0
1.2
Radius, m

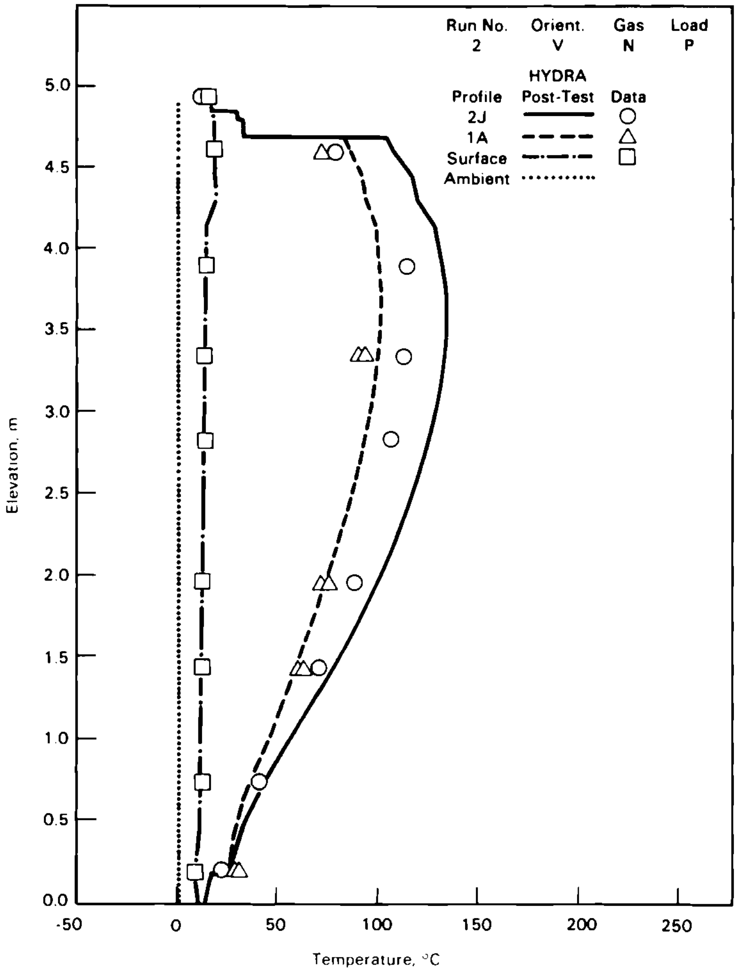
Run No. 2
Orient. V
Gas N
Load P
Profile
HYDRA Post-Test
Data
2J
1A
Surface
Ambient
Elevation, m
5.0
4.5
4.0
3.5
3.0
2.5
2.0
1.5
1.0
0.5
0.0
-50
0
50
100
150
200
250
Temperature, °C

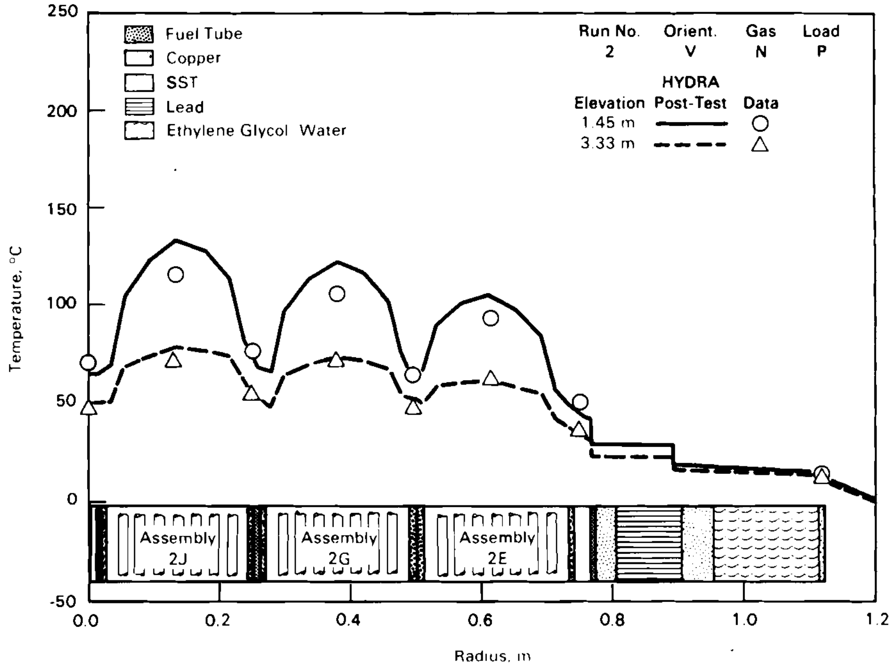
Fuel Tube
Copper
SST
Lead
Ethylene Glycol Water
Run No. 2
Orient. V
Gas N
Load P
Elevation
HYDRA Post-Test
Data
1.45 m
3.33 m
Assembly 2J
Assembly 2G
Assembly 2E
Temperature, °C
250
200
150
100
50
0
-50
0.0
0.2
0.4
0.6
0.8
1.0
1.2
Radius, m

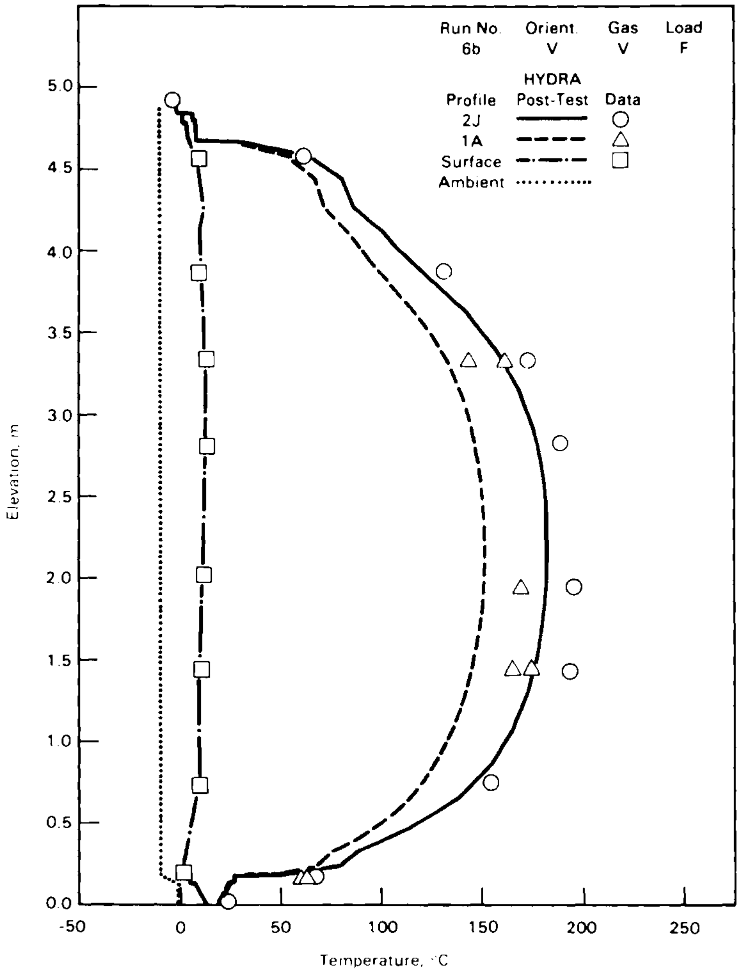
Run No. 6b
Orient. V
Gas V
Load F
Profile
HYDRA Post-Test
Data
2J ○
1A △
Surface □
Ambient
Elevation, m
5.0
4.5
4.0
3.5
3.0
2.5
2.0
1.5
1.0
0.5
0.0
-50
0
50
100
150
200
250
Temperature, °C

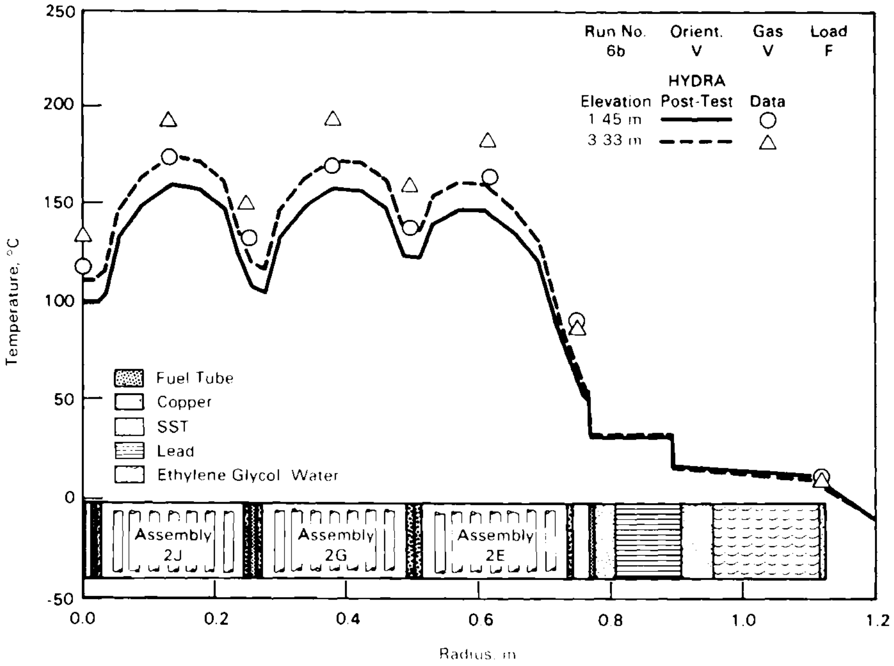
Run No. 6b
Orient. V
Gas V
Load F
Elevation
HYDRA Post-Test
Data
1.45 m ○
3.33 m △
Fuel Tube
Copper
SST
Lead
Ethylene Glycol Water
Assembly 2J
Assembly 2G
Assembly 2E
Temperature, °C
250
200
150
100
50
0
-50
0.0
0.2
0.4
0.6
0.8
1.0
1.2
Radius, m

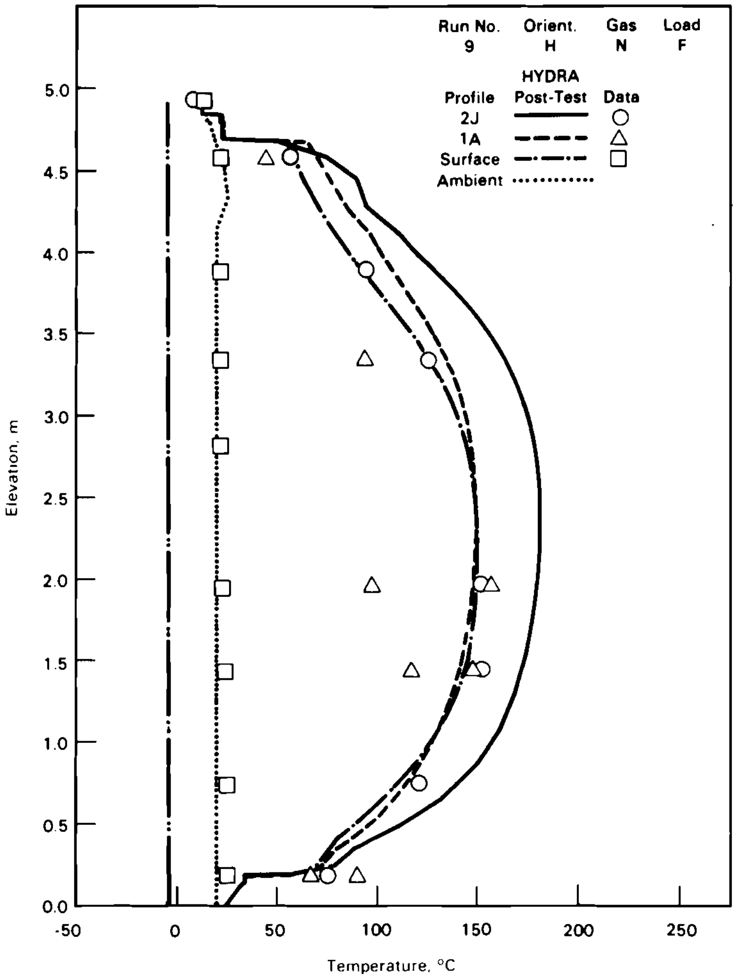
Run No.
9
Orient.
H
Gas
N
Load
F
HYDRA
Profile
Post-Test
Data
2J
1A
Surface
Ambient
Elevation, m
5.0
4.5
4.0
3.5
3.0
2.5
2.0
1.5
1.0
0.5
0.0
-50
0
50
100
150
200
250
Temperature, °C

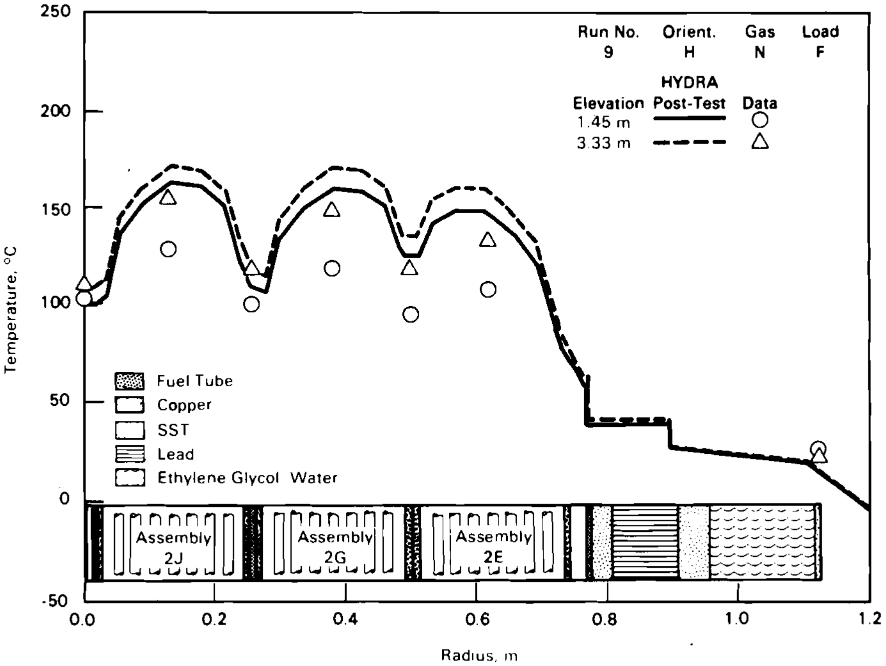
Run No.
9
Orient.
H
Gas
N
Load
F
HYDRA
Elevation
Post-Test
Data
1.45 m
3.33 m
Fuel Tube
Copper
SST
Lead
Ethylene Glycol Water
Assembly 2J
Assembly 2G
Assembly 2E
Temperature, °C
250
200
150
100
50
0
-50
0.0
0.2
0.4
0.6
0.8
1.0
1.2
Radius, m

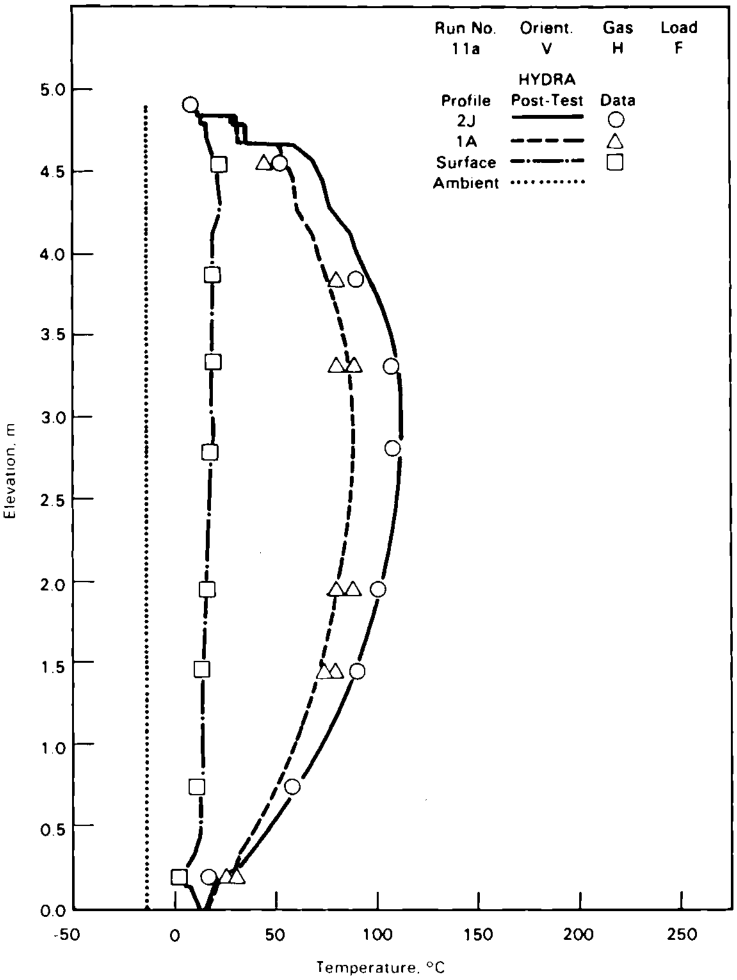

Run No. 11a
Orient. V
Gas H
Load F
HYDRA
Profile
Post-Test
Data
2J
1A
Surface
Ambient
5.0
4.5
4.0
3.5
3.0
2.5
2.0
1.5
1.0
0.5
0.0
Elevation, m
-50
0
50
100
150
200
250
Temperature, °C

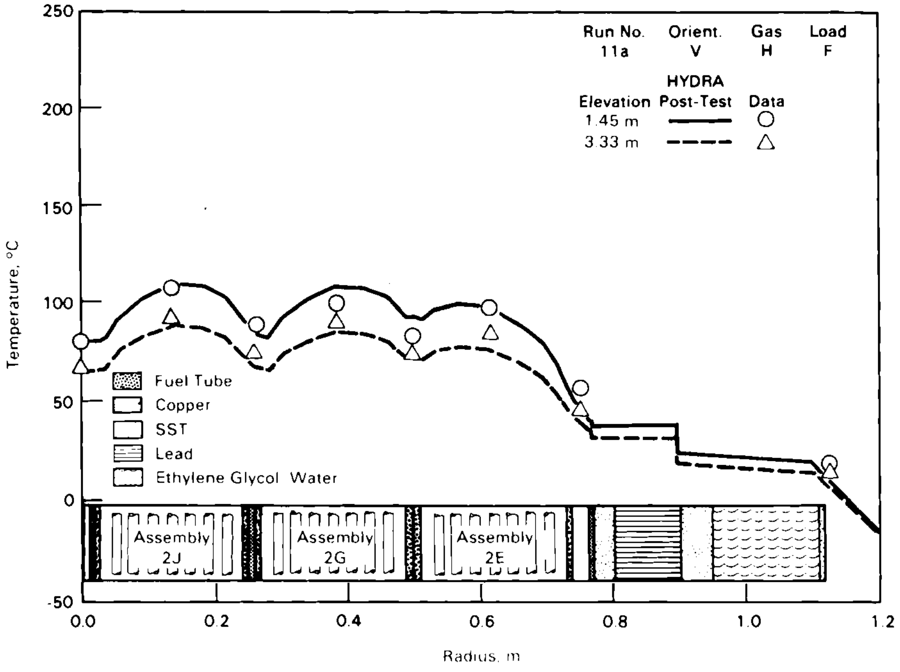

Run No. 11a
Orient. V
Gas H
Load F
HYDRA
Elevation
Post-Test
Data
1.45 m
3.33 m
250
200
150
100
50
0
-50
Temperature, °C
Fuel Tube
Copper
SST
Lead
Ethylene Glycol Water
Assembly 2J
Assembly 2G
Assembly 2E
0.0
0.2
0.4
0.6
0.8
1.0
1.2
Radius, m

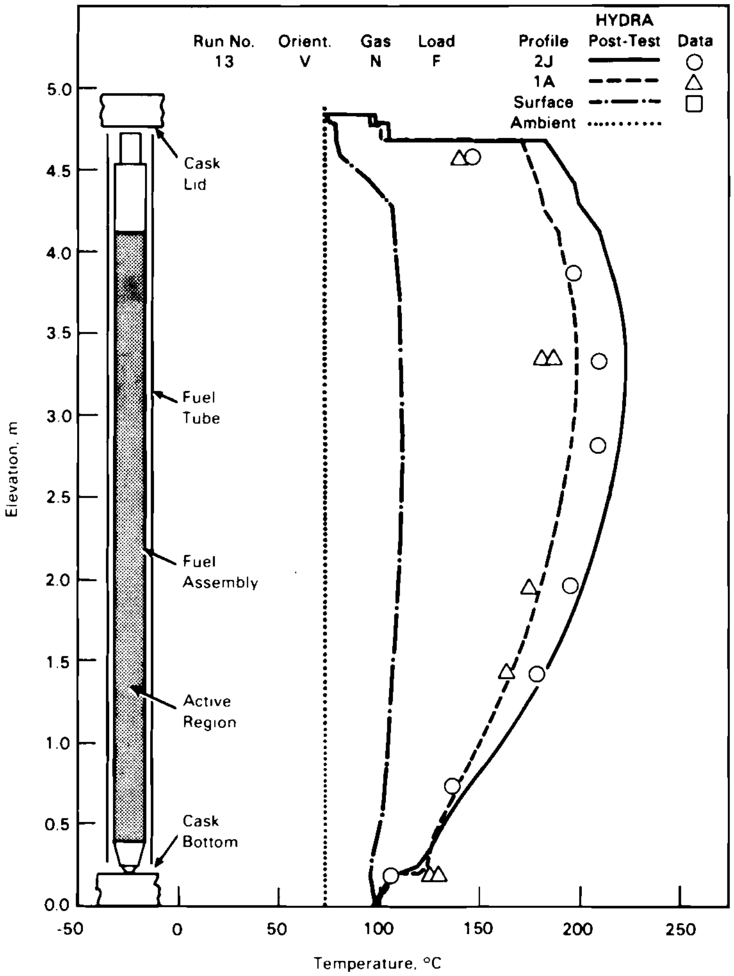
Run No. 13
Orient. V
Gas N
Load F
Profile
HYDRA Post-Test
Data
2J
1A
Surface
Ambient
Cask Lid
Fuel Tube
Fuel Assembly
Active Region
Cask Bottom
Elevation, m
5.0
4.5
4.0
3.5
3.0
2.5
2.0
1.5
1.0
0.5
0.0
-50
0
50
100
150
200
250
Temperature, °C

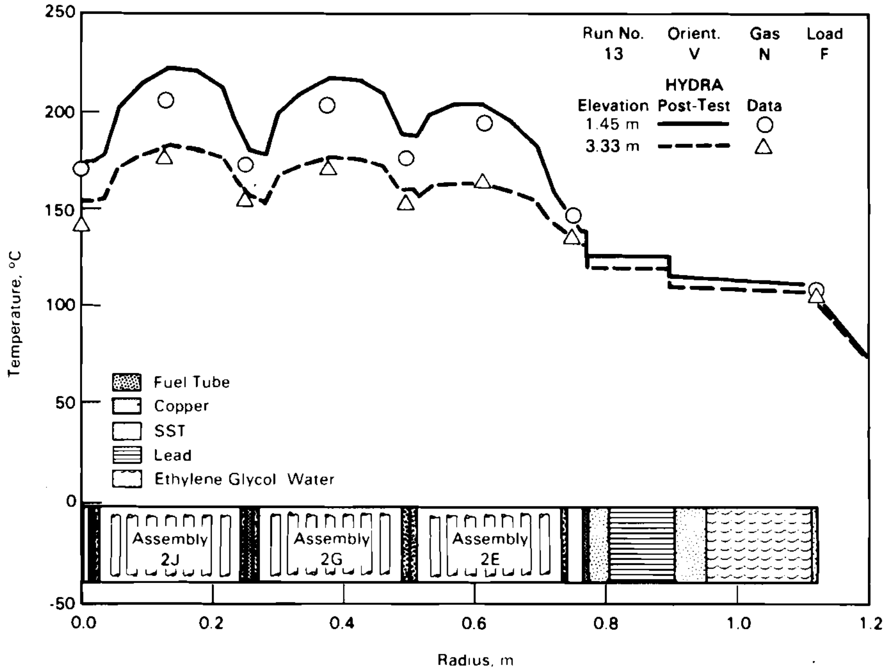
Run No. 13
Orient. V
Gas N
Load F
Elevation
HYDRA Post-Test
Data
1.45 m
3.33 m
Fuel Tube
Copper
SST
Lead
Ethylene Glycol Water
Assembly 2J
Assembly 2G
Assembly 2E
Temperature, °C
250
200
150
100
50
0
-50
0.0
0.2
0.4
0.6
0.8
1.0
1.2
Radius, m

APPENDIX E

ADDITIONAL COBRA-SFS PREDICTIONS COMPARED TO DATA

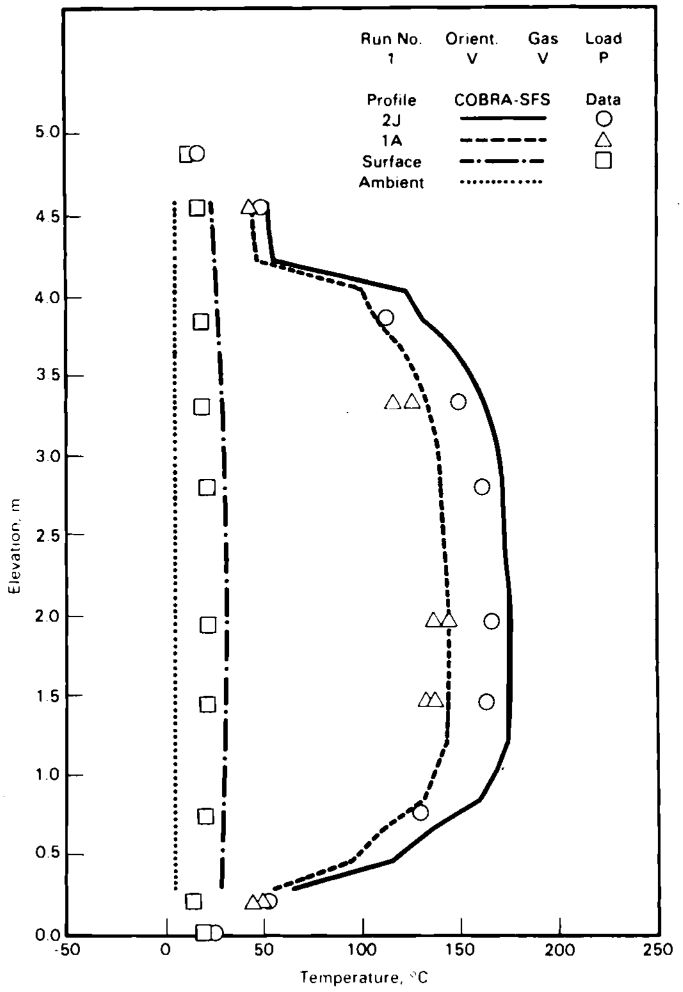
Run No.
1
Orient.
V
Gas
V
Load
P
Profile
COBRA-SFS
Data
2J
1A
Surface
Ambient
5.0
4.5
4.0
3.5
3.0
2.5
2.0
1.5
1.0
0.5
0.0
Elevation, m
-50
0
50
100
150
200
250
Temperature, °C

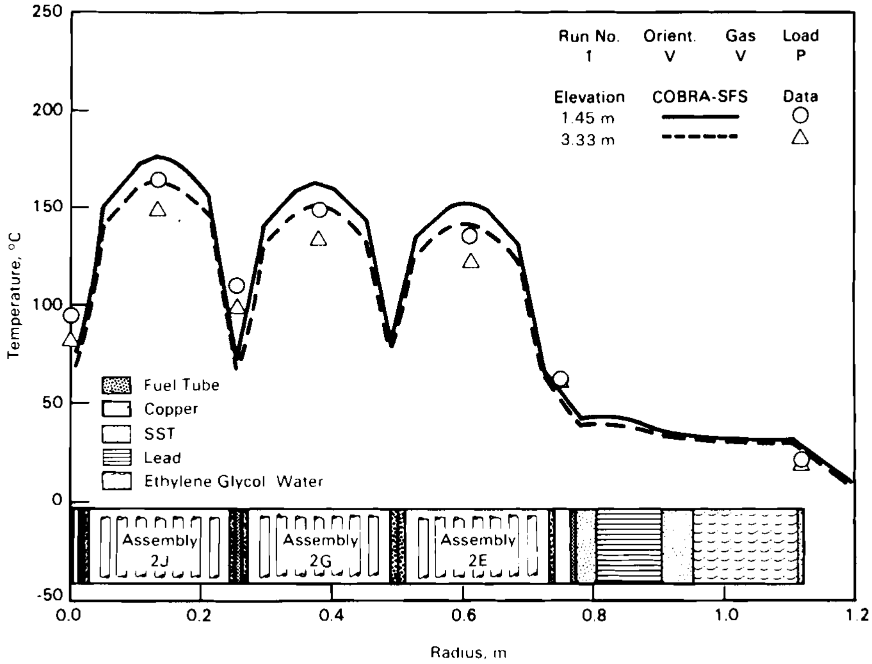
Run No.
1
Orient.
V
Gas
V
Load
P
Elevation
COBRA-SFS
Data
1.45 m
3.33 m
250
200
150
100
50
0
-50
Temperature, °C
Fuel Tube
Copper
SST
Lead
Ethylene Glycol Water
Assembly
2J
Assembly
2G
Assembly
2E
0.0
0.2
0.4
0.6
0.8
1.0
1.2
Radius, m

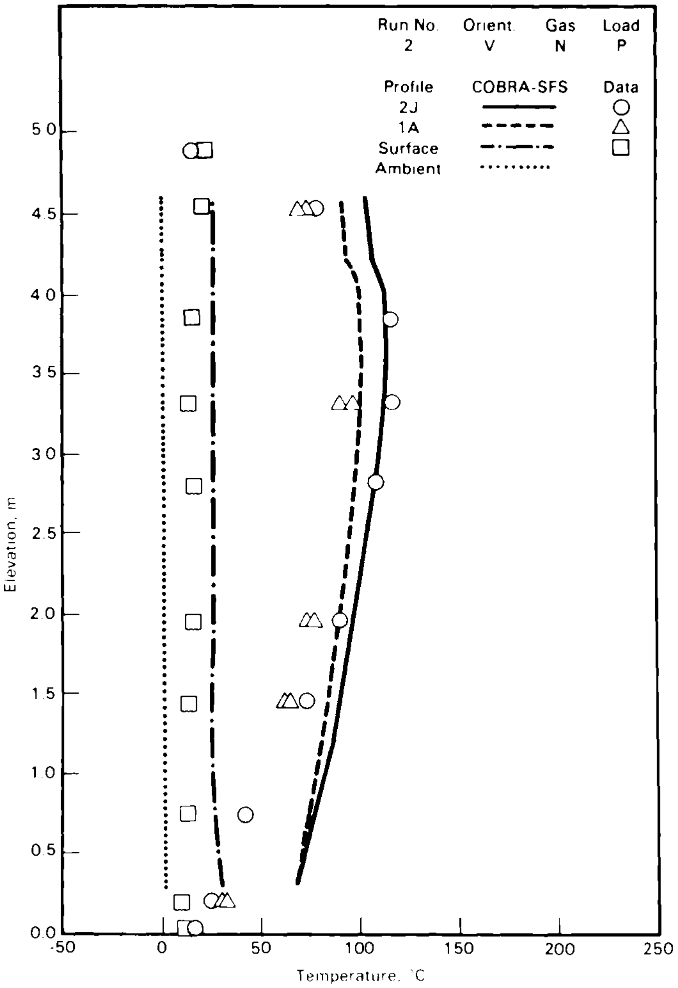
Run No. 2
Orient. V
Gas N
Load P
Profile
COBRA-SFS
Data
2J
1A
Surface
Ambient
Elevation, m
0.0
0.5
1.0
1.5
2.0
2.5
3.0
3.5
4.0
4.5
5.0
-50
0
50
100
150
200
250
Temperature, °C

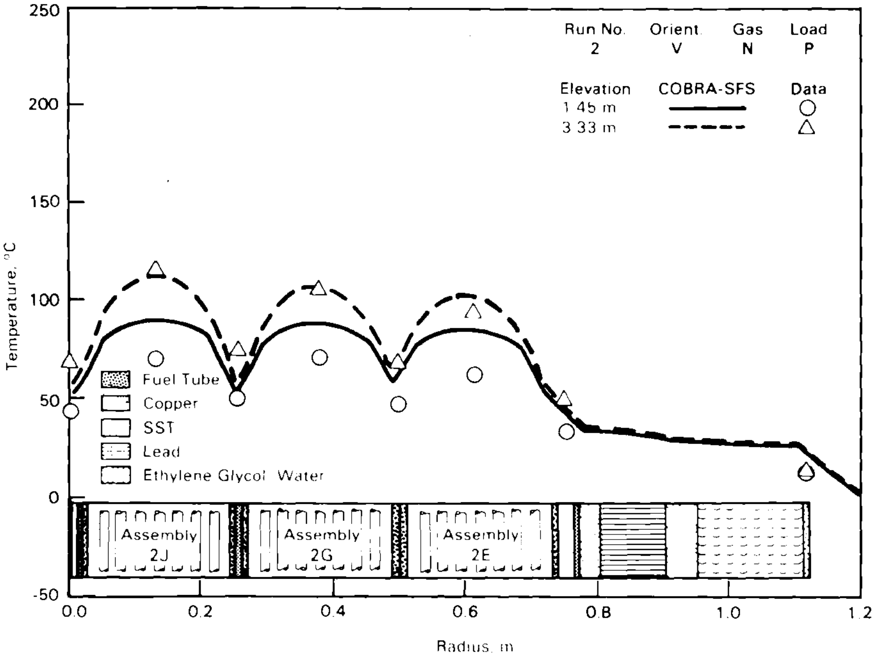
Run No. 2
Orient. V
Gas N
Load P
Elevation
COBRA-SFS
Data
1.45 m
3.33 m
Fuel Tube
Copper
SST
Lead
Ethylene Glycol Water
Assembly 2J
Assembly 2G
Assembly 2E
Temperature, °C
-50
0
50
100
150
200
250
0.0
0.2
0.4
0.6
0.8
1.0
1.2
Radius, m

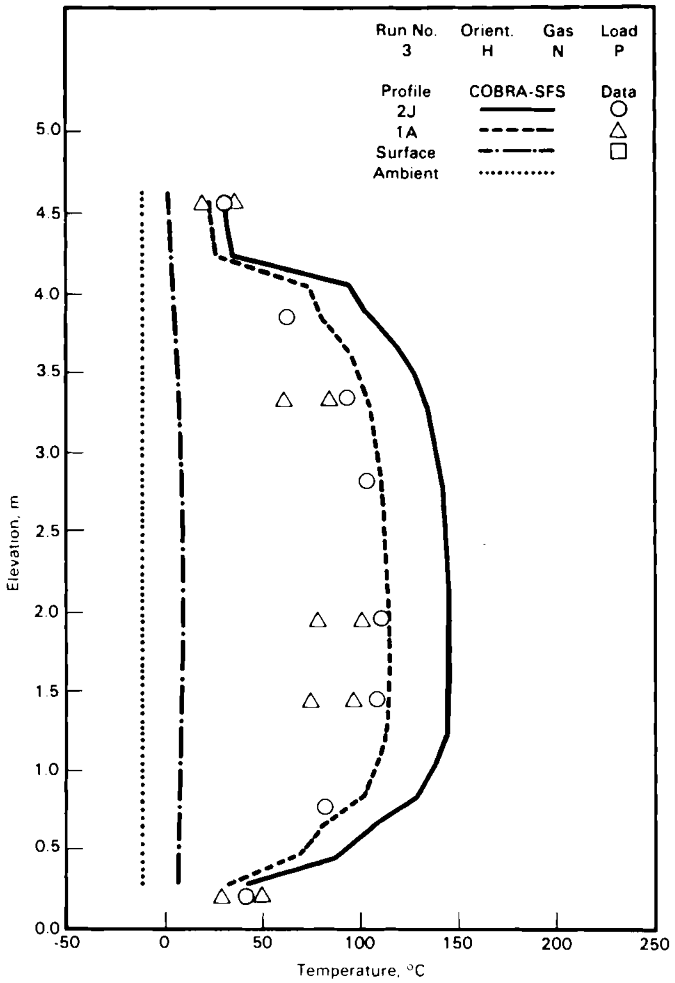
Run No. 3
Orient. H
Gas N
Load P
Profile
COBRA-SFS
Data
2J
1A
Surface
Ambient
Elevation, m
0.0
0.5
1.0
1.5
2.0
2.5
3.0
3.5
4.0
4.5
5.0
Temperature, °C
-50
0
50
100
150
200
250

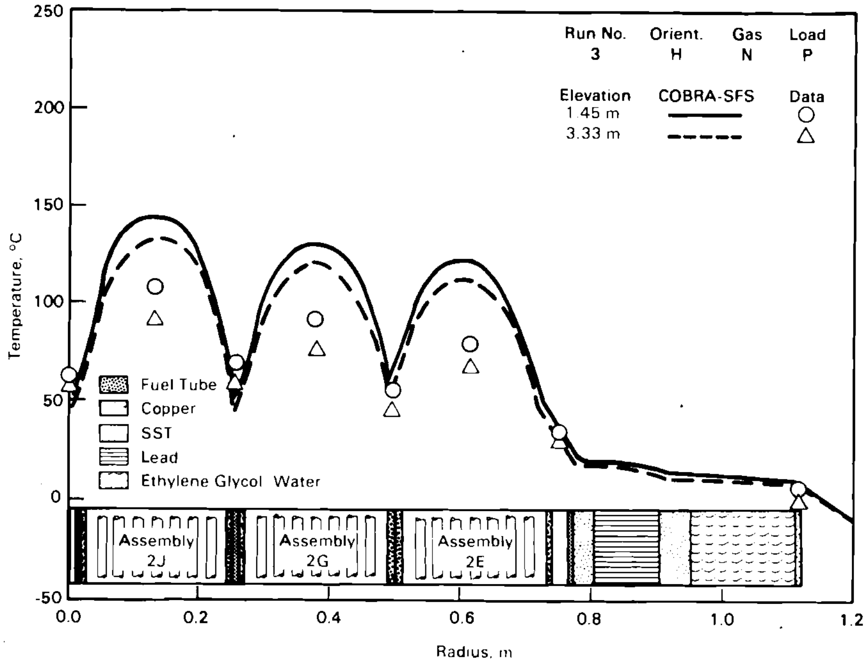
Run No. 3
Orient. H
Gas N
Load P
Elevation
COBRA-SFS
Data
1.45 m
3.33 m
Temperature, °C
-50
0
50
100
150
200
250
Fuel Tube
Copper
SST
Lead
Ethylene Glycol Water
Assembly 2J
Assembly 2G
Assembly 2E
Radius, m
0.0
0.2
0.4
0.6
0.8
1.0
1.2

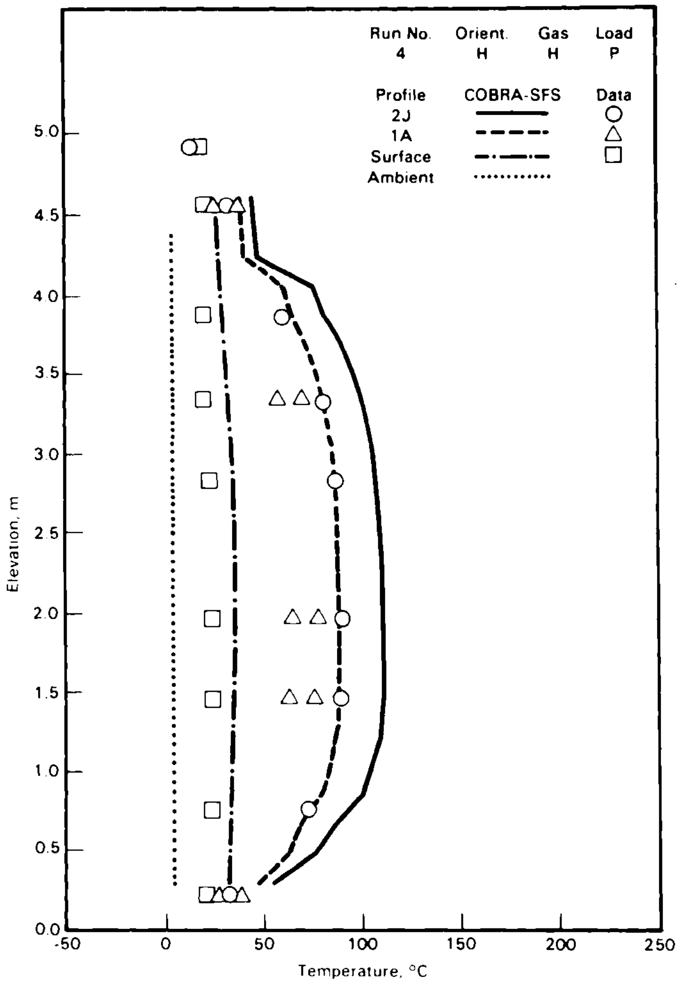
Run No. 4
Orient. H
Gas H
Load P
Profile
COBRA-SFS
Data
2J
1A
Surface
Ambient
Elevation, m
0.0
0.5
1.0
1.5
2.0
2.5
3.0
3.5
4.0
4.5
5.0
Temperature, °C
-50
0
50
100
150
200
250

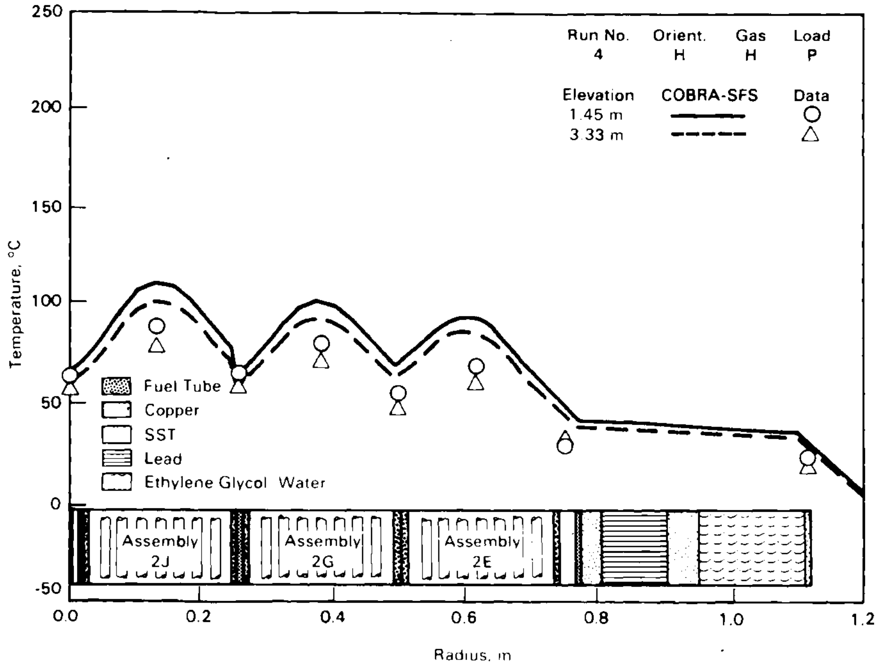
Run No. 4
Orient. H
Gas H
Load P
Elevation
COBRA-SFS
Data
1.45 m
3.33 m
Temperature, °C
-50
0
50
100
150
200
250
Fuel Tube
Copper
SST
Lead
Ethylene Glycol Water
Assembly 2J
Assembly 2G
Assembly 2E
Radius, m
0.0
0.2
0.4
0.6
0.8
1.0
1.2

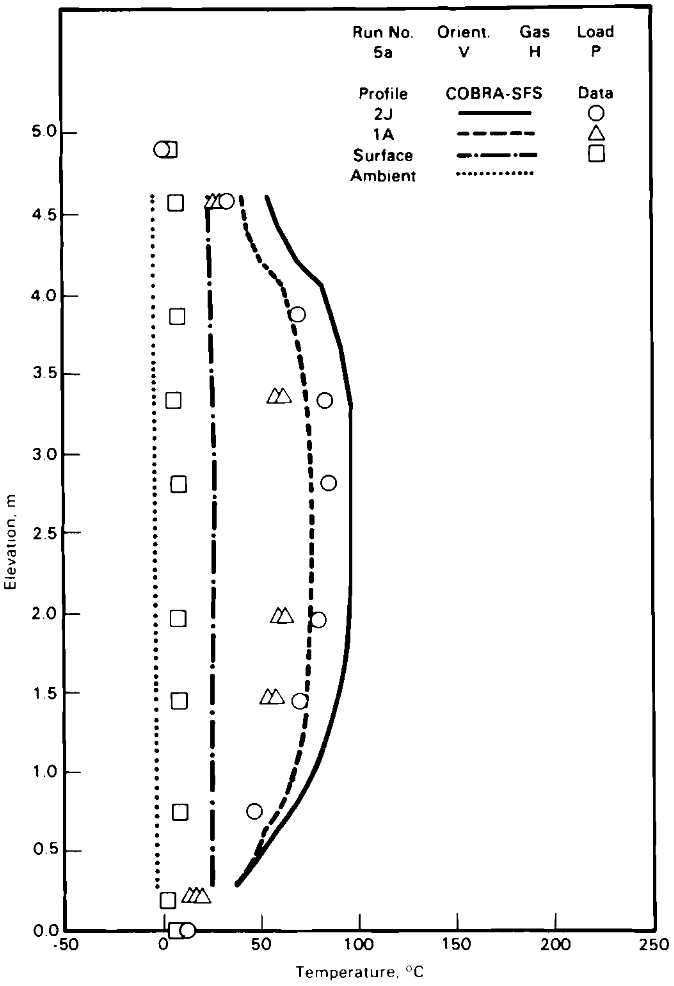
Run No. 5a
Orient. V
Gas H
Load P
Profile
COBRA-SFS
Data
2J
1A
Surface
Ambient
Elevation, m
0.0
0.5
1.0
1.5
2.0
2.5
3.0
3.5
4.0
4.5
5.0
Temperature, °C
-50
0
50
100
150
200
250

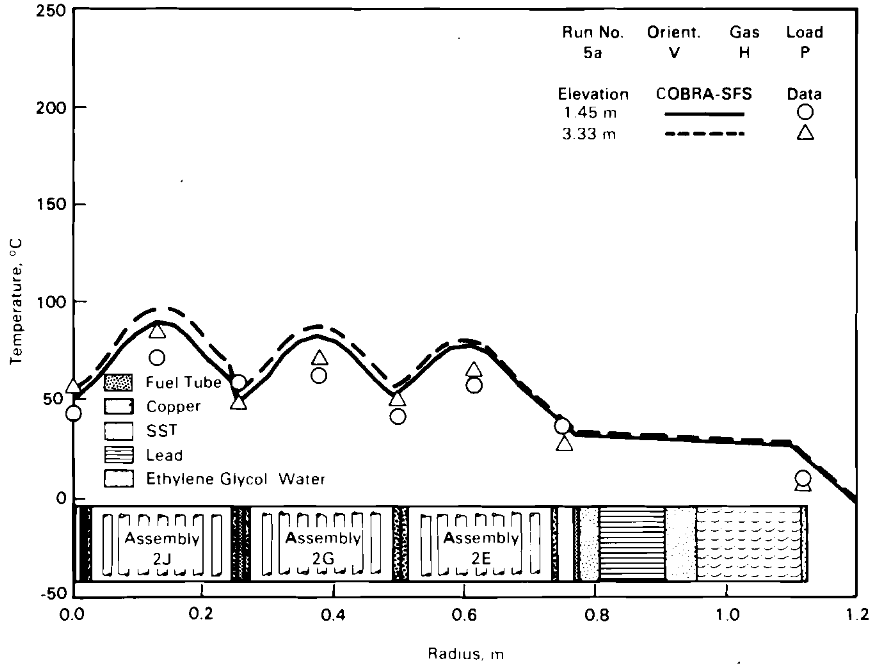
Run No. 5a
Orient. V
Gas H
Load P
Elevation
COBRA-SFS
Data
1.45 m
3.33 m
Fuel Tube
Copper
SST
Lead
Ethylene Glycol Water
Assembly 2J
Assembly 2G
Assembly 2E
Temperature, °C
-50
0
50
100
150
200
250
Radius, m
0.0
0.2
0.4
0.6
0.8
1.0
1.2

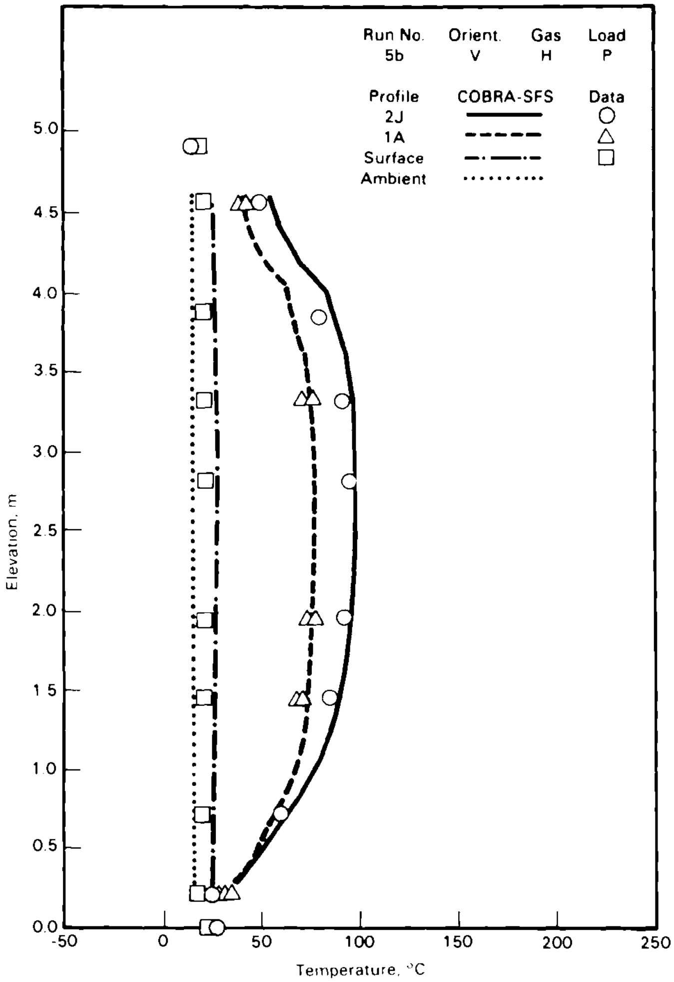
Run No. 5b
Orient. V
Gas H
Load P
Profile
COBRA-SFS
Data
2J
1A
Surface
Ambient
Elevation, m
0.0
0.5
1.0
1.5
2.0
2.5
3.0
3.5
4.0
4.5
5.0
Temperature, °C
-50
0
50
100
150
200
250

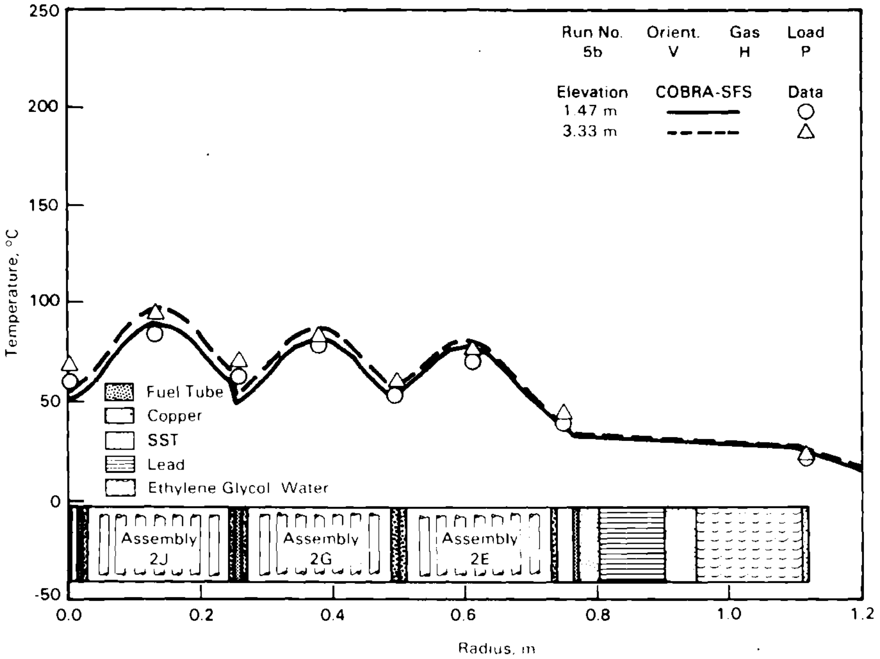
Run No. 5b
Orient. V
Gas H
Load P
Elevation
COBRA-SFS
Data
1.47 m
3.33 m
Fuel Tube
Copper
SST
Lead
Ethylene Glycol Water
Assembly 2J
Assembly 2G
Assembly 2E
Temperature, °C
-50
0
50
100
150
200
250
Radius, m
0.0
0.2
0.4
0.6
0.8
1.0
1.2

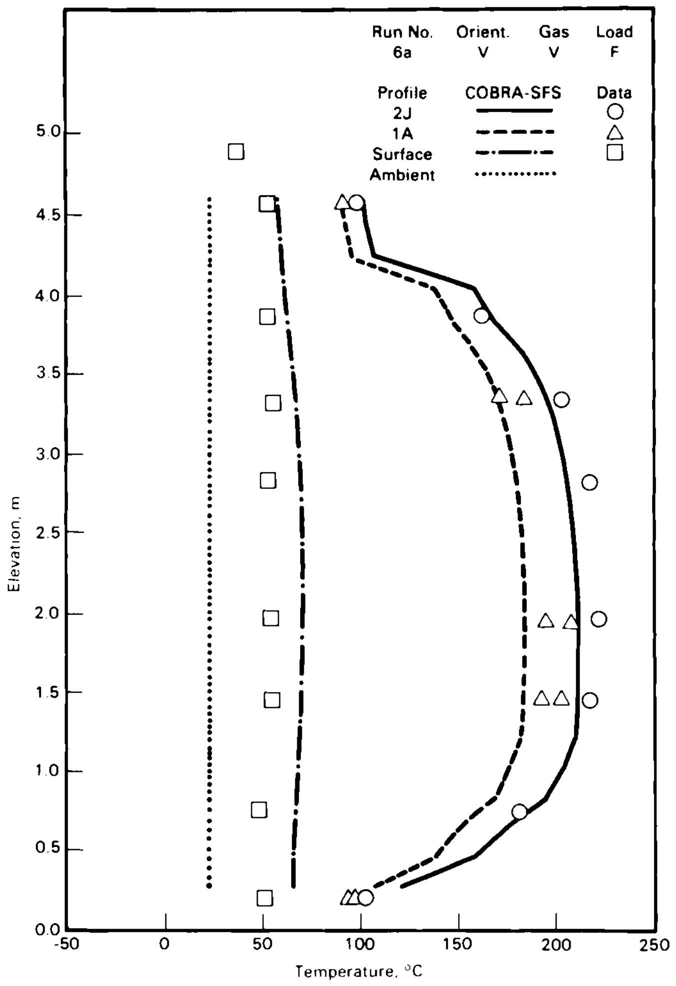
Run No. 6a
Orient. V
Gas V
Load F
Profile
COBRA-SFS
Data
2J
1A
Surface
Ambient
Elevation, m
0.0
0.5
1.0
1.5
2.0
2.5
3.0
3.5
4.0
4.5
5.0
Temperature, °C
-50
0
50
100
150
200
250

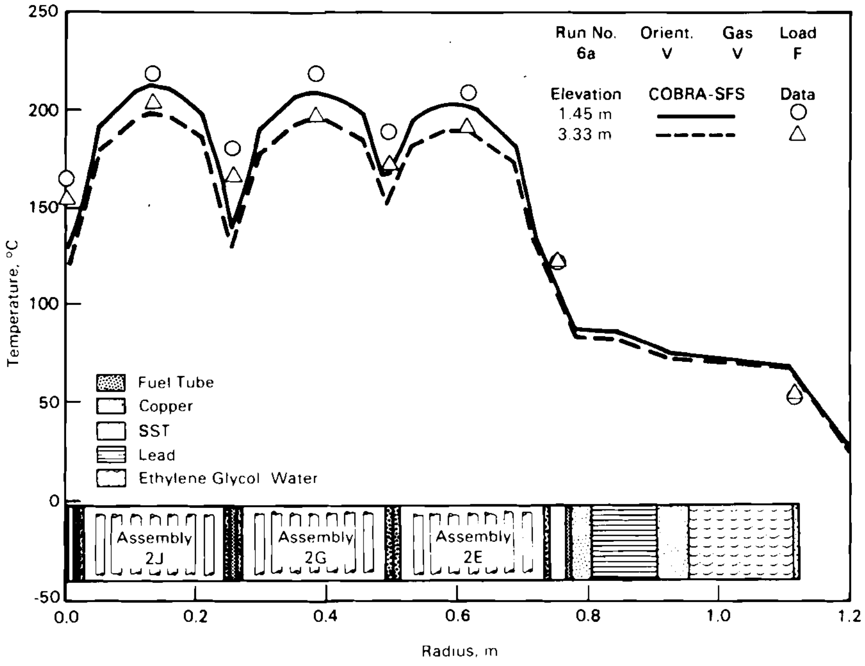
Run No. 6a
Orient. V
Gas V
Load F
Elevation
COBRA-SFS
Data
1.45 m
3.33 m
Fuel Tube
Copper
SST
Lead
Ethylene Glycol Water
Assembly 2J
Assembly 2G
Assembly 2E
Temperature, °C
-50
0
50
100
150
200
250
Radius, m
0.0
0.2
0.4
0.6
0.8
1.0
1.2

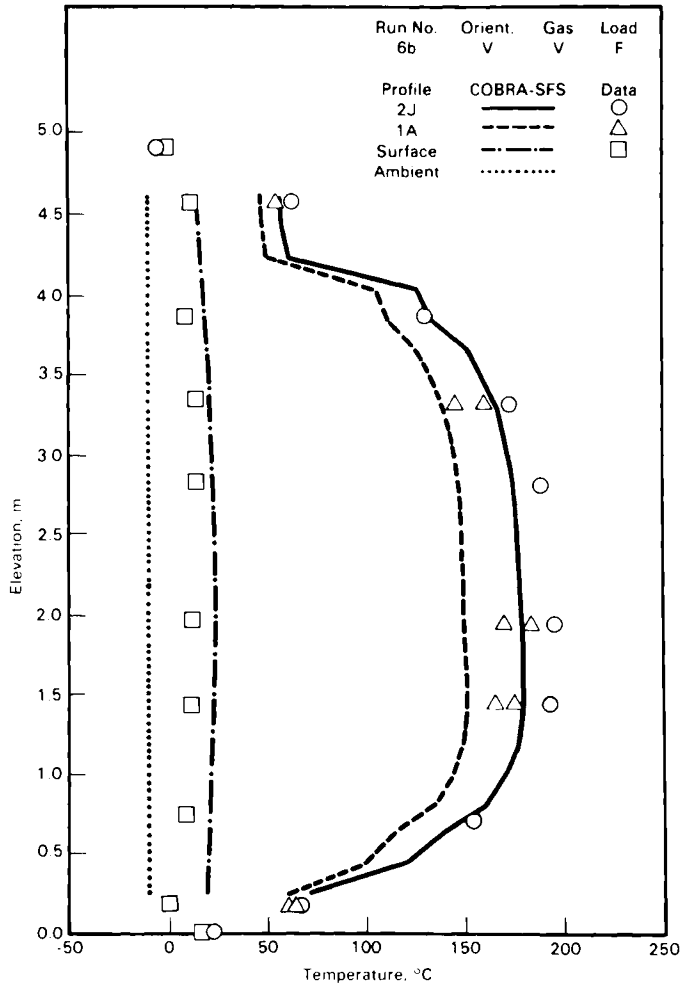
Run No. 6b
Orient. V
Gas V
Load F
Profile
COBRA-SFS
Data
2J
1A
Surface
Ambient
Elevation, m
0.0
0.5
1.0
1.5
2.0
2.5
3.0
3.5
4.0
4.5
5.0
Temperature, °C
-50
0
50
100
150
200
250

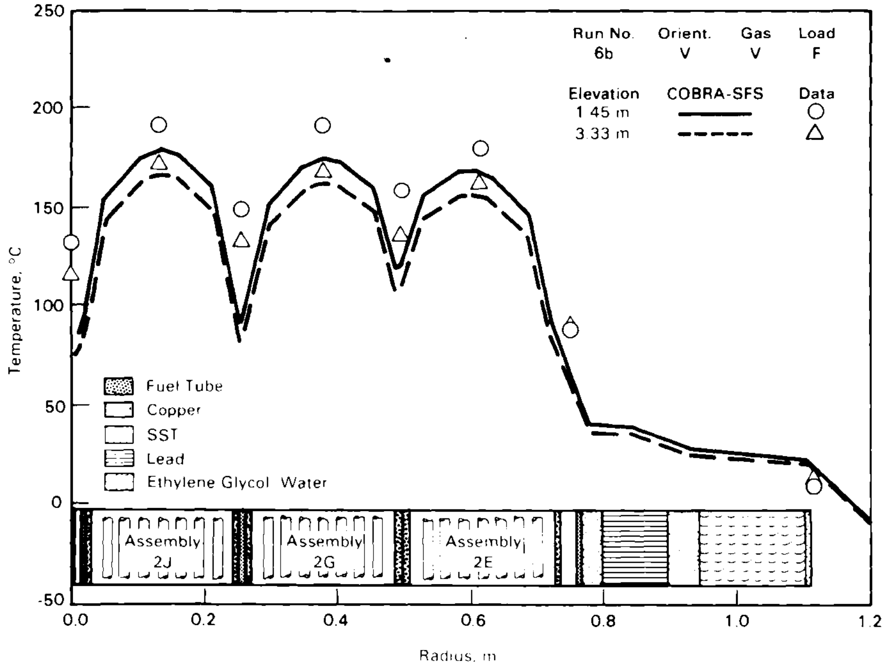
Run No. 6b
Orient. V
Gas V
Load F
Elevation
COBRA-SFS
Data
1.45 m
3.33 m
Fuel Tube
Copper
SST
Lead
Ethylene Glycol Water
Assembly 2J
Assembly 2G
Assembly 2E
Temperature, °C
-50
0
50
100
150
200
250
Radius, m
0.0
0.2
0.4
0.6
0.8
1.0
1.2

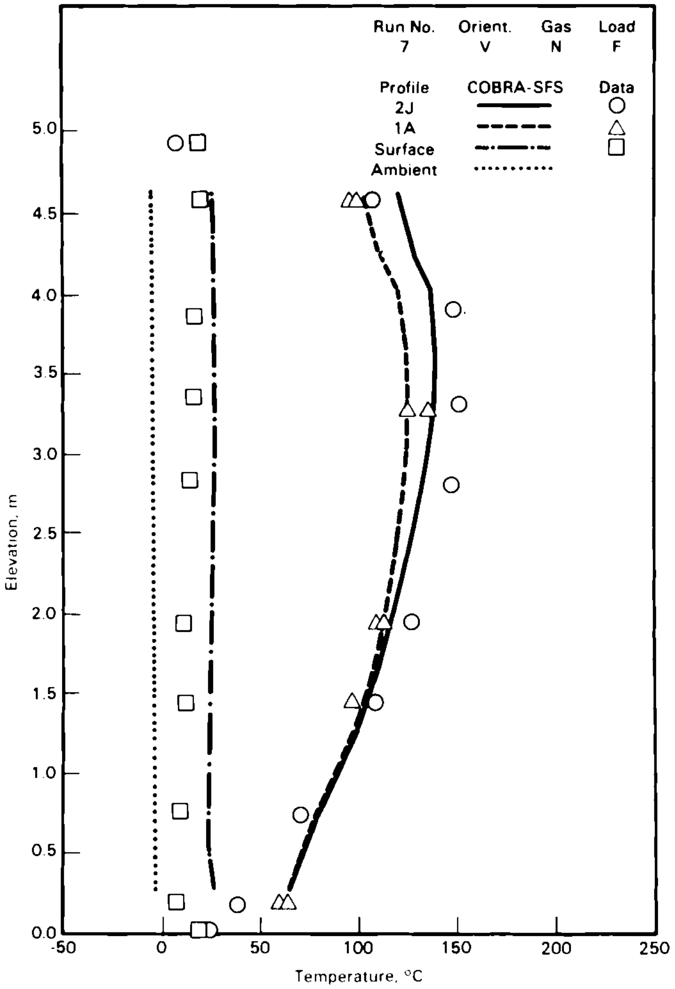

Run No. 7
Orient. V
Gas N
Load F
Profile
COBRA-SFS
Data
2J
1A
Surface
Ambient
Elevation, m
0.0
0.5
1.0
1.5
2.0
2.5
3.0
3.5
4.0
4.5
5.0
-50
0
50
100
150
200
250
Temperature, °C

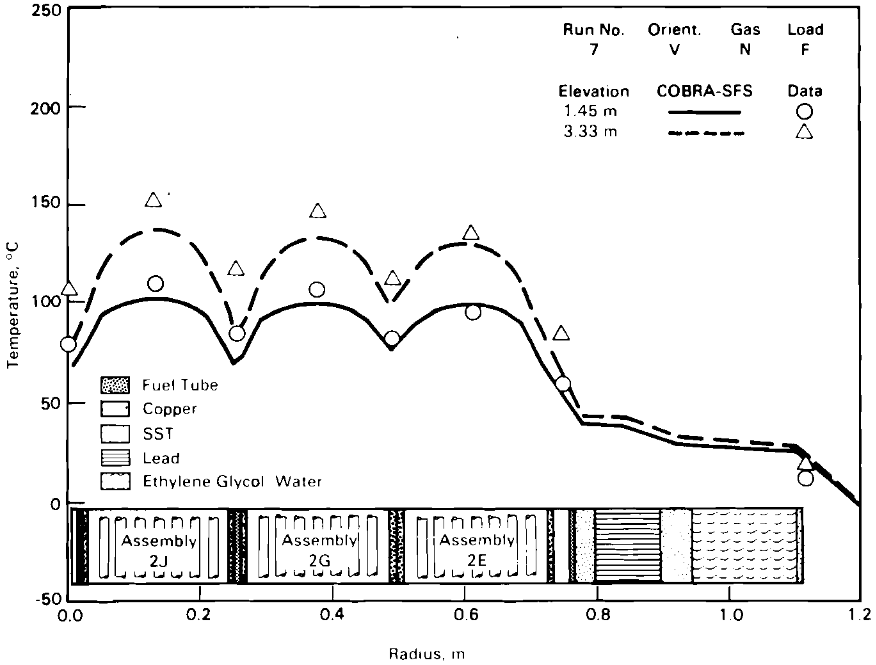

Run No. 7
Orient. V
Gas N
Load F
Elevation
COBRA-SFS
Data
1.45 m
3.33 m
Fuel Tube
Copper
SST
Lead
Ethylene Glycol Water
Assembly 2J
Assembly 2G
Assembly 2E
Temperature, °C
250
200
150
100
50
0
-50
0.0
0.2
0.4
0.6
0.8
1.0
1.2
Radius, m

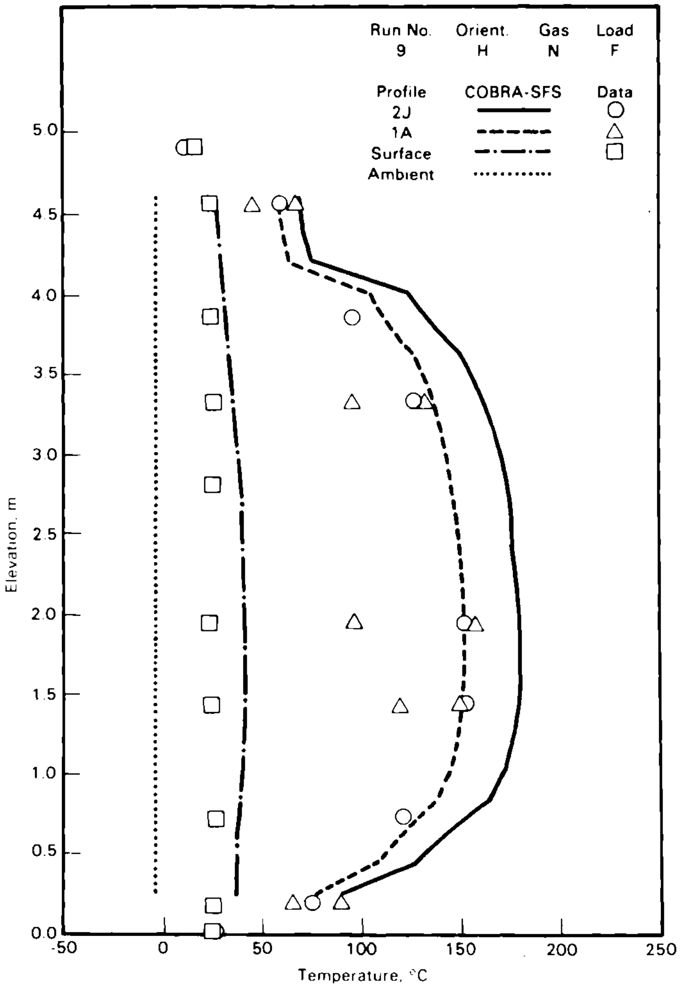
Run No. 9
Orient. H
Gas N
Load F
Profile
COBRA-SFS
Data
2J
1A
Surface
Ambient
Elevation, m
0.0
0.5
1.0
1.5
2.0
2.5
3.0
3.5
4.0
4.5
5.0
Temperature, °C
-50
0
50
100
150
200
250

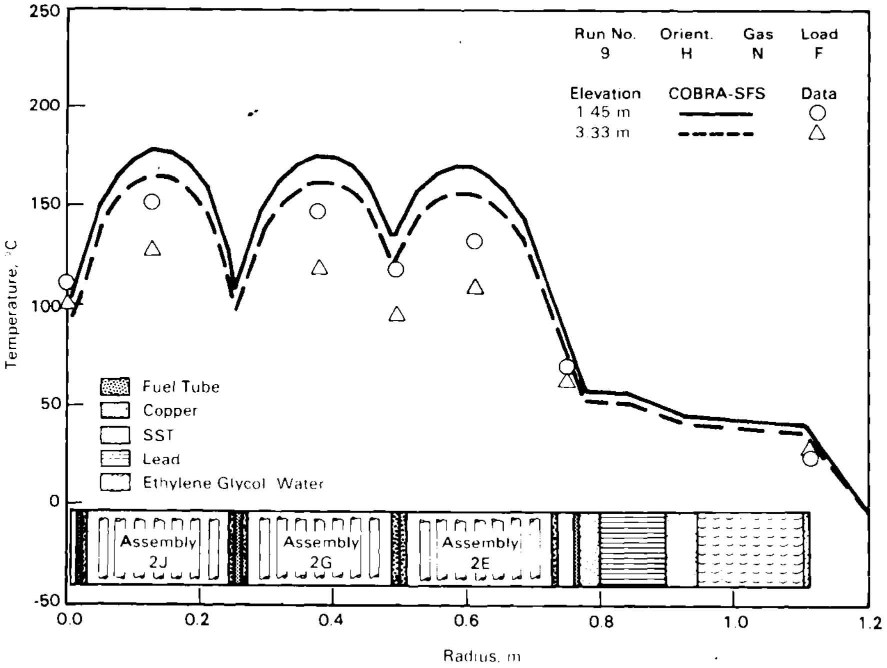
Run No. 9
Orient. H
Gas N
Load F
Elevation
COBRA-SFS
Data
1.45 m
3.33 m
Fuel Tube
Copper
SST
Lead
Ethylene Glycol Water
Assembly 2J
Assembly 2G
Assembly 2E
Temperature, °C
-50
0
50
100
150
200
250
Radius, m
0.0
0.2
0.4
0.6
0.8
1.0
1.2

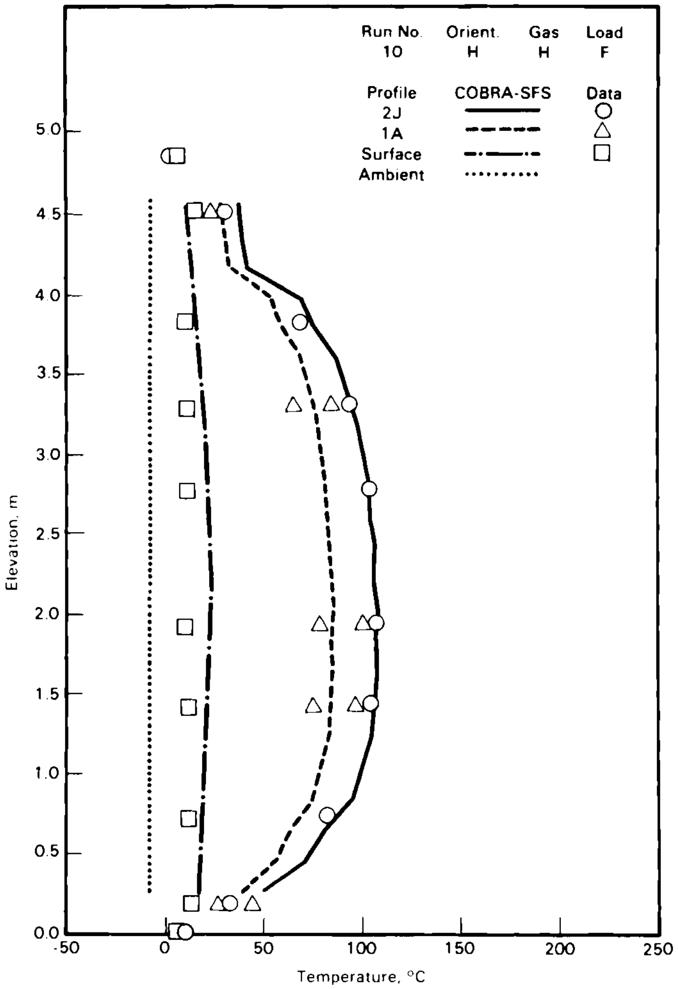
Run No. 10
Orient. H
Gas H
Load F
Profile
COBRA-SFS
Data
2J
1A
Surface
Ambient
5.0
4.5
4.0
3.5
3.0
2.5
2.0
1.5
1.0
0.5
0.0
Elevation, m
-50
0
50
100
150
200
250
Temperature, °C

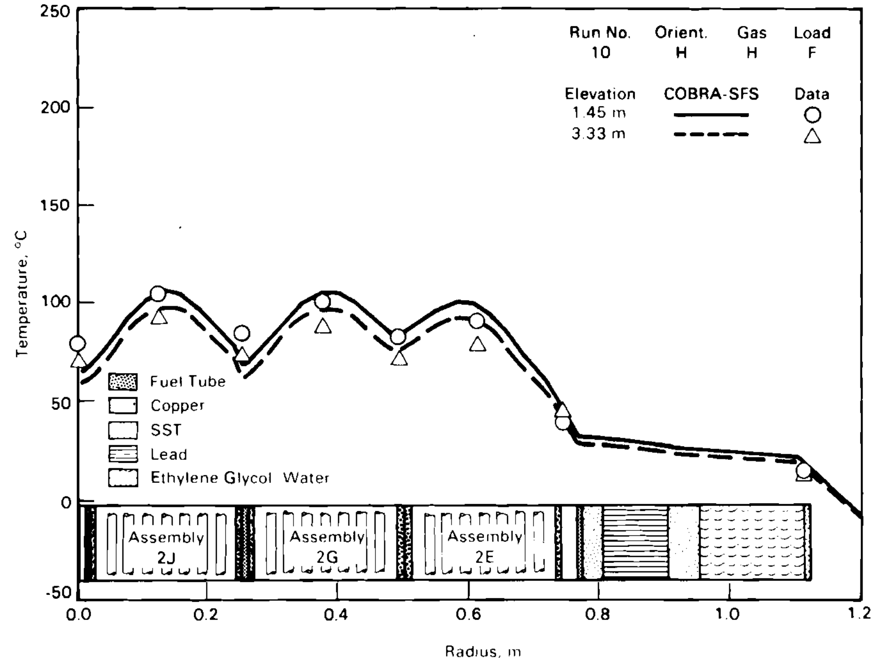
Run No. 10
Orient. H
Gas H
Load F
Elevation
COBRA-SFS
Data
1.45 m
3.33 m
250
200
150
100
50
0
-50
Temperature, °C
Fuel Tube
Copper
SST
Lead
Ethylene Glycol Water
Assembly 2J
Assembly 2G
Assembly 2E
0.0
0.2
0.4
0.6
0.8
1.0
1.2
Radius, m

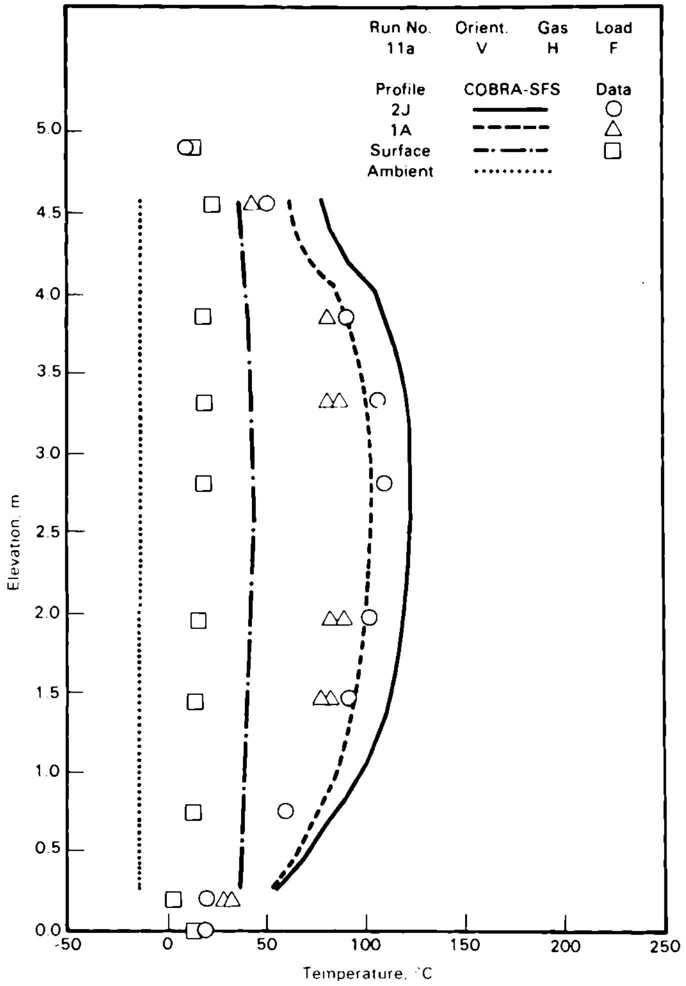
Run No. 11a
Orient. V
Gas H
Load F
Profile
2J
1A
Surface
Ambient
COBRA-SFS
Data
Elevation, m
0.0
0.5
1.0
1.5
2.0
2.5
3.0
3.5
4.0
4.5
5.0
Temperature, °C
-50
0
50
100
150
200
250

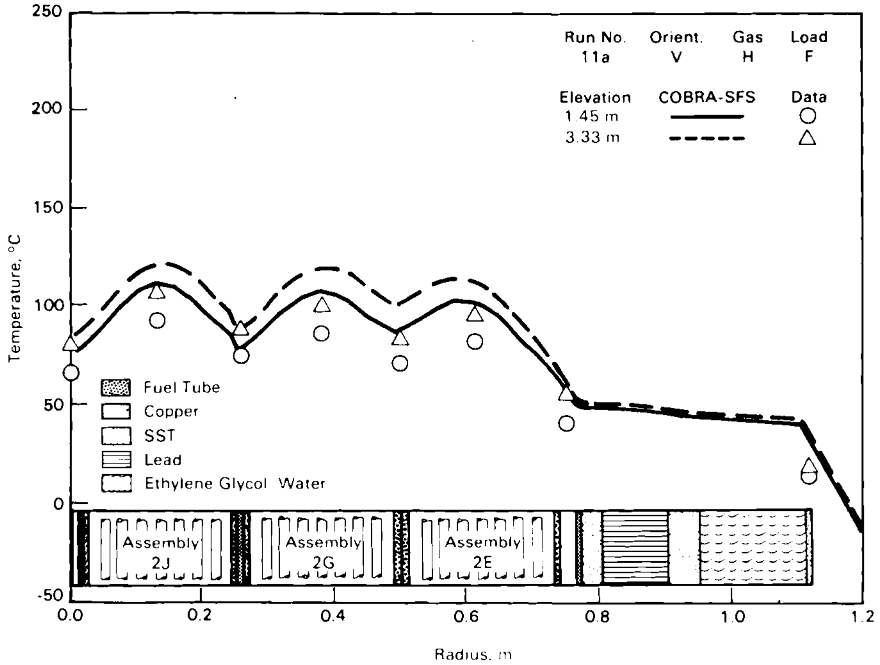
Run No. 11a
Orient. V
Gas H
Load F
Elevation
1.45 m
3.33 m
COBRA-SFS
Data
Fuel Tube
Copper
SST
Lead
Ethylene Glycol Water
Assembly 2J
Assembly 2G
Assembly 2E
Temperature, °C
-50
0
50
100
150
200
250
Radius, m
0.0
0.2
0.4
0.6
0.8
1.0
1.2

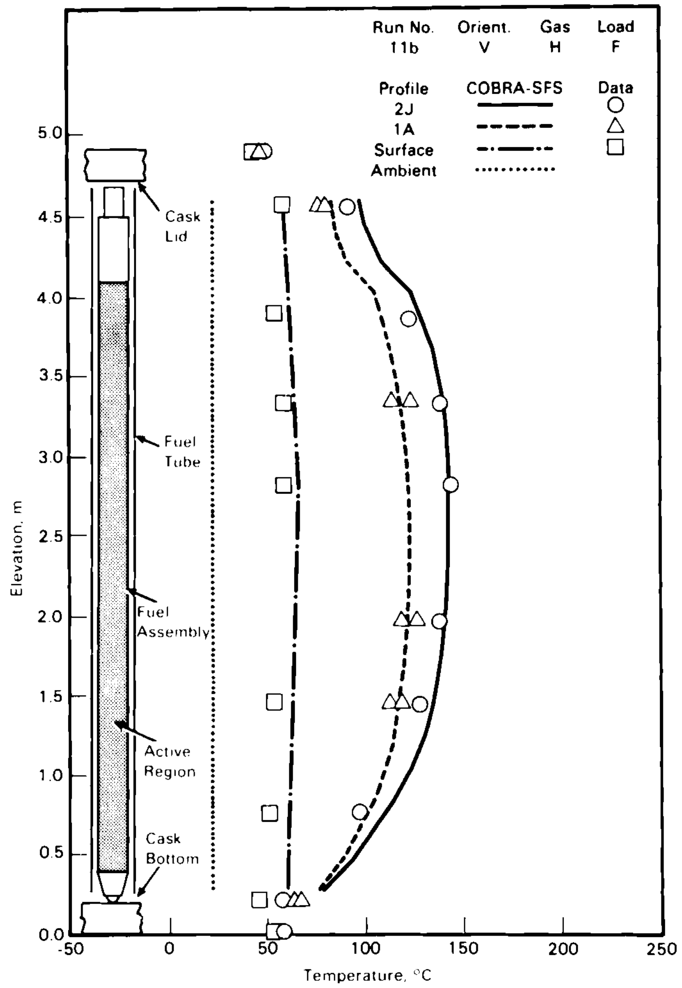
Run No. 11b
Orient. V
Gas H
Load F
Profile
COBRA-SFS
Data
2J
1A
Surface
Ambient
Cask Lid
Fuel Tube
Fuel Assembly
Active Region
Cask Bottom
Elevation, m
Temperature, °C
0.0
0.5
1.0
1.5
2.0
2.5
3.0
3.5
4.0
4.5
5.0
-50
0
50
100
150
200
250

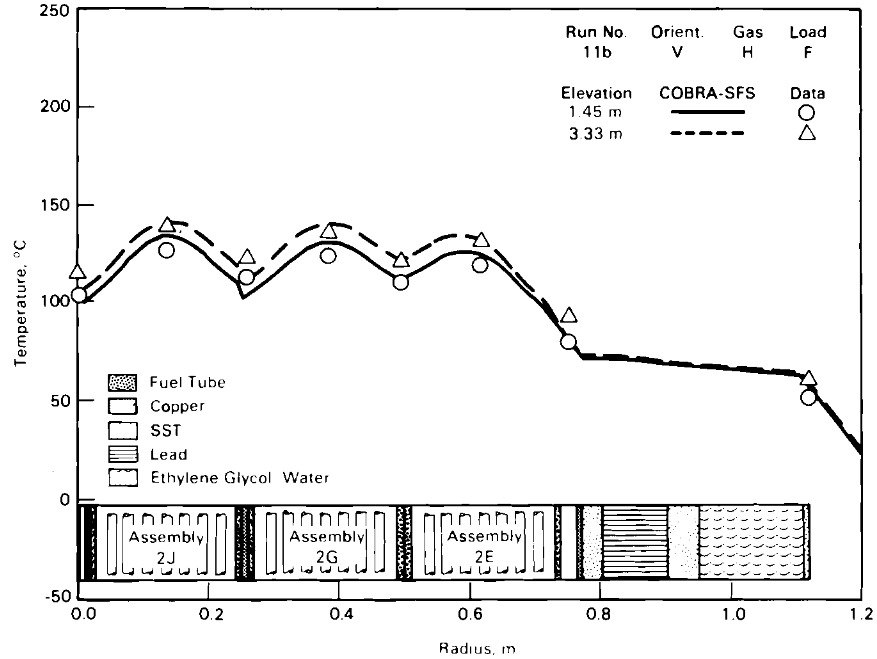
Run No. 11b
Orient. V
Gas H
Load F
Elevation
COBRA-SFS
Data
1.45 m
3.33 m
Fuel Tube
Copper
SST
Lead
Ethylene Glycol Water
Assembly 2J
Assembly 2G
Assembly 2E
Temperature, °C
Radius, m
-50
0
50
100
150
200
250
0.0
0.2
0.4
0.6
0.8
1.0
1.2

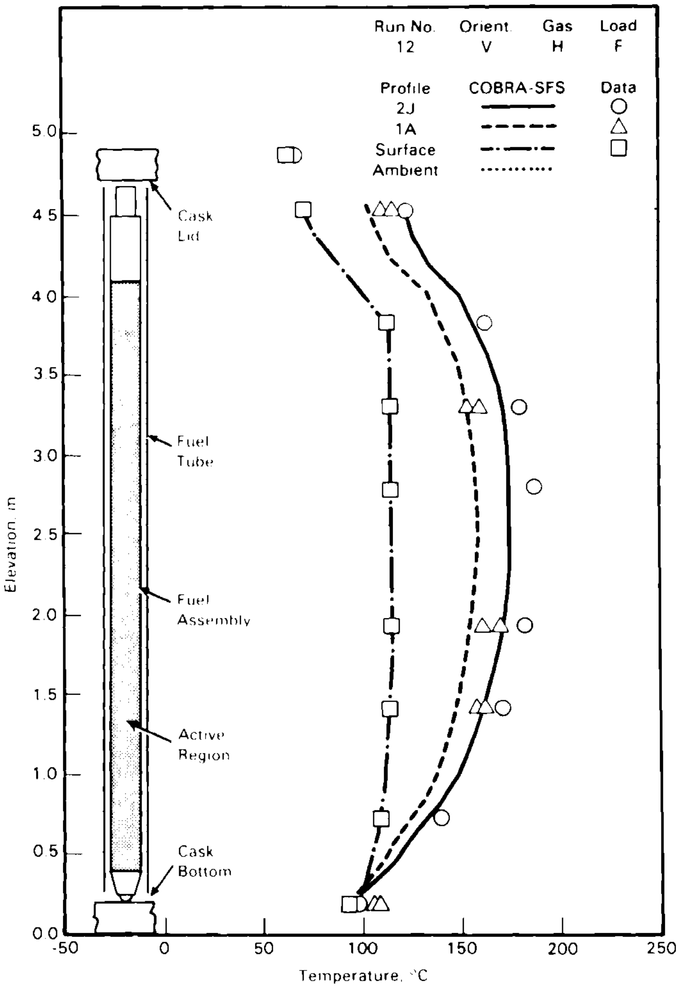
Run No.
12
Orient.
V
Gas
H
Load
F
Profile
COBRA-SFS
Data
2J
1A
Surface
Ambient
Cask Lid
Fuel Tube
Fuel Assembly
Active Region
Cask Bottom
Elevation, m
0.0
0.5
1.0
1.5
2.0
2.5
3.0
3.5
4.0
4.5
5.0
-50
0
50
100
150
200
250
Temperature, °C

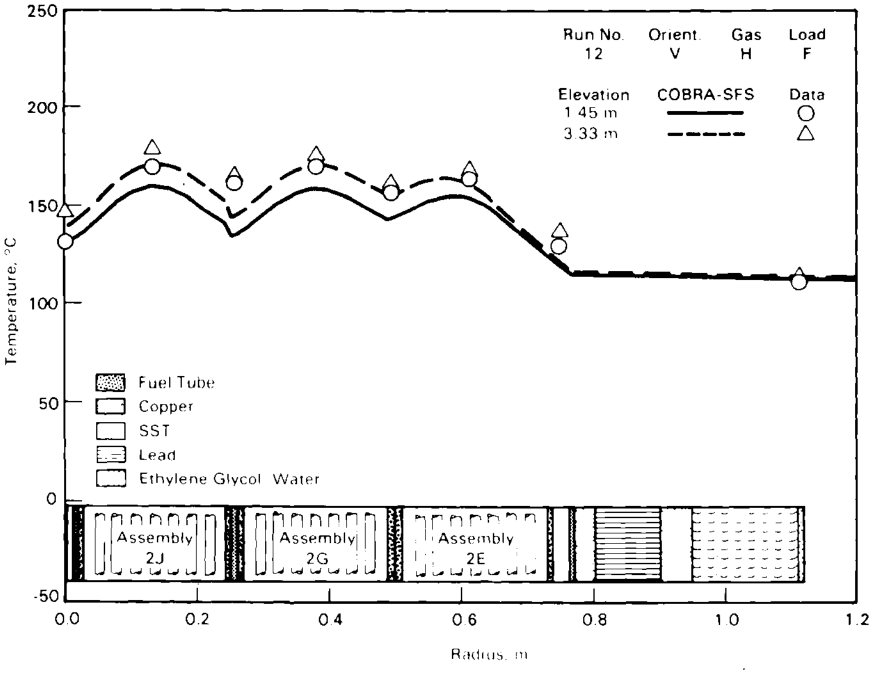
Run No.
12
Orient.
V
Gas
H
Load
F
Elevation
COBRA-SFS
Data
1.45 m
3.33 m
Fuel Tube
Copper
SST
Lead
Ethylene Glycol Water
Assembly 2J
Assembly 2G
Assembly 2E
Temperature, °C
-50
0
50
100
150
200
250
0.0
0.2
0.4
0.6
0.8
1.0
1.2
Radius, m

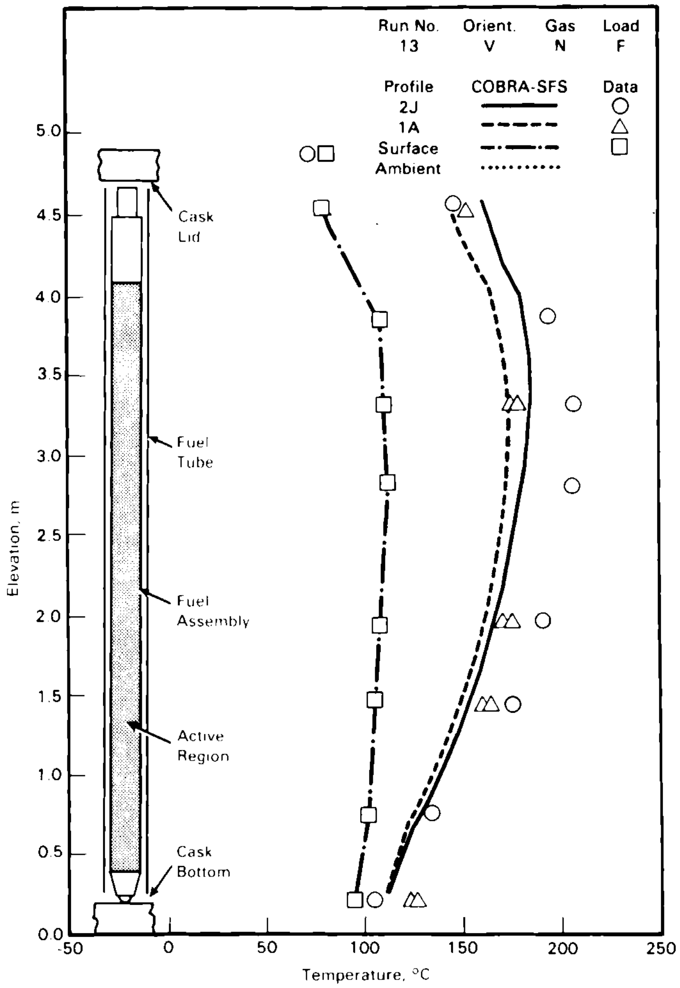

Run No. 13
Orient. V
Gas N
Load F
Profile
COBRA-SFS
Data
2J
1A
Surface
Ambient
Cask Lid
Fuel Tube
Fuel Assembly
Active Region
Cask Bottom
Elevation, m
0.0
0.5
1.0
1.5
2.0
2.5
3.0
3.5
4.0
4.5
5.0
-50
0
50
100
150
200
250
Temperature, °C

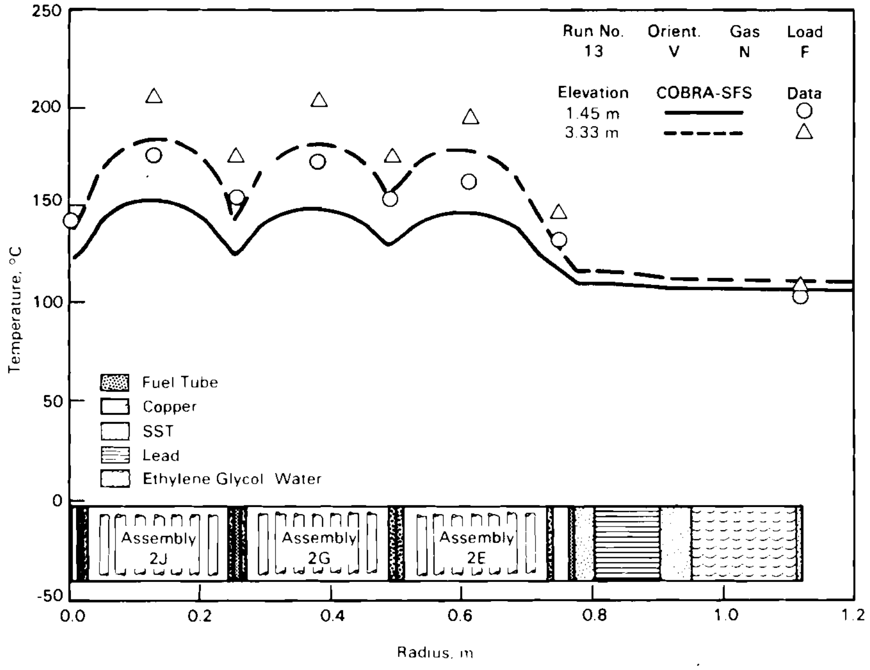

Run No. 13
Orient. V
Gas N
Load F
Elevation
COBRA-SFS
Data
1.45 m
3.33 m
Fuel Tube
Copper
SST
Lead
Ethylene Glycol Water
Assembly 2J
Assembly 2G
Assembly 2E
Temperature, °C
-50
0
50
100
150
200
250
0.0
0.2
0.4
0.6
0.8
1.0
1.2
Radius, m

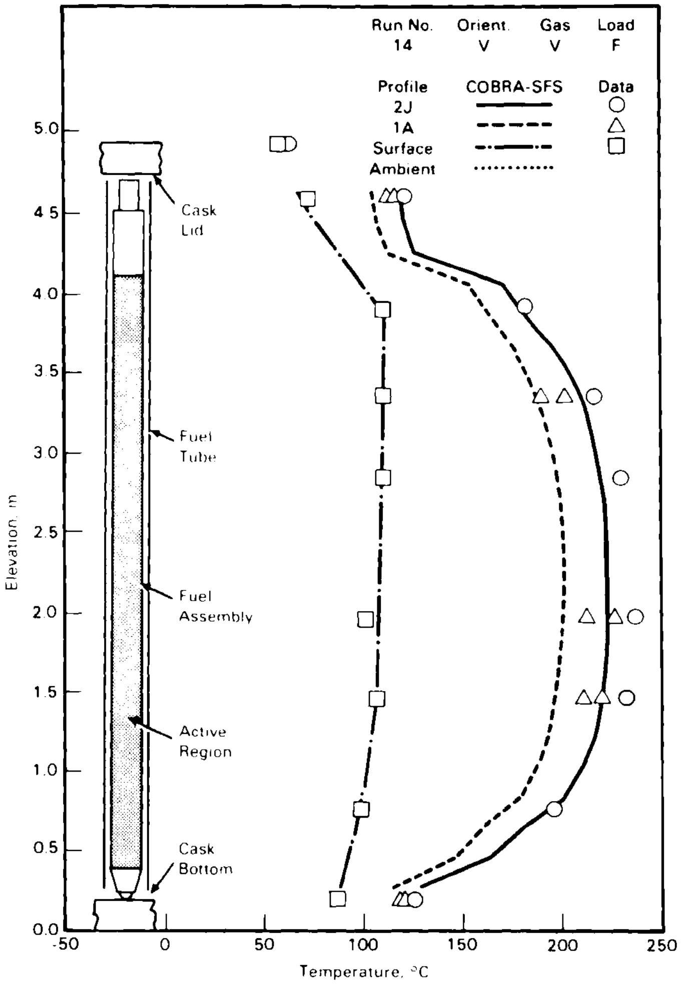

Run No. 14
Orient. V
Gas V
Load F
Profile
COBRA-SFS
Data
2J
1A
Surface
Ambient
Cask Lid
Fuel Tube
Fuel Assembly
Active Region
Cask Bottom
Elevation, m
0.0
0.5
1.0
1.5
2.0
2.5
3.0
3.5
4.0
4.5
5.0
-50
0
50
100
150
200
250
Temperature, °C

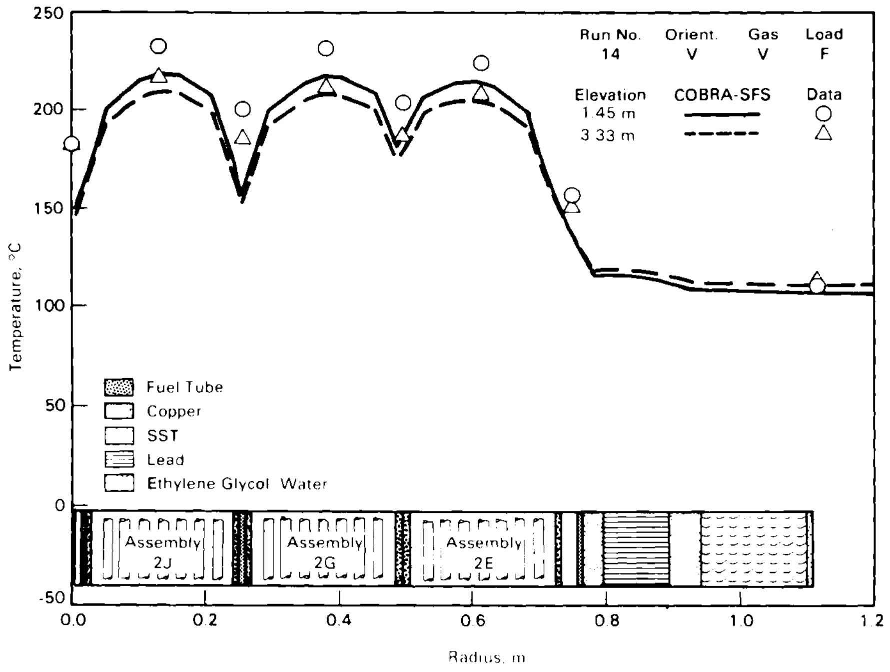

Run No. 14
Orient. V
Gas V
Load F
Elevation
COBRA-SFS
Data
1.45 m
3.33 m
Fuel Tube
Copper
SST
Lead
Ethylene Glycol Water
Assembly 2J
Assembly 2G
Assembly 2E
Temperature, °C
250
200
150
100
50
0
-50
0.0
0.2
0.4
0.6
0.8
1.0
1.2
Radius, m

DISTRIBUTION

No. of
Copies

OFFSITE

110 DOE Technical Information
Center

R. Bown
U.S. Department of Energy
Office of Civilian Radioactive
Waste Management
RW-30
Washington, DC 20545

J. Epstein
U.S. Department of Energy
Office of Civilian Radioactive
Waste Management
RW-30
Washington, DC 20545

J. R. Hilley
U.S. Department of Energy
Office of Storage and
Transportation Systems
Washington, DC 20545

D. E. Shelor
U.S. Department of Energy
Office of Civilian Radioactive
Waste Management
RW-32
Washington, DC 20545

H. Steinburg
U.S. Department of Energy
Office of Storage and
Transportation Systems
RW-33
1000 Independence Ave.
Washington, DC 20585

No. of
Copies

W. Stringfield
U.S. Department of Energy
Office of Civilian Radioactive
Waste Management
Washington, DC 20545

C. P. Gertz
U.S. Department of Energy
Idaho Operations Office
550 2nd Street
Idaho Falls, ID 83401

K. G. Golliher
U.S. Department of Energy
Albuquerque Operations Office
P.O. Box 5400
Albuquerque, NM 87115

L. Lanni
U.S. Department of Energy
Magnetic Fusion and Nuclear
Division
San Francisco Operations Office
1333 Broadway
Oakland, CA 94612

C. Matthews
U.S. Department of Energy
Oak Ridge National Laboratory
P.O. Box E
Oak Ridge, TN 37830

D. Veith
U.S. Department of Energy
Nevada Operations Office
P.O. Box 14100
Las Vegas, NV 89114

No. of
Copies

N. H. Davison
U.S. Nuclear Regulatory
Commission
Office of Nuclear Materials
Safety and Safeguards
Washington, DC 20555

C. Feldman
U.S. Nuclear Regulatory
Commission
Office of Nuclear Regulatory
Research
MS 5650 NL
Washington, DC 20555

W. Lake
U.S. Nuclear Regulatory
Commission
Office of Nuclear Materials
Safety and Safeguards
Washington, DC 20555

C. H. Peterson
U.S. Nuclear Regulatory
Commission
Office of Nuclear Material
Safety and Safeguards
MS 62355
Washington, DC 20555

J. A. Carr
Battelle Memorial Institute
Office of Nuclear Waste
Isolation
505 King Avenue
Columbus, OH 43201

B. A. Rowles
Battelle Memorial Institute
Office of Nuclear Waste
Isolation
505 King Avenue
Columbus, OH 43201

W. R. Juergens
Brooks & Perkins
12633 Inkster Road
Livonia, MI 48150

No. of
Copies

R. Kunita
Carolina Power & Light Co.
P.O. Box 1551
Raleigh, NC 27602

C. K. Anderson
Combustion Engineering, Inc.
1000 Prospect Hill Road
Windsor, CT 06095

Ebasco Services Incorporated
Two World Trade Center
New York, NY 10048

D. H. Schoonen
EG&G
P.O. Box 1625
Idaho Falls, ID 83415

P. E. Eggers
Eggers Ridihalgh Partners, Inc.
1445 Summit Street
Columbus, OH 43201

FLUOR Engineers, Inc.
Advanced Technology Division
P.O. Box C-11944
Santa Anna, CA 92711-1944

J. W. Doman
Morris Operation
General Electric Company
7555 E. Collins Road
Morris, IL 60450

E. E. Voiland
General Electric Company
Nuclear Fuel & Services
Division
7555 E. Collins Road
Morris, IL 60450

R. Anderson
General Nuclear Services, Inc.
135 Darling Drive
Avon, CT 06001

No. of
Copies

V. J. Barnhart
General Nuclear Services, Inc.
135 Darling Drive
Avon, CT 06001

L. B. Ballou
Lawrence Livermore National
Laboratory
P.O. Box 808
Livermore, CA 94550

M. W. Schwartz
Lawrence Livermore National
Laboratory
P.O. Box 808
Livermore, CA 94550

C. F. Smith
Lawrence Livermore National
Laboratory
P.O. Box 808
Livermore, CA 94550

G. Bosler
Los Alamos National Laboratory
Los Alamos, NM 87545

P. Rinard
Los Alamos National Laboratory
Los Alamos, NM 87545

H. Lowenburg
Lowenburg Associates
1091 Rosemont Drive
Rockville, MD 20852

J. Houston
Nuclear Assurance Corporation
5720 Peach Tree Parkway
Norcross, GA 30092

R. T. Haelsig
Nuclear Packaging Inc.
1010 S. 336th Street
Federal Way, WA 98003

No. of
Copies

L. E. Wiles
Numerical Applications, Inc.
825 Goethals Drive
Richland, WA 99352

J. V. Massey
NUTECH Engineers
145 Martinvale Lane
San Jose, CA 95116

C. V. Parks
Oak Ridge National Laboratory
P.O. Box X
Oak Ridge, TN 37831

D. Woods
Ralph M. Parsons Co.
100 West Walnut Street
Pasadena, CA 91124

T. L. Sanders
Sandia National Laboratory
Albuquerque, NM

M. E. Mason
Transnuclear, Inc.
1 N. Broadway
White Plains, NY 10601

B. R. Teer
Transnuclear, Inc.
1 N. Broadway
White Plains, NY 10601

TRW, Inc.
Energy Development Group
Suite 201
200 Union Blvd.
Denver, CO 80228

C. E. King
Uranium Mgt. Corp.
175 Curtner Ave. MC 620
San Jose, CA 95125

No. of
Copies

M. L. Smith
Virginia Power Co.
P.O. Box 26666
Richmond, VA 23261

A. R. Hakl
Westinghouse Electric Corp.
Waste Technology Services
Division
P.O. Box 10864
Pittsburg, PA 15236

J. H. Saling
Westinghouse Electric Corp.
Waste Technology Services
Division
P.O. Box 10864
Pittsburg, PA 15236

B. A. Chin
Mechanical Engineering Dept.
247 Wilmore Labs
Auburn University, AL 36849

ONSITE

2 DOE Richland Operations Office

R. D. Izatt
J. P. Collins

2 Rockwell Hanford Operations

C. L. Brown
G. T. Harper

No. of
Copies

51 Pacific Northwest Laboratory

G. H. Beeman
L. W. Brackenbush
B. M. Cole
J. M. Cuta
J. M. Creer (10)
M. D. Freshley
E. R. Gilbert
R. J. Guenther
R. L. Goodman
R. J. Hall
C. M. Heeb
U. P. Jenquin
A. B. Johnson, Jr.
D. K. Kreid
N. J. Lombardo
R. A. McCann
J. L. McElroy
M. A. McKinnon (10)
T. E. Michener
D. F. Newman
D. R. Oden, Jr.
D. R. Rector
R. A. Stokes
J. E. Tanner
D. S. Trent
C. L. Wheeler
Technical Information (5)
Publishing Coordination (2)